UNIVERSITY OF CALIFORNIA

Los Angeles

Constitutive Modeling of Peat in Dynamic Simulations

A dissertation submitted in partial satisfaction of the

requirements for the degree Doctor of Philosophy

in Civil Engineering

by

Samuel Yniesta

2016

ABSTRACT OF DISSERTATION

Constitutive Modeling of Peat in Dynamic Simulations

by

Samuel Yniesta

Doctor of Philosophy in Civil Engineering

University of California, Los Angeles, 2016

Professor Scott Joseph Brandenberg, Chair

Peat is a highly compressible organic material with unique properties that differ from inorganic mineral soils, which poses a challenge in their constitutive modeling. The main specific challenge addressed in this dissertation include matching dynamic properties (i.e., modulus reduction and damping behavior). Constitutive models used in 1D site response typically use modulus reduction and damping curves as input parameters, and usually introduce a misfit of the desired behavior, particularly at high strains. This is problematic for peat because large strains are expected to develop during cyclic loading due to the peat softness.

Nonlinear one dimensional ground response models generally present a compromise between fitting the backbone curve or the hysteretic damping curve. Fitting the damping curve depends on unloading and reloading rules. Most of the models use Masing rules or extended Masing to correct the overdamping at high strains resulting from using Masing rules. Frequency dependent Rayleigh damping is used to introduce damping at low strains. I present a new formulation of unloading and reloading rules completely departing from Masing rules. The main idea is to rotate the axis of the stress strain curve and change the point of reference to calculate the stress at the next time step. The small strain damping is made hysteretic by increasing the initial departure tangent modulus when unloading, in a way consistent with what has been observed in laboratory tests. The unloading-reloading rule is implemented in a nonlinear code and is able to match any backbone and hysteretic damping without Rayleigh damping.

Dynamic curves are typically not used in 2D or 3D models because their inclusion in a plasticity framework is complicated due to their dependence on confining pressure, which can change during earthquake loading (e.g. when excess pore pressure develops under undrained loading). Hence, the damping behavior is not an input of current 3D constitutive models. In order to facilitate the inclusion of dynamic curves in constitutive models, I present a new concept that plots modulus reduction and damping curves against stress ratio instead of shear strain. This results in pressure-independent modulus reduction and damping curves for three empirical relationships commonly-used to derive modulus reduction and damping curves. This finding is useful for implementation in one-dimensional effective stress ground response analysis codes for undrained loading conditions, and in advanced plasticity models.

I then extend the developed unloading-reloading rule and include it in a 3D constitutive model that uses modulus reduction and damping curves that are plotted against stress ratio by using the aforementioned concept. The formulation of the model allows to match dynamic properties (i.e., modulus reduction and damping curves), in 1D and 2D site response. At large strains the strength is controlled by a bounding surface algorithm following the formulation from Dafalias and Manzari (2004). The volumetric response is controlled by a dilation surface that introduces plastic volumetric strains based on deviatoric plastic strains. Most of the input parameters are well-known engineering properties easily measured in laboratory tests. Default values are defined for the input parameters that are not easily measured. I present the implementation of the model in FLAC and some typical predictions of the model through simulations of cyclic triaxial and simple shear tests. Finally, I present the calibration of the model for Sherman Island peat based on laboratory tests, and the performance of the model in 1D site response simulations.

The dissertation of Samuel Yniesta is approved.

Anne Lemnitzer

Jonathan Paul Stewart

Mladen Vucetic

Scott Joseph Brandenberg, Committee Chair

University of California, Los Angeles

2016

TABLE OF CONTENTS

LIST OF FIGURES

LIST OF TABLES

ACKNOWLEDGEMENTS

This research was funded by the National Science Foundation under grant No. CMMI 1208170. Any opinions, findings, and conclusions or recommendations expressed in this material are those of the author and do not necessarily reflect the views of the National Science Foundation.

Chapter 3 uses text and figures from three publications authored by the research group I was part of. The publications are: Cappa et al. (2014a), Lemnitzer et al. (2015) and Yniesta et al. (2015). Chapter 4 is a version of Yniesta and Brandenberg (2016) submitted for publication to the Journal of Geotechnical and Geoenvironmental Engineering. Chapter 5 is a version of Yniesta et al. (2016) submitted for publication to the Journal of Soil Dynamics and Earthquake Engineering.

I would like to warmly thank my dissertation committee, Professor Anne Lemnitzer, Professor Jonathan P. Stewart and Professor Mladen Vucetic, and my advisor, Professor Scott Brandenberg, for their help and guidance over the last four and half years. Professor Brandenberg, your support throughout this journey was incredible, and being your advisee confirmed my intention to become a professor. I hope I will become the kind of professor you are. You always find time for your students, no matter how busy you are, and as a graduate student I felt valued.

During my time at UCLA in the Civil and Environmental Engineering Department, I found an incredibly welcoming and friendly work environment. I would like to thank the professors, students, and staff of the department. In particular, I would like to thank Maida,

Erika, Paula and Jesse, who helped me with all of my administrative questions and problems.

A large part of this dissertation was written on the second floor of Boelter Hall in a place often referred to as “the dungeon”. I would like to thank my “dungeonmates” for their support and the laughs they gave me. In no particular order, thank you to: Sean, Mandro, Paolo, Margo, Ali, Kioumars, Bahar, Yi Tyan, Grace, Eva, and Dong Youp. I would like to thank Ben for always having good advice and for providing a couple of extremely valuable Mathcad sheets. Our discussions around coffee or while playing racquetball always gave me a lot to think about, and I learned a lot working with you.

Another part of my doctoral work was done at UC Davis, working on centrifuge tests with Riccardo Cappa. Riccardo, it was amazing to get to work with you for this project. We got very lucky to be paired together, and I like to think we were a good team! We were also lucky to get the help of the whole Center for Geotechnical Modeling staff, and I would like to kindly thank them. Our time at UC Davis was extremely enjoyable thanks to the people we met there, and in particular I would like to thank Mohammad Khosravi with whom we spent countless hours working on our respective centrifuge models, and Katerina Ziotopoulou who helped me immensely with FLAC and with the implementation of user-defined constitutive models.

Outside of my doctoral work, I would like to thank my friends at UCLA, in particular my soccer buddies for keeping me sane, and relatively in shape! I loved our bi-weekly workout, and I am going to miss the warm Californian weather in February.

Being far away from home was not always easy, but I knew I had the support of my friends and family in France, and I want to thank them for always being there for me. While the distance and the time difference was challenging, it felt like I had never left when I went back to France.

Finally, I would like to thank Katie, who not only supported me, but also helped me practice my presentations in French and in English. The support you gave me over the last few months helped me get through the process of writing this dissertation. It is now my turn to do the same for you.

CURRICULUM VITAE

2009	D.U.T. (Technical University Diploma) in Civil Engineering (2-year Degree) Université Claude Bernard Lyon 1 – Institut Universitaire de Technologie A, Villeurbanne, France
2012	M.S. in Civil Engineering Ecole Spéciale des Travaux Publics (ESTP), Paris, France
2012	M.S. in Civil and Environmental Engineering Department of Civil and Environmental Engineering University of California, Los Angeles (UCLA), Los Angeles, CA
2011-2013	Teaching Assistant Department of French and Francophone Studies University of California, Los Angeles (UCLA), Los Angeles, CA
2015	Teaching Assistant Department of Civil and Environmental Engineering University of California, Los Angeles (UCLA), Los Angeles, CA
2012-2016	Graduate Research Assistant Department of Civil and Environmental Engineering University of California, Los Angeles (UCLA), Los Angeles, CA

SELECTED PUBLICATIONS AND PRESENTATIONS

Journal Publications:

Yniesta, S., Lemnitzer, A., Cappa, R., and Brandenberg, S.J. (2015) "Vacuum Pluviation Device for Saturating Sand "*Geotechnical Testing Journal*, 38 (3), 355-360

Lemnitzer, A., Cappa, R., **Yniesta, S.** and Brandenberg, S.J. "Centrifuge Testing of Model Levees atop peaty soils: experimental data". *Earthquake Spectra* (accepted for publication)

Yniesta, S., Brandenberg, S.J., "Stress-Ratio-Based Interpretation of Modulus Reduction and Damping Curves" *Journal of Geotechnical and Geoenvironmental Engineering* (under review)

Yniesta, S., Brandenberg, S.J., and Shafiee A. "One-dimensional Non-linear Model for Ground Response Analysis" *Soil Dynamics and Earthquake Engineering* (under review)

Conference Papers:

Yniesta, S., and Brandenberg, S.J. "Unloading Reloading Rule for a One-dimensional Non-linear Model for Site Response Analysis" *Proceedings*, 6th International Conference on Earthquake Geotechnical Engineering (6ICEGE), Christchurch, New Zealand, November 1-4, 2015

Cappa, R., **Yniesta, S.,** Brandenberg, S.J and Lemnitzer, A. "Settlements and excess pore pressure generation in peaty soils under embankments during cyclic loading" *Proceedings*, 6th International Conference on Earthquake Geotechnical Engineering (6ICEGE), Christchurch, New Zealand, November 1-4, 2015

Cappa, R., **Yniesta, S.**, Lemnitzer, A., Brandenberg, S. and Shafiee, A. (2015). "Settlement Estimations of Peat during Centrifuge Experiments " *Proceedings*, International Foundations Congress and Equipment Exposition (IFCEE), San Antonio, Texas, March 17-21, 2015

Yniesta, S., Cappa, R., Lemnitzer, A. and Brandenberg, S. (2015). "Centrifuge Testing of Levees: Saturation Techniques during Model Construction " *Proceedings,* International Foundations Congress and Equipment Exposition (IFCEE), San Antonio, Texas*,* March 17-21, 2015

Cappa, R., **Yniesta, S.**, Lemnitzer, A., Brandenberg, S.J., and Stewart, J.P. (2014). "Centrifuge Experiments to Evaluate the Seismic Performance of Levees on Peaty Soils in the Sacramento-San Joaquin Delta" *Proceedings,* Dam Safety Conference, San Diego, CA, September 21-25, 2014

Data Reports:

Cappa R., **Yniesta S.**, Brandenberg S.J., Lemnitzer A., Stewart J.P. (2014). Averting an Impending Disaster. Data Report for Centrifuge Experiments 12L and 13L. *Data report for NEES* https://nees.org/groups/nees_2012_1161

Cappa R., **Yniesta S.**, Brandenberg S.J., Lemnitzer A., Stewart J.P. (2014). Averting an Impending Disaster. Data Report for Centrifuge Experiments 14L and 15L. *Data report for NEES* https://nees.org/groups/nees_2012_1161

Presentations (Presenters are underlined):

Yniesta, S., and Brandenberg, S.J. "Constitutive Modeling of Peat in Dynamic Simulations of Levees " *Geotechnical and Structural Engineering Congress Phoenix AZ, February 17th, 2016*

Yniesta, S., and Brandenberg, S.J. "Unloading Reloading Rule for a One-dimensional Non-linear Model for Site Response Analysis" *6th International Conference on Earthquake Geotechnical Engineering (6ICEGE), Christchurch, New Zealand, November 1-4, 2015*

Yniesta S., Cappa R., Brandenberg S.J., Lemnitzer A., "Centrifuge Testing of Levees: Saturation Techniques during Model Construction." *Geocongress, San Antonio TX, March 19th 2015*

Yniesta S. "Soil Modeling in Site Response Analysis". *Geotech Round Table, UCLA, February 25th 2015*

Yniesta S "Centrifuge Experiments to Investigate Levee Deformation Potential in the Sacramento San Joaquin Delta." *Presentation to the Department of Water Resources, Sacramento CA, October 23rd 2014*

Yniesta S., Cappa R. (2014). "Centrifuge Experiments to Investigate Levee Deformation Potential in the Sacramento San Joaquin Delta." *CalGeo Expo, UCLA, May 30th 2014*

1 INTRODUCTION

1.1 Presentation of the Sacramento San-Joaquin Delta

1.1.1 History of the Delta

The Sacramento-San Joaquin Delta is the hub of the California water system. It is a 2800 km2 estuary at the confluence of the Sacramento and the San Joaquin rivers. The Delta provides agricultural and urban water to 25 million residents, both in southern and northern California. It is also an agricultural center, generating about 500 millions of dollars every year (http://www.restorethedelta.org/), due to the appropriate climate, the fertile organic soil and continuous fresh water source.

Prior to 1850's, and the gold rush, the Delta was an inland freshwater marsh. Over 60% of the Delta's area was submerged by daily tides, and spring tides could submerge the entire area (Lund et al, 2007). Some natural levees in the Delta have formed over the years from sediments deposited by repeated flooding. In the marsh, the most common plants were tules, able to survive in fresh and salty water. The combination of sediment deposits (because of the flooding) and the dead plants deposits, led to thick deposits of extremely compressible peat. A study from Dexler et al. (2009) concluded that the peat deposit started 6,700 years ago.

During the gold rush, people started to settle in the Delta. The Delta was an attractive place because of the possibility of extensive farming. The nutrient-rich organic soil provided a perfect land for farming. The first settlers built their farms on the natural levees. Once the highland were full, farmers started to reclaim the low-lying areas. They began

placing fill on top of the natural levees, in order to protect their farm against flooding. The Delta became the property of the State of California in 1850, through the Swampland act. The state started selling the Delta lands for one dollar per acre, to encourage reclamation. Local reclamation districts were formed to accelerate the reclamation of the lands. With the creation of levees, “Islands” were created, enclosed by those levees. The levees built at that time were not engineered structures, but were composed of a mix of loose sand, clay and organic matter. A common method of reclamation of the islands was to burn the ground. Although this method was efficient for reclamation, it also increased the subsidence process, which is naturally occurring due to biodegradation. Technologies such as mechanized dredging, fill placement, and pumping of low-lying areas, accelerated the reclamation of the Delta. Between 1860 and 1930, more than 1800 km2 were reclaimed, enclosed by more than 1700 km of levees.

After most of the land was reclaimed, in the late 1920’s, the focus shifted on storing the water and delivering it to more arid areas of the state like the San Joaquin valley and Southern California. At that time the Los Angeles Aqueduct had been completed and providing water across the state was an important challenge. Many saw the Delta and the Sacramento and San Joaquin Rivers as good water sources. The Central Valley Project (CVP) funded in 1933 by the Federal government, was one of the first major projects to use the Delta. The main goals of the project were to deliver water and reduce salinity intrusion to the San Joaquin Valley, especially for agriculture. The CVP changed the Delta from a freshwater estuary with salinity intrusion to a freshwater area. This was achieved by discharging salt water off the Delta with controlled releases from the Shasta Reservoir. Those upstream water releases avoid the salt water to intrude the Delta. Canals were

constructed to deliver water to irrigators in the San Joaquin Valley. In 1960 the State of California enacted the State Water Project to deliver water to Southern California. This was achieved with the construction of the California Aqueduct and pumping stations. Both projects were originally considering constructing a peripheral canal in the eastern margin of the Delta, to avoid relying on the Delta levees when carrying water. The idea of a peripheral canal raised environmental concerns such as pollution and species protection. In 1982 the construction of the canal was rejected by a statewide referendum, and development of an alternative water conveyance system remains a contentious issue today.

Today the Delta provides water to most Californians. Almost 50 percent of California's water supply comes from the Delta. Figure 1-1 shows the distribution of water sources for daily urban demand. About 30% of the water consumption of the two biggest urban areas in California, the San Francisco Bay, and the South Coast, come directly from the Delta (Delta Vision 2008). The Delta is not only an important center for water supply, but it is also an agricultural center and the home of a rich but sensitive ecosystem, with a large variety of species, some unique to the Delta. It also has an important role as a drainage area for polluted agricultural and urban runoff.

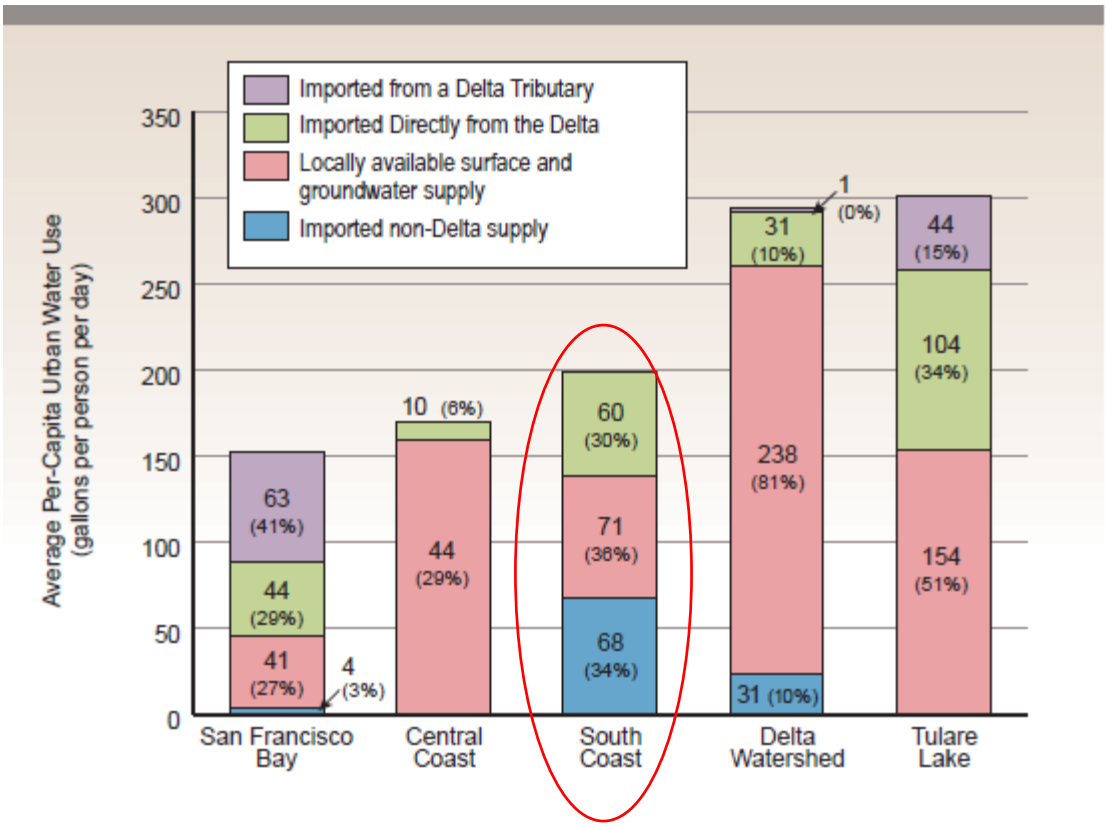

Figure 1-1 Distribution of water sources for daily urban uses in California (Delta Vision 2008)

1.1.2 Seismic Risk

The Delta region is a zone of moderate seismic hazard, with relatively low seismic activity compared to the San Francisco Bay area (Torres et al 2000). However, seismic hazard still constitutes an important threat for the levees and the water supply sustainability.

To evaluate the vulnerability of the levees, we need to first understand seismic hazard in the Delta. This seismicity has been well studied over the years, and has been formally defined by the California Department of Water Resources (DWR) in the section 6 of the DRMS (Delta risk management strategy) project. In the DRMS project, a probabilistic seismic hazard analysis (PSHA) was performed, to estimate the ground motion hazard. The study from the DRMS calculated time dependent hazard from the major Bay area

faults based on the study of the Working Group on California Earthquake Probabilities in 2003 (WGCEP). Three elements are needed to characterize the seismic source: (1) the identification, the location and the geometry of every source, (2) the distribution of magnitudes produced from each source, (3) the slip rate on each fault.

The seismic sources considered time dependent are San Andreas, Hayward/Rodger's Creek, Calaveras, Concord/Green Valley, San Gregorio, Greenville, and Mt. Diablo referred to as the San Francisco Bay Region (SFBR) model faults. The SFBR model has different rupture sources, and it considers several rupture scenarios. A certain weight is given to each scenario and a logic tree is built. The rupture probabilities for different return period (50, 100 and 200 years) are then calculated, also considering 4 starting times (in the time dependent prediction), 2005, 2050, 2100 and 2200.

Other smaller faults are considered, including blind faults, and they are modeled with a time independent probability model. The DRMS report computed hazard curves at several sites throughout the Delta, where the hazard generally increases from east-to-west (Torres 2000). The project pertaining to this dissertation focuses on the site of Sherman Island on the western edge of the Delta, because this is where the peat is the thickest. Sherman Island is one of the most problematic areas in the Delta, and this is the kind of site reproduced in the centrifuge tests presented hereafter. The DRMS report provides the disaggregation analysis for Sherman Island (Figure 1-2) and the contribution of seismic sources to mean peak horizontal acceleration time-dependent hazard (Figure 1-3). The PGA of the 100 years return period, is 0.24g for V_{s30} = 300m/s (1000 ft/s), which corresponds to the Pleistocene soil conditions underlying the peat. The peat is expected to amplify input motions in this range (Kishida et al. 2009). Seismic hazard for 100-year

ground motion at Sherman Island is mainly controlled by nearby events (<20km) and magnitude in the 6 to 7 range.

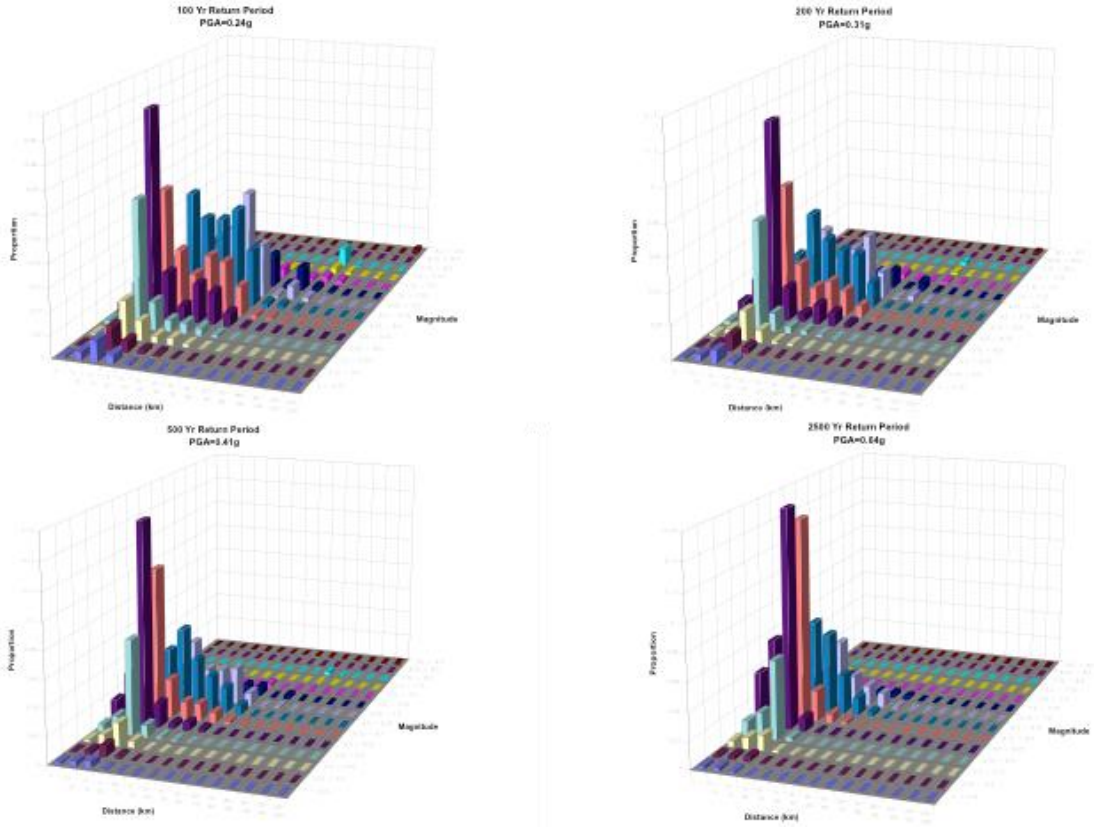

Figure 1-2 Disaggreagation analysis for the Sherman Island site from DRMS (2009)

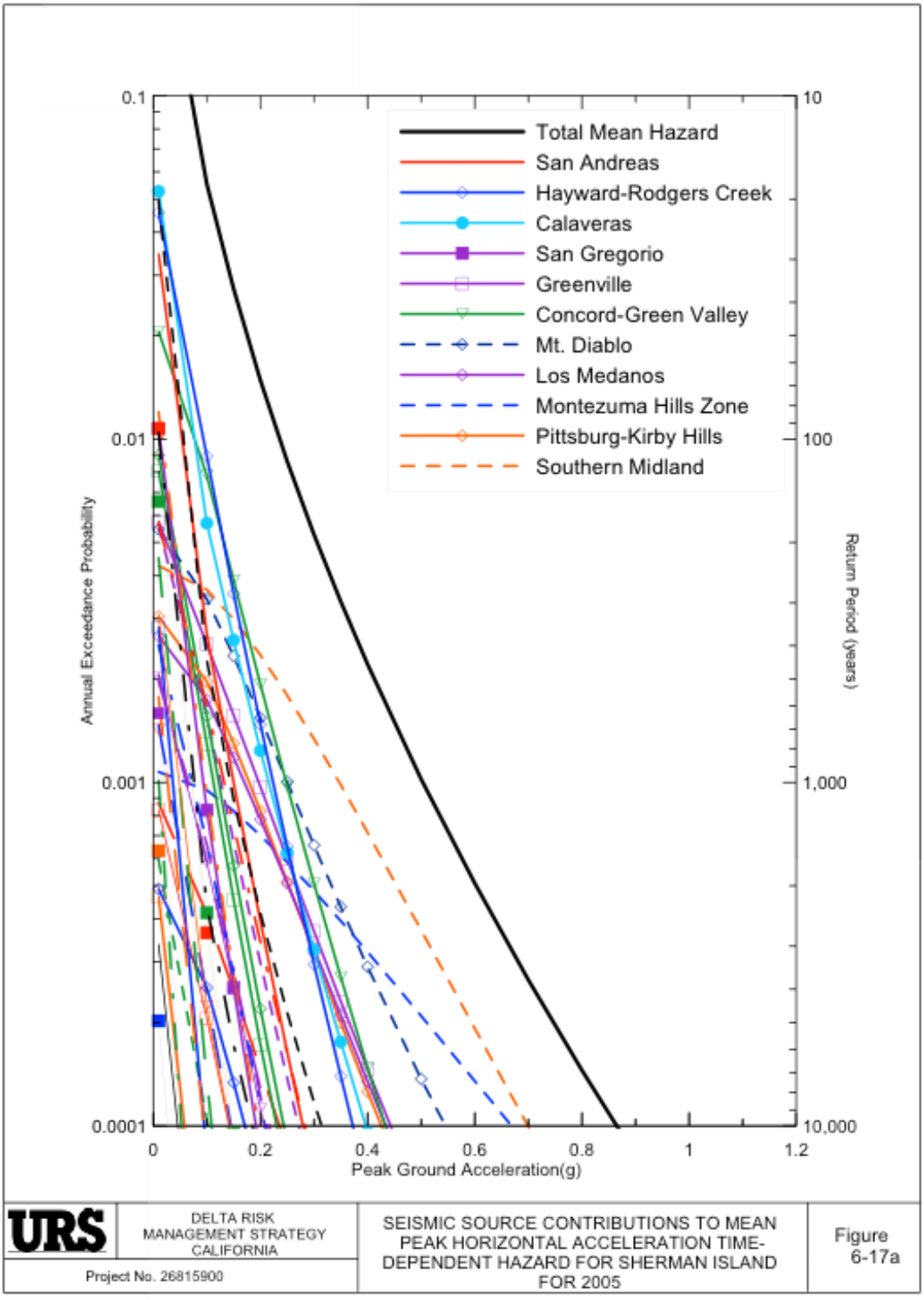

Figure 1-3 Seismic source contributions for Sherman Island (DRMS 2009)

1.1.3 Consequences of Levee Failures

The DRMS study showed that anticipated peak acceleration for a return period of 500 years would be close to 0.4g in the western part of the Delta, which is estimated to potentially cause between 10 to 70 levee failures. Most of these predicted failures are associated with liquefaction of coarse grained soils within and beneath the levees, but the contribution of the peat is not well understood at present, and not integrated in the possible modes of failure. The consequences of multiple failures would be tragic: multiple island floods, introduction of saline water in the islands, which will stop the water intakes at pumping stations. It has been forecast that the water delivery would be interrupted for twenty to thirty months. The worst case scenario would be that such an event could change permanently the regional morphology, and the Californian water system would have to be entirely reconfigured, and the economy and the population of California would be greatly affected by those changes.

In 2004 a single levee breach caused inundation of upper and lower Jones tracts (Figure 1-4). A single breach is easily manageable, and this was quickly repaired. But the cost for repairing was almost $50 million, and the event cost over $200 million in total losses. Several simultaneous breaches would be much more difficult to manage, and the cost would be much higher.

Figure 1-4 Upper Jones tract failure (2004)

1.2 Overview and Scope of the Research Project

Several studies have been lead on the vulnerability of the Delta levees. The DRMS (Delta Risk Management Strategy) have evaluated the potential of levee failures in case of earthquake, based on the liquefaction potential of the levees. The studies usually perform Newmark sliding block analysis and focus on liquefaction triggering to evaluate the vulnerability of the levees. Sand liquefaction behavior is pretty well understood, but peat seismic behavior is not a well-understood topic. Although levees founded on peat have not performed well in seismic events, little research on levees founded on peaty organic soils is available.

Tests in laboratory (Shafiee et al. 2013, Shafiee 2016) have shown that peat, when cyclically loaded, develops excess pore water pressure. Dissipation of the pore pressure leads to post-cyclic volume change. This mechanism has never been considered in the levees vulnerability. This settlement can induce significant cracking and loss of freeboard.

During a seismic event the base of the levee may experience rocking, along with the base shear, an earthquake can impose significant seismic stress demands. Those stress demands, in the levee and beneath it, need to be evaluated to fully understand the vulnerability of the levee. To do so, failure mechanisms should be analyzed. To answer those questions, this project proposed to conduct centrifuge model tests, to study the behavior of levees resting atop peat. The research program of this project consisted in twelve tests in the small centrifuge (1m radius Schaevitz centrifuge) and two tests in the large 9m radius centrifuge. All the tests used the NEES@UCDavis equipment site. The models were heavily instrumented (accelerometers, pore pressure transducers, linear potentiometer, bender elements) to be able to fully capture all the mechanisms acting in the levees failure. These tests provide valuable insights on the behavior of levees under seismic loading and on the post cyclic reconsolidation.

One of the objectives of this research project it to provide tools to practitioners to help them analyze the response of levees founded on peat. One of these tools is a constitutive model for peat since this has never been done before. The results of the centrifuge tests and previous lab tests are used to validate the constitutive model.

1.3 Organization and Scope of this Dissertation

This dissertation is a product of the aforementioned research project. As such, my doctoral work involved centrifuge testing and numerical simulations. The centrifuge tests are discussed in this dissertation but more details can be found in Cappa (2016). Riccardo Cappa was in charge of the centrifuge tests, and his dissertation covers every aspects of the tests, while this dissertation merely summarizes them.

The main focus of the present dissertation is the constitutive modeling of peaty organic soils. Two models are presented in this dissertation. The first model is for use in 1D ground response analyses, and is capable of matching any input modulus reduction and damping curves. This model can be used with any set of modulus reduction and damping curve. Previous models are typically unable to match both curves, and introduce a misfit of the desired behavior, especially at large strains. This is crucial for peat since large strains are expected because of the softness of peat. However the model can be used to model any material.

The second model adapts this 1D model and extends it into a multidimensional model for use in a 2D finite difference program called FLAC. The model is able to match input modulus reduction and damping curves, and a target strength via a bounding surface algorithm. The model follows the concept of critical state soil mechanics, which allow to model the deviatoric and volumetric response of soils, whether this latter is contractive (e.g. for normally consolidated soils) or dilative (e.g. for overconsolidated soils). This model does not account for viscous effect and does not model secondary compression. The integration of viscous effects is part of the future work resulting from this dissertation. Albeit this model is originally derived and calibrated for peat, it can be used for any kind of material in dynamic simulations, and in particular in ground response analyses.

This dissertation, focusing on the constitutive modeling of peaty organic soils, and on numerical simulations, is composed of nine chapters and two appendices.

Chapter 1: Introduction

The present chapter first introduces the Sacramento – San Joaquin Delta, the importance of it, and the associated risks. It then explains the objectives and the scope of the research project that this dissertation is part of.

Chapter 2: Review of Literature

The chapter presents an extensive review of literature that pertains to this dissertation. It is composed of the three distinct parts:

- The first part discusses the behavior of peat as observed by previous researchers. In particular, this section focuses on the compressibility and the shear strength of peat. Finally, the behavior of peat under cyclic loading as observed in laboratory tests is discussed.
- The second part deals with constitutive modeling in 1D ground response analysis. It introduces the theory behind equivalent linear and nonlinear ground response analysis, and presents the input parameters needed. It then presents a few nonlinear constitutive models for total stress 1D ground response analysis. It is shown that models typically use modulus reduction and damping curves as input, but are unable to respect precisely these curves.
- The last part reviews multidimensional constitutive models for soils. It first presents fundamental equations of plasticity and visco-plasticity theory and then presents some important concepts such as bounding surface plasticity and critical state soil mechanics. Finally, some constitutive models are presented.

Chapter 3: Centrifuge Tests of Levees atop Peaty Organic Soils

As part of my doctoral work, and as part of the research project team, I was involved in two large centrifuge tests conducted at UC Davis. Riccardo Cappa from UC Irvine took the lead on centrifuge tests and his dissertation extensively presents the tests and the findings associated with them. This chapter presents a summary of these tests, and also introduces the water-pluviation device that I have developed to use in the centrifuge tests.

Chapter 4: Modulus Reduction and Damping Curves Plotted vs. Stress Ratio

The chapter 4 presents a new concept in which modulus reduction and damping curves are plotted versus stress ratio (η) rather than shear strain. The resulting relationships for G/G_{max} and $D - D_{min}$ vs η are shown to be pressure-independent. Implications and potential uses of the new approach are discussed. This concept is used to integrate modulus reduction and damping curves in the 3D model presented in chapter 6 and can also be used in conjunction with the model presented in chapter 5.

Chapter 5: One Dimensional Nonlinear Model for Matching Modulus Reduction and Damping Curves in Ground Response Analysis

This chapter presents a one-dimensional nonlinear constitutive model for 1D total stress ground response analysis. This model is able to match any input modulus reduction and damping curves. The constitutive equations are presented first, and some examples of the model performance are presented. The derivation of the consistent tangent is presented in Appendix A.

Chapter 6: Formulation of a Nonlinear Constitutive Model for Dynamic Simulations

This chapter presents a nonlinear constitutive model for dynamic simulations. The base of the model is the 1D model presented in chapter 5. The concept presented in chapter 4 is used to adapt the constitutive equations of the 1D model in a multidimensional framework. This chapter provides all the constitutive equations and the input parameters of the model.

Chapter 7: Implementation in a Finite Difference Program: FLAC

The model is implemented in a finite difference program called FLAC. This chapter presents the theory behind FLAC, and how the model is implemented. It provides all the information needed to use the model in FLAC. The model response is illustrated through series of single element simulations. A short parametric study of some of the model's variables is provided.

Chapter 8: Calibration of Model with Laboratory Data and One-Dimensional Ground Response Simulations

The calibration of the model is presented through the calibration of Sherman Island peat based on lab tests. The model is then used in a 1D ground response analysis simulating the centrifuge tests configuration. The simulations are then compared with data and DEEPSOIL simulations.

Chapter 9: Summary and Conclusions, and Future Work

This chapter summarizes the work presented in this dissertation, and in particular the chapters 4 to 8. Future work pertaining to this dissertation and ideas for improvement of the models are presented.

2 REVIEW OF LITERATURE

2.1 Behavior of Peaty Organic Soils

2.1.1 Definition and Structure

The strict definition of peat is a soil with organic content (*OC*) higher than 75%. Organic content is defined as the organic mass of the solids divided by the total mass of the solids. It is obtained by incinerating a soil in a furnace and measuring the weight of organic matter burned (ASTM D2974-07a). Geotechnical engineers use the term “peat” as a generic term for organic soils, regardless of whether or not they comply with the ASTM specification. In this dissertation, I use the term “peat” to refer to organic soils.

Formation of peaty soils comes from the deposition and the accretion of dead plants under water, and their fossilization. The thickness of those peat deposits vary throughout the Delta, from a few meters, up to eleven meters. The organic content of those materials typically decreases with depth and varies from 10% to 80%.The structure of peat is made of layers of fibrous organic remains. The cellular structure of those fibers is mostly full of water. Peat collected from a site on Sherman Island as part of a UCLA field-testing program had water content between 410% and 480% (Shafiee et al 2013), corresponding to an approximate void ratio (*e*) of 6.1 to 7.2. Peat has a low unit weight (10 – 15 kN/m^3), due to its high void ratio and low specific gravity (1.85 for Sherman Island peat, Shafiee et al. 2013).

The fibrous peat particles are also highly permeable, compressible, bendable and degradable. The peat constantly undergoes biochemical decomposition, leading to the creation of gas, and peat is therefore only partially saturated even when submerged.

However, the behavior of peat is less affected by the partial saturation because of its softness (Chaney et al. 1980). Boulanger et al. (1998) tested samples at different B-values (0.96 and 0.81) and did not observe a different behavior.

2.1.2 Earth Pressure at Rest

The coefficient of earth pressure at rest (K_0) for normally consolidated inorganic soils is estimated using Jaky's Equation:

$$K_0 = 1 - \sin \phi'_{cs} \qquad \textit{Equation 2-1}$$

Where ϕ'_{cs} designates the critical state friction angle. Peats typically have a high friction angle and Jaky's equation would result in a very low value of coefficient of earth pressure at rest. Hayashi et al. (2012) studied the coefficient of earth pressure for peat ground in the Hokkaido region and found that for normally consolidated peat, Jaky's equation results in a good prediction and that the coefficient of earth pressure at rest is between 0.2 and 0.5. The low values of coefficient of earth pressure at rest are attributed to the frictional resistance of fibers (Mesri and Aljouni 2007). Hayashi et al. (2012) found that K_0 decreases when the organic content, i.e. the proportion of fibrous material, increases.

The coefficient of earth pressure at rest increases with the overconsolidation ratio, and can be greater than one for heavily overconsolidated peat. In the Sacramento San Joaquin Delta, the peat is overconsolidated beneath levees due to long-term secondary compression. In the free-field, a crust of overconsolidated soil has formed due to dessication, but the peat is essentially normally consolidated beneath the crust (Boulanger et al. 1998).

2.1.3 Permeability

Peat is highly permeable (Mesri and Aljouni 2007) due to its high void ratio combined with large fibrous particles and large pore sizes. For Sherman Island peat, the permeability is usually between 10^{-6} to 10^{-8} m/s, and decreases as void ratio decreases. Figure 2-1 presents the permeability from falling head test for Sherman Island peat from Shafiee et al. (2013), and shows a decrease in permeability with a decrease in void ratio. We typically designate the slope of e versus log k curve with C_k. For Sherman Island peat, this value is about 2.4 (Shafiee et al. 2013), which is consistent with prior observations for clays (e.g. Fox 1999).

Peat has a permeability much higher in the horizontal than in the vertical direction (Mesri and Aljouni 2007). This is due to the fibers being oriented in the horizontal direction, because of the mode of deposition.

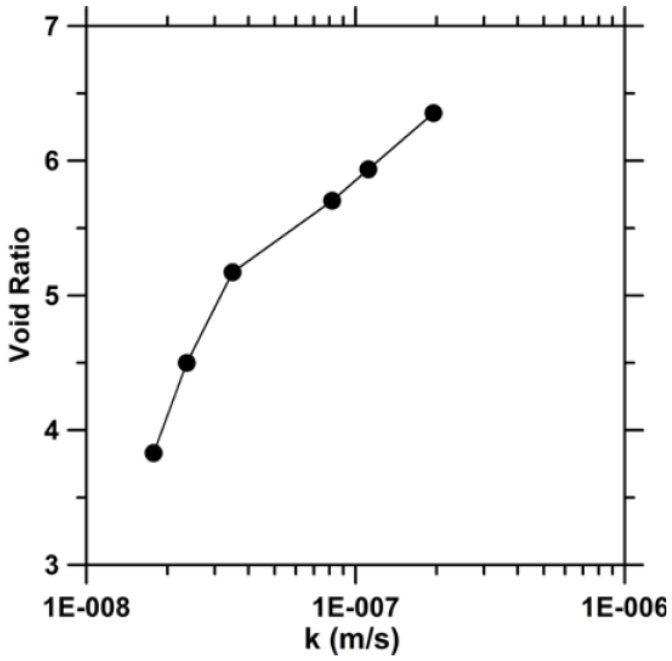

Figure 2-1 Void ratio vs. permeability (Shafiee et al. 2013)

2.1.4 Compressibility

Peat is a highly compressible material. Its compressibility is due to its high void ratio, and the compressible and bendable nature of the fibers that compose the structure of the peat. This compressibility is seen in both primary consolidation and secondary compression. During both phases water is expelled simultaneously from the inside of the peat particles and from between the particles.

2.1.4.1 Primary Consolidation

Primary consolidation of soils is defined as a change of volume due to a change in effective stress. The peat on the Sherman Island has a coefficient of compressibility (C_c) of about 3.9, and a coefficient of recompression (C_r) of about 0.4. Clays that are not highly sensitive have typically lower values than that by roughly an order of magnitude.

Coefficients of compressibility and recompression typically increase with organic content. The coefficient of consolidation c_v associated with Terzaghi's (1925) one-dimensional theory of consolidation is usually between 20 to 100 m^2/year for peat in the compression range, for clay it is usually between 0.5 to 5 m^2/year. For peat this coefficient decreases dramatically when the consolidation pressure increases. In the recompression range c_v can go up to 500m^2/year (Mesri and Aljouni 2007). Therefore primary compression usually occurs quickly.

The primary compression is described by the consolidation curve, which plots the void ratio at the end of primary consolidation (e) versus the logarithm of the vertical effective stress (σ'_v). This consolidation curve can also be plotted with the natural logarithm of the mean effective stress (p'). The consolidation curve depends on the time of end of primary consolidation (t_p) because during primary consolidation, peat will also experience secondary compression. A thick specimen with a longer time of end of primary consolidation will undergo more secondary compression than a thin specimen leading to a lower consolidation curve. Following this idea, a consolidation curve can be associated with a specific time of end of primary consolidation (Bjerrum 1967).

2.1.4.2 Secondary Compression

2.1.4.2.1 Mechanism of Secondary Compression

Secondary compression describes the tendency of soils to contract under constant effective stress, i.e. no change in loading. In mechanics of material this phenomenon is called creep. The secondary compression of peat is one of its significant characteristics, and is due to its compressibility and the constantly undergoing biodegradation. The

phenomenon can usually be described by the C_α/C_c law of compressibility (Mesri and Godlewski 1977), where C_α designates the coefficient of secondary compression. The law states that for any soil there is a unique value of this ratio during the whole secondary compression stage. Peat is showing the highest ratio of C_α/C_c among the soils, around 0.06. For granular soils, this ratio is commonly around 0.02, and for inorganic clays it is around 0.04. The amplitude of secondary compression of peat is important, and it is often hard to distinguish from primary consolidation from test value. Figure 2-2 shows the result of a consolidation test performed at UCLA for a traditional normally consolidated stress-controlled consolidation test in which the vertical load increment was doubled (Shafiee et al. 2013). The end of primary consolidation cannot be distinguished from these curves because the rate of secondary compression is so similar to the rate of primary consolidation.

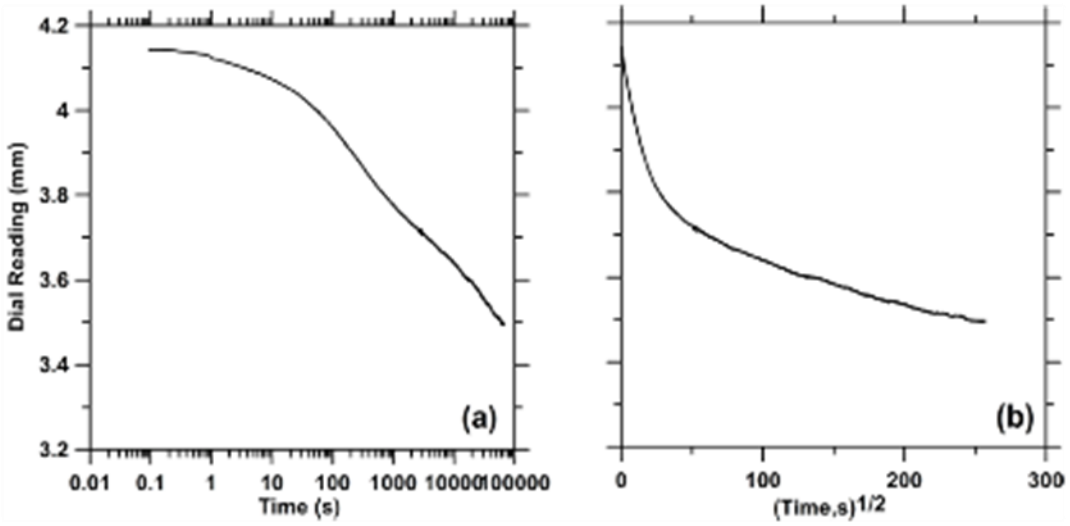

Figure 2-2 Results of a consolidation test on Sherman Island peat, (a) dial reading vs. log time (b) dial reading vs. square root of time (after Shafiee et al. 2013)

The classic interpretation of secondary compression assumes that secondary compression starts at the end of primary consolidation. It also assumes that a “clock”, i.e. a timescale, starts at the application of the load and that the settlement due to secondary compression is calculated at any given time on this clock, using the following formula:

$$s_s = \frac{C_\alpha}{1 + e_0} H_0 \log \frac{t}{t_p} \qquad \textit{Equation 2-2}$$

Where H_0 is the thickness of the layer. In reality, secondary compression is always ongoing, including during primary consolidation. As a thought experiment, the previous equation implies that a thick layer of soil that would take a long time to consolidate would not undergo secondary compression. This interpretation presents a second flaw. If an infinitesimal load was applied on the soil, it would still reset the clock. The settlement due to secondary compression would drastically increase because an increase of one log of time would now occur much faster in the new timescale.

2.1.4.2.2 Reset of Secondary Compression due to Cyclic Straining

Shafiee et al. (2015) studied the influence of cyclic straining on secondary compression. They tested samples of Sherman Island peat in a direct simple shear device, at different cyclic strain amplitude, and measured the settlement. They first observed generation of pore water pressure due to cyclic loading, and settlement associated with the dissipation of excess pore water pressure. Following the consolidation process they measured a continual settlement due to secondary compression and observed that the rate of secondary compression increased after cyclic loading. Figure 2-3 presents the results of

one of their test. In this test, they cyclically sheared a sample of peat at different strain levels. For every strain level, they applied 15 cycles at 1 Hz. During cyclic loading excess pore pressure is generated, and after the end of cyclic loading, the sample consolidates in about a minute. The figure clearly shows an increase in rate of settlement due to cyclic straining. The rate of settlement starts increasing for 1% shear strain. This seems to indicate that there is a cyclic strain threshold for the reset of secondary compression due to cyclic shearing. This increase in settlement has the potential to lead to a loss of freeboard of levees that would not have failed during a seismic event.

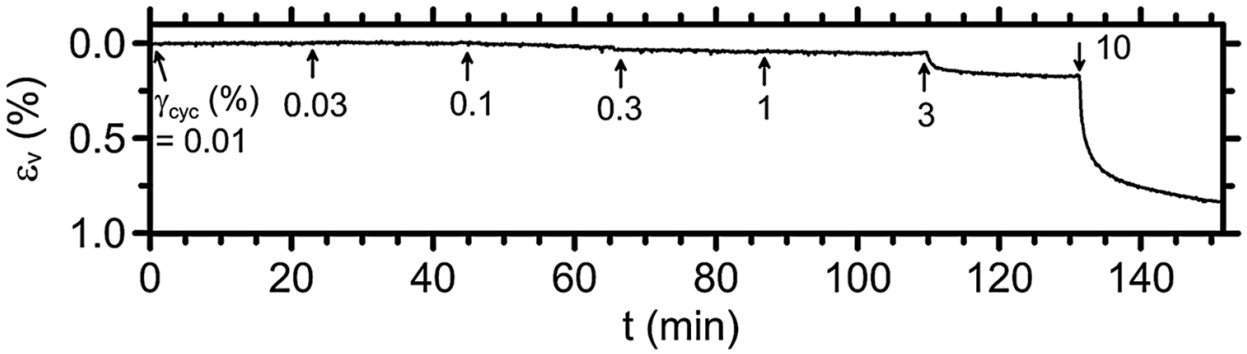

Figure 2-3 Settlement vs. time in a direct simple shear device (Shafiee et al. 2015)

2.1.5 Shear Strength

2.1.5.1 Frictional Behavior

Due to the interlocking, and the sliding resistance of the fibers, peats are frictional materials usually exhibiting high values of friction angle (MacFarlane 1969). Friction angles for peat typically range from 35 to 60° (Mesri and Ajlouni 2007). Marachi et al. (1983) tested peat retrieved in the Delta and measured friction angles of 44°. The peak friction angle is mobilized at shear strain levels that are 5 to 10 times higher than those

required for soft clay deposits (Tressider 1958, Hardy and Thomson 1956, MacFarlane 1969).

Upon shearing the friction angle decreases to a residual value that can be as low as half of the peak value in fibrous peat (Ajlouni 2000, Cola and Cortellazzo 2005). Cola and Cortelazzo attributed the peak value to the reinforcement effect of fibers. Sherman Island peat is not highly fibrous, and no decrease in shear strength was observed at large strains (Shafiee 2016).

2.1.5.2 Effect of Fibers

Because of the mode of deposition, the fibers are oriented horizontally. When sheared the highly fibrous peats exhibit a peak strength due to the tensile strength of the fibers. Cola and Cortellazzo (2005) compared the stress-strain behavior of undisturbed specimens and reconstituted specimens (Cola and Cortellazzo 2005). Figure 2-4 presents the results of their tests. Both specimens were isotropically consolidated to 50 kPa. ANI-50 was the undisturbed sample and ARI-50 was the reconstituted sample. The figure presents the deviatoric stress (q) and the pore pressure (u) versus the axial strain. Disturbing the specimen rearrange the fibers, and remove the reinforcement effect of fibers. As a result, the undisturbed specimens reached a peak shear strength, and the residual strength was the same as the reconstituted sample.

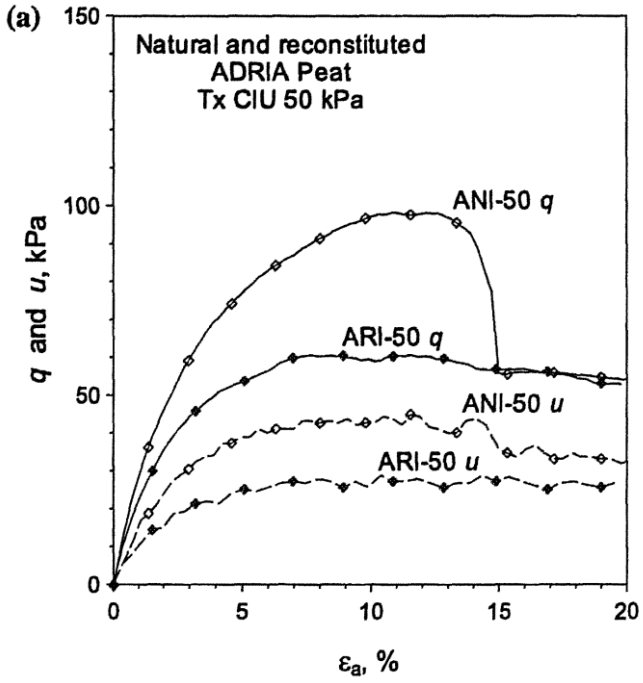

Figure 2-4 Cola and Cortelazzo (2005) Stress-strain curve for undrained triaxial tests on reconstituted (ARI) and undisturbed (ANI) samples

Undrained triaxial tests on undisturbed specimens cut in the vertical and the horizontal direction (parallel to the fibers) showed that the friction angle was greater for specimen cut in the vertical direction. In the vertical direction the friction angle was between 51 and 55°, for horizontal specimens, it was only 35° (Mesri 2007 and Yamaguchi et al. 1985 a,b). However in direct simple shear tests, the friction angle were almost the same in both directions, 40 and 41° (Yamaguchi et al. 1987). This is due to the tensile resistance of fibers. The friction angle being directionally dependent is a clear sign of anisotropy. Sherman Island peat is not a very fibrous peat, and it is expected that it is not a strongly anisotropic material.

2.1.5.3 Undrained Shear Strength

Despite this high friction angle, the undrained shear strength remains relatively low for peat deposit. Undrained shear strength depends on friction angle and effective stress

(Terzaghi et al 1996). For free-field peat deposits the effective stress is very low, due to a low unit weight (from 10 to 15 kN/m^3). Peat consolidated beneath a levee may have much higher consolidation stress, and therefore much higher shear strength. Primary consolidation and secondary compression also increase the shear strength of peat. The decrease of void ratio happening during those phases lead to a higher undrained shear strength (Mesri and Ajlouni 2007). However, even if the shear strength is low, peat have an exceptionally high value of undrained shear strength to consolidation pressure ratio. For peat this ratio is usually over 0.6, whereas for soft clay and silt deposit, it is typically 0.32 (Mesri and Ajlouni 2007). This observed high ratio may be caused by overconsolidation due to secondary compression, because it is complicated to keep a laboratory sample normally consolidated, because secondary compression occurs so quickly.

Marachi et al. (1985) found that in the free field, the undrained shear strength of peat in the Delta is between 10 and 25 kPa. Under the levees where the confining pressure is greater, the undrained shear strength measured was between 25 and 100 kPa.

2.1.6 Mechanical Behavior under Cyclic Loading

2.1.6.1 Dynamic Properties of Peat

Dynamic properties of peats are a major source of uncertainty to evaluate the seismic risk in the Delta. The dynamic properties of peat have been extensively studied (Kramer 2000, Stokoe et al. 1994) and specific studies about dynamic properties of Sherman Island peat are also available (Boulanger et al. 1998, Wehling et al. 2003, Kishida et al. 2009). I present some of their findings in this section.

2.1.6.1.1 Modulus Reduction and Damping Curves

Boulanger et al. (1998) and Wehling et al. (2003) performed numerous cyclic triaxial tests on peat from the Delta, to study their dynamic properties and derive modulus reduction and damping curves. Kishida et al. (2009) summarized their test results along with those from other researchers (Arulnathan 2000, Stokoe et al. 1994). Kishida et al. developed regression equations for Modulus Reduction and Damping Curves. All the researchers studied the influence of the following parameters on modulus reduction and damping curves:

- Effective confining pressure
- Overconsolidation ratio (OCR)
- Organic content

The OCR has little effect on the modulus reduction and damping curves at high confining pressure. In the free field, where the confining pressures are lower, the peat is essentially normally consolidated. Peat is more nonlinear at lower confining pressures, and the damping ratio tends to be higher at lower confining pressures. This is illustrated in Figure 2-5 that presents some of the test results from Wehling et al. (2003).

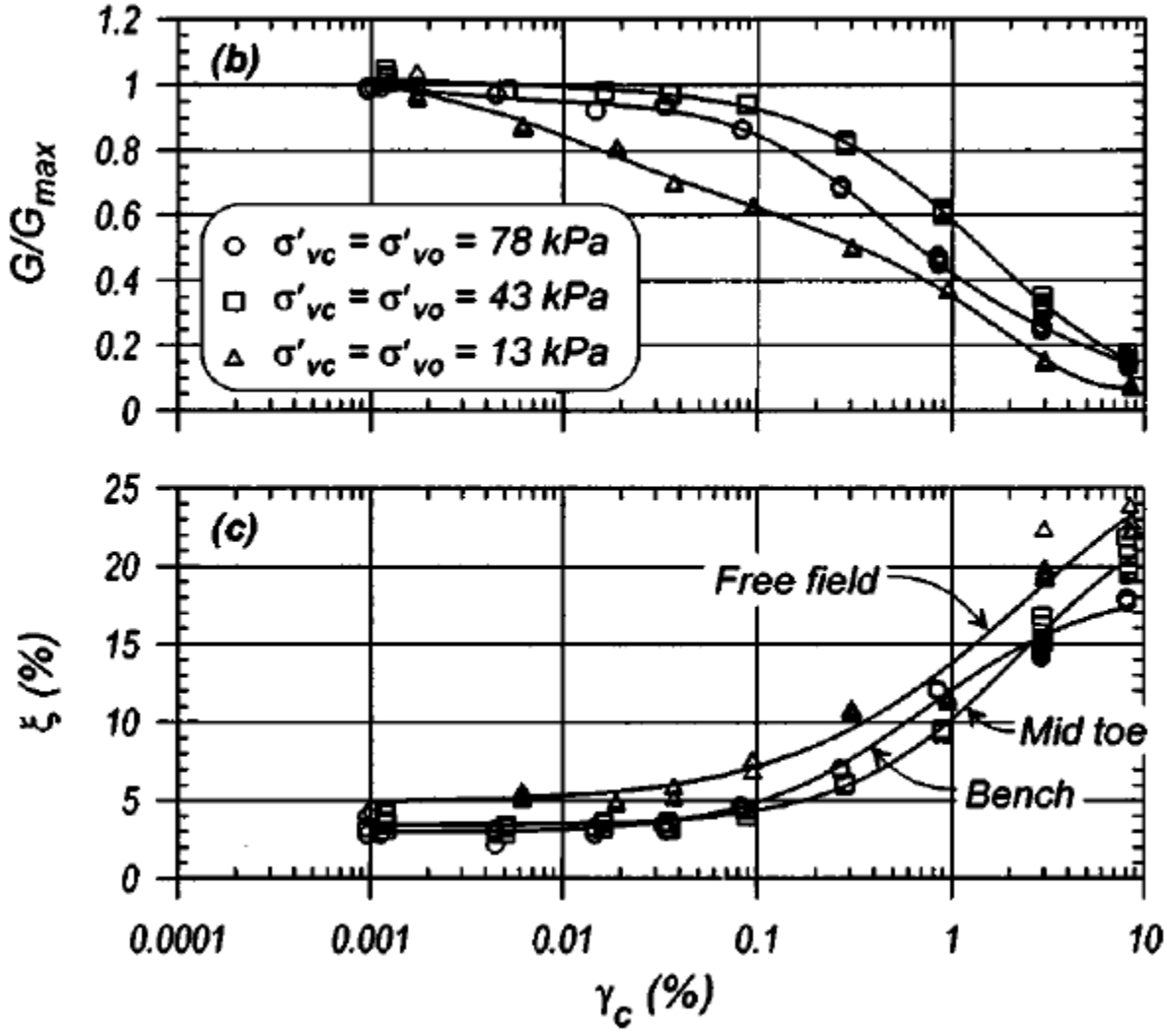

Figure 2-5 Modulus reduction and damping curves for peat in the delta (Wehling et al. 2003)

Kishida et al. (2009) showed that this trend is attenuated for highly organic peats. Figure 2-6 shows that for OC=65% the modulus reduction curve is relatively unaffected by the confining pressure.

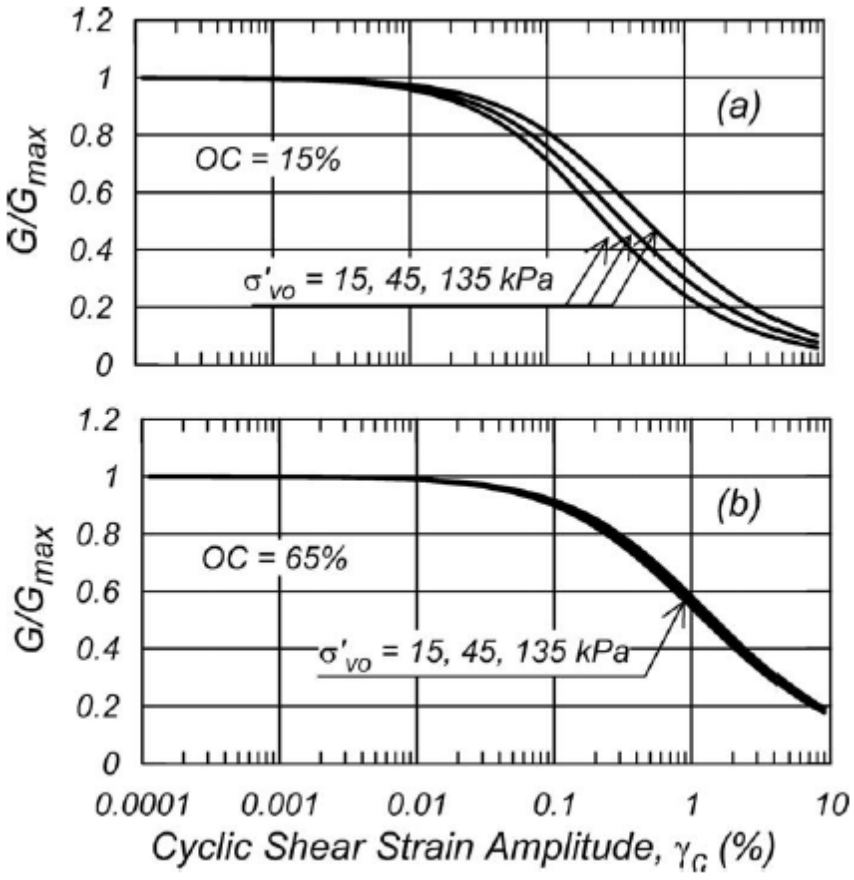

Figure 2-6 Influence of confining pressure and organic content on Modulus reduction curves (Kishida et al. 2009)

Damping ratio curves show the same trend. Figure 2-7 shows the damping ratio curves at different confining pressures for two different organic contents. It shows that the damping curve is less dependent of confining pressures for highly organic soils.

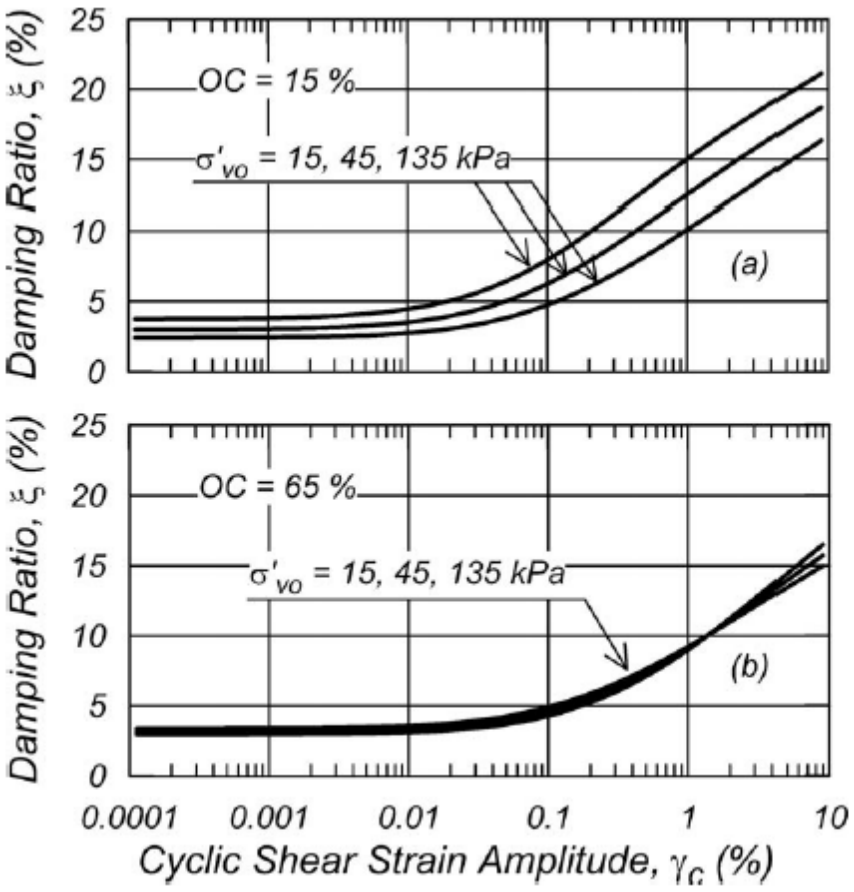

Figure 2-7 Influence of confining pressure and organic content on damping ratio curves (Kishida et al. 2009)

Kishida et al. also found that for higher organic content, the peat is more linear and exhibit less modulus reduction. The small strain damping is unaffected by the organic content and is generally higher than for clays. At higher strain levels, damping ratios increase with organic content. Figure 2-8 presents the modulus reduction and damping curves obtained from their model for different organic content and makes a comparison between their curves and the curves by Vucetic and Dobry (1991).

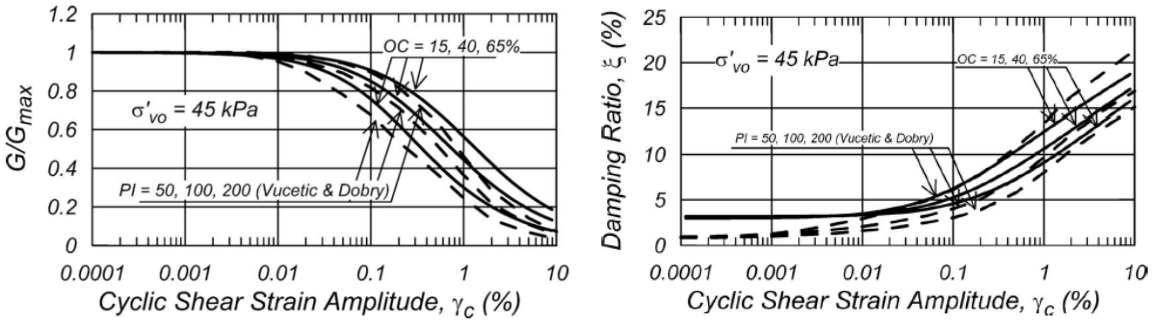

Figure 2-8 Influence of organic content on: (a) modulus reduction curves and (b) damping ratio curves (Kishida et al. 2009)

2.1.6.1.2 Maximum Shear Modulus

The same researchers have studied the maximum shear modulus of peat, based on in situ measurement and lab tests. In the lab the maximum shear modulus is calculated based on a measurement of the shear wave velocity on a small soil sample, and using the relationship between shear modulus and shear wave velocity:

$$G_{max} = \rho * V_s^{\,2} \qquad \textit{Equation 2-3}$$

Boulanger et al. (1998) measured the shear wave velocity of their samples in the lab, and found a shear wave velocity of about 84 m/s. Their samples were retrieved beneath a levee at a depth of about 13 m, and had a relatively high confining pressure (greater than 120 kPa). Their measurement agreed reasonably well with the in situ measurement that were around 87 m/s. Their measured maximum shear modulus was about 10 MPa and they found that the maximum shear modulus increases with loading frequency. In the free field, the shear wave velocity was measured as 25 m/s for highly organic peat, and the maximum shear modulus would be closer to 1 MPa.

Wehling et al. (2003) retrieved samples at a wide range of effective stresses, and found that the log of the maximum shear modulus increases linearly with the log of the effective stress, for a constant OCR. The shear modulus increases with OCR. They formulated the following expression for the maximum shear modulus:

$$\frac{G_{max}}{p_a} = A\left(\frac{\sigma_v'}{p_a}\right)^n OCR^m \qquad \textit{Equation 2-4}$$

Where p_a is the atmospheric pressure, and A, n and m are coefficients. Based on Equation 2-4 Kishida et al. (2006) developed regression equations for A, n and m, depending on the organic content (OC). This allows to calculate the maximum shear modulus (G_{max}), the density (ρ), and the shear wave velocity (V_s), based on the vertical effective stress (σ_v'), the overconsolidation ratio (OCR) and the OC. Kishida et al. found that the maximum shear modulus decreases when organic content increases.

2.1.6.2 Effect of Loading Frequency

Boulanger et al. (1998) studied the effect of loading frequency by studying the response of peat under two loading frequencies, 1 Hz and 0.01 Hz. They found that shear modulus increases and damping ratio decreases when loading frequency increases. Kramer (2000) studied the influence of loading frequency with strain controlled cyclic triaxial tests, with loading frequencies ranging from 0.006 Hz to 10 Hz. A low strains, no trend was discernable because of scatter. Figure 2-9 presents their results at high strains. They found that shear modulus increases by about 10% over a 10-fold increase in frequency. This observation is consistent with what Sheahan et al. (1996) found for clays. The

damping ratio initially decreases with frequency and then increases showing a more intricate behavior than what described by Boulanger et al. (1998).

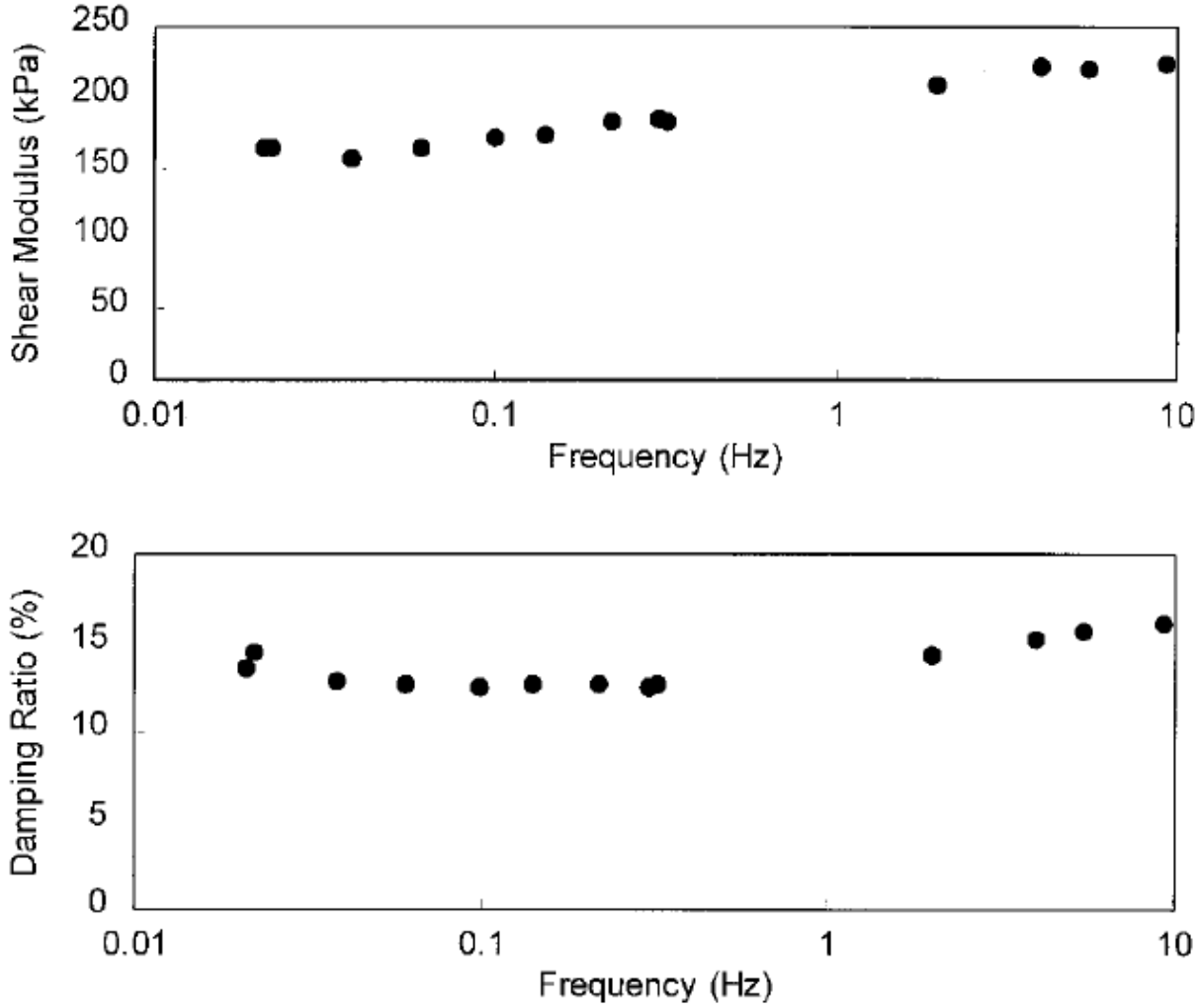

Figure 2-9 Influence on loading frequency on shear modulus and damping ratios (Kramer 2000)

2.1.6.3 Effect of Number of Cycles

Boulanger et al. (1998) and Wehling et al. (2003) studied the influence of the number of cycles by applying 30 cycles of constant amplitude. The cyclic degradation can be evaluated by the degradation parameter t. They found that the value of t is 0.017. Vucetic

and Dobry (1991) measured a degradation parameter of 0.06 for high plasticity clay. Thus the cyclic degradation is minor and negligible.

2.1.7 Influence of Peat on Ground Response

One dimensional site response analyses from Kramer (2000) showed that motions can be deamplified by peat, and that motions in peat can be characterized as having low accelerations, but high displacement amplitudes. Tokimatsu and Sekiguchi (2007) studied the acceleration recordings from three stations in Japan, one on rock, one of soft soil, and one on peat. They found that accelerations recorded on peat were 1.5 times greater than on rock and on soft soil. This suggests that peat can transmit certain kind of motions better than rock and soft soil.

Kishida et al (2009), performed site response analyses for the Sacramento San Joaquin Delta. They found that when the shaking is small the motion is amplified for every period. When the amplitude of shaking increases, the motion at lower periods (i.e. high frequencies) is deamplified, but the motion at higher period such as 1.0s is still amplified. Ground response of peat therefore poses a serious threat for the levees, because of its capability to amplify ground motion.

2.2 Unidimensional Modeling of Soil Behavior

The formulation of the three dimensional constitutive model presented in this dissertation is based on a constitutive model derived to be used in one dimensional ground response analysis. The constitutive equations and the performance of the one dimensional model are presented in Chapter 5. This section presents a literature review on soil modeling in

1D ground response analysis. The theoretical background of one dimensional ground response analysis is shortly described, and a few models are presented.

2.2.1 One Dimensional Ground Response Analysis

Site-Specific ground response analysis, often referred as site response analysis, simulate the propagation of ground motion through layers of soil to evaluate site effects. Site effects are changes in intensity and frequency content of ground motion that influence the response of structures. Site response analysis can be performed in one, two or three dimensions, to study the effect of shaking in multiple directions. The most commonly used method is one dimensional (1D) ground response analysis, where the vertical propagation of horizontal shear waves through a column of soil is evaluated. In one dimensional ground response, the soil is essentially defined by its stiffness through its shear modulus (G), its ability of dissipating energy through its damping ratio (ζ), and its mass, through its mass density (ρ).

There are multiple ways to perform a one dimensional ground response analysis. The generation, redistribution and dissipation of excess pore water pressure can be modeled (Effective stress analysis), or omitted (total stress analysis), the soil behavior can be represented by different methods, and the calculations can be performed in the Time or Frequency domain.

Time domain solutions calculate the response of the soil at every time step. Frequency domain solution only computes the Fourier spectrum of the response of the soil based on the input motion. The solution is based on a closed form solution of the equation of wave propagation. Frequency methods are typically faster than time domain methods and

displacement histories can be obtained by using an inverse fast Fourier transform. An exact solution is calculated based on transfer functions. The solution is described in Roesset and Whitman (1969), Lysmer et al. (1971.) and Schnabel et al. (1972). The use of time or frequency domain solutions is determined by the method used to model the soil behavior.

There are three different methods to model the soil behavior. A linear method can be used where the soil is considered linear elastic. In this case the stiffness (G) and the damping (ζ) are constant, and a frequency domain solution can be used. The Equivalent Linear (EL) method (Seed and Idriss 1969) can also be used in a frequency domain solution. It uses an iterative algorithm that introduces nonlinearity by performing a linear analysis with a shear modulus and a damping ratio adjusted for an equivalent strain. The EL method is described in details in the next section. The nonlinear (NL) method solves the equation of motion at every time step and updates the stiffness and the damping, based on a constitutive model.

2.2.2 Equivalent Linear Analysis

The equivalent linear method (EL), first described by Seed and Idriss (1969), is an iterative procedure usually donr in the frequency domain which requires simple input parameters:

- The density of the soil (ρ)
- The maximum shear modulus (G_{max}) that can be calculated based on the shear wave velocity (V_S) and the soil density (ρ) according to Equation 2-3

- The modulus reduction curve, used to represent the decrease of stiffness of the soil when shear strain increases
- The damping ratio curve that represents the capacity of the soil to dissipate energy when shear strain increases

This procedure models every soil layer with a linear spring and a dashpot. The spring and dashpot parameters are calculated from the modulus reduction and damping curves, based on an equivalent level of shear strain equal to 2/3 of the maximum strain level in a given layer. The analysis is ran first with initial parameters and a maximum strain is calculated in every layer. The parameters are re-calculated from the input curves, for a strain level equal to 2/3 of the maximum strain. The analysis is iterated until the maximum strain level calculated is consistent with the strain level used to choose the parameters. This procedure is widely used due to its simplicity and its low computational requirements. In some cases the equivalent linear method does not converge or does not yield satisfying results. In particular when the soil is highly nonlinear, and strains larger than 0.4% are expected (Kaklamanos et al. 2013, Stewart et al. 2008), the equivalent linear method should not be used, and a nonlinear analysis is then preferred. Recent studies indicate that NL procedures are superior to EL even at strains as low as 0.05% (Kaklamanos et al. 2015).

2.2.3 Nonlinear Analysis

2.2.3.1 Definition of Nonlinear Analysis

Nonlinear analysis is a time domain method where the equation of motion (Equation 2-5) is solved at every time step:

$$[M]\{\ddot{u}\} + [C]\{\dot{u}\} + [K]\{u\} = -[M]\{I\}\ddot{u_g}$$ *Equation 2-5*

where [M] is the mass matrix, [C] is the damping matrix, [K] is the stiffness matrix, $\{\ddot{u}\}$ is the vector of nodal relative accelerations, $\{\dot{u}\}$ is the vector of nodal velocities, $\{u\}$ is the vector of nodal displacements, $\ddot{u_g}$ is the acceleration at the base of the soil column and $\{I\}$ is the unit vector.

One dimensional nonlinear codes model the soil column either as a multiple-degree-of-freedom lumped mass system or a continuum discretized into elements with distributed mass (Figure 2-10). In a lumped mass system, every layer is represented by a mass, a nonlinear spring and a dashpot. In a continuum system, every layer is subdivided into smaller elements that have distributed mass.

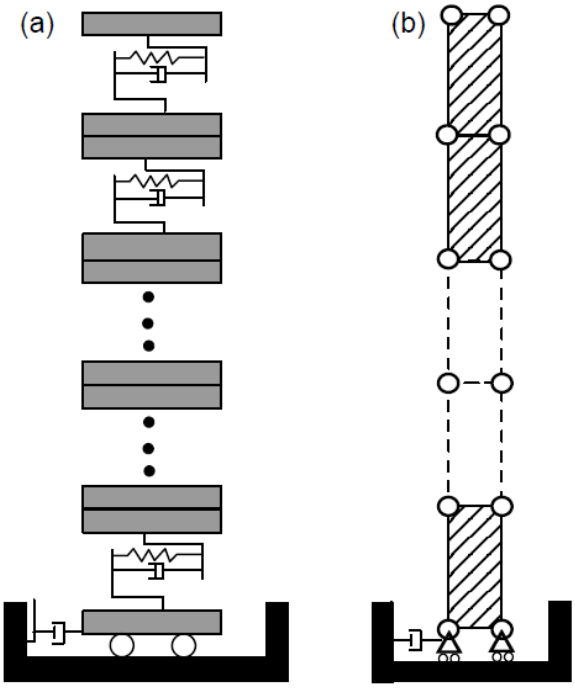

Figure 2-10 Representation of soil column (a) lumped mass system (b) distributed mass system (Stewart et al. 2004)

At every time step, the stiffness matrix updates to incorporate the nonlinear response of the soil. The equation of motion is solved using a time-stepping scheme such as the Newmark method (Newmark 1959). The soil response is obtained from a constitutive model that describes the soil behavior under cyclic loading. Recently, numerous nonlinear codes have been developed to model the behavior of soil under 1-D earthquake loading.

Some material models are relatively advanced, using the framework of plasticity, with complex yield surfaces, hardening laws and flow rules (Prevost 1977; Dafalias and Popov 1979). However, the cyclic behavior of the soil is most often described by a backbone curve (corresponding to the monotonic stress-strain curve), and a series of unloading and reloading rules to define the hysteretic behavior of the soil. In the most common nonlinear codes, Masing rules (Masing 1926) and extended Masing rules (Pyke 1979; Wang et al. 1980; Vucetic 1990) are used as unloading and reloading rules. Masing rules are described extensively in section 2.2.3.4.1. Damping is introduced by the hysteretic loops, as the result of the unloading and reloading rules, and can be associated with frequency dependent Rayleigh damping matrix, to account for small strain damping. Small strain damping solutions are described in section 2.2.3.3.

The inputs needed for nonlinear analysis depend on the constitutive model used. Models most commonly used in 1D ground response use modulus reduction and damping curves, along with other parameters. To evaluate a one-dimensional model, we typically analyze its ability to accurately match its input modulus reduction and damping curves. When a model is unable to match its input curves, it introduces a misfit of the desired behavior.

2.2.3.1 Empirical Relationships for Modulus Reduction and Damping Curves (MRD)

The maximum shear modulus is generally calculated from an in situ measurement of shear wave velocity. Measuring modulus reduction and damping curves requires an extensive laboratory testing program, and the behavior of soils at small strains is only obtained by advanced laboratory testing devices. In practice, it is common to use empirical relationships to calculate modulus reduction and damping curves, rather than perform multiple lab tests at different strain levels and different confining pressures.

Darendeli (2001) introduced empirical relationships to calculate modulus reduction and damping curves of clays based on the plasticity index (*PI*), the overconsolidation ratio (*OCR*), and the mean effective stress (σ'_0). His curves follow the original observations from Vucetic and Dobry (1991) who found that soils with a greater *PI* behaves more linearly and they show lower values of damping ratios. When the confining pressure increases the same trend is observed, and the soil behaves more linearly. Due to its database (Figure 2-11), Darendeli's equation are limited to strains lower than 0.3%. Thus, the model is not adapted to predict the response of soils at large strains.

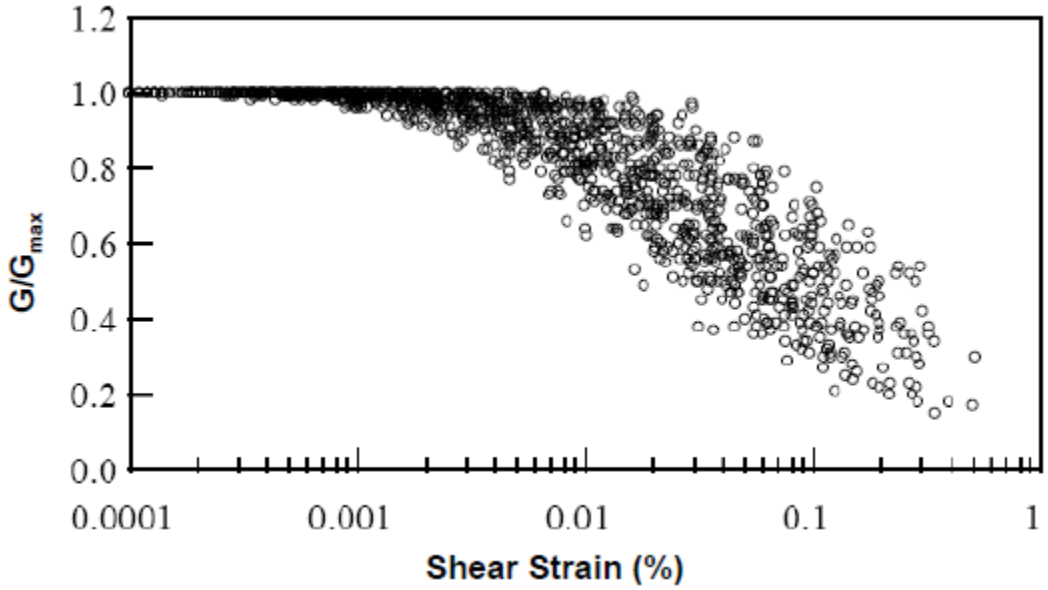

Figure 2-11 Darendeli's database (From Darendeli 2001)

Following the work from Darendeli, Menq (2003) introduced modulus reduction and damping relationships for sand. The input of the model are the mean effective stress, the coefficient of uniformity (C_u), and the mean grain size (D_{50}). Menq (2003) also observed that when the effective stress increases the behavior is also more linear.

Empirical relationships for peat derived by Kishida et al. (2009) was presented in section 2.1.6.1.1. That section described in details his findings and they are not discussed here.

2.2.3.2 Hyperbolic Model for the Backbone Curve

The modulus reduction curve can be used to calculate a backbone curve in the stress-strain space. The backbone curve describes the behavior of the soil during initial loading. Most of the available nonlinear codes such as DEEPSOIL (Hashash and Park 2001), D-MOD (Matasovic and Vucetic 1993; 1995; Matasovic 2006), and Tess (Pyke 2000), use a hyperbolic formulation to model the backbone curve. This formulation simply fits a

hyperbola to the monotonic stress-strain curve. The monotonic behavior is calculated based on the modulus reduction curve and the maximum shear modulus. The hyperbolic formulation was first introduced by Hardin and Drnevitch (1972) and later modified by Matasovic and Vucetic (1993) Darendeli (2001) and Phillips and Hashash (2009). This formulation has the advantage of being simple and easy to use with the Masing rules and the extended Masing rules. However, if the modulus reduction curve is only based on the hyperbolic model, Chiu et al (2008) have shown that the backbone curve will not capture the shear strength properly.

Yee et al (2013) proposed a hybrid procedure where the modulus reduction curve is modified to match a shear strength at high strains and obtain a more reasonable backbone curve. Any model using a hyperbolic fit of the backbone curve will not be able to match a modified modulus reduction curve perfectly.

2.2.3.3 Small-Strain Damping

At very low strains, the response of most existing models is essentially linear elastic, and their unloading reloading rules do not introduce hysteretic damping. To introduce small strain damping, nonlinear codes typically use frequency dependent Rayleigh damping which can-over predict or under-predict damping (Park and Hashash 2004). Rayleigh damping uses a damping matrix in the full equation of motion which consists of a combination of 2 matrices, one proportional to the mass matrix and one proportional to the stiffness matrix. Most of the nonlinear codes have implemented the original expression of Rayleigh damping first formulated by Rayleigh and Lindsay (1945). This formulation makes the damping frequency dependent, which is inconsistent with

laboratory results (Lai and Rix 1998; Vucetic et al. 1998). The full Rayleigh damping used by most of the nonlinear codes matches only 2 frequencies, whereas the extended Rayleigh damping matches 4 frequencies (Park and Hashash 2004). Phillips and Hashash (2009) established a frequency independent Rayleigh damping, based on the formulation by Liu and Gorman (1995). However, this formulation is computationally depending. TESS (Pyke 1979, Pyke 2000) uses a different unloading-reloading rule to produce hysteretic damping at low strains. The procedure can result in over prediction of damping at large strains (Stewart et al. 2004).

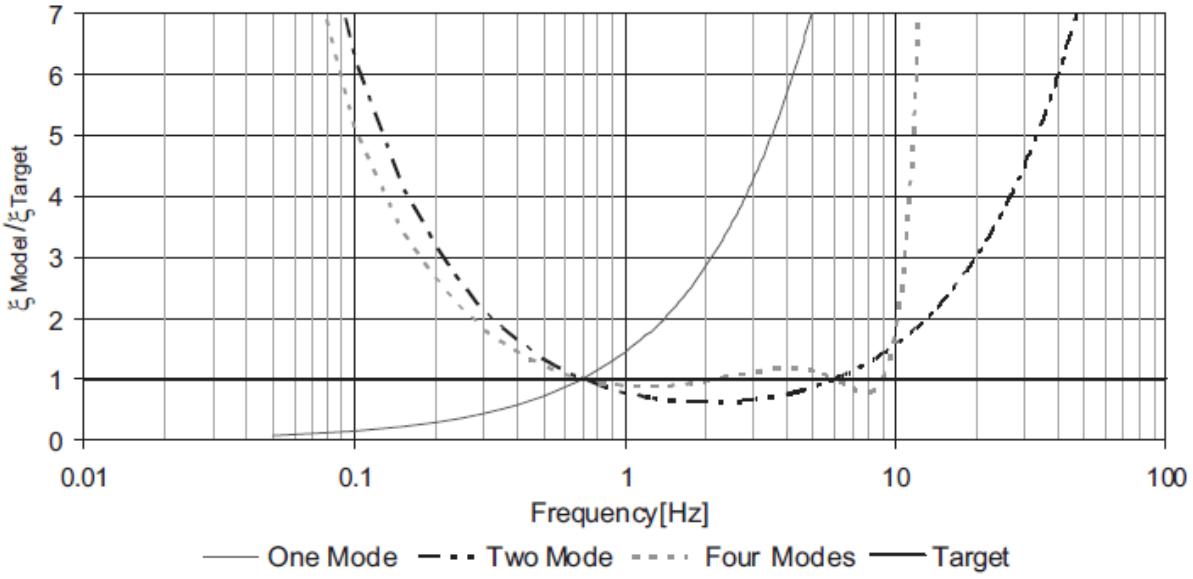

Figure 2-12 Effective damping for one, two and four modes frequency dependent Rayleigh damping (Phillips and Hashash 2009)

2.2.3.4 One Dimensional Nonlinear Models

This section presents some of the most widely used one-dimensional nonlinear models, and focuses on total stress models.

2.2.3.4.1 Masing Rules (Masing 1926)

The extended Masing rules are stated as follow:

1. The stress-strain curve follows the backbone curve during initial loading (Equation 2-6).

$$\tau = F_{bb}(\gamma) \qquad \textit{Equation 2-6}$$

where τ is the shear stress and $F_{bb}(\gamma)$ is the backbone function.

2. If a strain reversal happens at point (γ_{rev}; τ_{rev}), the unloading or reloading curve has a shape that is identical to the backbone curve enlarged by a factor *n*. In its original paper, Masing used *n*=2, it was later modified by Pyke (1979), where *n* can deviate from 2, to provide a better match of the damping at higher strain (Equation 2-7).

$$\frac{\tau - \tau_{rev}}{n} = F_{bb}\left(\frac{\gamma - \gamma_{rev}}{n}\right) \qquad \textit{Equation 2-7}$$

3. If the unloading or reloading curve exceeds the maximum past strain and intersects the backbone curve, it follows the backbone curve until the next stress reversal
4. If the unloading or reloading curve crosses an unloading or reloading curve from a previous cycle, it follows the curve of that previous cycle

When Masing rules are used with *n*=2, the initial slope of the unloading or reloading curve is equal to the maximum shear modulus G_{max}, and the model shows no hardening or softening, i.e. loops are closed; unloading and reloading from γ_{max} to $-\gamma_{max}$ back to γ_{max} will end up at the same stress.

Using the right backbone curve, any model using the Masing rules will be able to match a modulus reduction curve. However Masing rules are a poor way to match the damping behavior of a soil because they typically over predict damping at large strains (Phillips and Hashash 2009), and do not provide hysteretic damping at small strains.

2.2.3.4.2 Pressure Independent Multi-Yield Model

The OpenSees simulation platform contains a ground response module that uses plasticity models that are able to study problems where three directions of shaking are considered. One of the model implemented is the Pressure Independent Multi-Yield model (PIMY), implemented by Elgamal et al. (2003). The model is implemented in OpenSees in a fully three dimensional fashion.

The volumetric response is considered linear elastic and is uncoupled with the deviatoric response. The deviatoric response of the model is insensitive to a change in confining pressure. During cyclic loading, the pressure independent multi-yield model follows the framework of plasticity. It uses the concept of multiple-surface (nested-surface) plasticity to model the response of the soil (Iwan 1967, Prevost 1985, Mroz). The model is described in Yang (2000). The yield surfaces follow the Von Mises shape (Von Mises 1913) illustrated in Figure 2-13.

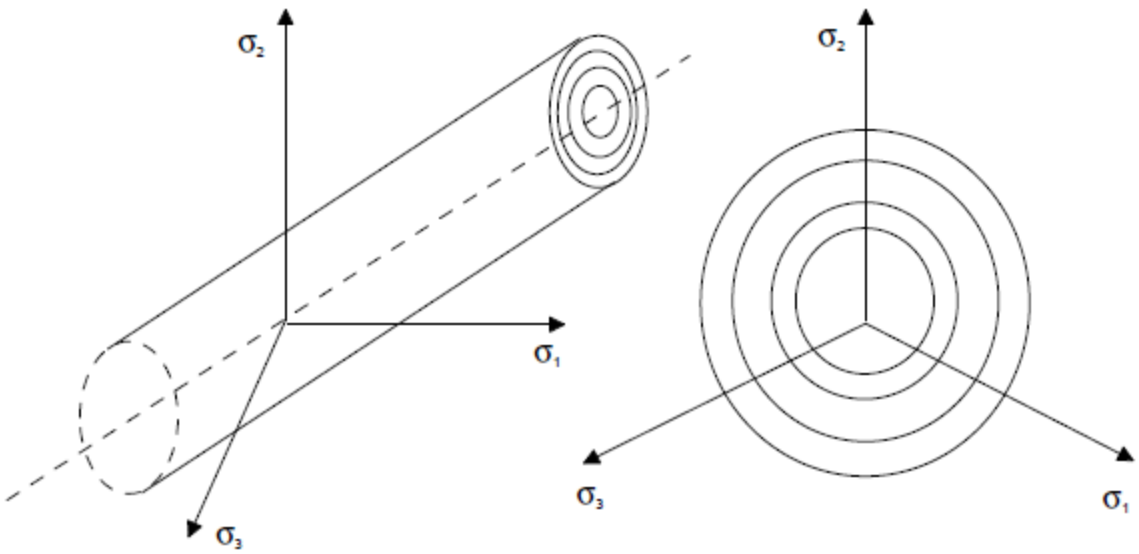

Figure 2-13 Nested Von Mises yield surfaces (after Prevost 1985, Lacy 1986, Parra 1996, and Yang 2000)

The yield surfaces are defined either by the use through an input modulus reduction curve that defines a backbone curve, or automatically generated by the model. To generate the yield surfaces, the code uses an input friction angle and cohesion to define a shear strength that is used to create a backbone curve that follows a hyperbola. Upon unloading the model would essentially follow Masing rules, and as a result would over predict damping at large strains.

2.2.3.4.3 Deepsoil MRDF-UIUC

The software Deepsoil uses a finite difference algorithm with lumped mass to perform one dimensional ground response. It is able to perform linear, equivalent linear, and nonlinear analyses. It embeds several models for nonlinear analysis, and the most advanced model is the MRDF-UIUC model (Hashash et al. 2012).

The MRDF-UIUC model uses a hyperbolic fit of the modulus reduction curve to model the backbone curve (section 2.2.3.2). The unloading-reloading response is governed by an

extension of the Masing rules (Phillips and Hashash 2009) in which the stress response is modified by a reduction factor to provide a better fit of the damping curve at large strains. For small-strain damping, the model uses frequency independent Rayleigh damping, described in Phillips and Hashash 2009.

The model provides a better fit, yet not perfect, of the damping curve, but has the drawback of using a hyperbolic fit of the modulus reduction curve, which is associated with the problems explained in section 2.2.3.2. However, Hashash et al. (2010) presented a procedure to match the strength with their model by introducing a misfit of the input modulus reduction curve, but the procedure is tedious. Groholski et al. (2015) developed the GQ/H model that fits the modulus reduction curve with a general quadratic equation, and matches an input target strength. That model is able to match precisely an input modulus reduction curve at low and large strains, and is implemented in the latest version of Deepsoil (Hashash et al. 2015).

2.3 Three Dimensional Constitutive Models

The core of this dissertation is a nonlinear constitutive model for dynamic simulations, formulated for peat. The model and its constitutive equations are described in Chapter 6 and implementation in a finite difference code is presented in Chapter 7. Chapter 8 presents the calibration process through lab testing and single elements simulations, and presents the results of 1D ground response analyses simulating a centrifuge test. The model integrates different concepts of plasticity previously introduced by other researchers, and this literature review aims to provide the reader the required theoretical background to understand the model. Viscous effects are not introduced in the model

because of the complexity of visco-plastic formulation. Future work includes the integration of viscous effect, in particular to capture the secondary compression of peat.

In this literature review, the fundamental theory and equations of elasto-plasticity and visco-plasticity in soil mechanics are first presented. Then, the critical state soil mechanics framework is introduced. Finally, a few models are described. Numerous models have been developed for clay and sand and every model strive to capture a specific feature of the soil behavior. To the writer's best knowledge there does not exist a constitutive model specifically derived for peat. The models presented in this section are either direct references for the new model developed and presented in this dissertation, or models that include important features and that have introduced new concepts in the domain of constitutive modeling of soils.

The Modified Cam-Clay model (Roscoe and Burland 1968) is presented first because it is the most fundamental model in critical state soil mechanics. A modified version of the Modified Cam-Clay called the bubble model is then described. This model uses a bounding surface algorithm and can be used in simulations involving cyclic loading to describe behavior of clays. A visco-plastic model for clays by Kutter and Sathialingam (1992) is also presented where visco-plastic strains are introduced based on the distance to the isotropically normally consolidated line (ICL). The model presented in chapter 6 uses a formulation in terms of change in stress ratio to assess the potential yielding of the soil. This stress ratio formulation was originally derived by Dafalias and Manzari (2004) to describe the behavior of sand, and their model is presented in this section as well.

Finally, two models incorporating stress anisotropy, SANISAND and SANICLAY, are briefly discussed for completeness. The model presented in chapter 6 does not account for anisotropy. Although peat is anisotropic, the fabric anisotropy is not well understood, and more tests are needed to fully define the effect of anisotropy on the peat behavior.

2.3.1 Introduction to Rate-Independent Soil Elasto-Plasticity

2.3.1.1 Fundamental Equations

Elasto-plastic models, combine plastic and elastic deformations. Those models make the assumption of an additive decomposition of the strain rate tensor ($\dot{\varepsilon}$) into an elastic ($\dot{\varepsilon}^e$) and a plastic (irrecoverable) part ($\dot{\varepsilon}^p$):

$$\dot{\varepsilon} = \dot{\varepsilon}^e + \dot{\varepsilon}^p \qquad \textit{Equation 2-8}$$

The superposed dot denotes a rate. Strains are also decomposed in purely deviatoric ($\dot{\varepsilon}_d$) and purely volumetric strains ($\dot{\varepsilon}_v$):

$$\dot{\varepsilon}_v = \mathrm{tr}[\dot{\varepsilon}] \qquad \textit{Equation 2-9}$$

$$\dot{\varepsilon}_d = \dot{\varepsilon} - \frac{1}{3}\dot{\varepsilon}_v I \qquad \textit{Equation 2-10}$$

where *I* is the second symmetric unit tensor. This formulation is presented in general stress/strain space, and $\dot{\varepsilon}_d$ and $\dot{\varepsilon}$ are second order tensors. Stresses (σ) are also separated in volumetric (p') and deviatoric components (s):

$$s = \sigma - p' I \qquad \textit{Equation 2-11}$$

$$p' = \frac{1}{3} tr[\sigma] \qquad \textit{Equation 2-12}$$

Note that *s* is the deviatoric stress tensor, σ is the stress tensor, and *p'* is a scalar called the mean effective stress. Equation 2-12 essentially relates *p'* to the first stress invariant I_1 ($I_1=tr[\sigma]$). Note that soil plasticity often deals with saturated soils and therefore stresses should be considered as effective stresses that exist between particle grains. Pore pressures induced during undrained or partially drained may also be included in plasticity models. For consistency with traditional plasticity notation, the apostrophe denoting effective stress is dropped in the rest of this chapter.

Plasticity models are often presented in the so-called "triaxial space *p*-*q*". The deviatoric stress invariant (*q*) is a scalar and is calculated based on the second deviatoric stress invariant J_2:

$$J_2 = \frac{1}{2}(s:s) \qquad \textit{Equation 2-13}$$

$$q = [3J_2]^{1/2} \qquad \textit{Equation 2-14}$$

In Equation 2-13 ":" indicates an inner product of tensors. In triaxial space the stress ratio is defined as:

$$\eta = \frac{q}{p} \qquad \textit{Equation 2-15}$$

The triaxial shear strain (ε_q) is defined as:

$$\varepsilon_q = \left[\frac{2}{3}(\varepsilon_d:\varepsilon_d)\right]^{1/2} \qquad \textit{Equation 2-16}$$

Note that despite its name, the triaxial space can also be used to describe the response of the soil under different types of loading, not simply under triaxial loading. The elastic response is expressed as:

$$\dot{\varepsilon}_v^e = \frac{\dot{p}}{K}$$ *Equation 2-17*

$$\dot{\varepsilon}_d^e = \frac{\dot{s}}{2G}$$ *Equation 2-18*

$$\dot{\varepsilon}_q^e = \frac{\dot{q}}{3G}$$ *Equation 2-19*

where *K* is the bulk modulus and *G* is the shear modulus. Different expressions can be used to defined *K* and *G*. For clays, *K* and *G* are often assumed to depend linearly on the mean effective stress *p*:

$$K = \frac{p\upsilon_0}{\kappa}$$ *Equation 2-20*

$$G = \frac{3(1-2\nu)}{2(1+\nu)}K$$ *Equation 2-21*

where υ_0 is the initial specific volume (related to the void ratio *e:* $\upsilon_0 = 1 + e$*)*, κ is the slope of the recompression line in a specific volume-logarithmic mean effective stress compression plane, and ν is the Poisson's ratio, assumed to be constant. For sand, Equation 2-20 and Equation 2-21 do not hold, in particular, *G* varies linearly with the square root of the mean effective stress. Section 2.3.5.4 provides an example of a constitutive model for sand and introduces expressions for bulk and shear modulus consistent with sand behavior.

Combining equations Equation 2-8, Equation 2-18, Equation 2-19 and Equation 2-20 the constitutive relations can be rewritten:

$$\dot{p} = K(\dot{\varepsilon}_v - \dot{\varepsilon}_v^p)$$ *Equation 2-22*

$$\dot{s} = 2G(\dot{\varepsilon}_d - \dot{\varepsilon}_d^p)$$ *Equation 2-23*

$$\dot{q} = 3G(\dot{\varepsilon}_q - \dot{\varepsilon}_q^p)$$ *Equation 2-24*

2.3.1.2 Ingredients of an Elasto-Plastic Constitutive Model

A constitutive model provides rules to define the response of a soil, in particular the calculations of the plastic strains. Elasto-plastic models are defined by four governing equations:

- The yield criterion, or yield surface, defining the stress state at which yielding occurs.

- The flow rule that describes the evolution of plastic strains when the material is yielding

- The hardening law which defines the strain hardening behavior of the material when plastic strain evolves

- Kuhn-Tucker Loading-unloading conditions and consistency equation that are used to derive solutions

The yield criterion or yield function (f) is used to check if the material is yielding. In the stress space, the yield function delimits the elastic region, where only elastic deformations occur. The yield function is a surface in the (p,q) plane. If $f<0$, the stress state is in the elastic region, and the soil behaves elastically. When $f \geq 0$, yielding occurs, and plastic strains are calculated based on the flow rule. Plastic deformations start when the stresses have reached the limit of the surface. The surface may then evolve so the current state of stress is always on the boundary of the surface. Unloading will typically result in going back inside the elastic region.

The flow rule defines the evolution of the plastic strains and is generally defined by the following equation:

$$\dot{\varepsilon}_p = \dot{\gamma}\frac{\partial g}{\partial \sigma} \;\; or \; \dot{\varepsilon}_p = \frac{\dot{\sigma}}{H} \qquad \textit{Equation 2-25}$$

where $\dot{\gamma}$ is the plastic consistency parameter, *g* is the plastic potential surface, and *H* is the plastic modulus. The normal to the plastic potential surface describes the direction of plastic flow. If the yield surface and the plastic potential surface coincide (i.e. *f*=*g*), the flow rule is called associated flow rule.

The hardening law describes the evolution of the hardening variables (*q*). This notation, from the general theory of plasticity, must not be confused with the deviatoric stress in triaxial space (*q*). Except for the rest of this section of this dissertation, *q* designates the deviatoric stress. The hardening law is defined as:

$$\dot{q} = \dot{\gamma} h(\sigma, q) \qquad \textit{Equation 2-26}$$

where *h* is the hardening function. If $h = \frac{\partial f}{\partial q}$, the hardening law is called associative hardening law. There exists three different types of hardening law:

- Isotropic hardening law, which changes the size of the yield surface during plastic loading.
- Kinematic hardening law, which translates the center of the yield surface.
- Rotational hardening law, which rotates the yield surface.

Plastic consistency parameter and yield function are used to describe the Kuhn Tucker loading/unloading conditions:

$$\dot{\gamma} \geq 0, f(\sigma, q) \leq 0 \ \ and \ \dot{\gamma} f(\sigma, q) = 0$$ *Equation 2-27*

The plastic consistency requirement can be expressed as:

$$\dot{\gamma} \dot{f}(\sigma, q) = 0$$ *Equation 2-28*

Those equations can describe any plasticity model. The Kuhn-Tucker unloading and loading conditions, along with the plastic consistency requirement can be used to solve those equations.

2.3.2 Bounding Surface Plasticity

The framework presented above can model reasonably well the behavior of soils, in particular under monotonic loading. However, it presents several flaws:

1. The elastic domain is often too large compared to experimental data.
2. Isotropic hardening increases the size of the elastic domain that yields unrealistic stress-strain curve during unloading and cyclic loading.
3. The abrupt change of stiffness when yielding is unrealistic, and inconsistent with laboratory test results showing a gradual change in stiffness.

The theory of bounding plasticity was introduce to overcome those problems. It was first introduced by Dafalias and Popov (1975) for metals and later used in the development of constitutive models for soils by Mroz (1979) and Dafalias and Herrmann (1982). The main feature of bounding plasticity is a bounding surface that encloses every possible state of stress. The distance between the state of stress and its image on the bounding surface is used to calculate the plastic modulus (Dafalias 1986). The image point on the bounding

surface can be defined by different mapping rules such as the radial mapping (Dafalias and Herrmann 1982). When the distance between the image point and the stress state is large, the material is stiff and the plastic modulus is large. When the stress state approaches the bounding surface, the plastic modulus decreases and the material softens. The plastic modulus changes gradually, and a bounding plasticity model provides a smooth stress strain curve.

2.3.3 Rate-Dependent Plasticity

Models accounting for viscous effects (i.e. rate dependence) can be classified according to four criteria (Kutter and Sathialingam 1992):

- Rate dependence of elastic response: the elastic response can be rate dependent or rate independent. Rate dependent elastic model (i.e. Visco-elastic models) are mathematically complicated (Perzyna 1966) and do not provide a significant improvement for soil mechanics.
- Ways of incorporating time: in a constitutive model, time can be incorporated explicitly or indirectly by updating an internal variable. Assuming direct time dependence may be complicated because it requires a certain knowledge of the stress history of the soil. Therefore incorporating time dependence in internal variable appears more suitable in soil mechanics.
- Fully time dependence of inelastic strains or not: plastic strains can have time dependent and time independent parts, or be only time dependent. Based on microscopic and macroscopic observations, Dafalias (1982) concluded that the behavior of the soil can be best captured by considering time dependent and time

independent plastic strains. Such a formulation can be tricky and lead to underestimation of high strain rates effect.

- Presence or absence of an elastic nucleus: inelastic strains can be considered to occur at all time or only after yielding, i.e. an elastic region exists in the stress space, defined by a yield surface, as explained in section 2.3.1

To introduce rate-dependence of the plasticity equations, several visco-plastic formulations have been defined in the past. The most common are the generalized Duvaut-Lion's model (1972) and the Perzyna model (1963 and 1966). This latter uses a loading function which essentially acts as a yield function but which value can be greater than 0. Perzyna's theory (1963), introduces a rate sensitive loading surface f_d=k_d (dynamic loading surface) and a static yield function f_s=k_s, k_d is a parameter representing the effect of work hardening and strain rate and k_S is a parameter representing the effect of work hardening only. An "excess stress function" *F* is defined as:

$$F = \frac{f_d}{f_s} - 1 \qquad \textit{Equation 2-29}$$

Perzyna (1963) defined the (associative) flow rule as follow:

$$\dot{\varepsilon}^{vp} = \Phi(F)\frac{\partial f_d}{\partial \sigma} \qquad \textit{Equation 2-30}$$

$\Phi(F)$ being the stress difference function, representing the difference between the current state of stress on the loading surface and the image stress on the reference surface. In Perzyna's formulation the stress difference function is only defined when F>0, i.e. when f_d>f_s.

2.3.4 Critical State Soil Mechanics

2.3.4.1 Definition of Critical State

Critical state is an ultimate condition in which shearing does not induce changes in deviatoric stress, mean effective stress or volume (i.e. void ratio) anymore. This state is mathematically described by the following equations:

$$\frac{\partial q}{\partial \varepsilon_q} = \frac{\partial p}{\partial \varepsilon_q} = \frac{\partial v}{\partial \varepsilon_q} = 0 \qquad \textit{Equation 2-31}$$

The void ratio at critical state is called the critical state void ratio (e_{cs}). At critical state the stress ratio is:

$$\frac{q_{cs}}{p_{cs}} = \eta_{cs} = M \qquad \textit{Equation 2-32}$$

The final deviatoric and mean effective stresses are not constant, they depend on the initial stress conditions and the stress path. Their ratio (*M*) is a material constant and define a line in *p*-*q* space (Figure 2-14(a)). The critical state void ratio also depends on the initial stresses and the stress path, but all the critical state void ratio also define a line in *e*-*p* space (Figure 2-14(b)). A soil is said to be at critical state if its state is on both lines. Those two lines are projections of the critical state line in their respective space.

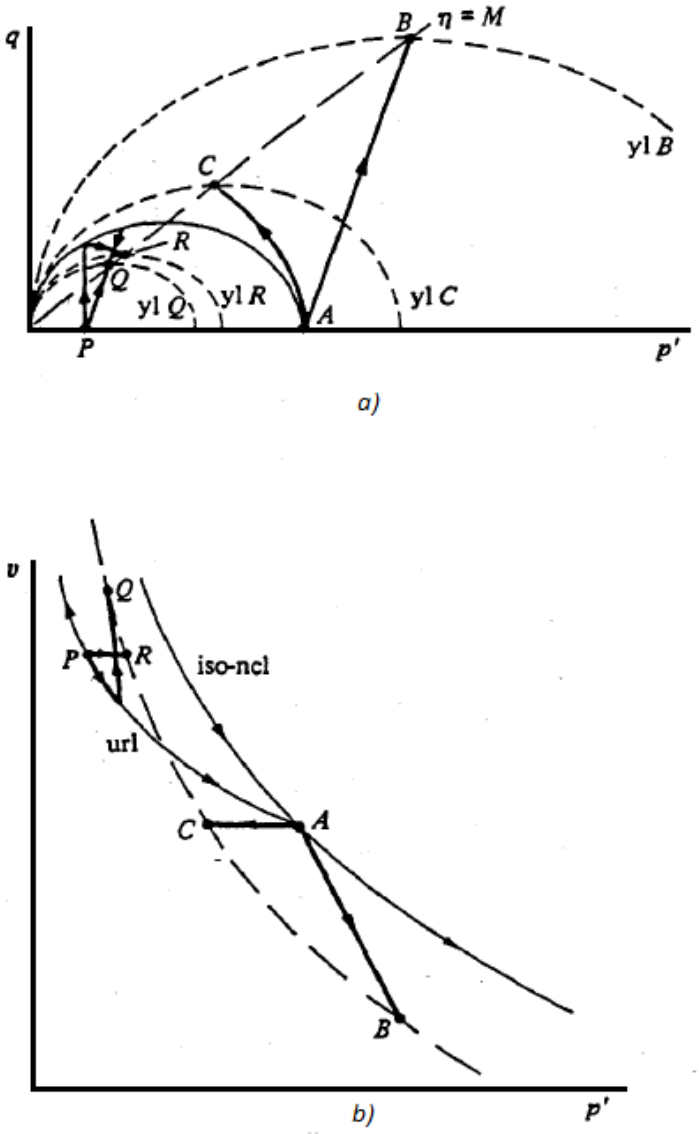

Figure 2-14 Critical state line in (a) p-q space and (b) υ-p space (Muir Wood 1990)

2.3.4.2 Critical State Line

The critical state line (CSL) is a unique line in the *p-q-*υ space as illustrated by Figure 2-15. The CSL of a soil depends on the nature of the soil and its physical properties, but it is independent of the stress state of the soil.

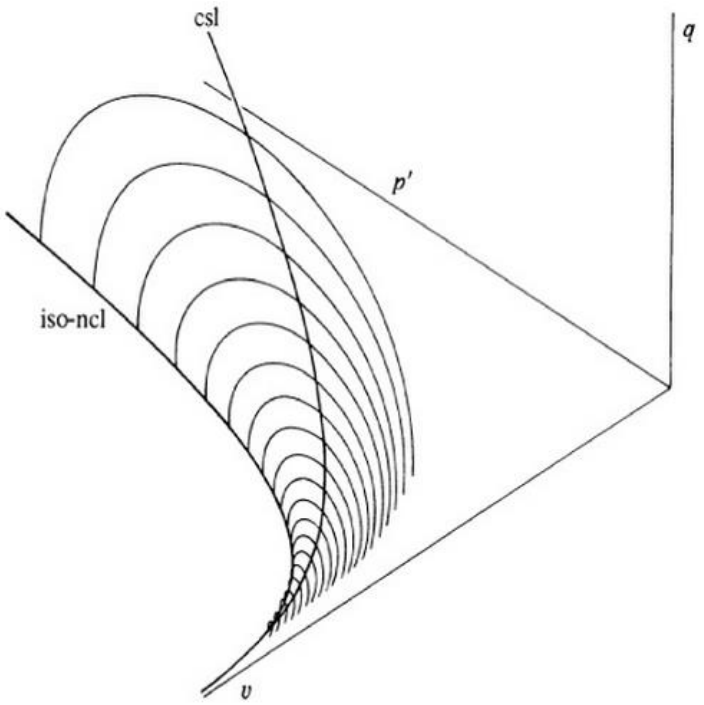

Figure 2-15 Three-dimensional view of the ICL and the CSL (Muir Wood 1990)

In the *p*-*q* space the projection of the CSL has the following equation:

$$q_{cs} = M p_{cs}$$ *Equation 2-33*

In the υ-*p* space the shape of the projection of the CSL depends on the nature of the soil. For clays the CSL is linear in the υ-ln p space and is parallel to the isotropically normally consolidated line (iso-NCL). The iso-NCL can be described by the following equation:

$$\upsilon = \mathrm{N} - \lambda \ln p_{cs}$$ *Equation 2-34*

In this equation *N* is the specific volume at unit pressure and *λ* is the slope of the isotropically normally consolidated line. The critical state line follows the following equation:

$$\upsilon_{cs} = \Gamma - \lambda \ln p_{cs}$$ *Equation 2-35*

In this equation Γ is the critical state specific volume at unit pressure. A soil is at critical state if both Equation 2-33 and Equation 2-35 are satisfied. For sands the critical state line in the υ-*ln p* space is not a straight line, but is curved down. Li and Wang (1998) introduced the following equation for the critical state line:

$$e_c = e_0 - \lambda_c \left(\frac{p_{cs}}{p_{at}}\right)^{\xi}$$ *Equation 2-36*

where λ_c and ξ are material constants and p_{at} is the atmospheric pressure.

2.3.4.3 Critical State Soil Mechanics Framework

Critical state soil mechanics is an effective stress framework that combines two concepts: (1) the consolidation behavior of soil and (2) the shear stress vs. normal stress behavior of soils. In this framework, the models' response tend to a critical state that satisfies both concepts for any stress path. This framework was validated against a wide body of available data (Muir Wood 1990), and proved to be an essential feature of the soil behavior. The next section presents few existing models that are all formulated within the framework of critical state soil mechanics.

2.3.5 Review of Existing Models

In this review of existing models, every model is presented following the same logic. The main principle of the model is presented first. The yield function and the different surfaces used by the models are then presented. The flow rule and hardening law are briefly described, and the performance of the model is discussed.

The list of constitutive equations of each model is not intended to be exhaustive, and this section does not list every input parameter for each model. For completeness the reader is referred to the paper associated with each model.

2.3.5.1 Modified Cam-Clay

2.3.5.1.1 Principles and History

One of the most fundamental constitutive models is the Cam-Clay model, derived for clays, and first formulated by Roscoe and Schofield in 1963. Since then, it has been modified several times until the current model formulated in 1968 by Roscoe and Burland. The 1968's formulation has been named Modified Cam-Clay to distinguish it from the original. In this section the phrase "Cam-Clay model" refers to the Modified Cam-Clay model. The Cam-Clay is an elasto-plastic model with an elliptic yield surface, which has served as a basis for various models for clays. The model considers an associative flow rule, and does not account for any viscous effect or anisotropy.

2.3.5.1.2 Input Parameters

The Cam-Clay model requires 5 material parameters:

- $M = \frac{6 \sin \phi'}{3 - \sin \phi'}$ where ϕ' is the friction angle measured under a triaxial compression stress path. M is the slope of the critical state line in the *p*-*q* plane
- λ, slope of the isotropic normal compression line of the soil in *e*-ln *p'* plane
- e_0 or *N*, respectively initial void ratio, or specific volume at unit pressure
- κ slope of the recompression line of the soil in *e*-ln *p'* plane
- Poisson's ratio ν

Those material parameters are used in almost all the models for clays. Some models add some new parameters to introduce additional features. Although not a material parameter, to use this model one must know the current state of stress (*p* and *q*) and the maximum past pressure named p_0. Note that the maximum past pressure is related to the overconsolidation ratio (*OCR*), in particular if the soil is isotropically consolidated: $p_0 = OCR.p.$

2.3.5.1.3 Yield Surface

The yield surface is an ellipse in the triaxial space (Figure 2-16) and has the following equation:

$$f = \frac{q^2}{M^2} + \left(p - \frac{p_0}{2}\right)^2 - \left(\frac{p_0}{2}\right)^2 = 0 \quad or \quad f = \frac{q^2}{M^2} + p^2 - p_0 p = 0 \qquad \textit{Equation 2-37}$$

In the multiaxial space, the yield surface has the following equation:

$$f = \frac{3}{2M^2} s : s + \left(p - \frac{p_0}{2}\right)^2 - \left(\frac{p_0}{2}\right)^2 \qquad \textit{Equation 2-38}$$

The critical stress ratio is considered to be the same in compression and in extension. The yield surface always has its apex on the critical state line.

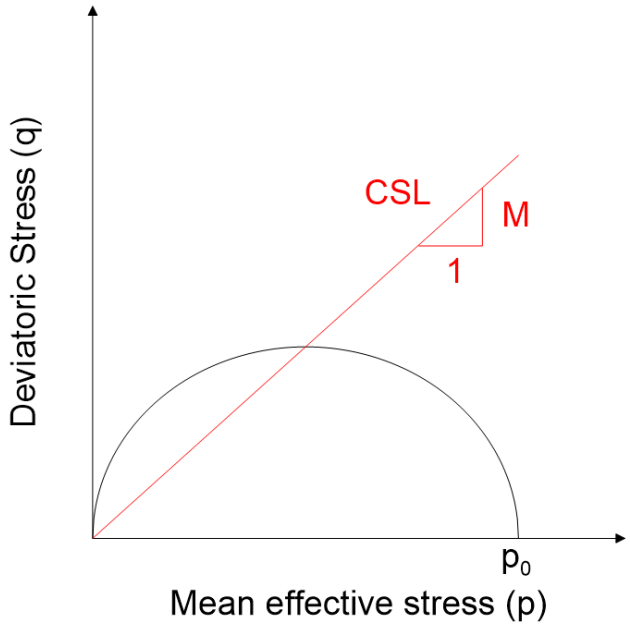

Figure 2-16 Modified Cam-Clay yield surface in p-q space

2.3.5.1.4 Flow Rule and Hardening Law

The Cam-Clay model follows an associative flow rule, which means that the plastic potential surface is equivalent to the yield surface:

$$\epsilon_q^p = \dot{\gamma}\frac{\partial f}{\partial q} \qquad \textit{Equation 2-39}$$

and

$$\epsilon_v^p = \dot{\gamma}\frac{\partial f}{\partial p} \qquad \textit{Equation 2-40}$$

The plastic consistency parameter can easily be calculated using the consistency condition (Equation 2-28). The plastic strain-stress relationship can be summarized by the following matrix equation (Muir Wood 1990):

$$\begin{bmatrix}\delta\varepsilon_v^p\\ \delta\varepsilon_q^p\end{bmatrix}=\frac{\lambda-\kappa}{\upsilon p(M^2+\eta^2)}\begin{bmatrix}(M^2-\eta^2) & 2\eta\\ 2\eta & \dfrac{4\eta^2}{(M^2-\eta^2)}\end{bmatrix}\begin{bmatrix}\delta p\\ \delta q\end{bmatrix}$$ *Equation 2-41*

The yield surface exhibits isotropic hardening, which means that the size of the yield surface changes as internal variables evolve. It also experiences kinematic hardening which means the center $\left(\frac{p_0}{2}\right)$ of the yield surface is moving when the soil is yielding. The position of the center and the size of the yield surface are controlled by the maximum past pressure. The change in maximum past pressure depends on the increment of plastic volumetric strains and is calculated by the following equation:

$$\dot{p_0}=\frac{\upsilon p_0\dot{\epsilon}_v^p}{\lambda-\kappa}$$ *Equation 2-42*

Note that in (*p,q*) plane the surface always goes through the origin, and that the center is only moving only along the p-axis.

2.3.5.1.5 Performance of the Modified Cam-Clay

Clay is known to exhibit nonlinearity at deviatoric strains as small as 0.001%, which is much smaller than the yield strain for overconsolidated soil using the traditional Cam-Clay model. A fundamental problem with the Cam-Clay model is that the elastic range is too big for overconsolidated clays. Consider the example problem shown in Figure 2-17 in which undrained loading is imposed in triaxial compression for various OCR values (model parameters specified in Figure 2-17). The stress paths are vertical until they touch the yield surface, and then evolve to eventually reach the critical state line. The yield surface also evolves during plastic loading, but only the yield surface at the start of loading is shown for simplicity. The shape of the stress-strain curves is not reasonable because

the linear elastic range is too big. In fact, for the case with OCR=2.0, the stress-strain curve becomes elastic-perfectly plastic because the stress path intersects the yield surface at the critical state. This is not acceptable for many earthquake problems where cyclic loading at stress amplitudes far smaller than the shear strength may occur.

However, the influence of consolidation stress on shear strength is properly modeled using the modified Cam-Clay model because, for a given maximum past pressure, the higher OCR values have lower undrained shear strength. The shear strength in this case conforms to SHANSEP (Ladd 1991) concepts with $(s_u/p_c') = 0.24OCR^{0.9}$. Therefore, this model is very useful for certain stability problems in which shear strength is the primary consideration.

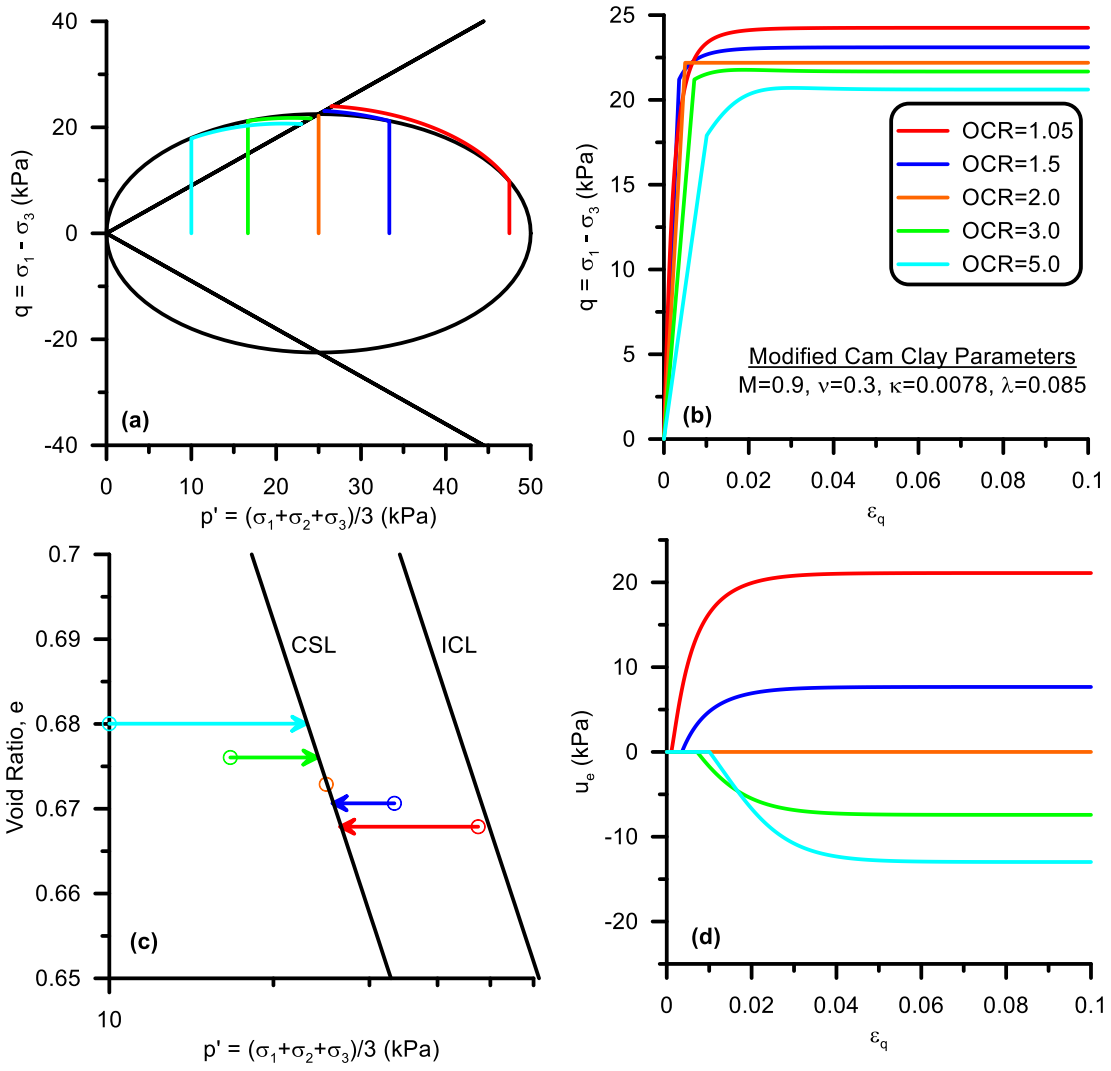

Figure 2-17 Numerical simulations for undrained stress path for a clay with different values of OCR using the modified Cam-Clay

2.3.5.2 Bubble Model

2.3.5.2.1 Principles

One approach to better capture small-strain nonlinearity is a “bubble model” in which the elastic region is enclosed within a small bubble (i.e. a yield surface) that moves within the modified Cam-Clay yield surface (Al Tabbaa and Muir Wood (1989)) and Rouainia and Muir wood (2001)). In this model, the modified Cam-Clay yield surface is treated as a

bounding surface, and the plastic modulus is a function of the distance between the current stress state on the small bubble and the bounding surface in stress space (Muir Wood 1990).

2.3.5.2.2 Input Parameters

The model requires seven material parameters. Four of them are essentially the input parameters of the Cam-Clay model:

- λ^*, slope of the isotropic normal compression line of the soil in ε_v-ln p' plane
- κ^* slope of the recompression line of the soil in ε_v-ln p' plane
- M slope of the critical state line in p-q space
- Poisson's ratio ν

Note that λ^* and κ^* are respectively equal to $\lambda/(1+e_0)$ and $\kappa/(1+e_0)$, where e_0 is the initial void ratio. The model introduces three additional input parameters:

- R, which represents the ratio of the sizes of the elastic bubble and the outer surface
- B, the stiffness interpolation parameter
- ψ, the stiffness interpolation exponent

Those two last parameters would presumably be selected to match laboratory test data.

2.3.5.2.3 Yield and Bounding Surfaces

The equation of the bounding surface is the same as the equation of the Cam-Clay yield surface. In the multiaxial domain, the surface has the following equation:

$$F = \frac{3}{2M^2} s : s + \left(p - \frac{p_0}{2}\right)^2 - \left(\frac{p_0}{2}\right)^2 \qquad \textit{Equation 2-43}$$

The bubble surface is a scaled down version of the bounding surface. The ratio of the sizes of the bubble surface and the bounding surface is R. The bubble surface has the following equation:

$$f = \frac{3}{2M^2} (s - s_{\bar{\alpha}}) : (s - s_{\bar{\alpha}}) + (p - p_{\bar{\alpha}})^2 - (R p_0)^2 \qquad \textit{Equation 2-44}$$

In this equation, $\bar{\alpha} = \{p_{\bar{\alpha}} \mathrm{I}, s_{\bar{\alpha}}\}$ is the center of the bubble in the stress space. The two surfaces are shown in Figure 2-18.

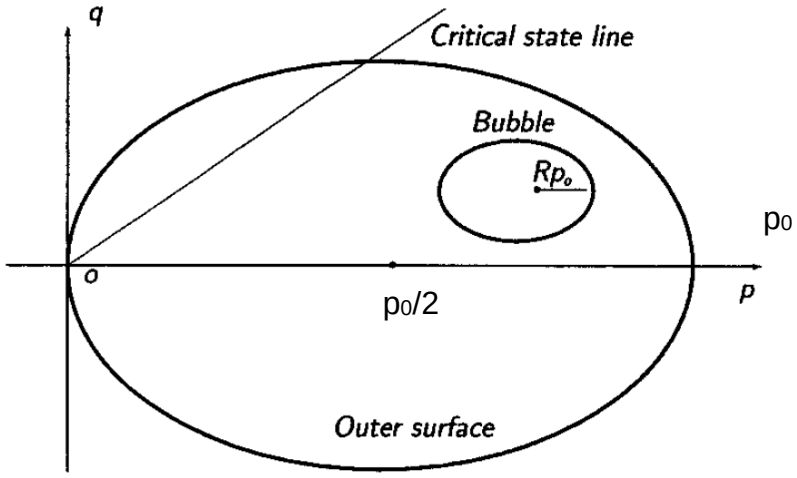

Figure 2-18 Kinematic hardening bubble model: outer (bounding) surface and bubble (yield) surface in the p-q plane (Rouainia and Muir Wood 2001)

2.3.5.2.4 Flow Rule and Hardening Law

The plastic flow follows an associative rule as described by Equation 2-25, and the plastic hardening is driven only by volumetric strain. The plastic consistency parameter is derived using the consistency condition and the Kuhn-Tucker conditions.

The outer surface follows an isotropic, and a kinematic hardening rule, identical to the modified Cam-Clay model when the inner surface and outer surface are in contact with each other. Note that the kinematic hardening of the outer surface results in translation of the center of the surface along the *p*-axis. Evolution of the outer surface also occurs when the bubble moves within the outer surface, in accordance with a relation derived from the consistency condition. The size of the bubble is always proportional to the outer surface. Therefore the bubble exhibits an isotropic hardening rule. The bubble also follows a kinematic hardening rule defining the movement of its center relative to the center of the outer surface. As the bubble is getting closer to the outer surface, the model tends to respond like the Cam-Clay model.

The plastic modulus depends on the distance between the current stress and the conjugate stress. The conjugate stress on the bounding surface and the current stress on the yield surface have the same direction of the outward normal as shown in Figure 2-19.

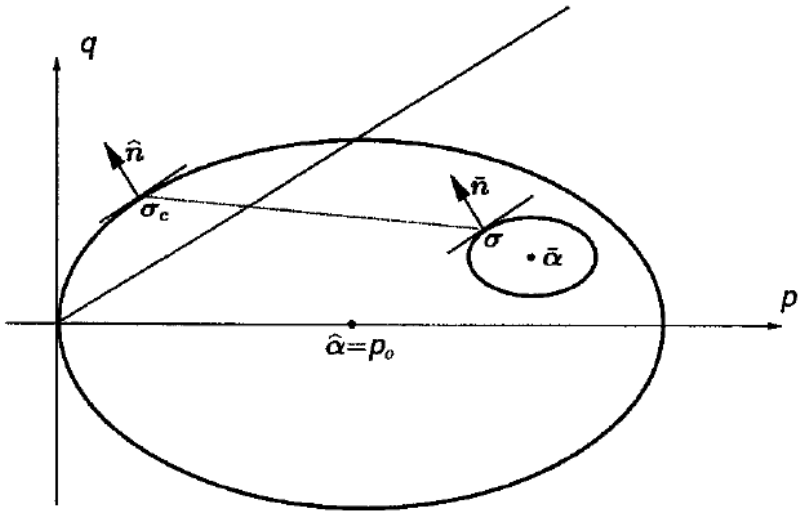

Figure 2-19 Conjugate stress and translation rule (Rouainia and Muir Wood 2001)

The conjugate plastic modulus H_c is given by the following expression:

$$H_c = \frac{4Rpp_0p}{\lambda^* - \kappa^*}(p - p_{\bar{\alpha}}) \qquad \textit{Equation 2-45}$$

When R is 1 the Modified Cam-Clay formulation is retrieved. The hardening modulus H can be calculated with the following equation:

$$H = H_c + \frac{Bp_0{}^3}{\lambda^* - \kappa^*}\left(\frac{b}{b_{max}}\right)^{\psi} \qquad \textit{Equation 2-46}$$

In the previous equation, b is the distance between the current state of stress (on the bubble) and the conjugated stress on the outer surface. b_{max} is the maximum value of b obtained when the bubble is touching the outer surface at a point diametrically opposite to the conjugate stress, but the current state of stress is diametrically opposite to the point of tangency. When the bubble and the outer surface are in contact, the plastic modulus is equal to the conjugate plastic modulus H_c. Note that this general expression of the hardening modulus can be modified to better the simulate the soil behavior.

2.3.5.2.5 Summary

Table 2-1 Summary of the bubble model (Rouainia and Muir Wood 2001)

(i) Non-linear elastic constitutive law

$$\dot{p} = K(\dot{\varepsilon}_v - \dot{\varepsilon}_v^p) \quad \text{with} \quad K = \frac{p}{\kappa^*}$$

$$\dot{\mathbf{s}} = 2G(\dot{\boldsymbol{\varepsilon}}_d - \dot{\boldsymbol{\varepsilon}}_d^p) \quad \text{with} \quad G = \frac{3K(1-2\nu)}{2(1+\nu)}$$

(ii) Yield functions

$$F := \frac{3}{2M^2}(\mathbf{s}):(\mathbf{s}) + (p-p_0)^2 - (p_0)^2 = 0$$

$$f := \frac{3}{2M^2}(\mathbf{s}-\mathbf{s}_\alpha):(\mathbf{s}-\mathbf{s}_\alpha) + (p-p_\alpha)^2 - (Rp_0)^2 = 0$$

(iii) Isotropic hardening law

$$\frac{\dot{p}_0}{p_0} = \frac{\dot{\varepsilon}_v^p}{(\lambda^* - \kappa^*)}$$

(iv) Kinematic hardening law

$$\dot{\bar{\boldsymbol{\alpha}}} = \dot{\hat{\boldsymbol{\alpha}}} + \frac{\dot{p}_0}{p_0}(\bar{\boldsymbol{\alpha}} - \hat{\boldsymbol{\alpha}}) + \dot{\mu}(\boldsymbol{\sigma}_c - \boldsymbol{\sigma})$$

(v) Plastic modulus at current stress

$$H = H_c + \frac{Bp_0^3}{(\lambda^* - \kappa^*)}\left(\frac{b}{b_{max}}\right)^{\psi}$$

(vi) Kuhn–Tucker complementary conditions

$$\dot{\gamma} \geqslant 0, \quad f(\bar{\boldsymbol{\sigma}}, p_0) \leqslant 0, \quad \dot{\gamma} f(\bar{\boldsymbol{\sigma}}, p_0) = 0$$

2.3.5.2.6 Performance of the Bubble Model

Figure 2-20 shows simulations utilizing the bubble model originally formulated by Al Tabaa and Muir Wood (1989) and refined by Rouainia and Muir Wood (2001). The bubble model simulations exhibit much more reasonable small-strain nonlinear behavior because yielding begins when the stress path touches the inner bubble rather than the outer surface. This yields smoother stress-strain curves. The size of the bubble was set

to 10% the size of the outer surface in Figure 2-20 for the purpose of visually representing the bubble. To adequately capture the small strain nonlinearity, the size of the bubble would need to be very small; too small to see in Figure 2-20.

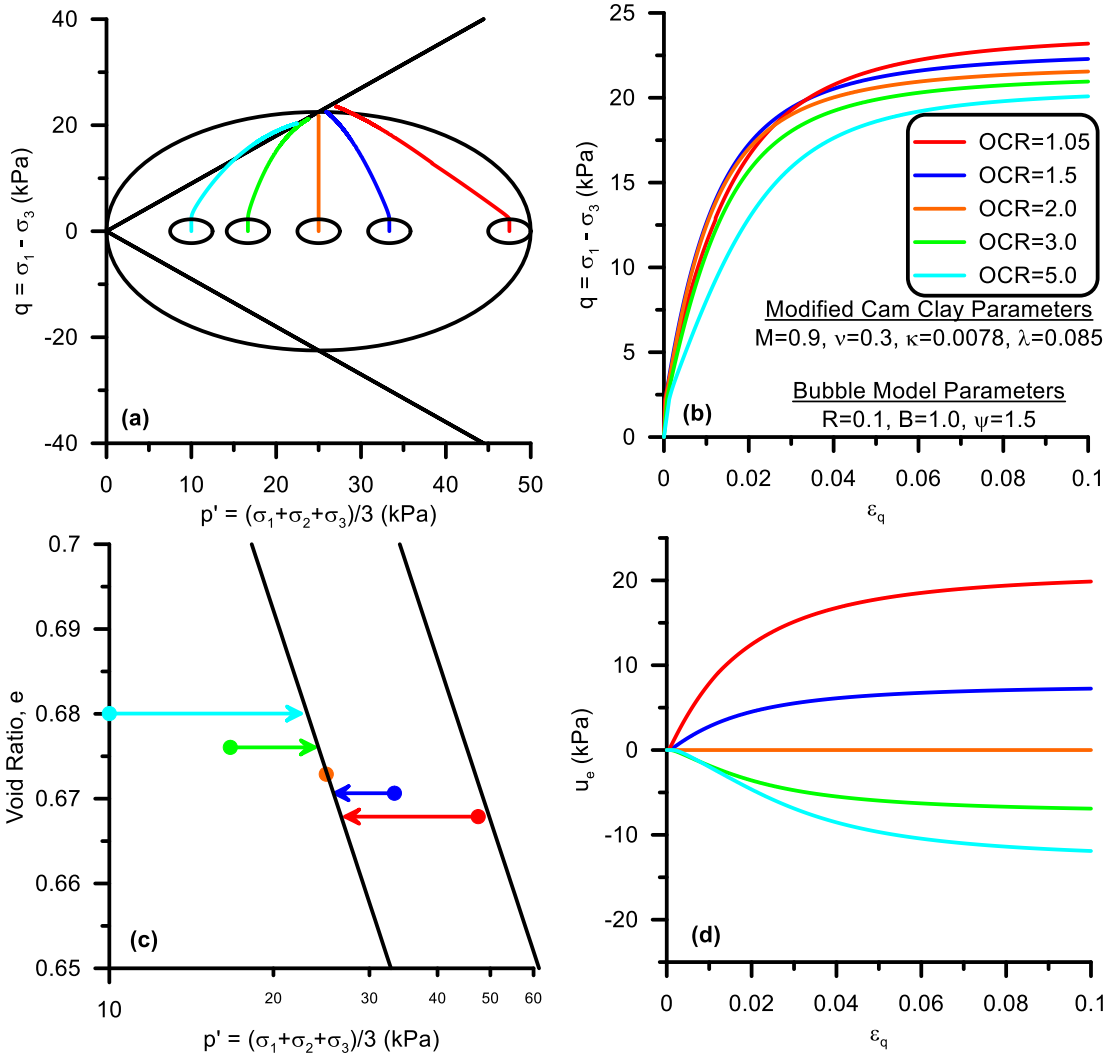

Figure 2-20 Numerical simulations for undrained stress path for a clay with different values of OCR using the bubble model

2.3.5.2.7 Drawbacks of the model

The Bubble model is an innovative modification of the Cam-Clay model. The model is attractive because it is able to capture the decrease of stiffness even at low strains. However, the model presents several drawbacks explained in this section.

First, the damping response of the model is not adequate. The hysteretic damping is controlled by the response of the model. When unloading and reloading inside the bubble, the model behaves as a linear elastic material, thus the hysteretic damping would be zero. At large strains, the hysteretic loops are too wide, and result in an over-prediction of the damping.

The response of the model can also be overly contractive or overly dilative under specific stress paths. If the soil is unloaded along the hydrostatic axis and then subjected to pure shear, the volumetric response would be highly dilative. This problem can also arise when the initial position of the bubble is not correctly specified.

Finally, the selection of the parameters B and ψ can be problematic. The two parameters are the most important to introduce early non-linearity (Rouainia and Muir Wood 2001). However, they are not physically meaningful and are selected to fit the laboratory tests. Using parameters that are not physically meaningful does not affect the model's performance, but can dissuade practitioners from using the model.

2.3.5.3 Kutter and Sathialingam

2.3.5.3.1 Principles

The model presented is an elastic-visco-plastic model capable of predicting primary consolidation, secondary compression, and strain rate effect. The equations for the rate of visco-plastic strains are based on a generalization of the visco-plastic theory of Perzyna (1963).

The assumptions of Kutter and Sathialingam are: (1) the elastic response is time independent, (2) time is incorporated in the model by updating the void ratio, (3) plastic strains are only time dependent, (4) plastic strains occur at all stress states, there is no elastic surface nor yield surface, only a reference surface and a loading surface. This does not mean that there is no elastic strains, but just that plastic strains develop at every strain level.

One of the hypothesis of the model is that plastic strains occur over time and that there is no instant plastic strains. To simulate primary consolidation visco-plastic strains occur rapidly at first. The strain rate is controlled by hydrodynamic lag. When the strain rates become very slow the secondary compression begins to dominate the volumetric strain, and the hydrodynamic lag does not control the phenomenon anymore.

The model has seven parameters: λ, κ, υ (Poisson's ratio), M, as described previously, e_N, void ratio at unit mean normal pressure after $\bar{t}$ days of normal consolidation (typically one day), $C_{\alpha 0}$ initial coefficient of secondary compression, and R, which is a shape parameter for the surface, and it represents the ratio of the mean normal stresses for the surfaces at $q=0$ and $q=Mp$. In the modified Cam-Clay model this ratio was assumed to be

equal to 2. Not that this ratio also defines the position of the CSL relative to the ISO-NCL. The model rate dependence is entirely introduced by $C_{\alpha 0}$. In the subsequent equations $\alpha = C_{\alpha 0}/ln10$. To predict pore pressure dissipation, another parameter should be introduced, the permeability *k*. All those parameters have been well defined in soil mechanics literature, and this kind of formulation is attractive to practicing engineers.

2.3.5.3.2 Surfaces of the Model

The model uses three surfaces. The reference surface ($\bar{f}$ =0) is the surface on which the soil is normally consolidated for the reference time. This is the equivalent of the static yield surface. The second surface is the loading surface, which has the same shape of the static surface, but it contains the current state of stress. This is equivalent to the dynamic loading surface. Although not useful in the model described in the paper, a potential surface ($\hat{f}$ =0) is also defined. This surface determines the direction of plastic flow. In the model, associative visco-plasticity is considered so the potential surface is the same as the reference surface. By changing the potential surface the model could use a non-associative flow rule.

As seen in Figure 2-21 all the surfaces have the same shape. They are composed of 2 different ellipses, but the surface is smooth, i.e. at the junction of the surfaces, they both have the same normal vector. The intersection of the reference surface with the *p*-axis is $\bar{p}_0$ and the intersection of the loading surface with the *p*-axis is p_L. Those two variables determine the size of the surfaces. p_L is found from the current state of stress, because

the current state of stress is always on the surface. For the reference surface, ellipses 1 and 2 have the following equations respectively:

$$\bar{f} = (\bar{p} - \bar{p}_0)\left[\bar{p} + \left(\frac{R-2}{R}\right)\bar{p}_0\right] + (R-1)^2\left(\frac{\bar{q}}{M}\right)^2 \qquad \textit{Equation 2-47}$$

$$\bar{f} = \bar{p}\left[\bar{p} - 2\frac{\bar{p}_0}{R}\right] + \left(\frac{\bar{q}}{M}\right)^2 \qquad \textit{Equation 2-48}$$

For the loading and the potential surface, $\bar{f}$, $\bar{p}$, $\bar{q}$ and $\bar{p}_0$ are replaced by f, p, q, and p_L and $\hat{f}$, $\hat{p}$, $\hat{q}$ and $\hat{p}_0$ respectively.

A radial mapping rule is used to map the current state of stress (σ) to the reference surface and to the potential surface. The image stress on the reference surface is $\bar{\sigma}$, and the image stress on the potential surface is $\hat{\sigma}$. As shown in Figure 2-21 the projection center is at the origin of the stress space.

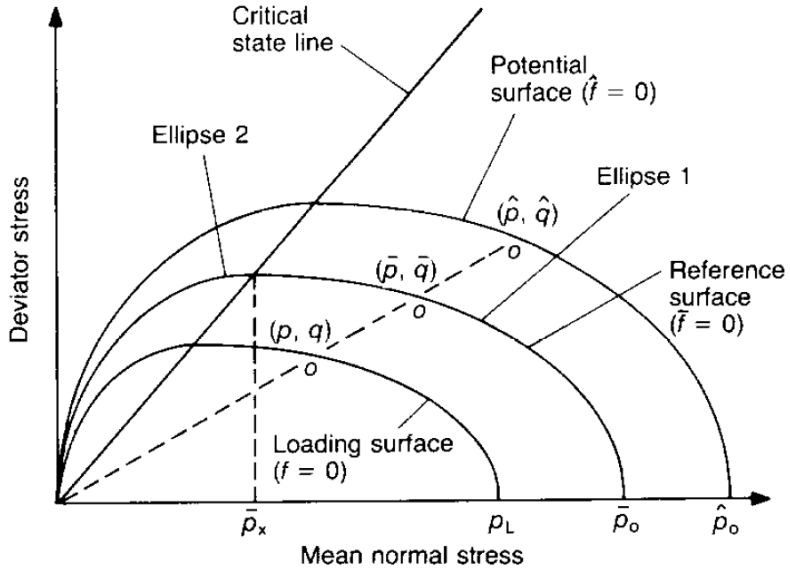

Figure 2-21 Loading, reference and potential surfaces in p, q plane (Kutter and Sathialingam 1992)

2.3.5.3.3 Introduction of Visco-plasticity (Flow Rule and Hardening Law)

Section 2.3.3 introduces Perzyna's theory of rate-dependent plasticity (1963). In Perzyna's formulation the stress difference function is only defined when F>0, i.e. when $f_d > f_s$. In the present model, the stress difference function is defined for any value of f_d and f_s, which means the current state of stress can be larger or smaller than the corresponding stress on the reference surface.

The stress difference function is derived based on Bjerrum's concept (1967). In the classic interpretation of consolidation problems, viscous strains (i.e. secondary compression) start after the completion of primary consolidation, i.e. when the pore pressure has dissipated. Bjerrum interprets the volume change as having two components. One 'instant compression' that occurs simultaneously with a change in effective stress, and a 'delayed compression' that is a change of volume at unchanged effective stress. There is a fine difference between those new terms and the terms 'primary and secondary compression'. In Figure 2-22 the dotted line corresponds to the settlement curve if the pore water pressure was not retarding the compression and if the compression due to a change in effective stress was instantaneous. This instant compression is different from the settlement at the end of primary consolidation because delayed compression, i.e. the viscous deformation, happens during primary consolidation.

To summarize, the concept essentially states that visco-plastic strains occur at all time during the consolidation process, and not only after the completion of the primary compression.

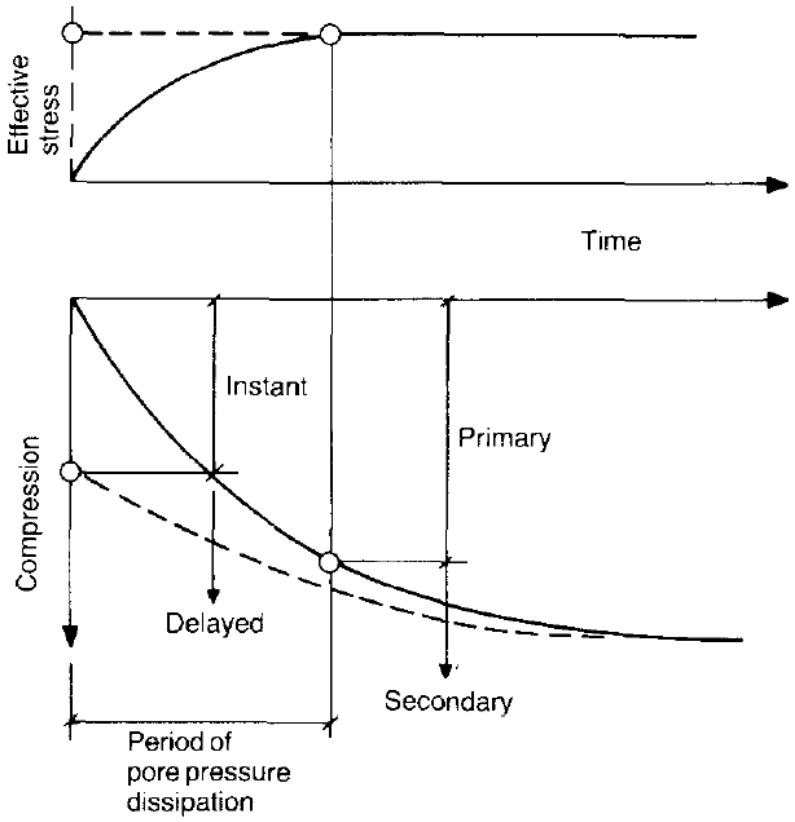

Figure 2-22 Bjerrum's concept of instant and delayed compression (Bjerrum 1967)

Bjerrum also states that the position of the compression curve depends on the time of consolidation under constant effective stress. When the secondary compression occurs, the void ratio decreases under constant effective stress. During a longer time of consolidation secondary compression will result in greater deformations, and it will results in a lower compression curve (Figure 2-23).

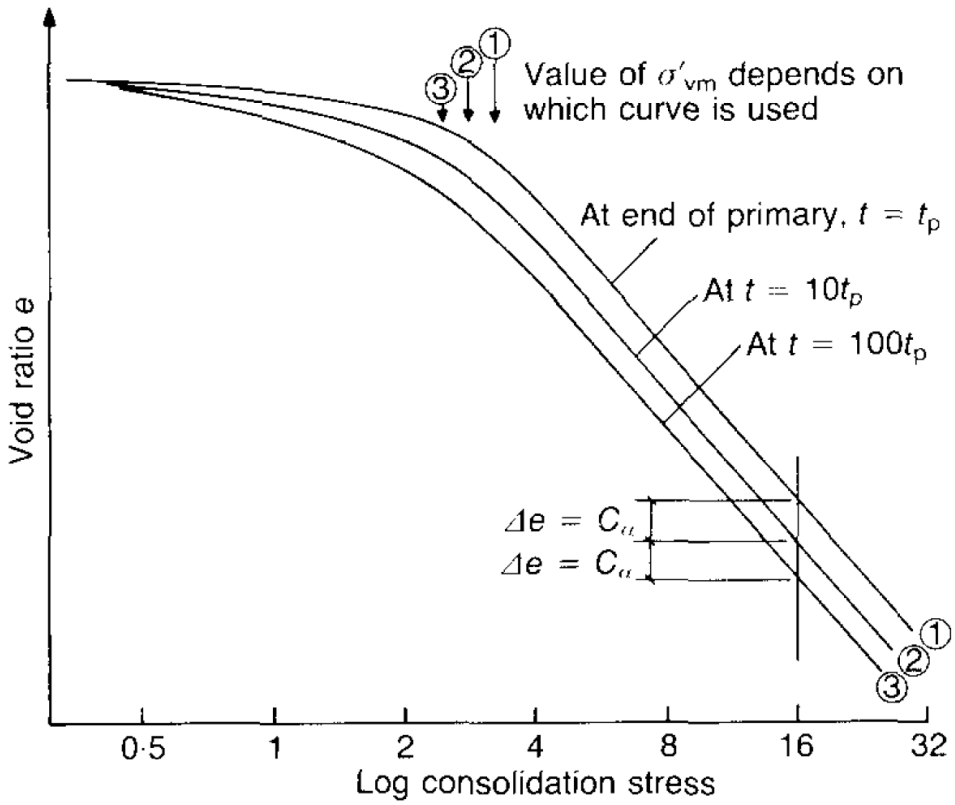

Figure 2-23 Effect of secondary compression on the location of the compression curve (Bjerrum 1967)

An increase in secondary compression is associated with an increase in apparent preconsolidation pressure. In Figure 2-24, the state of soil is initially at point *a*, the reference and the loading surfaces are the same (i.e. $\bar{p}_0 = p_L$). As the sample undergoes creep, the void ratio decreases from *a* to *b*. The apparent preconsolidation pressure now increases from *c* to *d*. If the stresses remain unchanged, p_L remains at point *c*.

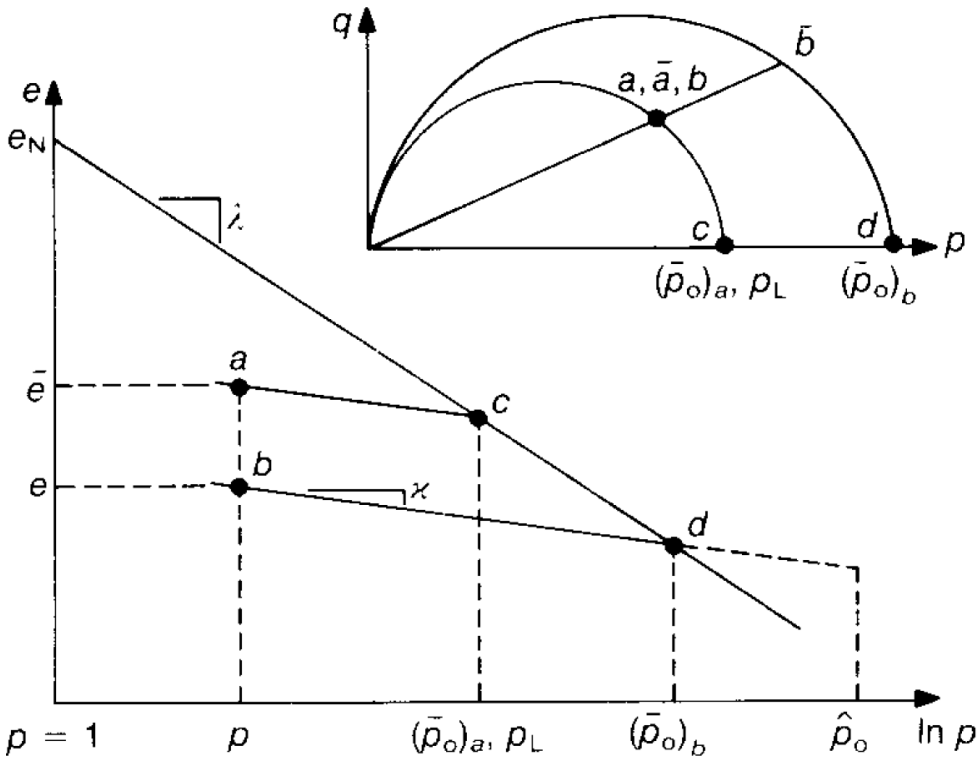

Figure 2-24 Evolution of the reference and the loading surface during secondary compression

Based on the concept of delayed compression the size of the reference surface (static surface) will increase with time, due to secondary compression, i.e. $\bar{p}_0$ moves with time. The new position can be calculated with the following formula (Murakami 1979):

$$\frac{\bar{p}_0}{p_0} = \left[\frac{t}{t_0}\right]^{\alpha/(\lambda-\kappa)} \qquad \textit{Equation 2-49}$$

where p_0 is the effective vertical consolidation pressure, and t_0 is the reference age of the clay (equivalent to t_p). In the model void ratio evolves with time.

The size of the loading surface will remain the same, i.e. p_L remains the same. The strain rate is assumed to be dependent of the distance from the current stress state to the

reference. Kutter and Sathialingam showed that visco-plastic volumetric strains depends on the evolution of those 2 surfaces and can be formulated:

$$\dot{\varepsilon}_v^{vp} = \frac{\alpha}{\bar{t}v_0}\left(\frac{p_L}{\bar{p}_0}\right)^{(\lambda-\kappa)/\alpha} \qquad \textit{Equation 2-50}$$

where $\bar{t}$ is the time reference which is an arbitrary quantity. It is taken as the number of days of normal consolidation. This is a hard quantity to define and it has an important influence on the behavior of the model. In laboratory results its value can be estimated easily, but for field simulations it may be more complicated. α is simply C_α/ln10, v_0 is the initial specific volume (1+e_0). In their model, the secondary compression parameter $C_{\alpha 0}$ is considered constant. Combining Equation 2-30 and Equation 2-50, we obtain the following expression for Φ:

$$\phi = \frac{\alpha_0}{\bar{t}v_0\left(\frac{\partial \hat{f}}{\partial \hat{p}}\right)_0}\left(\frac{p_L}{\bar{p}_0}\right)^{\frac{\lambda-\kappa}{\alpha}} \qquad \textit{Equation 2-51}$$

2.3.5.3.4 Performance of the Model

Figure 2-25 presents a comparison between a simulation and the test results of a consolidation test on New Haven clay. The data for this test comes from Mesri and Godlewski (1977). The model is able to match the behavior of the clay during primary consolidation, and after the excess pore pressure is dissipated. That includes the evolution of secondary compression.

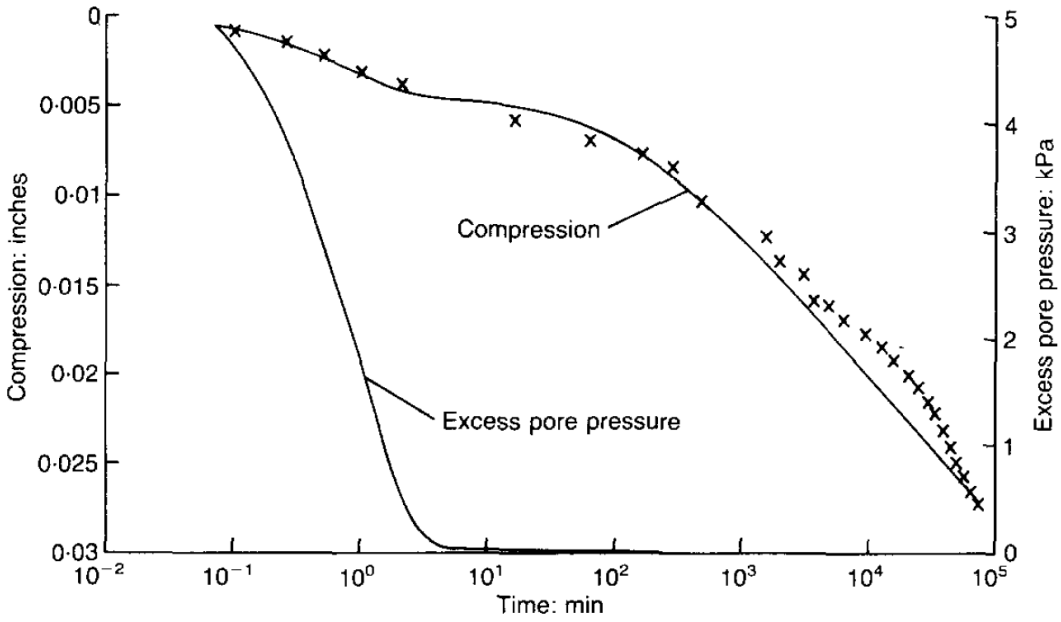

Figure 2-25 Simulation of a one dimensional compression test on New Haven clay (Kutter and Sathialingam 1992)

Figure 2-26 presents the results of simulations of undrained triaxial compression tests at four different OCRs: 1, 1.3, 2 and 6. The lab data comes from Herrmann et al. 1981. The model behaves well for the normally consolidated and slightly overconsolidated samples. For highly overconsolidated clay (OCR=6), the model tends to overestimate shear stresses for undrained stress path of dilative soils. Those predictions are close to what could be predicted by the Modified Cam-Clay model.

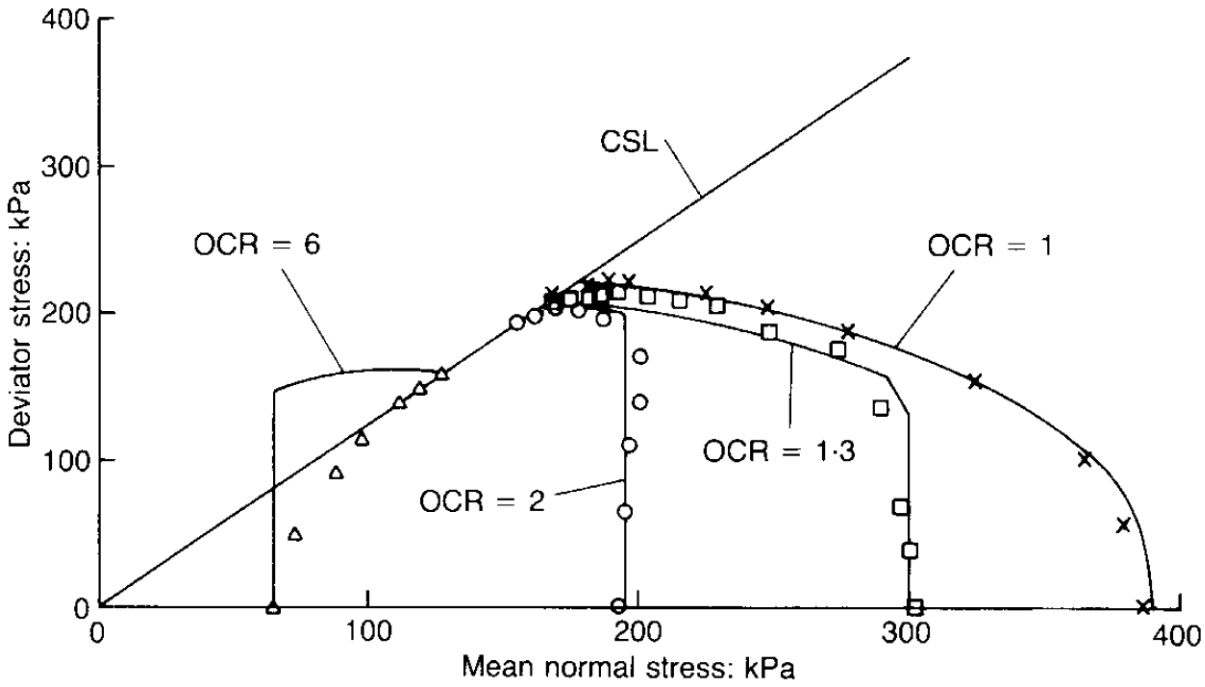

Figure 2-26 Simulations of undrained triaxial compression tests at different OCR's (Kutter and Sathialingam 1992)

2.3.5.3.5 Drawback of the Model

This model is proved to match the viscous behavior of clay very well. However the formulation of the model is in contradiction with the concept of the reset of the secondary compression clock, explained in section 2.1.4.2.2. Upon cyclic loading under undrained conditions, the model would predict a decrease of mean effective stress due to an increase in pore pressure. When cyclic loading ceases, drained conditions develop, the mean effective stress increases and the void ratio decreases. This would lead to a decrease of the rate of secondary compression, which is inconsistent with the observed behavior of peat by Shafiee et al. (2015).

2.3.5.4 Simple Plasticity Sand Model Accounting for Fabric Change Effects (Dafalias and Manzari 2004)

2.3.5.4.1 Principles

This simple sand model is a modification of a model initially derived by Dafalias and Manzari (1997). The basic assumption of the model is that only a change in stress ratio causes enough shearing to create plastic strains. Under this assumption an increase in stress under a constant stress ratio causes only elastic strains. To calculate plastic strains, the model uses a non-associative flow rule. In the model the deviatoric plastic strains are calculated based on the change in stress ratio and the plastic modulus. This latter depends on the difference between the current stress ratio and a bounding stress ratio that depends on the critical state parameter.

The amplitude of plastic volumetric strains depend on the amplitude of plastic deviatoric strains and a dilatancy variable (d). The dilatancy variable also depends on the difference between the current stress ratio and a dilatancy stress ratio that also depends on the critical state parameter.

The model also includes a so-called “fabric change effect”, to better model the behavior of sand, and the change of fabric that happens upon shearing. For the sake of brevity, the effect of fabric change on dilatancy is not discussed here. This effect is important to model the behavior of sand, but this section focuses on the stress-ratio formulation, more pertinent to model the behavior of peat.

In this section, the elastic response of the model is described first, then, the different surfaces, the flow rule and hardening laws of the model are presented. Finally, a monotonic and a cyclic example are presented to illustrate the performance of the model.

2.3.5.4.2 Elastic Response

The elastic response is governed by Equation 2-17 and Equation 2-19. This model is formulated for sand and the bulk and shear modulus depend on the void ratio *e* and the mean effective stress *p* following the definition of Richart et al. (1970) and Li and Dafalias (2000):

$$G = G_0 p_{at} \frac{(2.97 - e)^2}{1 + e} \left(\frac{p}{p_{at}}\right)^{1/2} \quad \textit{Equation 2-52}$$

$$K = \frac{2(1 + \nu)}{3(1 - 2\nu)} G \quad \textit{Equation 2-53}$$

where G_0 is a constant.

2.3.5.4.3 Yield, Bounding and Dilatancy Surfaces

The model uses four surfaces that are lines in the triaxial (p-q) space. The surfaces are represented in Figure 2-27. The yield surface that delimits the elastic region is defined as:

$$f = |\eta - \alpha| - m = 0 \quad \textit{Equation 2-54}$$

This equation represents a wedge (Figure 2-27) where α is the slope of the bisecting line (i.e. the center of the yield surface), and *m* is the size of the yield surface. The wedge

opening is 2*mp.* If the current stress ratio is inside the wedge, the model behaves elastically.

The critical state line is defined by its slope *M*. The critical state line is used to define the bounding and dilatancy lines, that depend on the state parameter ψ. The state parameter is defined as the distance in the *e*-*p* space between the current point and the critical state line:

$$\psi = e - e_{cs} \qquad \textit{Equation 2-55}$$

This state parameter is considered in this model as a state variable. The state parameter can change as a result of a change in void ratio or a change in mean effective stress. A change of mean effective stress induces a change in critical state void ratio. The equations for the bounding and the dilatancy stress ratios are:

$$M_b = Me^{-n^b\psi} \qquad \textit{Equation 2-56}$$

$$M_d = Me^{n^d\psi} \qquad \textit{Equation 2-57}$$

In those equations, n^b and n^d are positive material constants. When the material reaches critical state, the state variable is zero and the dilatancy and bounding lines collapse onto the critical state line.

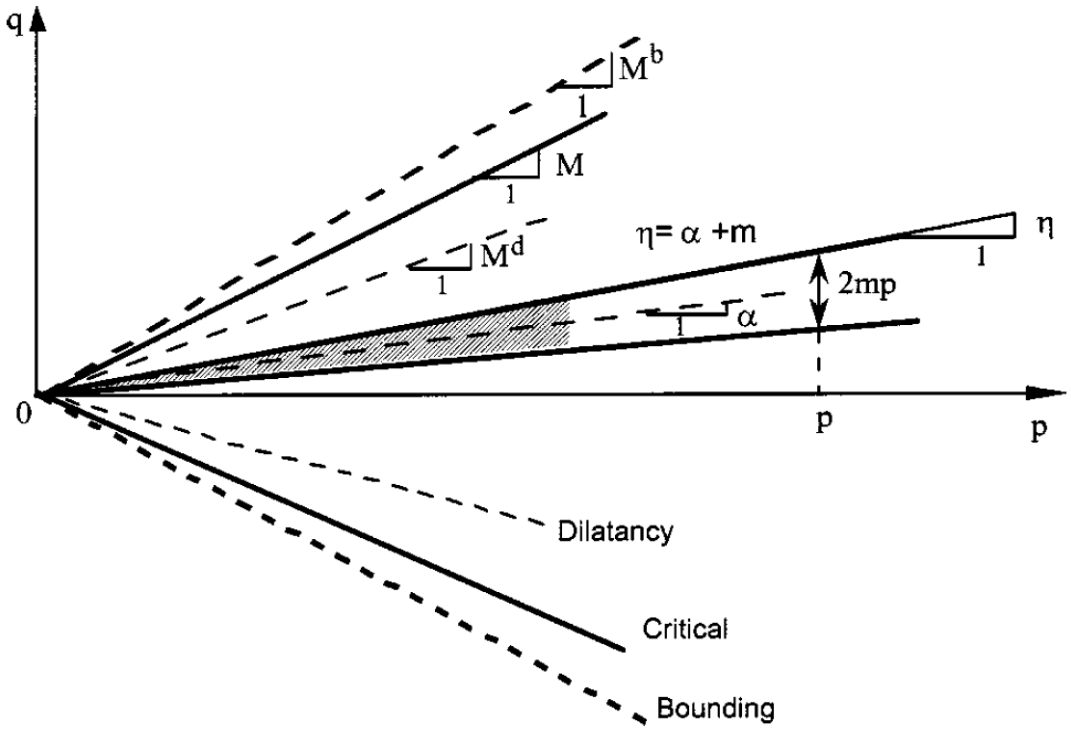

Figure 2-27 Schematic of the Yield, Critical, Dilatancy, and Bounding Lines in p-q space(Dafalias and Manzari 2004)

2.3.5.4.4 Flow Rule and Hardening Law

As mentioned in the introduction of this section, the model uses a non-associative flow rule. The plastic deviatoric strains depend on the increment of stress ratio and the plastic modulus (*H*):

$$d\varepsilon_q^p = \frac{d\eta}{H}$$ *Equation 2-58*

The plastic modulus depends on the distance between the current stress ratio and the bounding surface:

$$H = h(M^b - \eta)$$ *Equation 2-59*

In this equation, *h* is positive and depends on state variables. The value of *h* can be defined by different expressions. The simplest assumption is to use a constant *h*. However the behavior of the model can be improved by using a value of *h* that depends on *e, p* and η. In their model, Dafalias and Manzari present the following equation for *h*:

$$h = \frac{b_0}{|\eta - \eta_{in}|} \text{ where } b_0 = G_0 h_0 (1 - c_h e) \left(\frac{p}{p_{at}}\right)^{-1/2} \qquad \textit{Equation 2-60}$$

In this equation G_0, h_0 and c_h are material constants. η_{in} is the stress ratio at the beginning of the plastic loading phase. Hence *h* and *H* go to infinity when plastic loading begins. The plastic volumetric strains depend on the amplitude of plastic deviatoric strains, and on the dilatancy:

$$d\varepsilon_v^p = d\left|d\varepsilon_q^p\right| \qquad \textit{Equation 2-61}$$

The dilatancy is calculated based on the difference between the current stress ratio and the dilatancy stress ratio:

$$d = A_d (M^d - \eta) \qquad \textit{Equation 2-62}$$

Where A_d is a material parameter that can be a constant of that can evolve with the state, to be made dependent of fabric. In their paper, Dafalias and Manzari provides a definition of A_d that accounts for fabric change. This definition is not presented here. Note that the previous equation implies that if $\eta < M_d$ then $d > 0$ and the soil is contractive. If $\eta > M_d$ then $d < 0$ and the soil is dilative. If $\eta = M_d$, for example at critical state, then $d = 0$ and the plastic volumetric strains are then equal to zero.

2.3.5.4.5 Summary of the Model

Table 2-2 Summary of the Dafalias and Manzari model (Dafalias and Manzari 2004)

Triaxial equations	Multiaxial equations	Constants
Critical state line		
—	$e_c = e_0 - \lambda_c (p_c / p_{at})^{\xi}$	e_0, λ_c, ξ
Elastic deviatoric strain increment		
$d\varepsilon_q^e = dq/3G$	$d\mathbf{e}^e = d\mathbf{s}/2G$	—
—	$G = G_0 p_{at} [(2.97-e)^2/(1+e)](p/p_{at})^{1/2}$	G_0
Elastic volumetric strain increment		
—	$d\varepsilon_v^e = dp/K$	
	$K = 2(1+\nu)G/3(1-2\nu)$	ν
Yield surface		
$f = \lvert\eta - \alpha\rvert - m = 0$	$f = [(\mathbf{s}-p\boldsymbol{\alpha}):(\mathbf{s}-p\boldsymbol{\alpha})]^{1/2} - \sqrt{2/3}pm = 0$	m
Plastic deviatoric strain increment		
$d\varepsilon_q^p = d\eta/H$	$d\mathbf{e}^p = \langle L \rangle \mathbf{R}'$	
$H = h(M^b - \eta)$	$K_p = (2/3)ph(\boldsymbol{\alpha}_\theta^b - \boldsymbol{\alpha}):\mathbf{n}$	
$M^b = M \exp(-n^b \Psi)$	$\boldsymbol{\alpha}_\theta^b = \sqrt{2/3}[g(\theta,c)M \exp(-n^b\Psi) - m]\mathbf{n}$	M, c, n^b
$h = b_0 / \lvert\eta - \eta_{in}\rvert$	$h = b_0 / (\boldsymbol{\alpha} - \boldsymbol{\alpha}_{in}):\mathbf{n}$	
—	$b_0 = G_0 h_0 (1 - c_h e)(p/p_{at})^{-1/2}$	h_0, c_h
Plastic volumetric strain increment		
$d\varepsilon_v^p = d\lvert\varepsilon_q^p\rvert$	$d\varepsilon_v^p = \langle L \rangle D$	
$d = A_d(M^d - \eta)$	$D = A_d(\boldsymbol{\alpha}_\theta^d - \boldsymbol{\alpha}):\mathbf{n}$	
$M^d = M \exp(n^d \Psi)$	$\boldsymbol{\alpha}_\theta^d = \sqrt{2/3}[g(\theta,c)M \exp(n^d\Psi) - m]\mathbf{n}$	n^d
$A_d = A_0(1 + \langle sz \rangle)$	$A_d = A_0(1 + \langle \mathbf{z}:\mathbf{n} \rangle)$	A_0
Fabric-dilatancy tensor update		
$dz = -c_z \langle -d\varepsilon_v^p \rangle (sz_{max} + z)$	$d\mathbf{z} = -c_z \langle -d\varepsilon_v^p \rangle (z_{max}\mathbf{n} + \mathbf{z})$	c_z, z_{max}
Back-stress ratio tensor update		
$d\alpha = d\eta$	$d\boldsymbol{\alpha} = \langle L \rangle (2/3)h(\boldsymbol{\alpha}_\theta^b - \boldsymbol{\alpha})$	

2.3.5.4.6 Performance of the Model

This section presents the simulations of four monotonic undrained triaxial compression tests and an undrained cyclic triaxial test on Toyoura sand. This section provides a discussion on the results and on the model's prediction capability. For more details on the simulation and the selection of the model's variables, the reader is invited to read Dafalias and Manzari (2004).

Figure 2-28 presents a comparison between lab results and model predictions for four triaxial tests on the Toyoura Sand. The lab data comes from Verdugo and Ishihara (1996). The four samples have the same void ratio (e=0.833), and the same relative density

(37.9%), but are consolidated at different effective stresses: 100, 1000, 2000 and 3000 kPa. The set of variables used is the same in all four simulations, the only difference arises from the initial stress conditions.

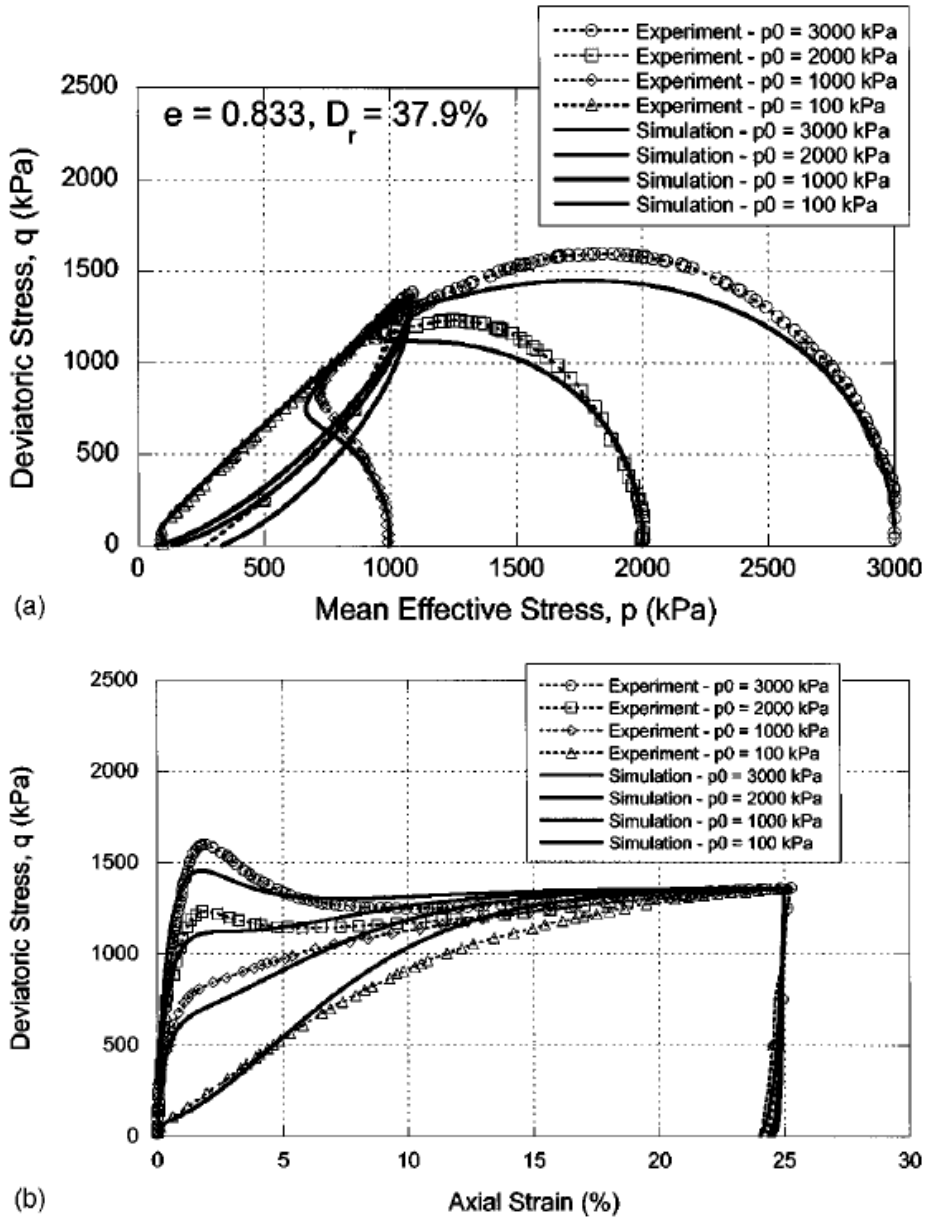

Figure 2-28 Comparison of test results and numerical simulations of undrained triaxial compression tests on Toyoura sand: (a) stress path in p-q space (b) stress-strain behavior (Dafalias and Manzari 2004)

The model proves to match the observed behavior very closely, being able to correctly predict the dilative and contractive behavior of the sand. The model also predicts a peak shear strength, although it somewhat underestimates it. The unloading is also correctly captured by the model.

Figure 2-29 presents the results of a simulation of a cyclic undrained triaxial test. The lab data comes from Ishihara et al. (1975). The initial void ratio is 0.808, and the sample is consolidated at a mean effective stress of 294 kPa.

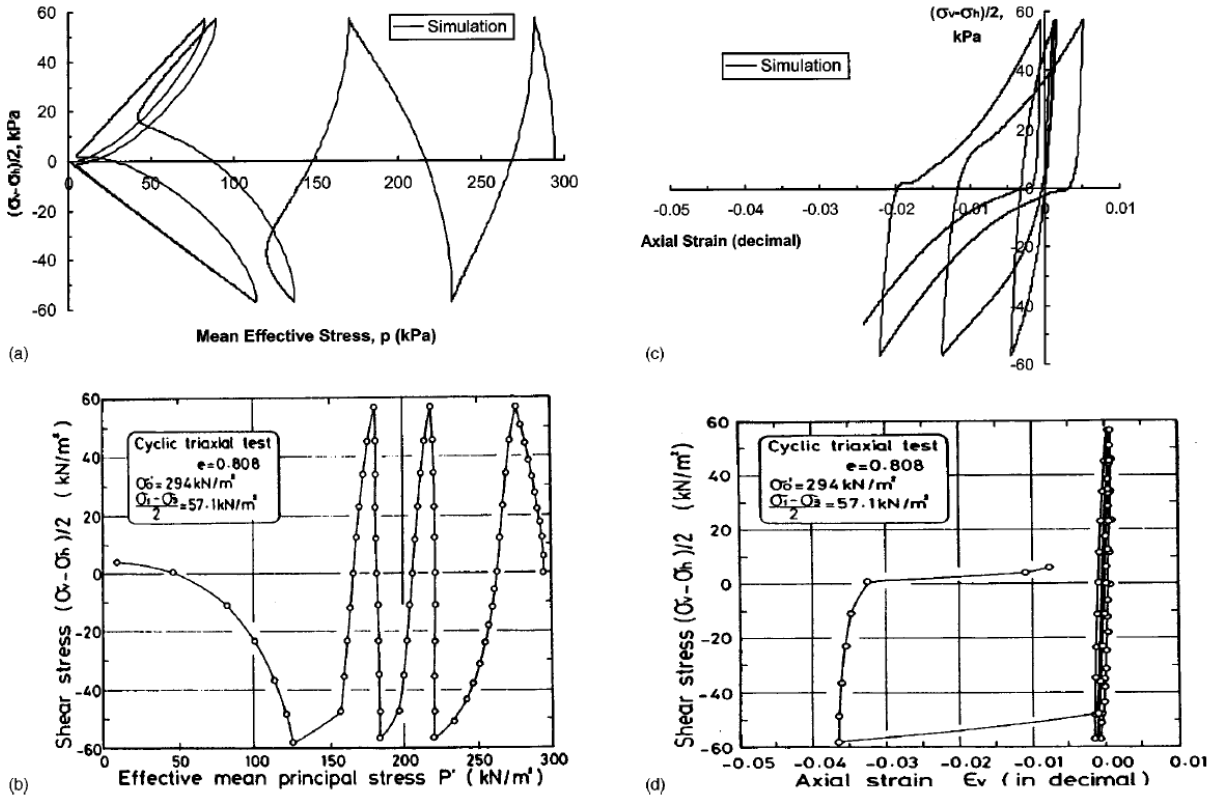

Figure 2-29Comparison of test results ((b) and (d)) and numerical simulations ((a) and (c)) of a cyclic triaxial undrained tests on sand (Dafalias and Manzari 2004). (a) and (b) shear stress vs. effective mean principal stress, (c) and (d) stress-strain curves

The model does not match the behavior observed in this test. However the shape of the loops are realistic and representative of the dilative behavior of the soil. The stress path

in the lab test is not what is commonly observed for sand. Dafalias and Manzari attributes this difference to the fact that the test was done in 1975, about twenty years earlier than the monotonic tests, and that the instruments and preparation methods were different.

2.3.5.5 SANISAND: Simple Anisotropic Sand Plasticity Model (Taiebat and Dafalias 2008)

2.3.5.5.1 Principles

This SANISAND model is based on the model derived by Dafalias and Manzari (2004). The main improvement is the introduction of a cap to the yield surface. This allows the model to generate plastic strains without a change of stress ratio. The yield surface is governed by a rotational hardening law and an isotropic hardening law.

The plastic strain rate is decomposed in two parts. One part of the plastic strain is due to a change in stress ratio, and the second part is generated under constant stress ratio. The isotropic hardening is governed by the volumetric plastic strain generated under constant stress ratio. The rotational hardening governs the anisotropic response of the model. It has been modified from the Dafalias and Manzari (2004) model because of the introduction of the closed yield surface. The stress ratio α is the rotational hardening variable and is called the back ratio. The back ratio is the bisector of the yield surface.

2.3.5.5.2 Yield, Bounding and Dilatancy Surfaces

The bounding and dilatancy surfaces of the model are not modified from Dafalias and Manzari (2004). The closed yield surface has the following equation:

$$f = (q - p\alpha)^2 - m^2 p^2 [1 - (p/p_0)^n]$$ *Equation 2-63*

In this equation p_0 is the tip of the yield surface, m is the size of the yield surface, and n is an exponent governing the shape of the yield surface (Figure 2-30). Note that when p_0 goes to infinity the yield surface is equivalent to the yield surface derived by Dafalias and Manzari (2004).

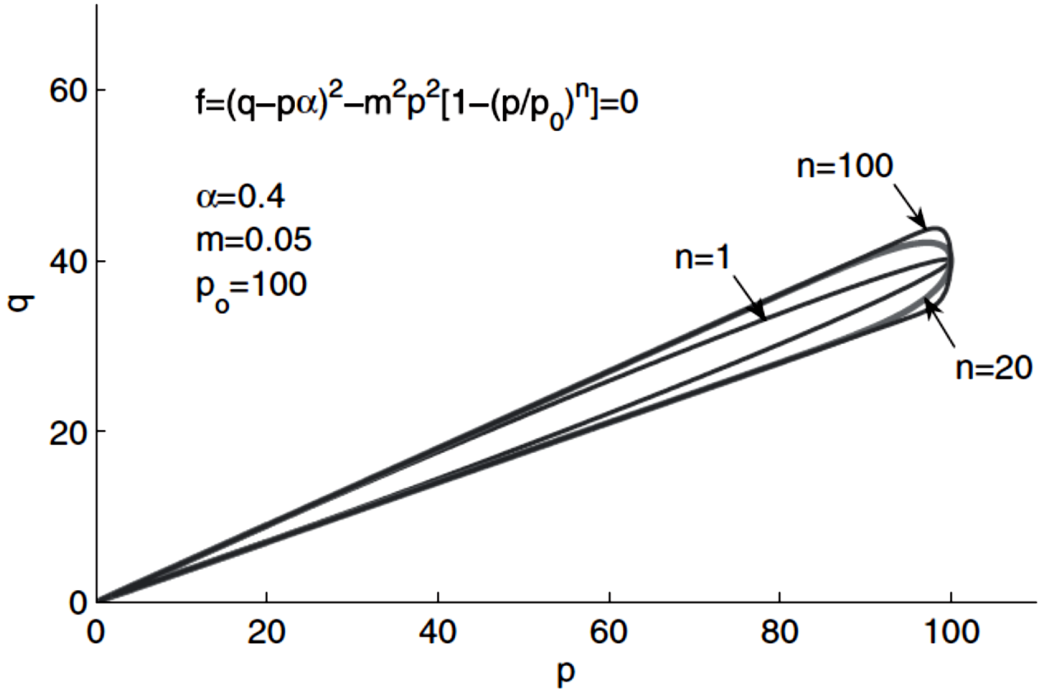

Figure 2-30 Influence of parameter n on the shape of the yield surface (Taiebat and Dafalias 2008)

2.3.5.5.3 Performance of the Model

Figure 2-31 presents the results of lab tests and simulation of isotropic compression tests performed on Sacramento River Sand. The original data comes from Lee and Seed (1967). In this test the stress ratio remains constant, and the model is able to match the nonlinear behavior of the sand well. The nonlinear behavior is captured because of the

introduction of the cap and the generation of plastic volumetric strains under constant stress ratio.

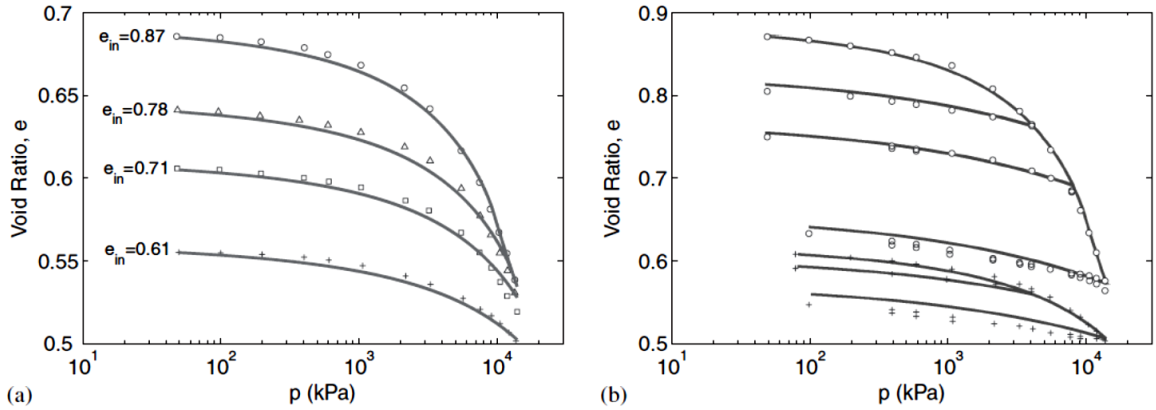

Figure 2-31 Comparison between data and simulations for isotropic compression on Sacramento River sand (Taiebat and Dafalias 2008)

2.3.5.5.4 Summary of the Model

Table 2-3 Summary of the SANISAND model (Taiebat and Dafalias 2008)

Triaxial formulation	Multiaxial formulation
Elasticity	
$\dot{\varepsilon}_q^e = \dot{q}/(3G)$	$\dot{\mathbf{e}}^e = \dot{\mathbf{s}}/(2G)$
$\dot{\varepsilon}_v^e = \dot{p}/K$	$\dot{\varepsilon}_v^e = \dot{p}/K$
Yield surface	
$f = (q - p\alpha)^2$	$f = (3/2)(\mathbf{s} - p\boldsymbol{\alpha}) : (\mathbf{s} - p\boldsymbol{\alpha})$
$-m^2 p^2[1 - (p/p_0)^n] = 0$	$-m^2 p^2[1 - (p/p_0)^n] = 0$
Flow rule	
$\dot{\varepsilon}_q^p = \langle L\rangle[sr_{ef} + X\eta e^{-Vr_{ef}}]$	$\dot{\mathbf{e}}^p = \langle L\rangle[\sqrt{3/2}\mathbf{n}r_{ef} + (3/2)X\mathbf{r}e^{-Vr_{ef}}]$
$\dot{\varepsilon}_v^p = \langle L\rangle[Dr_{ef} + e^{-Vr_{ef}}]$	$\dot{\varepsilon}_v^p = \langle L\rangle[Dr_{ef} + e^{-Vr_{ef}}]$
$r_{ef} = \lvert\eta - \alpha\rvert$	$r_{ef} = [(3/2)(\mathbf{r} - \boldsymbol{\alpha}) : (\mathbf{r} - \boldsymbol{\alpha})]^{1/2}$
Evolution laws	
$\dot{\alpha} = \langle L\rangle h(\alpha^b - \alpha)r_{ef}$	$\dot{\boldsymbol{\alpha}} = \langle L\rangle h(\boldsymbol{\alpha}^b - \boldsymbol{\alpha})r_{ef}$
$\dot{p}_0 = \langle L\rangle p_0(1 + e)e^{-Vr_{ef}}/$ $[e(\rho_c - (p_0/p_{at})^{1/3}/K_0)(1 - (\operatorname{sgn}\delta)\lvert\delta\rvert^\theta)]$	
$h = b_0/[b_{ref} - s(\alpha^b - \alpha)]^2$	$h = b_0/[(3/2)(\mathbf{b}_{ref} - (\boldsymbol{\alpha}^b - \boldsymbol{\alpha})) : \mathbf{n}]^2$
$D = sA_d(\alpha^d - \alpha)$	$D = \sqrt{3/2}A_d(\boldsymbol{\alpha}^d - \boldsymbol{\alpha}) : \mathbf{n}$
$s = (q - p\alpha)/\lvert q - p\alpha\rvert$	$\mathbf{n} = (\mathbf{s} - p\boldsymbol{\alpha})/\lvert\mathbf{s} - p\boldsymbol{\alpha}\rvert$
$\alpha^{c,b,d} = sg\alpha_c^{c,b,d}$	$\boldsymbol{\alpha}^{c,b,d} = \sqrt{2/3}g\alpha_c^{c,b,d}\mathbf{n}$
$\alpha_c^b = \alpha_c^c \exp(-n^b\psi)$	
$\alpha_c^d = \alpha_c^c \exp(n^d\psi)$	
Yield surface derivatives	
$\partial f/\partial p = -2\alpha(q - p\alpha) - 2m^2 p$ $+ (2 + n)m^2 p(p/p_0)^n$	$\partial f/\partial p = -3\boldsymbol{\alpha} : (\mathbf{s} - p\boldsymbol{\alpha}) - 2m^2 p$ $+ (2 + n)m^2 p(p/p_0)^n$
$\partial f/\partial q = 2(q - \alpha p)$	$\partial f/\partial \mathbf{s} = 3(\mathbf{s} - p\boldsymbol{\alpha})$
$\partial f/\partial \alpha = -2p(q - \alpha p)$	$\partial f/\partial \boldsymbol{\alpha} = -3p(\mathbf{s} - p\boldsymbol{\alpha})$
$\partial f/\partial p_0 = -(n/p_0)m^2 p^2(p/p_0)^n$	$\partial f/\partial p_0 = -(n/p_0)m^2 p^2(p/p_0)^n$

2.3.5.6 SANICLAY: Simple Anisotropic Clay Plasticity Model (Dafalias et al. 2006)

2.3.5.6.1 Principles

The SANICLAY model is a plasticity model derived to account for stress anisotropy and softening response of clays under undrained compression after K_0 consolidation. The stress-anisotropy is taken into account through a rotational hardening variable that rotates the yield surface upon loading and also by the introduction of an anisotropic critical state line in e-p' space.

The model uses a non-associative flow rule by introducing a plastic potential surface that is different from the yield surface. This non-associative flow rule is introduced to simulate the softening response of the soil under undrained compression after K_0 consolidation.

The model also uses a bounding surface principle, where the response of the model depends on the distance between the current stress ratio and a bounding stress ratio. In a triaxial setting the bounding surfaces are the critical state stress ratio in compression and extension, respectively M_c and M_e.

2.3.5.6.2 Yield and Plastic Potential Surfaces

Figure 2-32 shows the yield and plastic potential surfaces. The yield surface has the following equation:

$$f = (q - p\beta)^2 - (N^2 - \beta^2)p(p_0 - p) = 0 \qquad \textit{Equation 2-64}$$

where β is the rotational hardening variable, p_0 is the isotropic hardening variable and the value of p at $\eta = \beta$, and N is a constant that is similar to M but it is the same in extension or in compression. For evolution laws of the rotational and isotropic hardening variables, the reader is invited to read Dafalias et al. (2006). The plastic potential surface has the following equation:

$$g = (q - p\alpha)^2 - (M^2 - \alpha^2)p(p_\alpha - p) = 0 \qquad \textit{Equation 2-65}$$

where α is a non-dimensional anisotropic variable, and p_α is the value p at $q = p\alpha$. Note that α evolves during loading, and for the sake of brevity its evolution law is not described here.

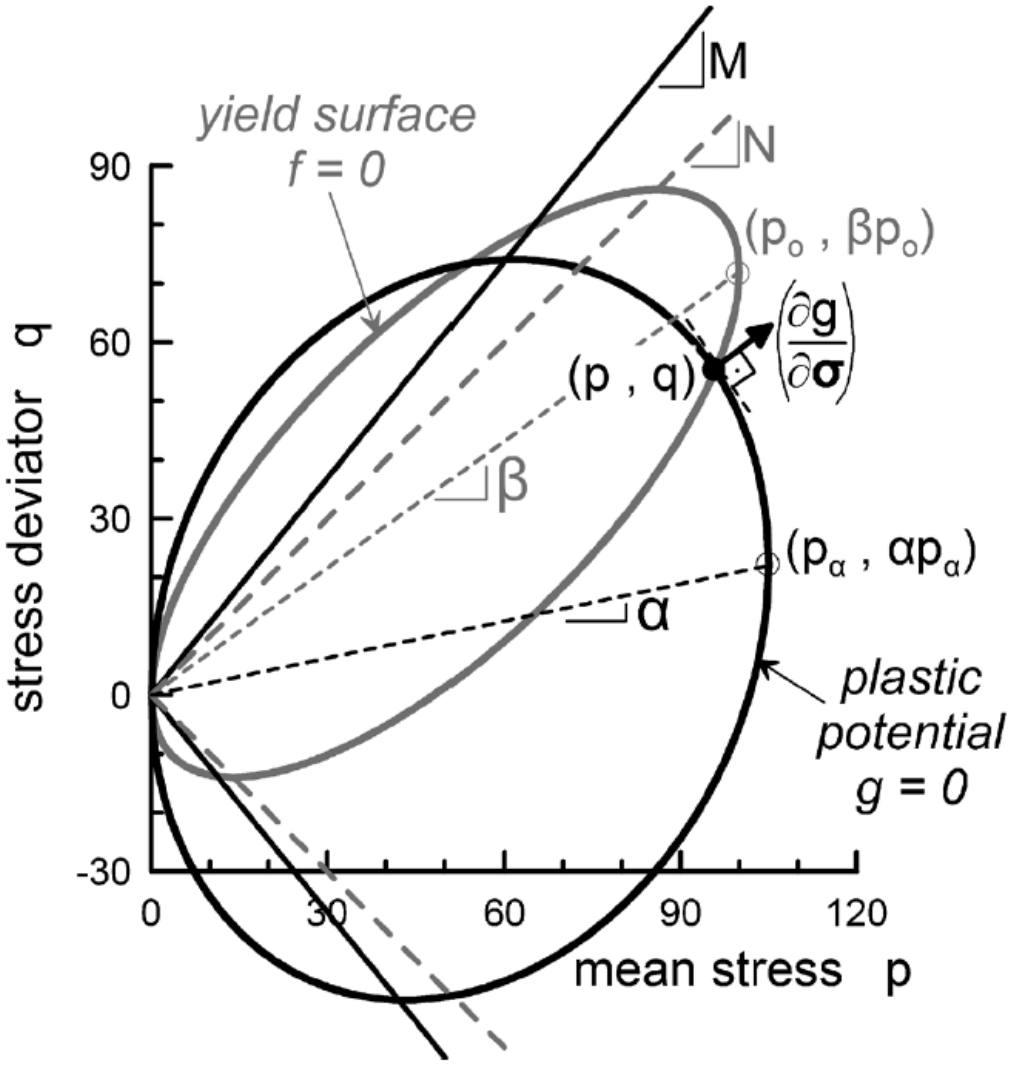

Figure 2-32 Yield and plastic potential surfaces for the SANICLAY model Dafalias et al. (2006)

2.3.5.6.3 Performance of the Model

This section presents the simulations of lab tests performed on low plasticity clays by Gens (1982). Figure 2-33 presents the results of a simulation of undrained triaxial compression and extension tests. The samples where isotropically consolidated at various OCRs. In this configuration the response of the model is close to the Modified Cam Clay because the model surfaces are not rotated.

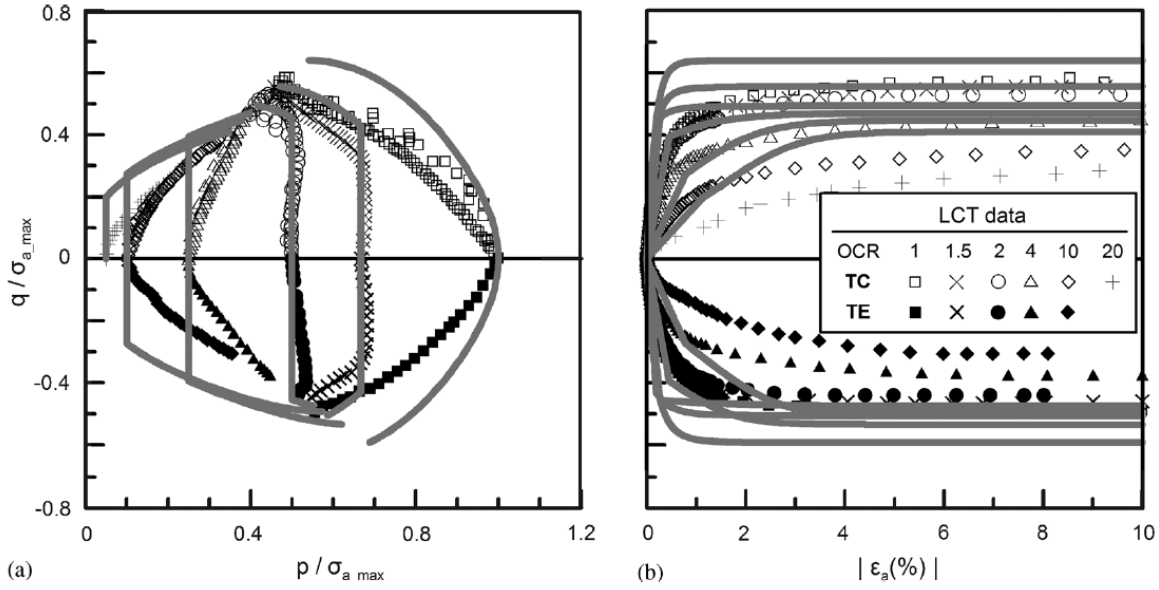

Figure 2-33 Comparison of lab results and simulations of undrained triaxial compression and rxtension tests on isotropically consolidated samples of clays with different OCRs (Dafalias et al. 2006)

Figure 2-33 presents the results of a similar simulation of undrained triaxial compression and extension tests. In this test the samples where anisotropically consolidated at various OCRs. In this simulation the model is able to reproduce the softening response observed after K_0-consolidation. The best fit is obtained for K_0=0.5. This is because the model was calibrated based on test results done at K_0=0.5.

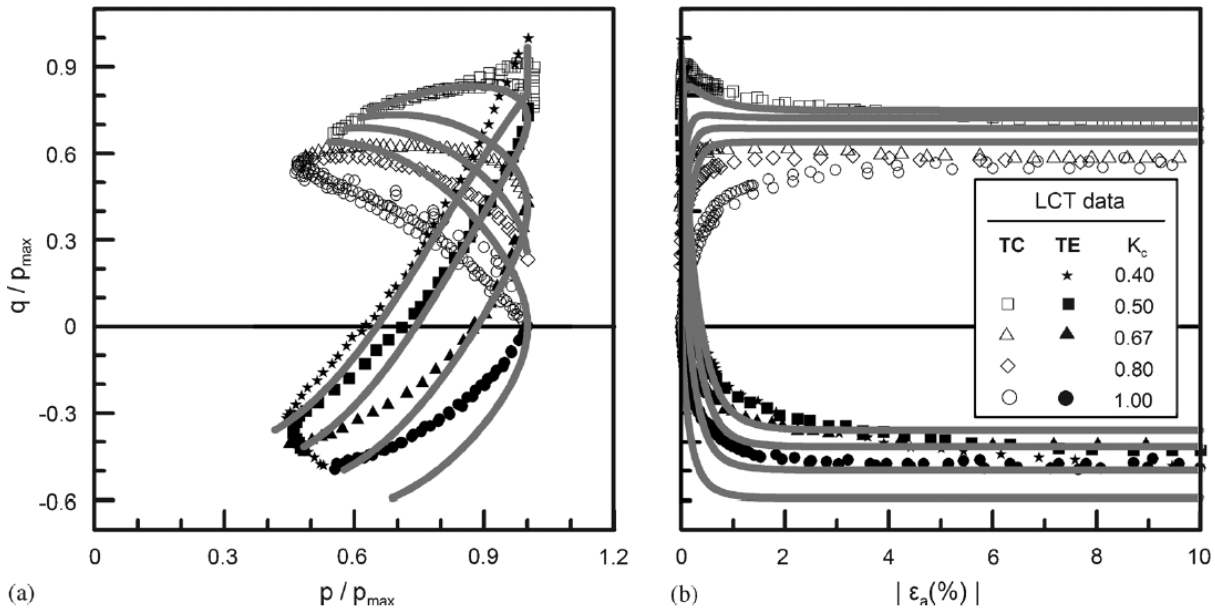

Figure 2-34 Comparison of lab results and simulations of undrained triaxial compression and extension tests on anisotropically consolidated samples of clays with different OCRs (Dafalias et al. 2006)

3 CENTRIFUGE TESTS OF LEVEES ATOP PEATY ORGANIC SOILS

This chapter presents the centrifuge tests of model levees atop peaty organic soils performed at the University of California Davis (UCD). These tests are part of a large research effort including the work presented in this dissertation, and involving the University of California Los Angeles (UCLA) and the University of California Irvine (UCI). Riccardo Cappa from UCI, was in charge of the centrifuge tests and spent a significant amount of time working on the preparation of the tests and the analysis of the test results. My doctoral work focuses on the development of the constitutive model presented in chapter 6 and its validation through numerical simulations of the tests, which is presented in chapter 8. As part of my doctoral work, I was also involved in the centrifuge testing especially in the construction of the models, and part of my doctorate was spent at the UCD Center for Geotechnical Modeling (CGM).

This chapter combines text and figures from three publications authored by the research group, Cappa et al. (2014a), Lemnitzer et al. (2015) and Yniesta et al. (2015). The chapter first presents the objectives of the tests, and discusses the preliminary work done as part of the preparation of the centrifuge tests. The testing program is then described, and the core of the chapter focuses on the construction of the models, and the testing process. Some preliminary results are presented as a sample of data collection, but they do not intend to present the main important findings. For more information on the findings of the centrifuge tests, the reader is invited to read Riccardo Cappa's dissertation (Cappa 2016). His dissertation discusses extensively the test results and also includes more details about the tests, while this chapter is merely a summary. For more details on the

preparation of the tests, the reader is also invited to read the data reports (Cappa et al. 2014b and Cappa et al. 2014c).

3.1 Centrifuge Principles

Centrifuge tests are used in geotechnical engineering because centrifuging a model increases its weight and increases the stresses in the model. The stresses in a small centrifuge model are comparable to the stresses of a larger prototype. Because the soil behavior is stress dependent, this allows to model with accuracy the behavior or large prototype. In particular, stiffness, strength and dilatancy, are stress-dependent (Kutter 1992). Centrifuge tests present the advantage of being easily repeatable and this allows to study the variation of important parameters.

In a centrifuge test, length, mass and time are scaled from model to prototype. Table 3-1 presents the scaling factors to consider during centrifuge testing. For example the ratio of the model length to the prototype length is 1/N. In a centrifuge test *N* is the centrifugal acceleration. Note that the scale factor of the diffusion time depends on whether the coefficient of diffusion is scaled or not. If the same soil is used in the model and in the prototype, then the coefficient of diffusion is the same and $t_{dif}=1/N^2$.

Table 3-1 Scaling factors for centrifuge model tests (from Kutter 1992)

Quantity	Symbol	Unit	Scale Factor
Length	L	L	1/N
Volume	v	L^3	$1/N^3$
Mass	M	M	$1/N^3$
Gravity	g	LT^{-2}	N
Force	F	MLT^{-2}	$1/N^2$
Stress	σ	$ML^{-1}T^{-2}$	1
Moduli	E	$ML^{-1}T^{-2}$	1
Strength	s	$ML^{-1}T^{-2}$	1
Acceleration	a	LT^{-2}	N
Time (dynamic)	t_{dyn}	T	1/N
Frequency	f	T^{-1}	N
Time (Diffusion)	t_{dif}	T	1/N or $1/N^2$

3.2 Objectives and Preliminary Work.

The objective of the project is to understand the contribution of peaty soil to the seismic response of levees in the Delta using centrifuge tests. In this project, different mechanisms are investigated, such as the post cyclic settlement of peat, the liquefaction potential of the levee, and the interaction between the peat and the levee.

Non-liquefiable clay levees were tested to study the post-cyclic volumetric strain behavior of the peat, and to study the deformation modes of the comparatively stiffer levee using concepts from soil-structure interaction theories. Levees composed of loose liquefiable sand were also tested to mimic a condition that characterizes some levees in the Sacramento / San Joaquin Delta, and to study the influence of the peat on the liquefaction behavior of the sand.

The preliminary testing phase consisted in laboratory testing and small centrifuge tests. Eleven preliminary small scale tests on the 1-m radius Schaevitz centrifuge helped establish the most suitable model construction techniques, which was complicated by (1) the very high compressibility of the peat material and associated geometry changes during spin-up, and (2) the need to maintain a water channel on one side of the liquefiable levee. Two investigations were then performed on the 9m-radius centrifuge at 57g, implementing lessons learned from small scale testing and preliminary analytical studies. Table 3-2 reports a summary of all centrifuge experiments performed as part of this project. A comprehensive set of detailed reports and drawings (Cappa et al. 2014 b,c) along with test data for all experiments listed in Table 3-2 are available at the NEES project warehouse under project #1161: http://nees.org/warehouse/project/1161. Hereafter, and in consistency with the NEES data repository, investigation 1 will be labeled RCK01 and investigation 2 is named RCK02 accordingly following the NEES@UCDavis convention of identifying each investigation by the lead investigator's initials. The primary difference between the two investigations is the peat layer thickness and its impact on the seismic response of the levee peat system. The two investigations were divided in two phases, one with a clayey levee (experiment 12 and 14) and one with a sandy levee (experiments 13 and 15).

Table 3-2 Testing program (Lemnitzer et al. 2015)

Investigation	Experiment	Centrifuge Radius	Brief Description*	DOI
Small Scale Investigations	1	1m	Peat slurry under surcharge.	10.4231/D32V2C96M
	2	1m	Peat passed through #4 sieve, under surcharge.	10.4231/D3TD9N80K
	3	1m	Peat processed through blender, under surcharge.	10.4231/D3PN8XF79
	4	1m	Peat passed through #4 sieve, no surcharge.	10.4231/D3JW86N3J
	5	1m	Peat passed through #4 sieve, no surcharge.	10.4231/D3F47GT8M
	6	1m	Sandy levee on peat shaken by SGM.	10.4231/D39C6S14W
	7	1m	Sandy levee shaken by SGM.	10.4231/D35M62704
	8	1m	Consolidation of peat under a sand layer.	10.4231/D31V5BD6C
	9	1m	Sandy levee on peat shaken by SGM.	10.4231/D3X63B55H
	10	1m	Sat. sandy levee constructed on arm by water pluviation.	10.4231/D3Z31NP21
	11	1m	Clay levee on peat shaken by SGM sequence.	10.4231/D3G73748K
RCK01	12	9m	Clay levee on peat shaken by SGM sequence.	10.4231/D34M91B6S
	13	9m	Saturated sandy levee on peat shaken by MGM.	10.4231/D30V89J2N
RCK02	14	9m	Clay levee on peat shaken by SGM sequence.	10.4231/D3W37KW7Z
	15	9m	Saturated sandy levee on peat , MGM & aftershocks.	10.4231/D3RB6W337

** SGM = Strong Ground Motion, MGM = Moderate Ground Motion*

3.3 Model Construction

3.3.1 Configuration of the Tests

The general test setup of the levee systems is depicted in Figure 3-1. Each configuration consisted of a drainage layer of coarse sand with thickness D at the bottom of the model, followed by a peat layer with varying thicknesses (H) and a model levee consisting of (a) modeling clay or (b) saturated sand, with geometries as indicated in Figure 3-1. The levee system was constructed inside a rigid wall container with dimensions of 175.8 cm in length, 90.9 cm in width and 53.7 cm in height (Figure 3-2a). The rigid container has transparent side walls to enable the acquisition of videos during testing, which was important for this project and outweighed the undesired boundary conditions imposed at the rigid soil/container contact. Figure 3-2b shows the placement of the container on the centrifuge arm with its respective global coordinate system. Each of the two large scale investigations (RCK01 and RCK02) consisted of two Experiments: (1) a levee composed

of non-liquefiable modeling clay rests on soft peat and several ground motions and sinusoidal sweeps are applied in flight to observe the seismic performance of the peat and the levee-peat interaction (Experiments 12 & 14 in Table 3-2); (2) the clayey levee is removed and substituted with a saturated sandy levee, and subsequently subjected to the target ground motion to investigate the system behavior (interaction & liquefaction) (Experiments 13 & 15 in Table 3-2).

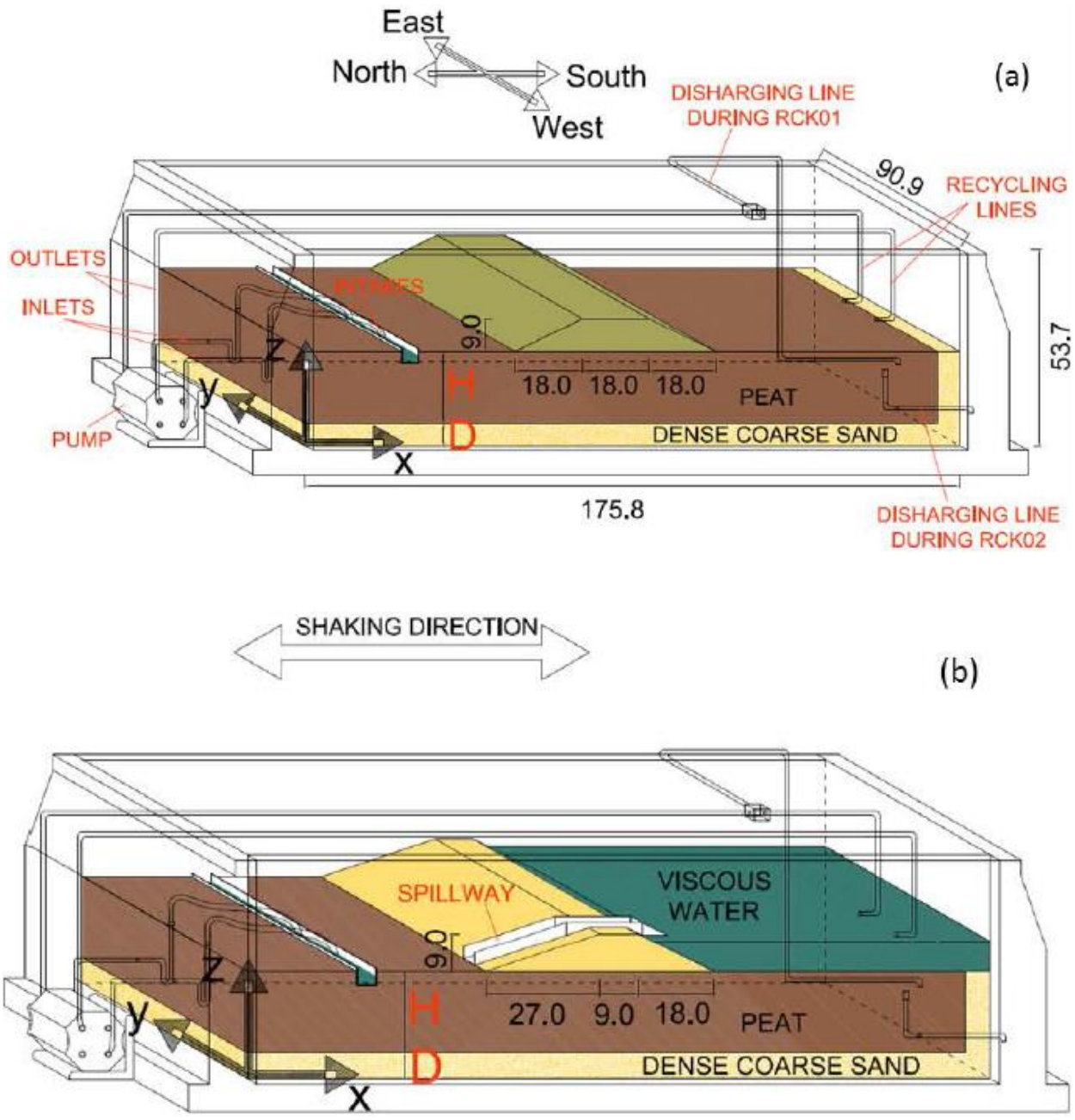

Figure 3-1 General setup of the tests (a) clayey levee (b) sandy levee (Lemnitzer et al. 2015)

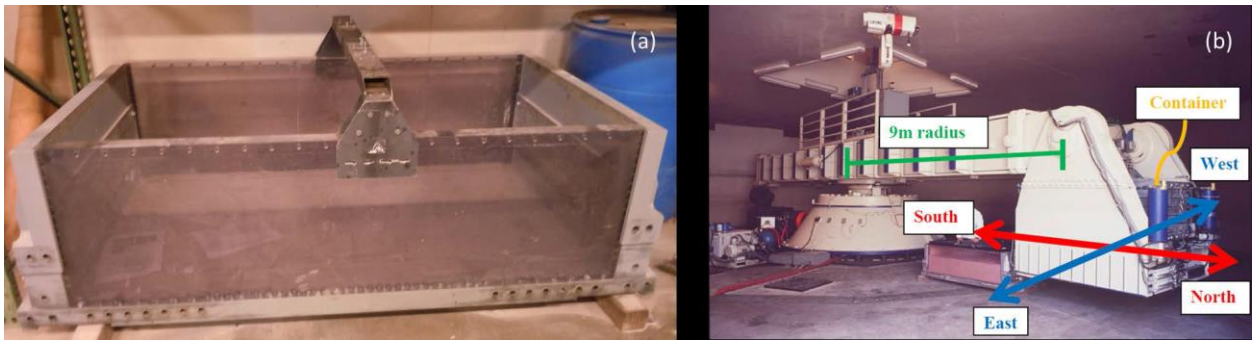

Figure 3-2 Photos of the 9m radius centrifuge at UC Davis a) container b) centrifuge (Lemnitzer et al. 2015)

The prototype system consists of a 5 m tall levee resting atop a 9.5 m and 6 m thick layer of soft peat for RCK01 and RCK02, respectively. The models were spun to a centrifugal acceleration of 57g, therefore the model scale dimensions were a 9 cm tall levee resting atop 16.5 cm and 10.5 cm of peat for RCK01 and RCK02, respectively. The peat thickness during RCK01 was selected to match conditions at a site on Sherman Island where a previous field testing program was conducted on a non-liquefiable model levee using the UCLA eccentric shaker (Reinert et al. 2014). Figure 3-3 shows photographs of the clayey levee resting atop the peat for RCK01 and RCK02 before the container was installed on the centrifuge arm.

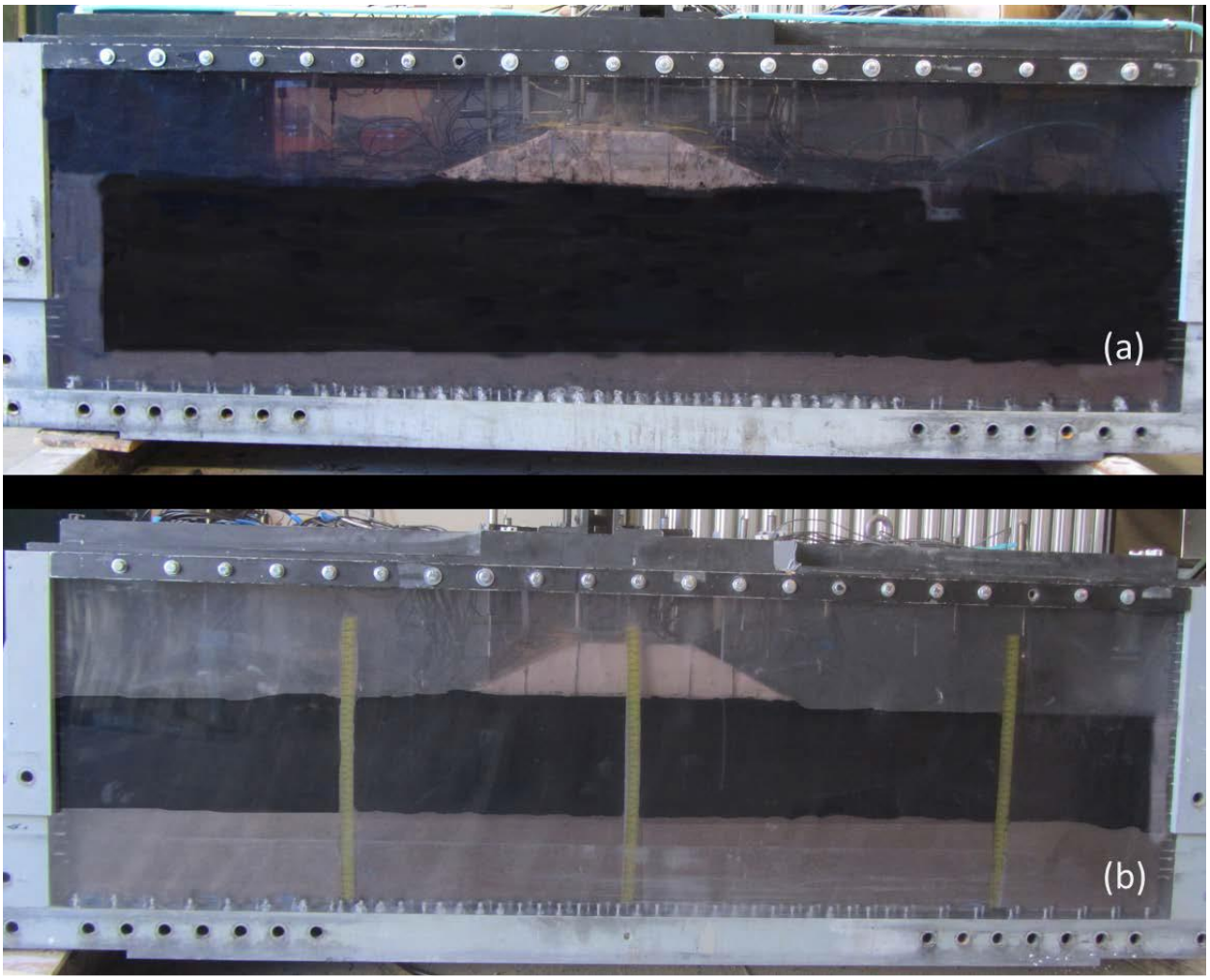

Figure 3-3 Photos of the models before going on the arm (a) RCK01 (b) RCK02 (Lemnitzer et al. 2015)

Model configurations and sensor positions for the four experiments are shown in Figure 3-4 through Figure 3-7. The high compressibility of the peat resulted in significant settlement of the levee during spin-up, and the figures depict the models in their configurations during testing, with dashed-lines indicating the pre-spin-up model geometry. In the second test a thin layer of a mix of dense sand and yolo loam was added on top of the levee to protect it against erosion.

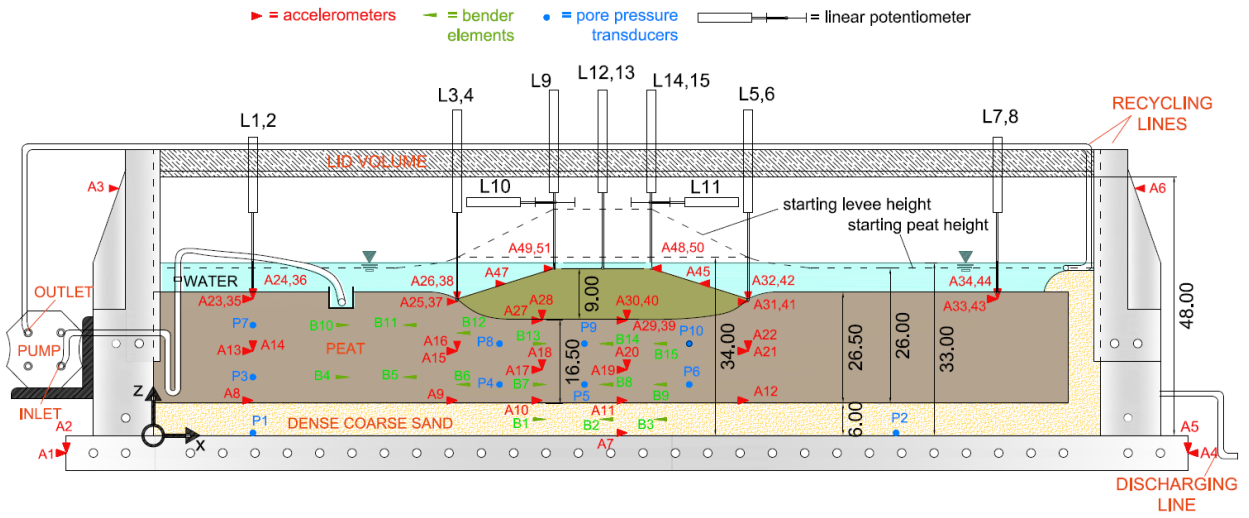

Figure 3-4 Experiment 12: configuration during testing (Lemnitzer et al. 2015)

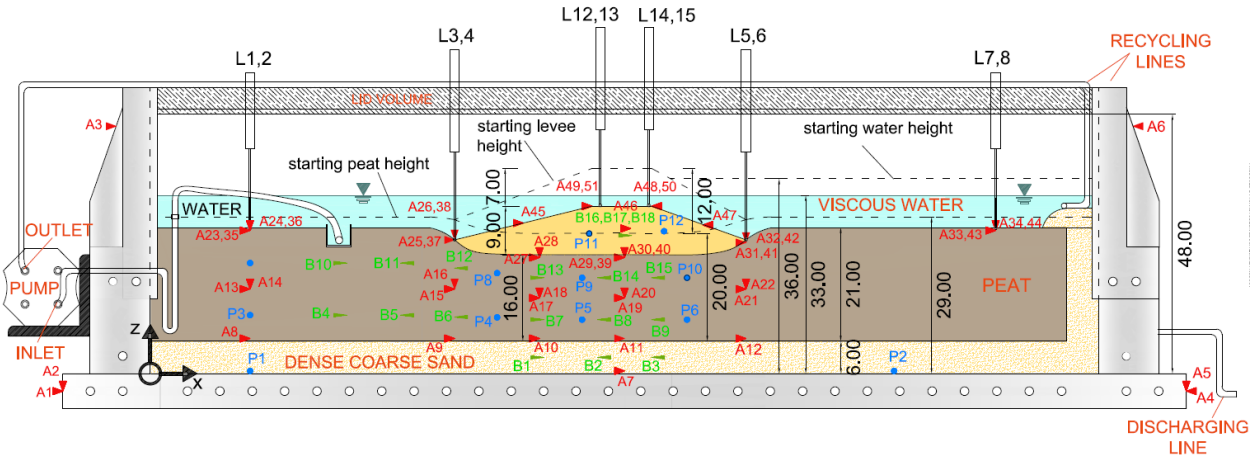

Figure 3-5 Experiment 13: configuration during testing (Lemnitzer et al. 2015)

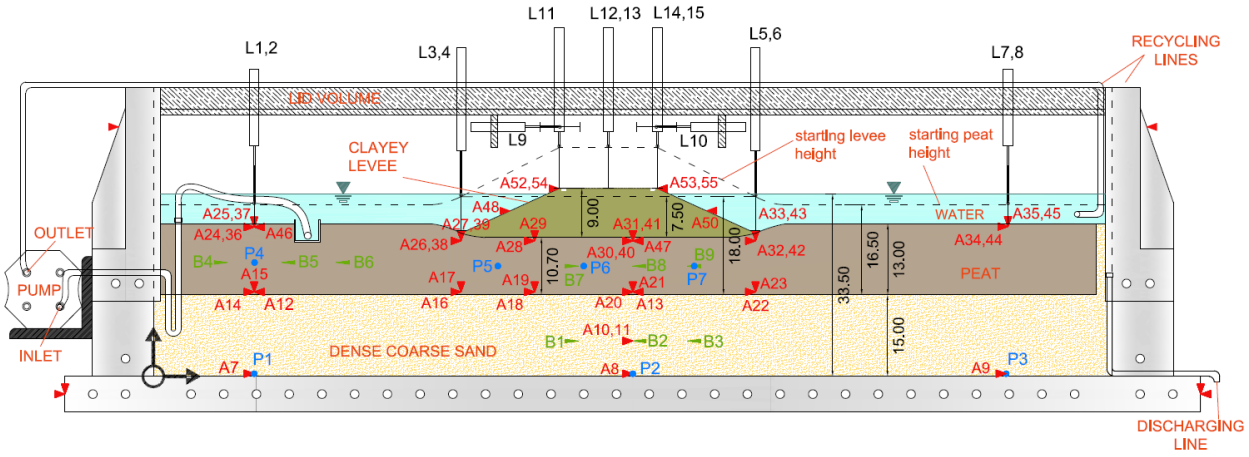

Figure 3-6 Experiment 14: configuration during testing (Lemnitzer et al. 2015)

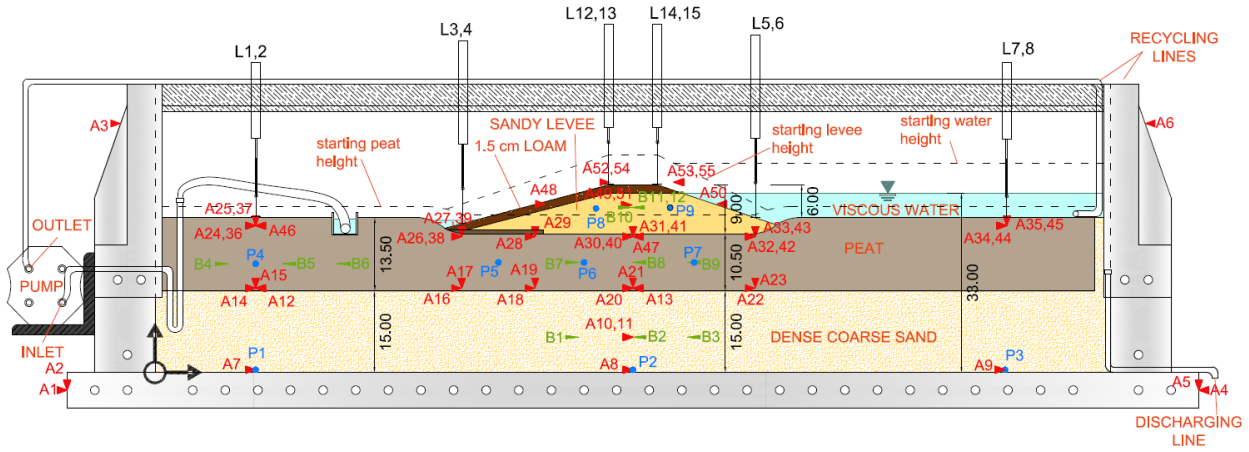

Figure 3-7 Experiment 15: configuration during testing (Lemnitzer et al. 2015)

3.3.2 Material

3.3.2.1 Sherman Island Peat

Bulk samples of peat were recovered from depths of 2-3 m at the field test site on Sherman Island in the Sacramento-San Joaquin Delta documented by Reinert et al. (2014). The samples were stored in plastic-lined metal barrels filled with water at UC Davis. Prior to placement in the model container, the material was hand processed to remove coarse particles and long fibers that are unsuitable for use in relatively small

centrifuge models. Careful handling was important to avoid the loss of water in the fibers due to squeezing and to obtain a homogeneous and soft soil matrix. The peat was maintained submerged during model construction. Important material characteristics of the processed peat were determined via laboratory studies (Cappa et al., 2015). Additional in-situ test results of the peat from geophysical testing, hand augering and cone penetration testing (CPT) are available in Reinert et al. (2014).

The peat had a specific gravity G_s of 1.79 and an average organic content, *OC*, of 64%. Across an overburden pressure range of 5-150 kPa, the virgin compression index C_c and the recompression index C_r were determined to be 3.9 and 0.4, respectively. Two sets of bender elements recorded shear wave velocities at accelerations of 1, 5, 10, 20, 40, and 57g during spin-up, thereby enabling characterization of the shear wave velocity as a function of confining pressure. Figure 3-8 presents a sample measurement of shear wave velocities during RCK02 at 57g. The bender elements exhibited capacitive coupling with the conductive peat soil, and the desired elastic wave signal is superposed on an undesired portion of the signal corresponding to capacitive decay. The travel time corresponding to first arrival of the shear wave can nevertheless be measured from the two receivers, enabling calculation of the shear wave velocity. Equation 3-1 is a general form for characterizing shear wave velocity as a function of vertical effective stress, σ_v'.

$$V_s = V_{s1}\left(\frac{\sigma_v'}{p_a}\right)^n \qquad \textit{Equation 3-1}$$

By plotting shear wave velocities measured across a range of centrifugal accelerations, the parameters V_{s1} and n can be determined via least squares regression, as shown in Figure 3-9. In the peat, V_{s1} and n were found to be 33 m/s and 0.31, respectively.

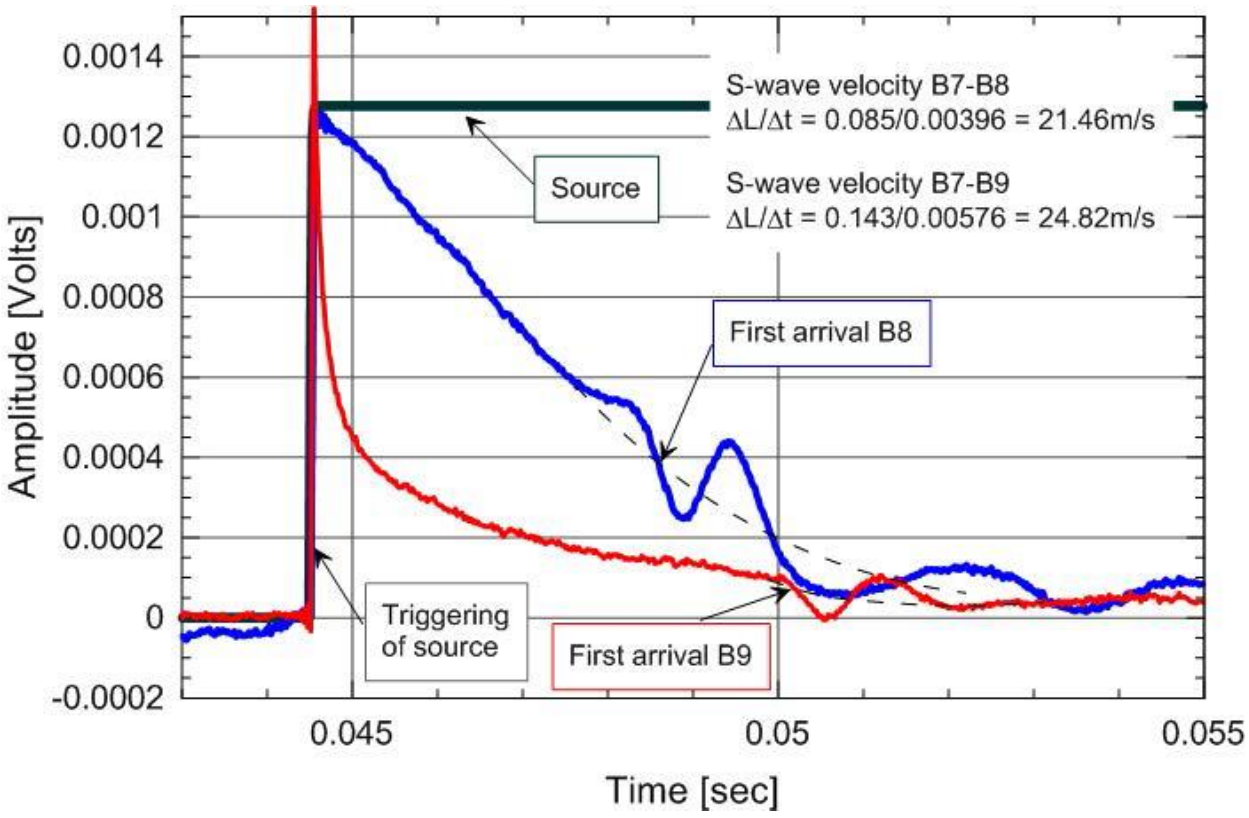

Figure 3-8 Sample shear wave velocity (Vs) measurements in the peat layer at 57g during RCK02 (Lemnitzer et al. 2015).

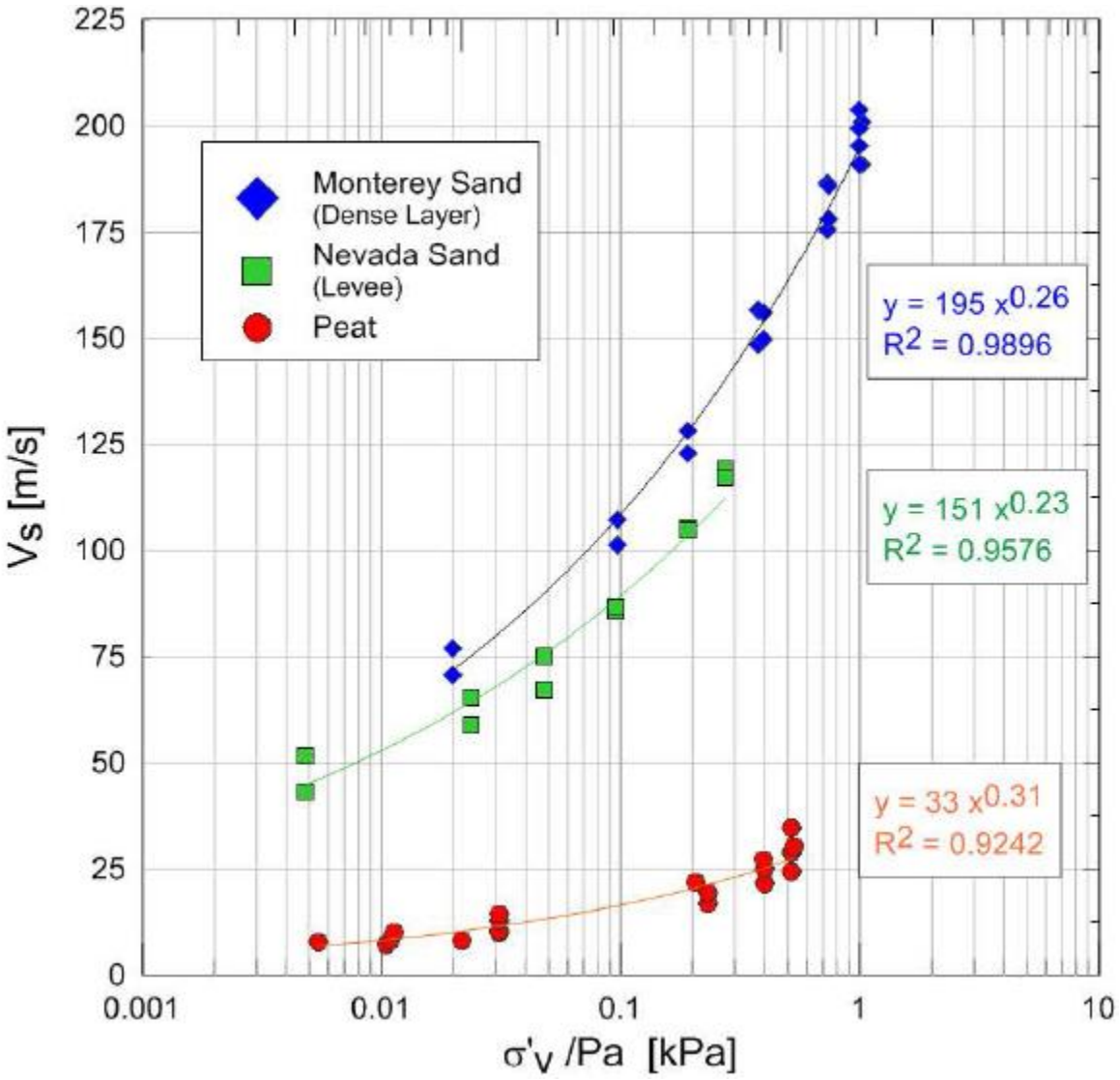

Figure 3-9 Parabolic data fitting to estimate V_{s1} and n for the various materials during RCK02. (Lemnitzer et al. 2015)

P-wave velocity was measured by gently striking the top of the modeling clay levee and measuring the downward-propagating compressive wave using vertical accelerometers. The p-wave velocity of the peat was found to be approximately 419 m/s in RCK01 and approximately 172 m/s in RCK02. Both measurements indicate that the peat was unsaturated. This is consistent with field conditions, in which the peat holds a significant amount of entrapped gasses due to its past and ongoing decomposition. A miniature CPT

test was performed in-flight during RCK02, measuring tip resistance over a depth range of 27 cm. The CPT apparatus was placed in the free field region during Experiment 14 and was pushed through the mid-point of the upstream levee slope during Experiment 15. The free-field peat exhibited a very low tip resistance that increased slightly with depth, reaching a maximum near 0.24 MPa at the bottom of the peat layer. The relatively low tip resistance is due to low consolidation stresses in the free field. By contrast, the resistance in the peat beneath the sandy levee was significantly higher, increasing from about 0.5 MPa at the top of the peat to 1.0 MPa at the bottom of the peat. Consolidation stresses from the overlying levee clearly increased the peat strength. Tip resistance increased dramatically below the peat as the CPT probe pushed into the dense coarse sand.

3.3.2.2 Modeling Clay

Impermeable, oil based modeling clay with a unit weight γ of 18 kN/m^3 was formed into a clayey levee by pouring molten clay into a mold. The clay levee was moderately deformable, allowing for small differential settlements in flight. Shear wave velocity of the modelling clay measured at 1g was about 400 m/s, and this is anticipated to be the same as the shear wave velocity in-flight since the modelling clay does not consolidate during spin-up.

3.3.2.3 Nevada Sand (Levee Fill)

The liquefiable levee fill (Experiments 13 and 15, Table 3-2) consisted of saturated Nevada sand with a mean grain size D_{50} of 0.14 mm, a specific gravity G_s of 2.66, a maximum and minimum void ratio e_{max}/e_{min} of 0.78 and 0.51 respectively, a coefficient of

uniformity C_u of 2, and a hydraulic conductivity k of approximately 10^{-3} cm/s in non-viscous water (Dashti 2009). The fines content passing # 200 sieve was removed from the sand. Shear wave velocity measurements of the material obtained during the second investigation (RCK02) suggested shear wave velocity parameters V_{s1} and n of 151 m/s and 0.23, respectively.

3.3.2.4 Monterey Sand (Coarse Dense Sand)

A coarse sand layer consisting of #0/30 Monterey Sand was placed at the bottom of the container to represent the natural geologic strata typical for the Delta, and to provide drainage at the bottom of the peat layer during consolidation. The granular material was dry pluviated to a relative density of 90%, thereby preventing liquefaction during shaking. A chimney drain constructed of the same coarse sand material was placed along the south wall of the container (Figure 3-1). Dashti (2009) determined this particular material to have a grain size D_{50} = 0.40 mm, a coefficient of uniformity C_u = 1.3, a specific gravity G_s of 2.64, and a maximum/minimum void ratio emax/min of 0.843 and 0.510, respectively. The hydraulic conductivity *(k*) is approximately 10-2 cm/s. Shear wave velocity parameters V_{s1} and n were 195 m/s and 0.26, respectively.

3.3.2.5 Yolo Loam

To provide erosion protection, and to better visualize the crack and deformation patterns of the sandy levee during testing, the liquefiable levee fill was covered with a dry-pluviated, 1.5cm thick mixture of 75% Yolo loam and 25% Monterey sand (by mass). This particular loam is frequently found in the Sacramento region and was excavated from an open area at the centrifuge facility.

3.3.2.6 Viscous Pore Fluid

The liquefiable sandy levees were saturated with a viscous pore fluid to provide undrained loading conditions during shaking. The viscosity of the methylcellulose/water mixtures was 14 cSt and 18 cSt (1 centistokes = 1 mm^2/s) for RCK01 and RCK02, respectively. Measurements were taken at 20°C prior to testing. Water expelled during consolidation of the peat mixed with the viscous fluid, resulting in a post-test viscosity of about 4 cSt in the free fluid in the channel. However, the fluid inside the levee fill was not prone to this mixing, and therefore the viscosity remained high.

3.3.3 Pumping System

The pumping system was crucial for maintaining a steady state water table during Experiment 15M, and its performance was tested during Experiment 14M. A diaphragm pump (model Coleparmer 75320-60) was mounted on the outside of the container and connected to hoses inside the model (Figure 3-1). A computer-controlled valve was connected to the pump so that the viscous fluid collected from the "dry" (ditch) side of the model could be pumped back into the slough at any time. Another computer-controlled valve permitted to discharge water out of the model container by collecting the fluid in the sandy drainage chimney. This was important to lower the water table of the slough while the model was settling during consolidation in order to prevent overtopping.

The pump was mounted outside of the model on the load frame of the centrifuge arm. The inlets of the pump ran through holes drilled at the end of container at mid-height of the peat layer, and the hoses ran down the container wall to the lower part of the peat layer to avoid movement due to large anticipated peat settlement. The intakes were fixed

inside the ditch. The outlets were run on top of the lid back to the other side of the model. The ends of the outlets were enclosed in a sponge to avoid erosion of the soil resting beneath (coarse sand or peat). The discharging line ran through the bottom of the container.

3.3.4 Vacuum Pluviation Device for Achieving Saturated Sand

For the purpose of the tests, a new saturation device was created in order to obtain well saturated sand capable of simulating undrained shearing behavior during liquefaction. Traditional vacuum saturation techniques normally used in centrifuge modeling were not suitable for application with peat because the gas bubbles in the peat would expand under vacuum, thereby resulting in model disturbance. The text presented in this section comes from Yniesta et al. (2015) and summarizes the development of the device.

3.3.4.1 Introduction

Obtaining a high degree of saturation in sandy soil is crucial for reproducing liquefaction potential in laboratory specimens or specimens in centrifuge modeling. Sands below the water table in the field are often saturated because any gasses present during deposition have had adequate time to dissolve or migrate out of the sand. Achieving a high degree of saturation in an experiment, where time scales are too limited to wait for dissolution or migration, often involves some combination of (1) the application of backpressure, (2) use of de-aired water, (3) flushing the sand with carbon dioxide (which is much more soluble than air) prior to saturation, and (4) application of vacuum to the sand during saturation (e.g., Lowe and Johnson 1960; Takahashi et al. 2006; Poncelet 2012). Many traditional

methods, however, are limited in that their application is only suitable for initially dry, remolded soil specimens (Rad and Clough 1984). Common saturation methods utilized in centrifuge testing adapted laboratory procedures to comply with the needs for testing at high accelerations (Miura and Toki 1982; Garnier and Cottineau 1988; Stuit 1995; Takahashi et al. 2006; Zhao et al. 2006). Rietdijk et al. 2010 suggested the use of the "drizzle method" in which saturated sand is wet pluviated via showerheads into de-aired water and compaction was achieved by shockwave compaction. Other researchers, such as Okamura and Inoue (2012), placed the model in a hermetic box and saturated the model via vacuum in flight. In this study, a centrifuge model consisting of a saturated sandy levee resting atop submerged peaty organic soil was constructed at the Network for Earthquake Engineering Simulation (NEES@UCDavis) experimental facility to model a common condition encountered in the Sacramento/San Joaquin delta (Cappa et al. 2014). A channel was maintained on one side of the levee, creating a steady-state seepage condition that was maintained by pumping water collected on the dry side of the levee back into the channel. The traditional saturation procedure at the centrifuge facility involves subjecting the model to nearly full vacuum to de-air the model, slowly releasing the vacuum as CO_2 is allowed to percolate into the model and displace any air in the pore space of the sand, again subjecting the model to nearly full vacuum, and subsequently percolating de-aired water or a viscous solution of water and methylcellulose through saturation tubes that extend to the base of the model while maintaining vacuum. As the water level slowly rises to the top, the sand becomes gradually submerged. The vacuum is then released and the hermetic lid is removed. Furthermore, the increased gravity during centrifuge spinning increases pore pressures, which improves saturation in a

manner similar to backpressure saturation employed in laboratory strength tests. Although this method has given satisfying results by producing highly saturated sand deposits with P-wave velocity, V_p, higher than 1500 m/s, it could not be used in the present study because of the presence of peat in the model. The peat is partially saturated because of entrapped gasses that form as a result of biodegradation of the organic material. Applying vacuum to model would cause gas bubbles inside the peat to expand and potentially disrupt the fabric of the peat or possibly even rupture the fibers and cells, thereby altering its physical behavior. Furthermore, pore pressures within the levee fill ranged from 0 to 30 kPa (gauge pressure) because of steady-state seepage during spinning, which is significantly lower than backpressures commonly used to saturate laboratory specimens in strength testing devices. This paper presents an alternative procedure that produces highly saturated sand at atmospheric pressure without applying vacuum to the model container.

3.3.4.2 Relation Between B-Value and P-Wave Velocity

Degree of saturation is typically represented by Skempton's (1954) B-value in laboratory strength-testing devices. For this reason, studying the relation between B and V_p is insightful. Analytical expressions for computing B and V_p are provided in Equation 3-2 and Equation 3-3 for a soil with pore fluid consisting of water and air:

$$M = B_{sk} + \frac{B_g}{1 - n + n\frac{B_g}{B_f}} + \frac{4\rho V_s^2}{3} \qquad \textit{Equation 3-2}$$

$$B = \frac{1}{1 + n\frac{B_{sk}}{B_f}} \qquad \textit{Equation 3-3}$$

where:

M = constrained modulus,

ρ = the soil total mass density,

$V_p = \sqrt{M/\rho}$,

n = porosity,

V_s = shear wave velocity,

S = degree of saturation,

ν = soil skeleton Poisson ratio,

$B_{sk} = \frac{2\rho V_s^2(1+\nu)}{3(1-2\nu)}$ = the soil skeleton bulk modulus,

B_g = the mineral grain bulk modulus,

B_w = water bulk modulus,

B_a = air bulk modulus, and

$B_f = \frac{1}{\frac{S}{B_w} + \frac{1-S}{B_a}}$ = the pore fluid bulk modulus assuming perfect mixing of the water and air phases (reasonable when the wavelength is long relative to the size of the air bubbles).

Note that Equation 3-2 assumes $B_{sk} << B_g$, which is reasonable for uncemented soils at confining pressures of engineering interest. For a given V_s, n, ν, B_g, B_a, and B_w, a unique relation exists between V_p and B, as implied by Equation 3-2 and Equation 3-3, and shown in Figure 3-10. The curves show that, when V_p is higher than about 1500 m/s, the degree of saturation is higher than 0.9999, and the B-value is high. Furthermore, for a given

degree of saturation near unity, V_p is nearly constant, whereas *B*-value is more sensitive to V_s. Hence, measuring a V_p higher than 1500 m/s is a clear indication of a high degree of saturation in uncemented soils with small air bubbles entrapped in the pore fluid. Naesgaard et al. (2007) showed that an erroneously high V_p can be measured when sand is saturated with viscous pore fluids often used in geotechnical centrifuges because waves may travel around fairly large pockets of entrapped air.

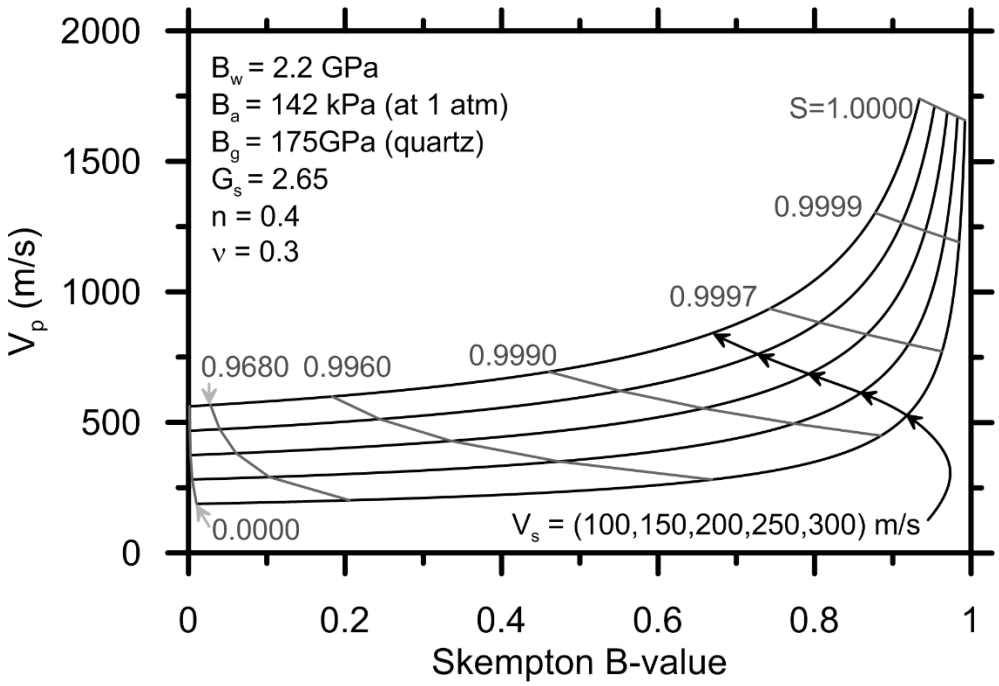

Figure 3-10 Relation between P-wave velocity (V_p) and Skempton's B-value (Yniesta et al. 2015)

3.3.4.3 Ultrasonic Measurement of P-Wave Velocity

For this study, a 500-kHz ultrasonic testing system originally described by Lee and Santamarina (2005) was used to measure V_p of sand deposits constructed by various techniques. The experimental configuration consists of a submerged layer of sand of known thickness with ultrasonic transducers slightly submerged (Figure 3-11, right). The source transducer generates a compressive wave that propagates through the water to

the surface of the sand, and the wave is partially reflected and partially transmitted in accordance with the interface impedance contrast (solid arrows). The reflected wave travels back through the water to the receiver (first receiver signal), and the transmitted wave propagates downward to the bottom of the bucket where it is reflected back upward and reaches the sand/water interface. At this interface, some of the wave energy is transmitted into the water and some is reflected back into the sand (dotted arrows). The time difference between these two reflections recorded by the receiver corresponds to the travel time, *tt*, needed for the P-wave to travel through the sand layer (dashed arrows in Figure 3-11). By knowing the thickness of the sand, the P-wave velocity can be calculated as $V_p = 2H/tt$. A benefit of using such high-frequency ultrasonic measurements is the resolution provided by the extremely short wavelength (i.e., λ = 3mm in water with V_p =1500m/s), which permits very accurate travel time determination. Furthermore, the short wavelengths would reflect from or be scattered by gas bubbles similar in size to the wavelength, thereby prohibiting measurements in such heterogeneous systems (e.g., Santamarina et al. 2001), and avoiding the problem discussed by Naesgaard et al. (2007).

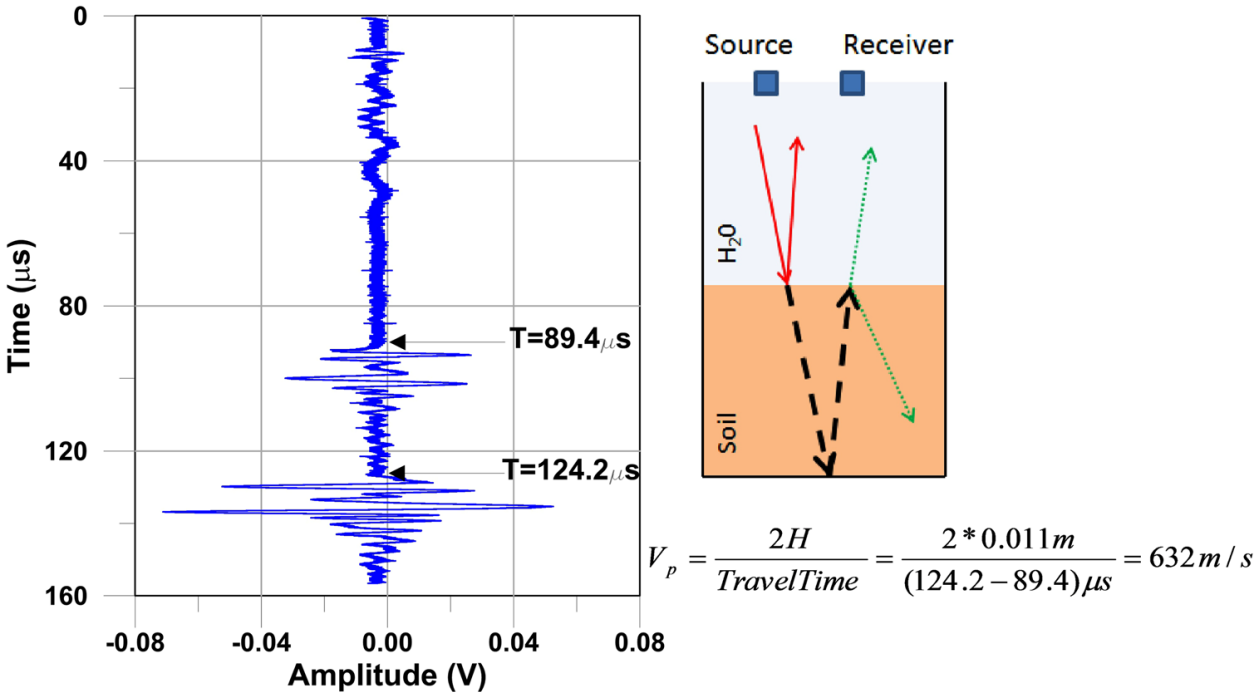

Figure 3-11 Sample ultrasonic P-wave velocity measurement for water-pluviated sand (left) and schematic measurement of ultrasonic P-wave velocity (right) (Yniesta et al. 2015)

3.3.4.4 P-Wave Velocity of Water Pluviated Sand

A preliminary study of water-pluviated sand was conducted to ascertain whether this simple preparation technique would result in adequate saturation. Dry sand was slowly pluviated through a sieve into a bucket of water. The sand had a median particle size D_{50} of 0.12 mm, a uniformity coefficient C_u of 1.73, a coefficient of curvature C_c of 0.95, and a minimum and maximum void ratio e_{min} and e_{max} of 0.557 and 0.936, respectively. The grains briefly rested atop the water, supported by surface tension, before breaking through the surface and falling to the bottom of the bucket. Because of the low depositional energy, the sand tended to be very loose, with a relative density near 0. A sample measurement for a 0.011-m thick sand layer yielded a wave travel time *tt* of $3.48*10^{-5}$ s (Figure 3-11) resulting in a P-wave velocity V_p=632 m/s, which indicates that the sand is not fully saturated. Small air bubbles adhere to the sand particles as they

break through the water surface tension. With adequate time, these bubbles would dissolve, or with adequate backpressure they would become small enough to achieve adequate saturation, but immediate saturation with no backpressure was needed in this project.

3.3.4.5 Device for Saturating the Sandy Levee Material

Considering that simple water pluviation does not provide an adequate degree of saturation, and vacuum cannot be applied to the model because of the presence of the peat, a new device was developed for the purpose of constructing highly saturated sand deposits by water pluviation. The device permits the sand to be vacuum saturated in a chamber, and subsequently water pluviated into the model without contacting air. The goals for the device were to (1) create a sandy fill that is adequately saturated at low backpressure, and (2) mimic the density of the loose saturated sand encountered in some levees in the delta ($D_R \approx$ 30 % to 50 %). The device, shown in Figure 3-12, consists of an acrylic de-airing chamber with a hose attached at the bottom. Dry sand is placed in the chamber, and a full vacuum is applied. Carbon dioxide (CO_2) is then introduced from the bottom of the chamber via a coil of perforated tubing. Once the chamber is filled with CO_2, vacuum is again applied to the chamber, and de-aired water is slowly introduced into the system, and the vacuum is removed when the water surface rises above the sand surface. This procedure mimics the approach commonly used for dry models on the centrifuge. High-pressure de-aired water is then injected into the coil of tubing at the bottom of the acrylic chamber, so that the sand inside the chamber begins to “boil” under the upward hydraulic gradient. Simultaneously, the valve on the bottom hose is opened and the sand is water pluviated through the hose at the bottom into the model. The hose must be

saturated before opening the valve to avoid contact with air. The device was initially constructed without the coiled tubing at the bottom, and arching of the sand prevented it from flowing through the bottom hose. A similar device was developed by Poncelet (2012) to prepare saturated specimens of mine tailings and sands for triaxial tests without backpressure [high backpressure was found to increase the liquefaction potential of the tailings (M. Aubertin, personal communication)]. They achieved *B* values well above 0.95 with no backpressure, which is further evidence that this procedure produces saturated specimens. The saturated silt tested by Poncelet would flow through a relatively small tube, whereas the sands tested herein would not. The high pressure coil for boiling the sand is, therefore, an improvement that permits the technique to be applied to sand.

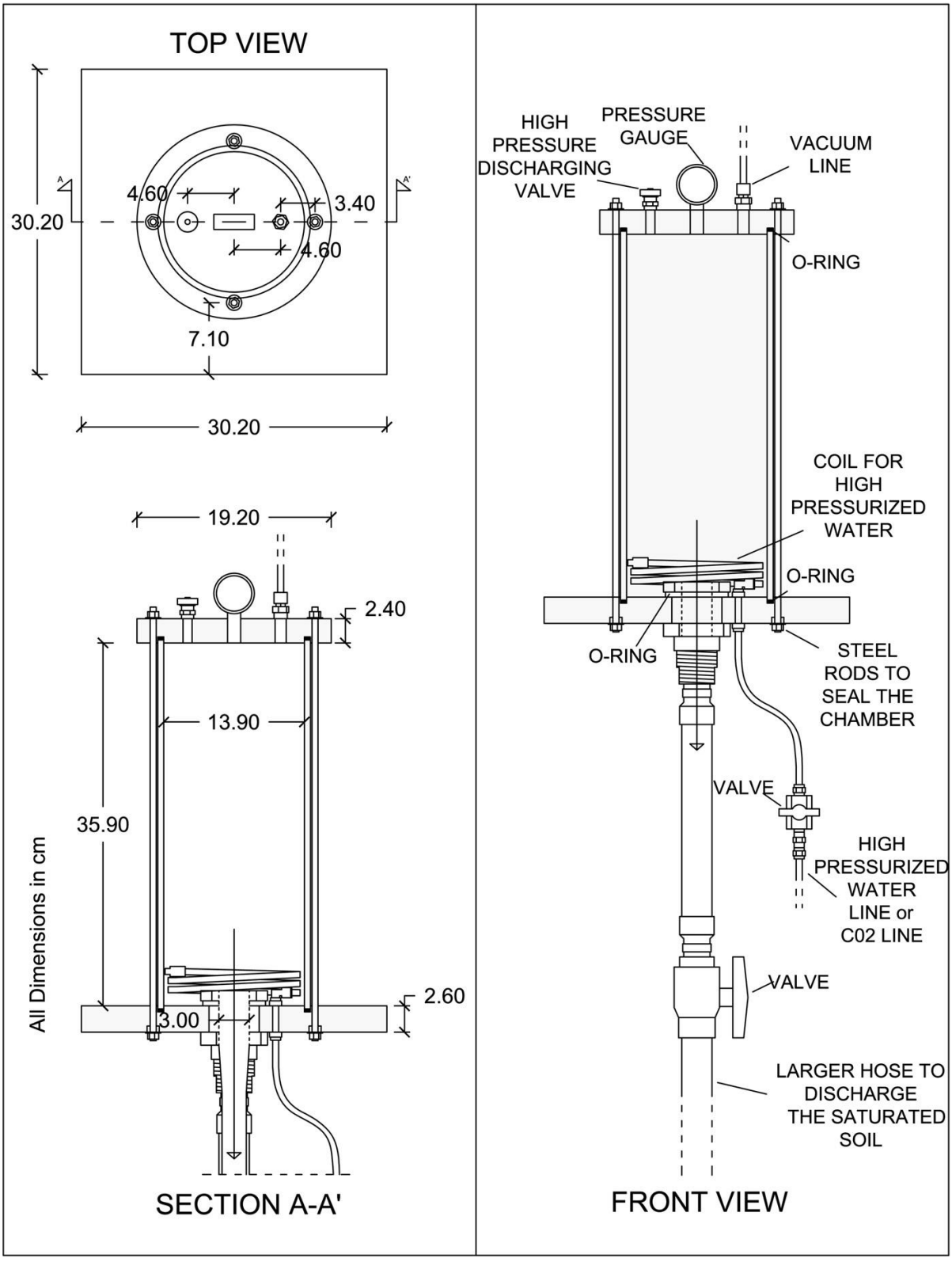

Figure 3-12 Schematic of device for preparing saturated sand (Yniesta et al. 2015)

3.3.4.6 P-Wave Velocity of Sand Pluviated by a New Device

A sample ultrasonic measurement of the P-wave velocity of sand prepared using the new device is shown in Figure 3-13. The measured P-wave velocity is now 1564 m/s, which is far higher than for the water-pluviated sand, and indicates that the new device produced sand with a high degree of saturation. Two additional specimens were prepared to indicate repeatability of the device, and the measured P-wave velocities were 1610 m/s and 1640 m/s (average V_p=1590 m/s) (Table 3-3).

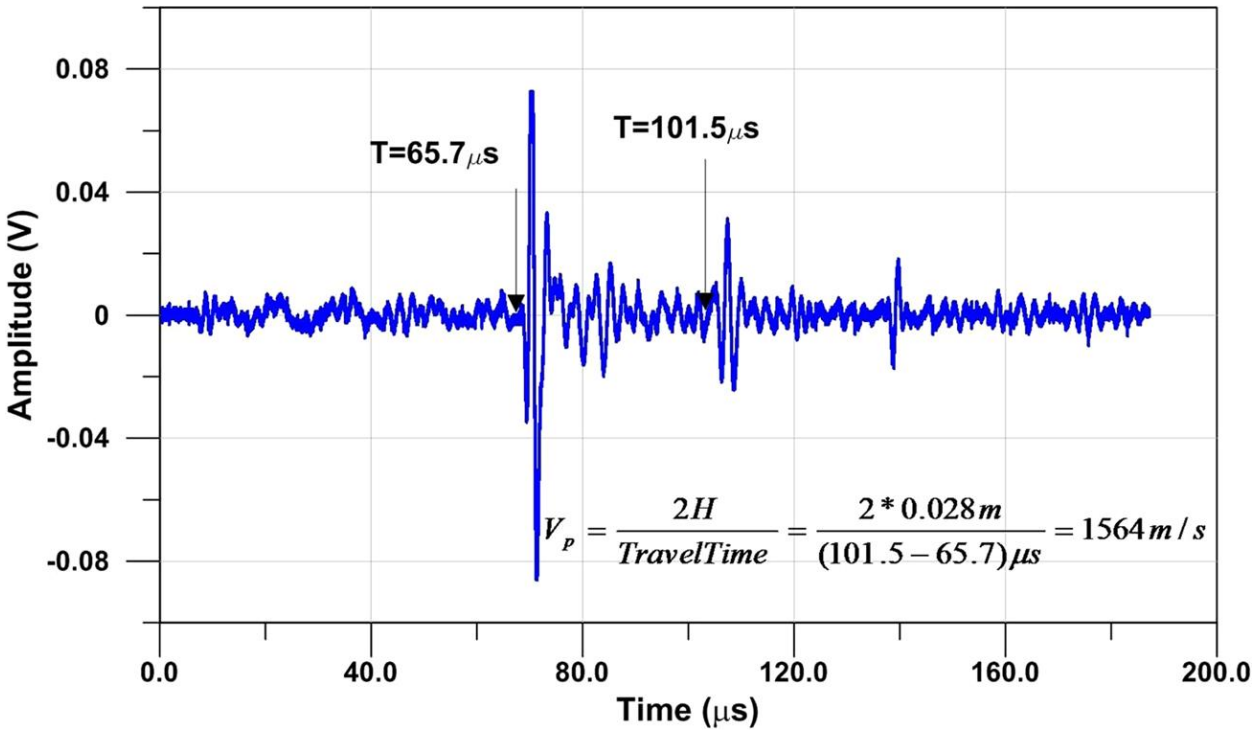

Figure 3-13 Sample ultrasonic P-wave velocity measurement for sand pluviated using a new device (Yniesta et al. 2015)

Table 3-3 Results of P-wave velocity measurements in the laboratory using the pluviation device (Yniesta et al. 2015)

Test	1	2	3	4	5	6
Sample Preparation	Traditional Water Pluviation			Vacuum Pluviation Device		
P-wave Velocity (m/s)	750	790	632	1640	1610	1564

A sequence of 20 experiments was performed to measure the relative density of the sand prepared in this manner and to investigate the repeatability of the results. Saturated sand was pluviated into a container of known volume, and the mass of the dry sand was measured. The relative density ranged from 27 % to 58 %, with an average of 42 %, and a standard deviation of 8.3 %. The achieved densities were well within the range desired for the levee fill, which have an in situ density range of 30 % ─ 50 %. The relative density is higher than zero because the sand exits the hose at high velocity, thereby resulting in higher depositional energy compared with simple water pluviation. Furthermore, variability in the relative density of the sand fill was desired in this case to mimic the natural variability in the levees. A more uniform relative density near 0 % could be achieved by running the sand through an underwater mesh to reduce its depositional velocity, or by increasing the drop height to allow the sand particles to slow down and reach a terminal velocity prior to deposition. Such experiments are beyond the scope of this study. The device is poorly suited to producing uniform medium dense or dense sand specimens because of spatial variations in depositional energy that will inevitably exist.

3.3.5 Construction Sequence

The coarse dense sand stratum at the bottom of the model was dry pluviated in two lifts to accommodate placement of sensors after the first lift. The sand was water saturated by pouring water on a sponge resting on the sand surface.

Peat slurry was then poured from buckets onto the sand and smoothed with trowels at elevations where sensors would be placed (Figure 3-14). The amount of peat slurry required to achieve the target peat thickness after consolidation in-flight was based on observations from the Schaevitz centrifuge test program (Cappa et al. 2015), laboratory consolidation studies (Shafiee et al. 2013), and settlement predictions using Settle 3D (Rocscience 2014). The peat slurry was too weak to support the clay levee, so a layer of Nevada sand (γ_{dry} = 17 kN/m^3) was placed on top of the peat to pre-consolidate the material over the course of three days (Figure 3-15). The thickness of the Nevada sand was 3.5 cm for RCK01 and 9 cm for RCK02. Following the pre-consolidation at 1g, the Nevada sand layer along with the expelled water was removed and the clayey levee was placed on a thin geotextile atop the peat (Figure 3-16 and Figure 3-17). Based on anticipated settlement of the peat beneath the levee, peat was removed from the free-field to achieve an approximately horizontal peat surface after consolidation at 57g (Cappa et al. 2014 b&c). Figure 3-17 shows the model before installing the lid. Final construction steps included the installation of lights, attachment of racks for sensor instrumentation, placement of all external sensors and CPT, installation of video cameras and connection of all instrumentation to the data acquisition system.

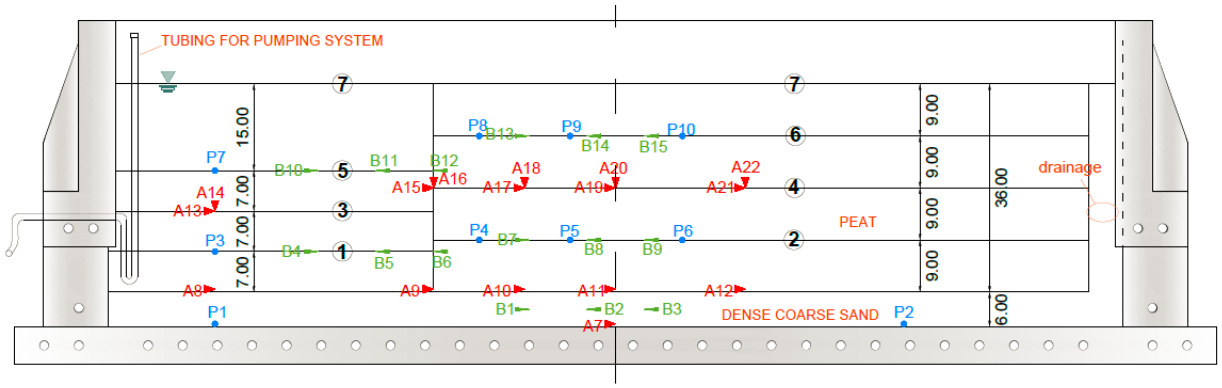

Figure 3-14 Configuration of the model before consolidation (Cappa et al. 2014b)

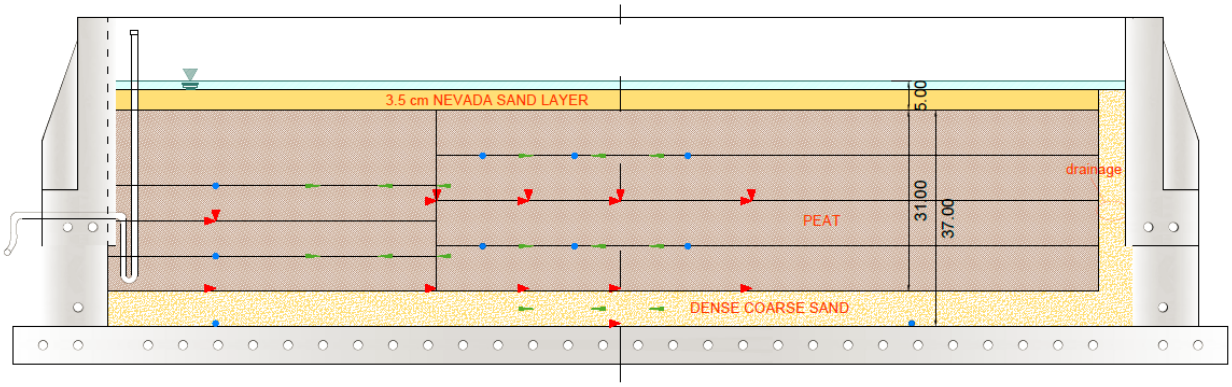

Figure 3-15 Configuration after consolidation under a layer of Nevada sand (Cappa et al. 2014b)

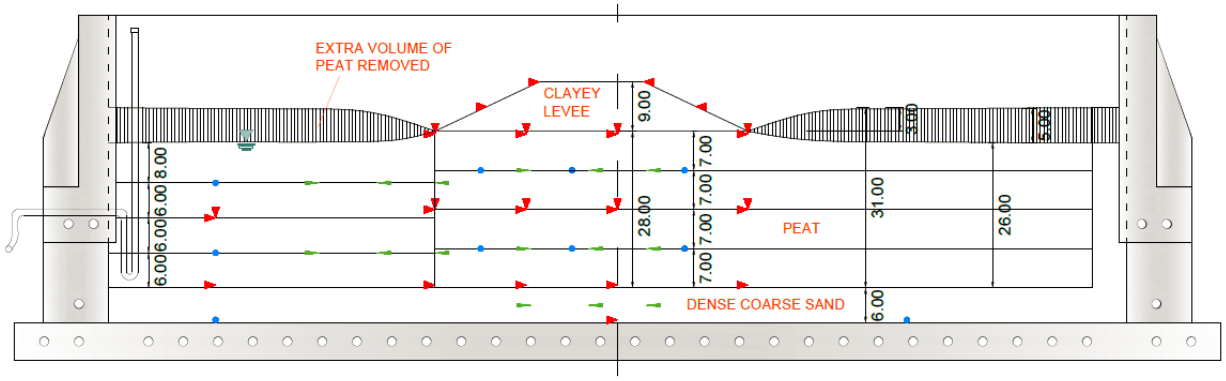

Figure 3-16 Configuration after consolidation under the clayey levee (Cappa et al. 2014b)

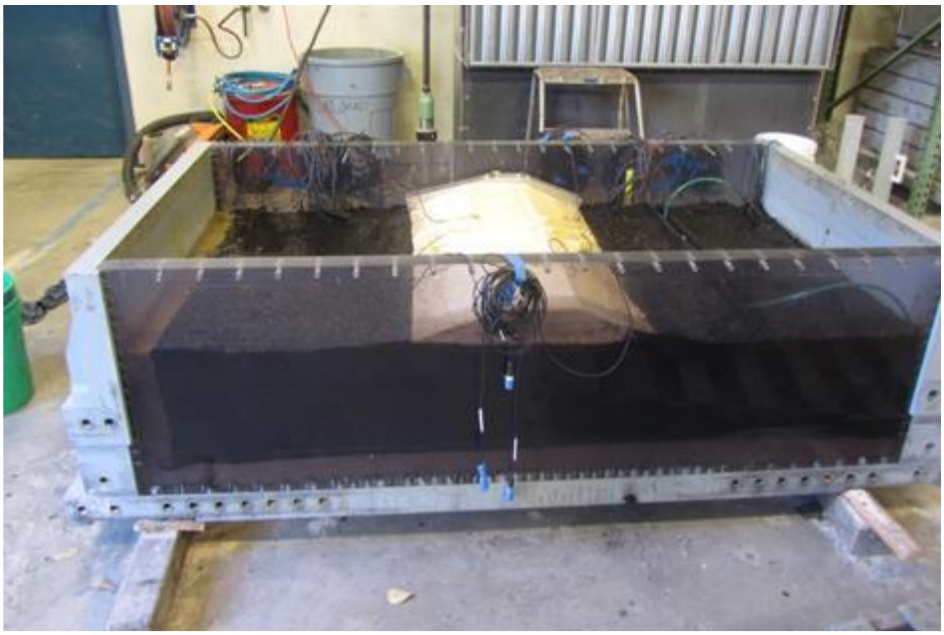

Figure 3-17 Picture of the levee before going on the arm (Cappa et al. 2014b)

Centrifuge spin-up proceeded incrementally to avoid undrained bearing failure of the peat. Pore pressures in the peat beneath the levee were monitored to guide the spin-up rate. This procedure is similar to staged construction techniques commonly utilized to construct embankments on soft foundations (e.g., Ladd 1991), except that the gravity load is staged rather than the fill height. The clayey levee was tested for two consecutive days in RCK01, dedicated to consolidating the peat for several hours at various g-levels (day 1) and applying a series of ground motions with different peak base accelerations at 57-g (day 2). During investigation RCK02 the clayey levee test required only one day because the peat thickness was less and consolidation therefore required less time.

During spin-up, the levees settled significantly and became submerged in water expelled from the peat. The original plan was to pump the expelled water out of the models to bring the water table near the surface of the peat. However, the pumping system failed during RCK01, and it was decided to test RCK02 with the free water in place to facilitate

comparison with RCK01. Furthermore, during spin-down the peat swelled back to near its initial position, re-absorbing the expelled water. If this water were pumped out, the peat could have become desiccated during spin-down and saturation of the peat for the sandy levee experiments was a key issue.

Upon test completion, the clayey levee was removed and replaced with a sandy levee. A 10 cm wide drainage blanket consisting of coarse sand wrapped with filter paper was placed beneath the downstream toe of the levee to prevent piping erosion and maintain the phreatic surface within the levee prism. The container was filled with viscous fluid and the sandy levee was pluviated into the model using the new device described previously.

Vertical sheet metal barriers constrained the pluviated sand within the desired footprint area, and the levee was then manually re-shaped to the desired geometry. The sandy levee was constructed with a 3:1 slope on the dry side to reduce the amount of erosion due to seepage during flight and to represent typical levee conditions in the field. The upstream slope was constructed with a 2:1 angle. After water pluviation, the fluid was slowly siphoned from the dry-side of the levee.

During spinning, viscous water that seeped through the levee was collected in a U-shaped ditch installed in the downstream peat, and collected fluid was pumped back to the channel to maintain a steady-state seepage condition. Furthermore, a spillway was installed in the levee to regulate the elevation of the channel relative to the levee crest and prevent over-topping during spin up as the levee settled. For RCK01, the spillway was formed of a stiff metal U-channel that settled less than the levee during consolidation, resulting in erosion of the sand from beneath the channel. As a result, the water table was

hydrostatic. A more flexible spillway was implemented in RCK02, enabling a channel to be maintained on one side of the levee.

3.4 Data Collection

3.4.1 Sensors

Sensors used to characterize model response include accelerometers [PCB Piezotronics, models 352B68, 352C68, 352M54, 355M69, 353B18 & 353B31; range: 50g, 100g and 500g], pore pressure transducers [Keller, model 2Mi-281 100-81840 range: 0 - 689.5kPa], linear potentiometers (L) [BEI Duncan, models: 606R6KL.12 & 604R4KL.15, stroke: 10cm and 15cm], and bender elements [Piezo Systems Inc., 2 layer transducer with PSI-5A4E piezoceramic (nickel electrodes) and brass center reinforcement]. The general instrumentation layout for each experiment is shown in Figure 3-4 to Figure 3-7. Accelerometers and bender elements were coated with a waterproofing layer prior to being placed into the model. Linear potentiometers were attached to a rack mounted to the top of the container. Vertical linear potentiometer rods rested on small footing plates to prevent penetration into the soft soil. Horizontal linear potentiometer rods were attached to a metal frame cantilevered from the soil. These horizontal linear potentiometers provide accurate low frequency response for measuring permanent ground deformations, but the metal frame alters the high frequency response. The high frequency response is typically obtained from an accelerometer embedded in the soil near the anchor frame. Some of the accelerometers were fastened to a right-angle connector to maintain a 90° angle between sensors, which sometimes tend to shift during model construction and/or testing on the centrifuge. The position of each sensor was measured during installation and again during excavation following testing. Tables containing sensor

positions, orientations, serial numbers, calibrations and measurements are available at the NEES project warehouse. Some of the sensors ceased to function properly during experimental activities, and a list of such sensors is available in the NEEShub repository. Loss of sensor functionality is a natural part of experimental testing, and only a small fraction of the sensors failed to function properly. A total of eight cameras supported the surveillance of the specimen behavior during flight. Two high speed cameras captured the behavior of the levee from the east and west side of the container during the application of the ground motions. The models were also documented by photographs taken during construction and testing, and a time-lapse video of the model construction sequence was constructed from automated photos recorded at set time intervals. All videos, photos, and construction time lapses are available on the NEEShub repository.

3.4.2 Data Processing

Experimental data are categorized as "Unprocessed Data", "Converted Data", and "Corrected Data" in accordance with NEES standards. Experimental data is further categorized as "slow data" sampled at 1 Hz during spin-up, spin-down and between ground motion applications, and "fast data" sampled at 4167 Hz during the application of ground motions. Slow data helped observe the low frequency response of the model and time dependent consolidation settlement of the peat, while fast data captured the dynamic response of the model during base excitation. For each experiment, Trial 1 contains the slow data while Trials 2 and higher contain fast data.

3.4.2.1 Unprocessed Data

Unprocessed data are in engineering units in binary format. Prior to testing, a calibration file is uploaded to the data acquisition system, and the recorded voltage signals are then automatically converted to engineering units. All recordings are in model scale. A LabView virtual instrument (vi) file is required to view the binary data files, and it is unlikely that users will download and utilize this data. It is archived for completeness, and compliance with NEES standards.

3.4.2.2 Converted Data

The Unprocessed Data are then converted from binary to ASCII format and saved as text files in the "Converted Data" folder in the NEES repository. Generally, zero voltage does not correspond to a value of zero for the engineering quantity being measured. For example, the rod of the vertical linear potentiometers measuring settlement of the levee were initially retracted as far into the housing as possible to facilitate the maximum possible useful range for these sensors during consolidation. A fully retracted linear potentiometer returns a non-zero voltage. Therefore the reference condition corresponding to zero settlement does not correspond to zero voltage. In accordance with NEES standards, offsets are not applied to Converted Data. For this reason, users are not expected to utilize the Converted Data as the primary data source, and it is archived for completeness and compliance with NEES standards.

3.4.2.3 Corrected Data

Corrected Data are the data files that will be most useful to users of the curated dataset. The following operations are applied to the Converted Data to obtain Corrected Data:

(i) Offsets were applied such that zero corresponds to a desired reference condition. Specifically, the mean value was subtracted from all acceleration records, and the initial value prior to spin-up was subtracted from all displacement and load cell records. Offsets to pore pressure transducers were set such that zero corresponds to atmospheric pressure. During testing, some of the linear potentiometer rods fell off the bearing pads, resulting in an abrupt offset in the settlement record. These offsets were removed from the corrected linear potentiometer data.

(ii) The data were sorted such that they are grouped by sensor type in ascending numerical order (e.g., A1, A2, A3, …, L1, L2, L3, …). The unprocessed and converted data files are ordered in accordance with the data acquisition channel used to collect the data, but this order is inconvenient for interpreting the data.

(iii) The data files were truncated to remove excess data collected before and after shaking to reduce file size. Typically, 15 seconds of data are collected for each fast data file, but only approximately 1 second corresponds to the shaking event. Enough pre- and post-event data are left in the signals to facilitate proper interpretation of the dynamic processes. However, the data files are too short to monitor pore pressure dissipation following long shaking events, and the slow data should be used for this purpose.

(iv) Sign conventions were assigned to the data quantities to maintain consistency with the global coordinate system. Furthermore, centrifuge scaling factors are applied to the data to produce prototype units. The centrifugal acceleration was 57g for all experiments, and appropriate scale factors followed Kutter (1992).

3.5 Results

3.5.1 Loading

Table 3-4 summarizes the base excitations applied to the models for both investigations. The organization of data into trials and repetition follows NEES requirements. Applied ground motions include: (1) scaled versions of ground motions recorded during the 1989 Loma Prieta Earthquake at the USCS/Lick Lab, Ch. 1 – 90°, and the 1995 Kobe Earthquake recorded at a depth of 83 m at the Port Island downhole array, (2) low-amplitude step waves imposed primarily to verify sensor function, and (3) sine sweeps intended to characterize the dynamic response of the model. The magnitudes of the Loma Prieta and Kobe earthquakes are in the range that contributes the most to seismic hazard in the Delta (DRMS 2009). Scaled versions of these motions with amplitudes ranging from 0.006g to 0.52g in prototype scale were imposed on the base of the model container.

Table 3-4 Base excitation summary (Lemnitzer et al. 2015)

Investigation	Experiment	Trial	Repetition	Date	Time Stamp	Description	Peak base acceleration, PBA (g) in prototype scale
RCK01	12	1	1	11/4/2013	12:01:51	Slow data file for first spin	-
	12	1	2	11/4/2013	15:36:41	Slow data file for first spin	-
	12	1	3	11/4/2013	9:26:00	Rpm record	-
	12	2	1	11/4/2013	15:50:46	Step wave 1	0.006
	12	3	1	11/5/2013	10:18:50	Slow data file for second spin	-
	12	4	1	11/5/2013	13:25:45	Step wave 2	0.006
	12	5	1	11/5/2013	14:03:14	Sine sweep 1	0.021
	12	6	1	11/5/2013	14:31:51	Small Loma Prieta	0.036
	12	7	1	11/5/2013	14:45:16	Small Kobe	0.034
	12	8	1	11/5/2013	14:57:21	Medium Loma Prieta	0.174
	12	9	1	11/5/2013	15:13:14	Medium Kobe	0.194
	12	10	1	11/5/2013	15:39:51	Large Kobe	0.491
	12	11	1	11/5/2013	16:29:07	Large Loma Prieta	0.476
	12	12	1	11/5/2013	17:13:39	Sine sweep 2	0.021
	13	1	1	11/21/2013	10:31:08	Slow data file for second spin	-
	13	2	1	11/21/2013	14:43:30	Step wave 3	0.005
	13	3	1	11/21/2013	14:50:49	Moderate Kobe	0.375
RCK02	14	1	1	2/27/2014	7:53:12	Slow data file for first spin	-
	14	2	1	2/27/2014	12:50:38	Step wave 1	0.006
	14	3	1	2/27/2014	13:01:20	Sine sweep 1	0.018
	14	4	1	2/27/2014	13:45:13	Large Kobe	0.526
	14	5	1	2/27/2014	16:27:04	Large Loma Prieta	0.439
	14	6	1	2/27/2014	17:23:09	Sine sweep 2	0.020
	14	7	1	2/27/2014	17:37:01	Step wave 2	0.007
	14	8	1	2/27/2014	17:45:34	Medium Kobe	0.270
	14	9	1	2/27/2014	17:54:24	Small Kobe	0.131
	15	1	1	3/12/2014	12:00:21	Slow data file for second spin	-
	15	2	1	3/12/2014	17:04:41	Step wave 3	0.006
	15	3	1	3/12/2014	17:17:15	Moderate Kobe	0.336
	15	4	1	3/12/2014	17:33:41	Small Kobe	0.101
	15	5	1	3/12/2014	17:43:42	Very small Kobe	0.057

3.5.2 Preliminary Results of Centrifuge Tests

This section presents a sample of preliminary results through two examples of data interpretation. The first example focuses on the analysis of the rocking motion of the levee. For more details, the reader is invited to read Cappa et al. (2014a). The second example focuses on the liquefaction of the sandy levee, and is detailed in Lemnitzer et al. (2015).

3.5.2.1 Rocking of the Levee

The fundamental frequency of a structure is commonly estimated by applying a sweep function and finding the frequency producing the peak response. In the centrifuge tests a prototype-scale sine sweep over a frequency range of 0.12 to 5.84 Hz was applied. The motion had a constant amplitude in velocity (to maintain similar strain levels), which produces variable acceleration and displacement amplitudes. The target peak acceleration amplitude was set at 0.025g at the centrifuge base. The sine sweep produced max strains in the FF and CL arrays of about 0.05 to 0.1% for both RCK01 and RCK02, which resides essentially within the linear elastic range of peat behavior (Kishida et al. 2009). Figure 3-18 shows an example of the acceleration histories recorded for RCK01 and RCK02 at the peat base, free field peat ground surface and levee crest.

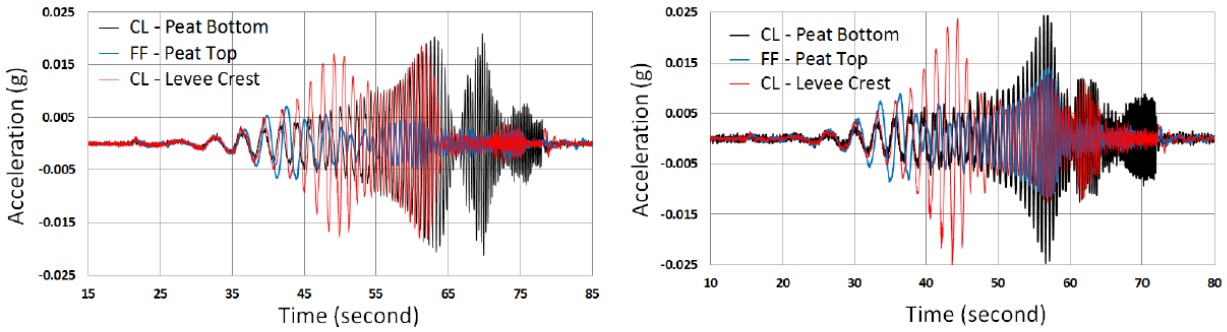

(a) – RCK01 (b) – RCK02

Figure 3-18 Acceleration records during sine sweep at different locations (Cappa et al. 2014a)

To further interpret the recorded responses, transfer functions were computed from the data by taking ratios of the Fourier amplitude spectra. Observed transfer functions in RCK01 are compared in Figure 3-19 to predictions from 1-D ground response analyses (using material properties Figure 3-20). The 1-D ground response analyses were performed with the intent of identifying features in the data that differ from the 1-D model predictions. Such differences may be interpreted in part as being associated with 2-D responses not captured by the analysis. To facilitate these analyses, shear wave velocities were measured using bender elements. Results of these measurements from specimen RCK02 were used to define a relationship between effective stresses and shear wave velocity (Equation 3-1).

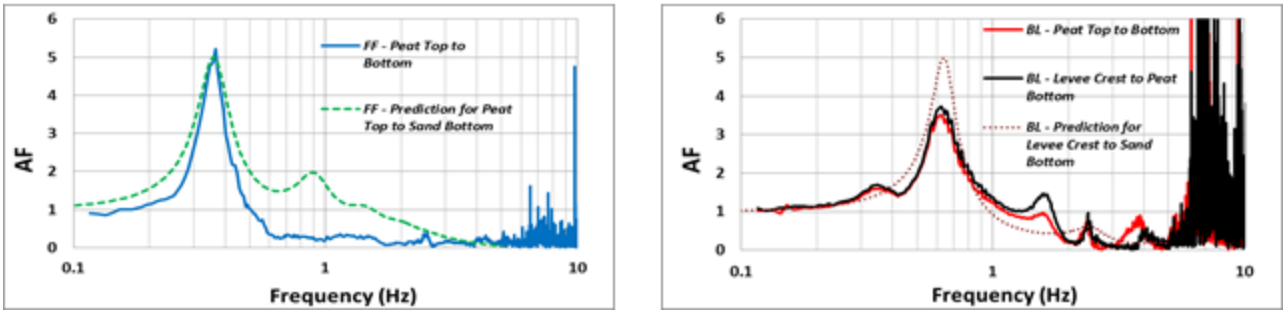

Figure 3-19 Transfer function for the free field (a) and the base of the levee (b) for RCK01 (Cappa et al. 2014a)

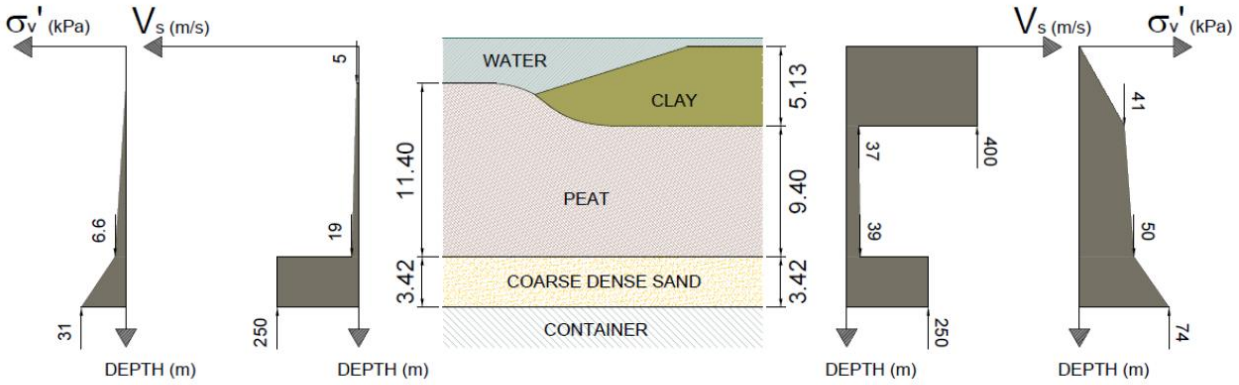

(a) – RCK01

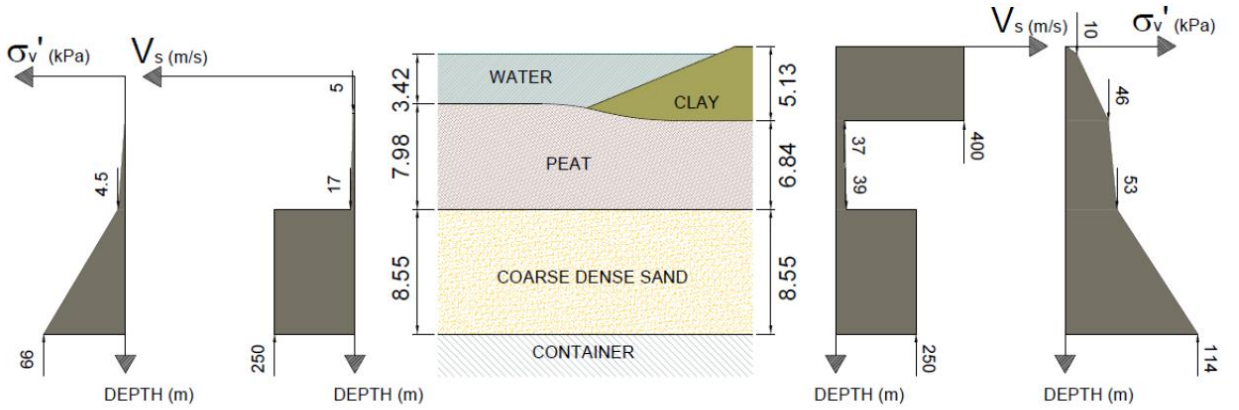

(b) – RCK02

Figure 3-20 Free-field (FF) and crest of levee (CL) soil profiles for RCK01 and RCK02 (Cappa et al. 2014a)

Damping values were not measured directly. Initially, the recommendations of Kishida et al. (2009a) were utilized, but predicted significantly higher amplification than was

measured. A damping ratio of 20% was found to produce reasonable agreement with the measured free-field amplification functions for both RCK01 and RCK02. Damping curves in centrifuge experiments have been found higher than in literature (Conti and Viggiani 2012; Elgamal et al. 2005). According to Brennan et al. (2005) this is due to the increased loading frequencies in centrifuge testing, and for normally consolidated clay they observed an increase by 50 % in the dynamic damping when frequency is scaled from 1 to 50 Hz.

The transfer function in Figure 3-19a shows a FF first mode at 0.36 Hz (2.77 sec). This peak is well captured by the 1-D ground response analysis. The transfer function ordinate at resonance is approximately 5. No clear second mode of vibration can be identified in the FF data, but is predicted by ground response analyses to be 0.87 Hz. The lack of a measured peak may be caused by higher damping at higher frequency, sensor resolution, or other unknown factors.

For the CL array (Figure 3-19b) the maximum transfer function ordinate is 3.7 at a frequency of 0.63 Hz (1.59 sec). There are three additional local peaks at 1.65 Hz, 2.41 Hz and 3.83 Hz. The 1-D ground response analysis slightly overestimates the first mode frequency (0.68 Hz) and over predicts the peak amplification by about 50%. These features could be attributed to 2-D effects not captured by the 1-D analysis. A second mode is predicted in the 1-D analysis for the CL array at 2.31 Hz, which is lower than the observed second mode of 1.65 Hz.

We hypothesize that the local peak near 1.65 Hz in the data is associated with a rocking mode, which naturally is not present in the 1-D analysis results. This hypothesis is tested

by computing levee rotation using (1) a pair of vertical acceleration histories (divided by their horizontal separation distance to produce angular acceleration) from accelerometers at the peat-levee interface beneath the two edges of the embankment and (2) a pair of horizontal acceleration histories (divided by their vertical separation distance) from accelerometers at the levee base and crest in the CL array. Figure 3-21a shows the Fourier spectra of the levee rotational accelerations, which peak at 1.65 Hz, confirming that this mode from the transfer function in Figure 3-19b is from rotation. Figure 3-21b shows the transfer function of horizontal acceleration at the levee crest to that at the base, and again a peak occurs around 1.68 Hz, reinforcing the existence of a rocking mode.

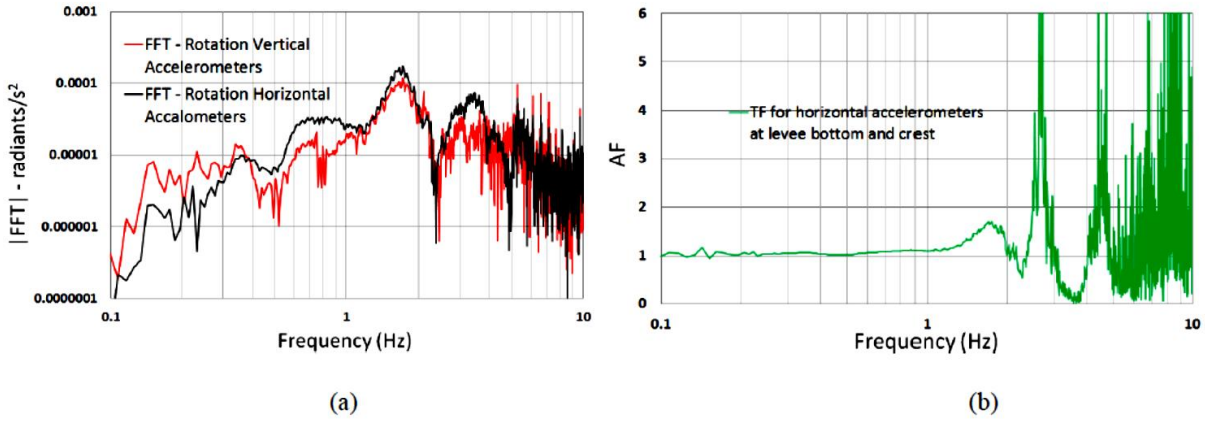

Figure 3-21 FFT of the vertical and horizontal rotations (a) and transfer function of the horizontal accelerometers at the bottom and the crest of the levee (b) for RCK01 (Cappa et al. 2014a)

Figure 3-22 shows a similar comparison between 1-D ground response analysis results and recorded data for RCK02. The recorded FF transfer function has a peak ordinate of 3.6 at 0.37 Hz (2.7 sec), which is well captured by 1-D analysis. The CL array transfer function has a peak ordinate of 5.4 (levee crest/peat bottom) at 0.69 Hz (1.45 sec). Two additional local peaks occur at 2.66 Hz and 3.91 Hz, which are comparable to the 3rd and 4th peaks observed in the recorded data for the same array in RCK01. The 1-D simulation

overestimates the resonant frequency (0.88 Hz) but slightly under predicts amplification at resonance. The 1-D analysis also predicts a second mode peak near the 3.14 Hz that is again lower than the observed second mode of 2.68 Hz. Similar analyses of levee rocking are shown in Figure 3-23 and confirm that this peak in the transfer function is due to rotation.

We attribute the variable fundamental mode resonant frequencies from RCK01 and RCK02 of 0.63 and 0.69 Hz for the CL array to the varying peat thicknesses. However, proximity to the rigid wall of the container may also have played a role in the observed response. Further analysis of the data will be required to characterize these effects.

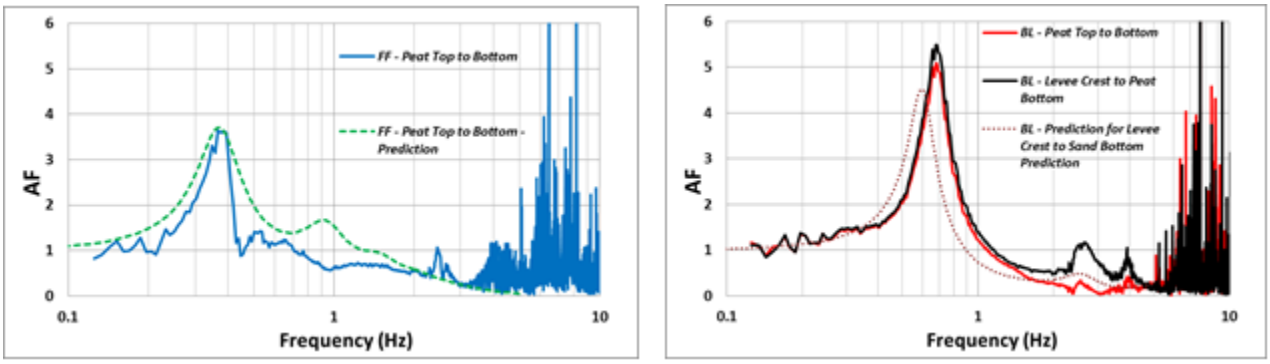

Figure 3-22 Transfer function for the free field (a) and the base of the levee (b) for RCK02

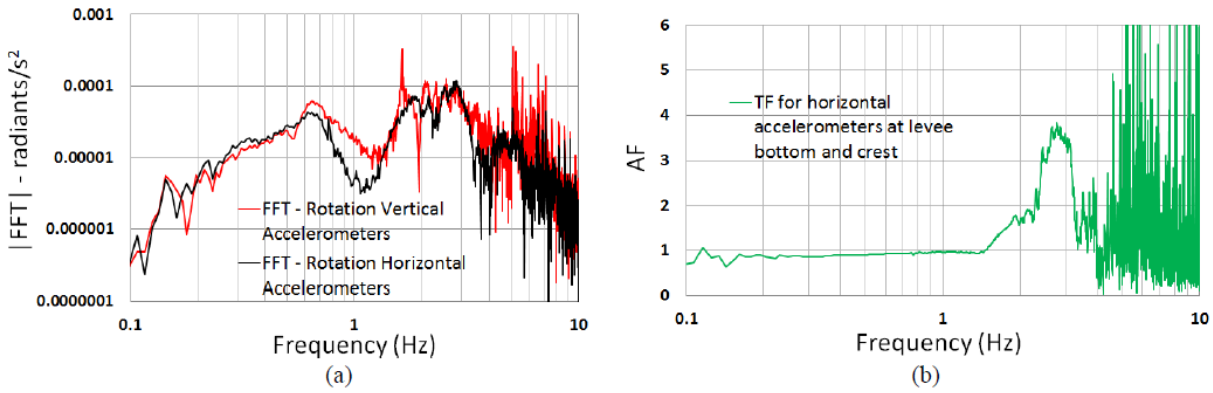

Figure 3-23 FFT of the vertical and horizontal rotations (a) and transfer function of the horizontal accelerometers at the bottom and the crest of the levee (b) for RCK02 (Cappa et al. 2014a)

3.5.2.2 Liquefaction of the sandy Levee.

In the second phase of both investigations a sandy levee replaces the clayey levee and the liquefaction potential of the levee fill is studied. In RCK02 the sandy levee is shaken with a moderate Kobe motion. Under the motion, the levee fill liquefied and slumped, resulting in a breach with water from the channel pouring over the levee and eroding it away until the water elevation equalized on both sides of the levee (Figure 3-24). Two more ground motions with smaller amplitude were applied after the moderate Kobe motion to observe the threshold for liquefaction triggering in the levee fill and to simulate aftershocks. These motions induced a measurable pore pressure and settlement response. Fast data recorded during the moderate Kobe motion are shown in Figure 3-25, including acceleration, pore pressure, and settlement, all in prototype units. The peak base acceleration of the moderate Kobe was 0.38g and the peak acceleration of the levee crest was 0.28g, indicating that the soil profile de-amplified the input motion. The pore pressure in the center of the sandy levee increased by approximately 30 kPa, which is equal to the initial vertical effective stress at the levee center, indicating the levee fill

liquefied. The excess pore pressure within the levee fill recorded by P9 abruptly rises during application of the Kobe motion and quickly dissipates due to the high permeability of the sand, whereas the excess pore pressure in the peat beneath the levee decreases slowly after the ground motion. Pore pressure in the free-field on the landward-side of the levee abruptly increases and remains elevated. This is due to the water in the channel being released, thereby permanently elevating the groundwater table on the landward free-field side of the levee. Settlement records exhibit significant high frequency noise, but a dynamic response is evident, superposed on the noise, and the permanent component is clear. The levee crest settled 0.7 m at the position of LP 14, which is near the center of the levee. The breach occurred where settlement was highest, between the center of the levee and the container wall. Videos capturing the liquefaction process and sandy levee failure are available on the NEES project warehouse.

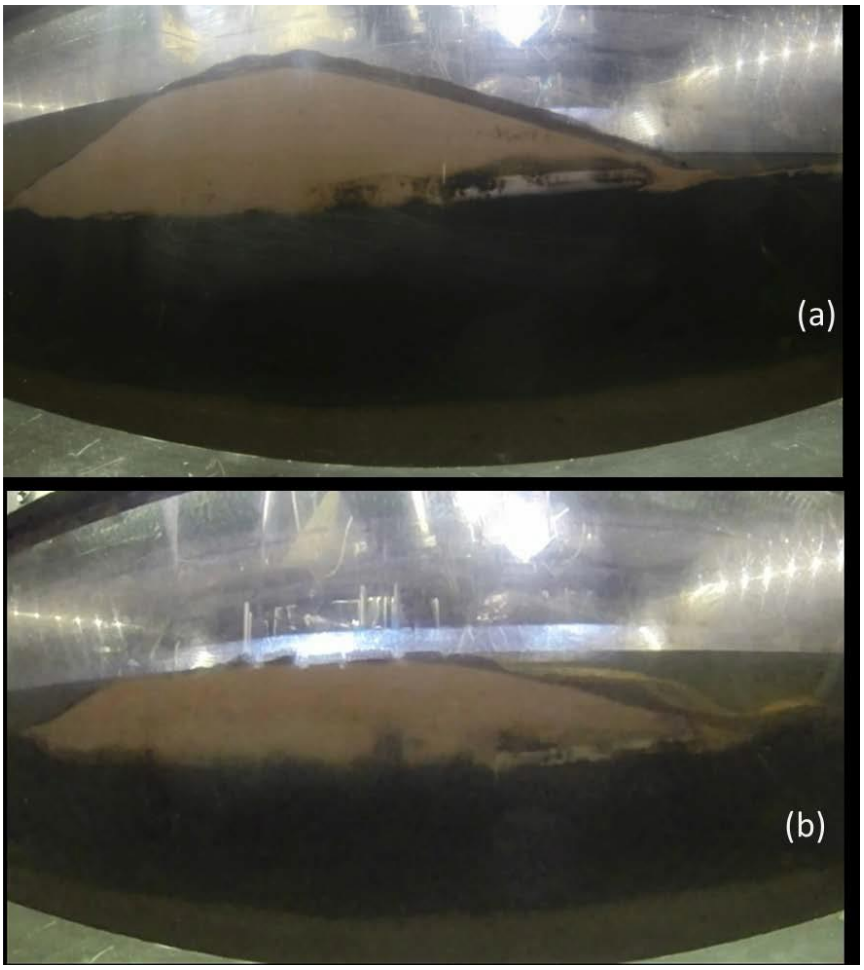

Figure 3-24 Photos of the sandy levee before (a) and after the earthquake (b) (Lemnitzer et al. 2015)

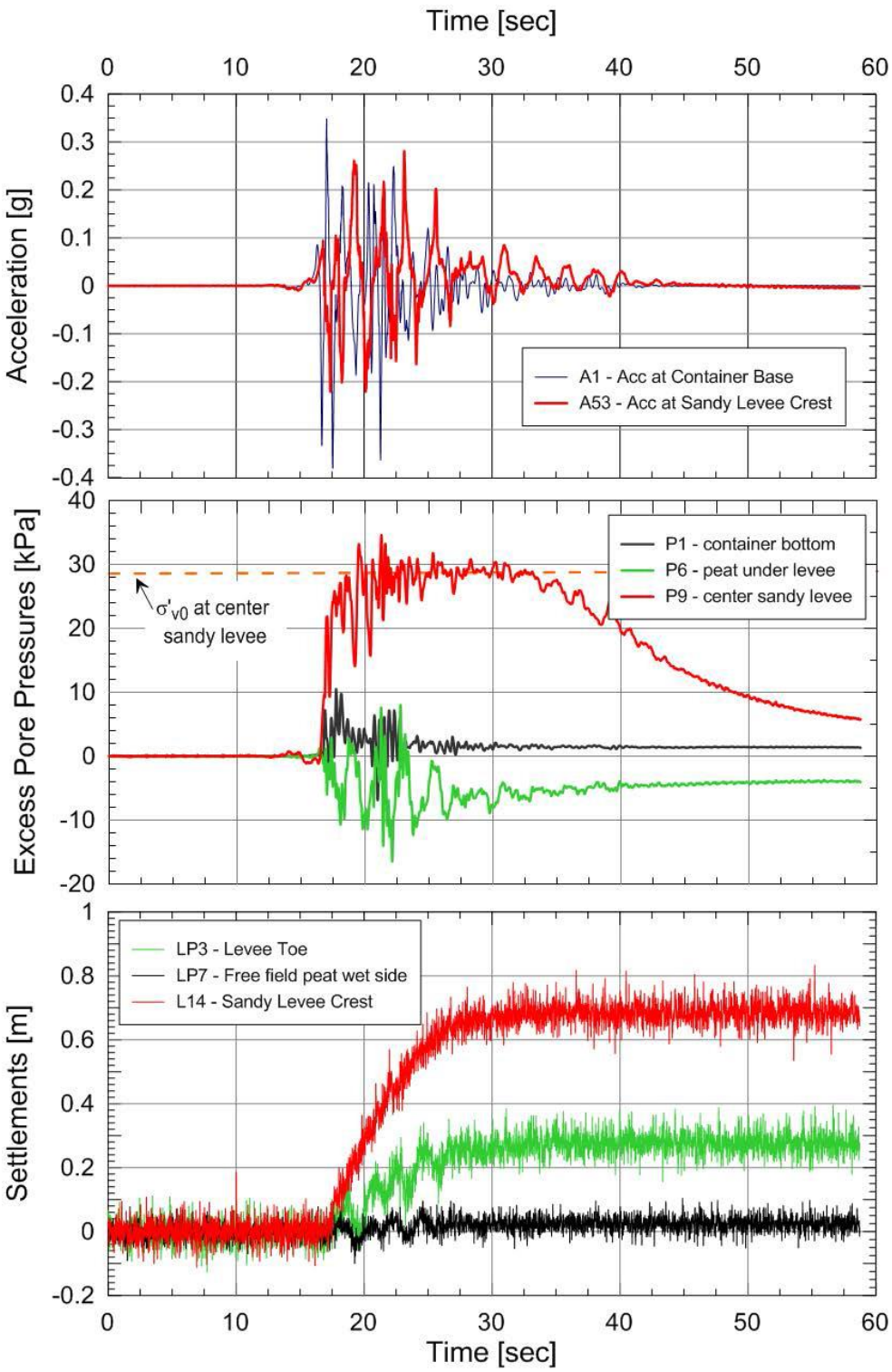

Figure 3-25 RCK02 recordings during ground motion (a) accelerometers, (b) pore pressure transducers, (c) linear potentiometers (Lemnitzer et al. 2015)

4 MODULUS REDUCTION AND DAMPING CURVES PLOTTED VS. STRESS RATIO

This chapter is issued from Yniesta and Brandenberg (2016) and presents a new concept in which modulus reduction and damping curves are plotted versus stress ratio (η) rather than shear strain. First, the motivations are discussed. Second, the procedure for computing the G/G_{max} vs η curve is presented. The procedure is then applied to relationships formulated by Darendeli (2001) for clay, Menq (2003) for sand, and Kishida et al. (2009) for peat. The resulting relationships for G/G_{max} and $D - D_{min}$ vs η are shown to be pressure-independent. Finally, implications and potential uses of the new approach are discussed. This concept is used in the model presented in chapter 6, but can also be used for the model presented in chapter 5.

4.1 Motivations

The cyclic stress-strain behavior of soil is commonly characterized using modulus reduction and damping (MRD) curves in which secant shear modulus and percent damping are expressed as functions of cyclic shear strain amplitude (γ_c). Curves have been derived from cyclic laboratory testing equipment capable of measuring small-strain behavior, including specialized simple shear devices (e.g., Vucetic and Dobry 1991, Doroudian and Vucetic 1995), specialized triaxial compression devices (e.g., Wehling et al. 2003, Kishida et al. 2009), and resonant column / torsional shear devices (e.g., Menq 2003, Darendeli 2001). Research studies have found that modulus reduction and damping curves depend on the following factors: soil type, effective stress (e.g., Darendeli 2001, Menq 2003, Kishida et al. 2009, EPRI 1993), plasticity index (e.g., Vucetic and

Dobry 1991, Darendeli 2001), number of loading cycles (e.g., Matasovic and Vucetic 1995), and strain rate (e.g., Matesic and Vucetic 2003).

Pressure-dependence of MRD curves is often evaluated in the laboratory by consolidating soils to different pressures, and shearing them either in drained or undrained loading. When sheared in undrained loading, specimens may develop excess pore pressure that reduces the effective stress. Effective stress ground response analysis codes often explicitly model excess pore pressures, in which case the MRD curves evolve during loading due to their pressure-dependence [e.g., Deepsoil (Hashash et al. 2015) and D-MOD (Matasovic 2006)]. Formulating modulus reduction and damping curves in a manner that does not depend on effective stress would therefore be beneficial for implementation in effective stress ground response analysis codes, and potentially for plasticity formulations.

4.2 Calculation of Modulus Reduction and Damping Curves as Functions of Stress Ratio

The approach to computing G/G_{max} and D versus η for a particular soil type follows these steps: (1) select a soil type and an associated MRD relationship, (2) select a mean effective stress value p', (3) compute the small-strain shear modulus, G_{max}, (4) compute the stress-strain backbone curve using Equation 4-1, (5) compute $\eta = \tau / p'$, and (6) repeat steps (2) through (5) for various p' values in the range of engineering interest for the selected soil type. Values of G/G_{max} and D (or alternatively D-D_{min}) are then plotted versus η. Note that the mean effective stress is usually calculated as a third of the trace of the stress tensor. In the absence of knowledge of the coefficient of earth pressure at rest K_0,

the mean effective stress is taken as equal to the vertical effective stress i.e. $p' = \sigma'_v$. In the empirical relationships used to calculate the MRD curves, the use of vertical effective stress is preferred.

$$\tau(\gamma) = G_{max} \cdot \left(\frac{G}{G_{max}}(\gamma) \right) \cdot \gamma \qquad \textit{Equation 4-1}$$

4.3 G/G_{max} and D-D_{min} vs η for Commonly Used Relations

Equations defining the modulus reduction and damping behavior of sand, clay, and peat are utilized to demonstrate the proposed concept. The models were selected because they are widely used in practice and cover a wide range of material types. The equations are too lengthy to reproduce herein, but the input parameters are provided so that readers can reproduce the results after consulting relevant sections of the references associated with each model. This section presents the input parameters selected to generate the modulus reduction and damping curves for each soil type selected for the example. In each case, the input parameters are consistent with the database from which the relations were derived.

4.3.1 Relationship for Sand

Menq (2003) constructed a large-scale, multi-mode, free-free resonant column device and studied the dynamic properties of non-plastic sandy and gravelly soils. Based on his tests, Menq developed regression equations for G_{max} and modulus reduction and damping curves. The modulus reduction and damping curves depend on the mean effective stress (p'), the coefficient of uniformity (C_u), the mean grain size (D_{50}), and the

number of cycles (N_c). Gmax also depends on the void ratio (e). Input properties utilized herein are provided in Table 4-1.

Table 4-1Soil properties for the Menq (2003) relationship for sand

Property	Value
C_u	3
D_{50}	0.5 mm
e	0.7
N_c	1000
p'	20, 50, 100, 200 kPa

4.3.2 Relationship for Clay

Darendeli (2001) developed regression equations defining the modulus reduction and damping behavior measured in resonant column / torsional shear tests of clayey soils. The equations depend on the plasticity index (*PI*), the overconsolidation ratio (*OCR*), the number of cycles, and frequency. Darendeli did not provide recommendations for computing G_{max}, so we adopt Equation 4-2 developed by Hardin and Drnevich (1972b) and normalized by Schneider et al. (1999), e is void ratio, *OCR* is overconsolidation ratio, M and N depend on soil type, and pa is atmospheric pressure. M and N were selected based on the recommendations of Hardin and Drnevich (1972b) and Schneider et al. (1999). Other models exist for computing G_{max}, but this relationship was selected because of its simplicity. The important aspect of such equations is the exponent on the effective stress term. The pressure-dependence of G_{max} counterbalances the pressure-dependence of G/G_{max} versus γ_c to render a pressure-independent G/G_{max} versus η relationship.

$$\frac{G_{max}}{p_a} = 321\frac{(2.973-e)^2}{1+e}OCR^M\left(\frac{p'}{p_a}\right)^N$$ *Equation 4-2*

Equation 4-2 depends on *e*, which is a function of consolidation condition for clays according to Equation 4-3:

$$e = e_N - \lambda \ln\left(\frac{p'_c}{p_1}\right) + \kappa \ln\left(\frac{p'_c}{p'}\right)$$ *Equation 4-3*

where e_N is the void ratio at reference pressure p_1, λ is the slope of the virgin compression line and κ is the slope of the recompression line in *e*-ln *p'* space, and p_c is the maximum past pressure computed as $p'_c = OCR \cdot p'$. Input parameters utilized herein are provided in Table 4-2. The modulus reduction and damping curves were computed using the regression constants from Table 8-12 in Darendeli (2001).

Table 4-2 Soil properties input to the Darendeli (2001) relationship for clay

Property	Value
PI	20
OCR	1
e_N	1.515
P_1	1
λ	0.151
κ	0.018
M	0.18
N	0.5
N_c	1000
Freq	1 Hz
p'	30, 75, 125, 200 kPa

4.3.3 Relationship for Peat

Kishida et al. (2006, 2009) developed a regression model for MRD curves and Gmax for peat based on *p'*, organic content (*OC*), and the laboratory consolidation ratio (*LCR*). The *LCR* is defined as the laboratory consolidation stress divided by the in-situ vertical effective stress. Soil properties input to the Kishida et al. (2009) model are summarized in Table 4-3.

Table 4-3 Soil properties input to the Kishida et al. (2009) relationship for peat.

Property	Value
OC	45%
LCR	1.0
p'	10, 30, 75, 125 kPa

4.4 Example of Modulus Reduction and Damping Curves Plotted against η

Modulus reduction curves computed for sand, clay, and peat are plotted in Figure 4-1a,b,c versus γ_c and in Figure 4-1d,e,f versus η . Different MRD curves arise for different values of *p'* when G/G_{max} is plotted versus γ_c. The influence of *p'* on MRD is significant for all three soil types, and is highest for sand, and lower for clay and peat. However, the G/G_{max} and D-D_{min} curves are essentially pressure-independent when plotted versus η for each soil type. The reason why this occurs is that the overburden scaling for G_{max} combines with the overburden scaling for G/G_{max} versus γ_c in a manner that renders G/G_{max} versus η insensitive to *p'*.

The small-strain damping value, D_{min}, is subtracted from the strain-dependent damping relationship when plotting versus η. This procedure was adopted because $D - D_{min}$ versus η is pressure-independent for each soil type, whereas D versus η is not. Hysteretic damping formulations typically do not capture small-strain damping, relying instead on Rayleigh damping formulations. Subtracting D_{min} is therefore reasonable and convenient for typical implementations.

This approach was repeated for the three relationships presented here with different sets of input parameters in order to verify the concept. The results are not presented here for

the sake of brevity, but the concept proved to be true for any set of input parameters consistent with the model's database.

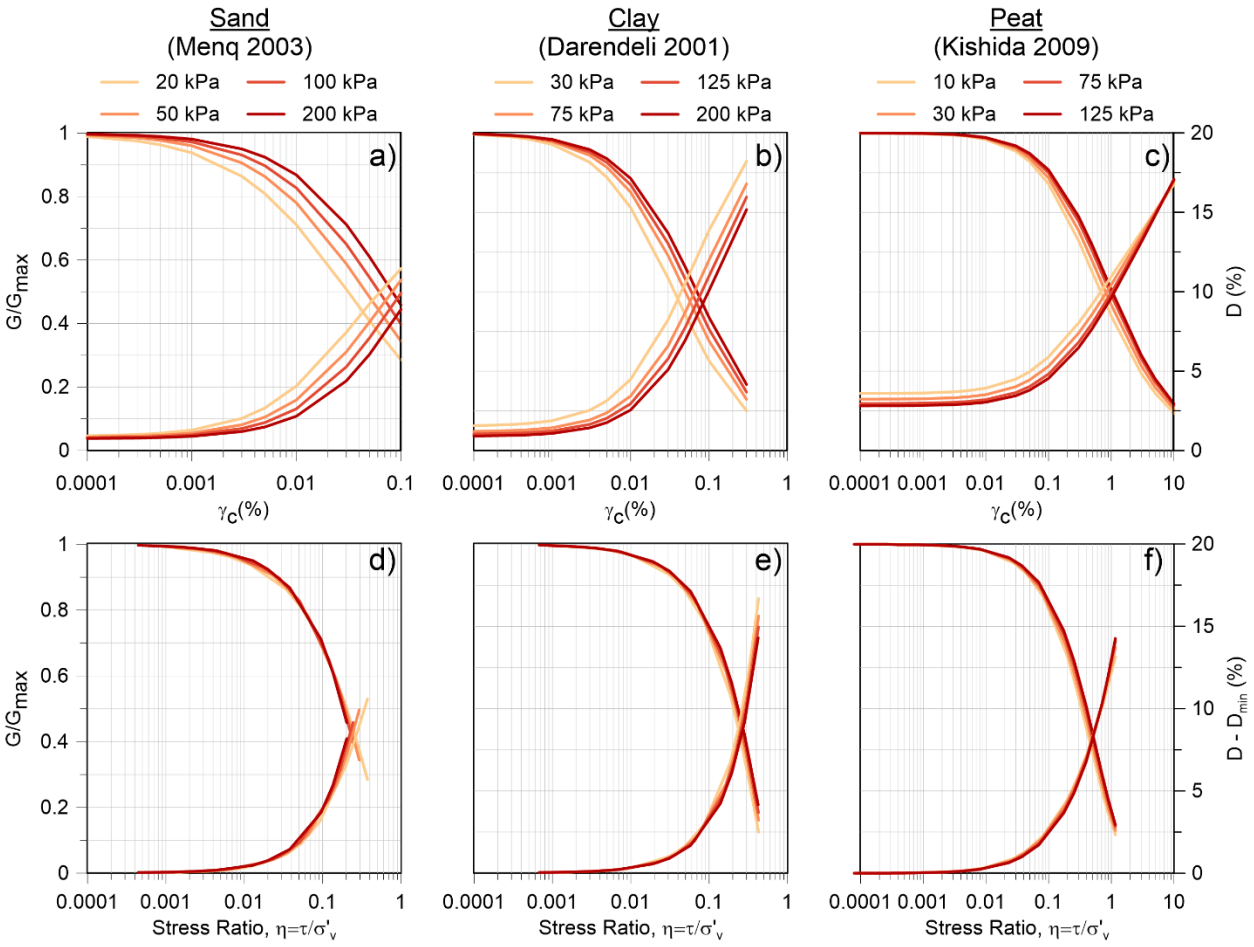

Figure 4-1 Modulus reduction and damping curves vs. γ_c and η for sand (a and d), clay (b and e) and peat (c and f).

4.5 Benefits of Proposed Approach

The proposed approach provides four distinct benefits compared with the traditional approach. First, the MRD curves studied herein are independent of *p'* when plotted versus *η*. Effective stress ground response analysis for undrained loading conditions is much simpler when the soil behavior is independent of *p'* because excess pore pressure development does not necessitate changes to the backbone curve or damping

relationship. Different models have been proposed to include the effect of change in confining pressure on MRD curves. For example, Hardin and Drnevich (1972a and b) proposed a modified hyperbolic model that normalizes the curves by a reference shear strain and renders a pressure independent curve. However, the reference shear strain is itself pressure-dependent and the modulus reduction curves are still a function of effective stress, and would need to be adjusted as effective stress changes during an effective stress ground response analysis.

Second, modulus reduction and damping curves are often extrapolated to large strains beyond the range of empirical validation, which can result in significant errors in the implied shear strength (e.g., Yee et al. 2013, Afacan et al. 2014). The relationships presented herein were constrained within the range of experimental validation, but ground response analysis often exceeds this range, requiring extrapolation. Very small differences in the large-strain tail of the G/G_{max} vs. γ_c curve can result in significant differences in the implied shear strength. By contrast, representing G/G_{max} as a function of η instead of γ_c provides direct control over the mobilized shear strength because a single peak stress ratio can easily be specified.

Third, advanced constitutive models are often formulated such that the plastic modulus is defined in stress-ratio space. For example, Dafalias and Manzari (2004) and Boulanger and Ziotopoulou (2015) developed stress-ratio based bounding surface plasticity models in which the plastic modulus is a function of the distance in stress space between the current stress ratio and the stress ratio at an image point on the bounding surface. Adjusting bounding surface model parameters to provide desired G/G_{max} versus γ_c

behavior is a complex and difficult task. The proposed approach could conceivably be utilized to simplify this task, or possibly to directly define plastic modulus based on position in stress-ratio space.

Fourth, the proposed framework provides a new approach for interpreting laboratory test data in a manner that may eliminate *p'* as an influential variable, which can reduce uncertainties when developing regression models.

4.6 Discussion

The G/G_{max} and $D\text{-}D_{min}$ versus η curves are independent of *p'* for the particular relationships utilized here, which is valuable because these relationships are commonly utilized in engineering practice. However, independence may not be achieved for other relationships. Readers are encouraged to verify pressure independence of the G/G_{max} and $D\text{-}D_{min}$ relationships for equations that are not presented herein.

Furthermore the effect of *OCR* is not included in this formulation. G/G_{max} versus η curves are independent of *p'* but not *OCR*. Since *OCR* can change during loading as effective stress changes, this is a limitation of the concept. However, G/G_{max} versus γ_c curves present the same limitation.

5 ONE DIMENSIONAL NONLINEAR MODEL FOR MATCHING MODULUS REDUCTION AND DAMPING CURVES IN GROUND RESPONSE ANALYSIS

This chapter presents a one dimensional model capable of matching both input modulus reduction and input damping curves. All the damping introduced by the model is hysteretic and therefore the model does not need to be associated with a viscous damping scheme. Most of the text of this chapter comes from Yniesta et al. (2016). Some of the notations and the terminology have been modified to preserve consistency between the different chapters. This model constitutes the basis of the multidimensional model presented in chapter 6, and it is advised that the reader gets familiar with the 1D model before moving to the multidimensional model.

5.1 Motivations for One-Dimensional Model

Earthquake ground motions are influenced by source, path, and site effects. Site effects are most commonly considered using either (1) nonlinear site amplification functions that depend on the average shear wave velocity in the upper 30m (V_{s30}), or (2) site-specific one-dimensional ground response analysis. Ground response analyses are performed using equivalent linear (EL) procedures, in which the shear modulus and damping are taken as time-invariant values set to be consistent with mobilized shear strains, or nonlinear (NL) procedures, in which a plasticity model is utilized to match desired modulus reduction and damping behavior. Recent studies indicate that NL procedures are superior to EL when mobilized shear strains exceed about 0.4% (Kaklamanos et al. 2013, Stewart

et al. 2008) or even as low as 0.05% (Kaklamanos et al. 2015). These strain levels are exceeded at many sites where strong ground motions are imposed on soft soil profiles.

Nonlinear site response models focus on matching small-strain behavior measured in laboratory devices at shear strains lower than about 0.1 to 0.3%, but these models are often extrapolated beyond their range of experimental validation to larger strains. This extrapolation can cause an under- or over-prediction of shear strength depending on the ratio of shear strength to small strain shear modulus, G_{max}. These shear strength errors can translate to under- or over-prediction of ground surface motion (Groholski et al. 2015, Afacan et al. 2014, Zalachoris and Rathje 2015). Developing models that accurately capture small strain behavior and shear strength is obviously important for nonlinear site response simulations.

This chapter presents a one-dimensional nonlinear stress-strain model capable of reproducing any user-input modulus reduction and damping curve. Existing models commonly used in site response modeling are discussed first to illustrate the need for improved models. This is followed by presentation of the proposed modeling equations, which are shown to precisely match any user-input modulus reduction and damping curve. The proposed model is then compared with simple shear laboratory experiments conducted on sand and peat soils to illustrate key features of behavior and compare with existing model formulations.

5.2 Modulus Reduction Behavior of Existing Models

User inputs to a one-dimensional ground response analysis required to define the dynamic properties of each soil layer include: (1) maximum shear modulus, (2) modulus

reduction curve, and (3) damping ratio curve. Existing nonlinear models vary in their ability to capture the desired modulus reduction and damping behavior. Models are categorized as either one-dimensional, consisting of a backbone curve and unload-reload relations, or multi-dimensional plasticity formulations consisting of a yield surface, hardening law, and flow rule.

Many nonlinear codes use a hyperbolic equation to model the backbone curve (e.g., Deepsoil: Hashash and Park 2001; D-MOD: Matasovic and Vucetic 1993; and Tess: Pyke 2000). The hyperbolic formulation was first introduced by Kondner and Zelasko (1963) and later modified by Hardin and Drnevich (1972) and Darendeli (2001). In the special case where the desired modulus reduction curve happens to be hyperbolic, then these models are capable of precisely matching the desired modulus reduction curve. However, the desired modulus reduction curve generally does not correspond to a hyperbolic backbone function, resulting in a misfit between the user-input modulus reduction curve and the hyperbolic curve.

Small misfits in the modulus reduction curve can translate to significant misfits in the stress-strain curve at high strain, resulting in errors in the desired shear strength (e.g., Chiu et al. 2008, Groholski et al. 2015, Afacan et al. 2014, Zalachoris and Rathje 2015). To address this problem Hashash et al. (2010) suggests that the high strain portion of the user-specified modulus reduction curve should be adjusted so that the resulting fitted curve provides the correct shear strength. However, this increases the misfit at low strain. Furthermore, Matasovic and Vucetic (1993) introduced a modified version of the hyperbolic Kondner and Zelasko model where the introduction of two curve-fitting constants improves matching the modulus reduction curve. Yee et al (2013) proposed a

hybrid procedure where the modulus reduction curve is modified to match the shear strength at high strains and obtain a more reasonable backbone curve. The procedure utilizes the prescribed modulus reduction curve below a transition strain, γ_t, and a hyperbolic model above γ_t. The stress and tangent modulus values are continuous at γ_t. However, the Yee et al. model cannot be perfectly fit by a hyperbolic model, often resulting in a mismatch between the desired shear strength and that achieved in the nonlinear site response code.

Multi-dimensional plasticity models incorporate nonlinear behavior using either multiple nested yield surfaces or bounding surface formulations. In multiple yield surface models (e.g., Prevost 1985, Elgamal et al. 2003), the backbone curve is controlled by setting the plastic modulus associated with each yield surface. The resulting backbone curve is piecewise linear when a constant plastic modulus is assigned to each yield surface. The PressureDependMultiYield and PressureIndependMutliYield (Elgamal et al. 2003) material models implemented in OpenSees can be configured to match a user-specified modulus reduction curve. In bounding surface plasticity models, the plastic modulus is defined based on the distance in stress space between a current point and an “image” point on a bounding surface (e.g., Assimaki et al. 2000, Dafalias and Manzari 2004, Boulanger and Ziotopoulou 2015). The hardening function that controls the evolution of the plastic modulus may be adjusted to match a desired modulus reduction curve. For example, Boulanger and Ziotopoulou (2015) adjusted the PM4Sand model to match the modulus reduction and damping curves for sand by EPRI (1993). However, the modulus-reduction curve is not an input to the PM4Sand model, though users could conceivably alter the modeling constants to provide a fit (a significant effort).

5.3 Damping Behavior of Existing Models

Soil damping can arise from hysteretic cyclic loading behavior of the soil skeleton, relative displacement between the solid and fluid phases, or other sources of energy loss. Damping is commonly divided into “small-strain” damping, which is often modeled using numerical procedures such as Rayleigh damping, or “large-strain” damping, which is modeled by the unload-reload behavior of the stress-strain model. Masing (1926) rules and extended Masing rules (e.g., Pyke 1979, Wang et al. 1980, Vucetic 1990) are most common in nonlinear site response codes (Stewart et al. 2008).

The extended Masing rules are stated as follow:

5. The stress-strain curve follows the backbone curve during initial loading.
6. If a strain reversal happens at point (γ_{rev}; τ_{rev}), the unloading or reloading curve has a shape that is identical to the backbone curve enlarged by a factor n. In its original paper, Masing used n=2, it was later modified by Pyke (1979), where n can deviate from 2, to provide a better match of the damping at higher strain.
7. If the unloading or reloading curve exceeds the maximum past strain and intersects the backbone curve, it follows the backbone curve until the next stress reversal.
8. If the unloading or reloading curve crosses an unloading or reloading curve from a previous cycle, it follows the curve of that previous cycle.

When Masing rules are used with n=2, the initial slope of the unloading or reloading curve is equal to the maximum shear modulus G_{max}, and the model shows no hardening or softening (i.e. loops are closed).

Masing rules tend to over predict damping at large strains (Phillips and Hashash 2009), and do not provide hysteretic damping at small strains (i.e., in the range where G/G_{max} = 1). Several solutions have focused on modifying the second Masing rule to obtain reasonable hysteretic damping at high strains. The Cundall-Pyke hypothesis (Pyke 1979) evaluates *n* based on the shear strength. This formulation improves damping at high strain and creates some degradation. To match the damping curve, Darendeli introduced a damping reduction factor now used in several codes (Darendeli 2001). This formulation does not create degradation, and only acts on the area of the stress-strain loops. Based on Darendeli's work, Phillips and Hashash (2009), introduced a damping reduction factor that provides a better fit or the curve at large strains.

Small-strain damping is commonly modeled using frequency-dependent Rayleigh damping, which introduces mass- and stiffness-proportional viscous damping terms to the equation of motion. Most nonlinear codes utilize the formulation by Rayleigh and Lindsay (1945), which enables matching a desired damping value at either 2 frequencies (full Rayleigh damping) or 4 frequencies (extended Rayleigh damping). At other frequencies, damping is either too low or too high, making the damping frequency-dependent in a manner that is inconsistent with laboratory results (Lai and Rix 1998; Vucetic et al. 1998). Phillips and Hashash (2009) established a frequency-independent Rayleigh damping formulation, based on the work of Liu and Gorman (1995). TESS (Pyke 1979, Pyke 2000) uses an unload/reload rule to produce hysteretic damping at low strains. The procedure however can result in over prediction of damping at large strains (Stewart et al. 2008).

An important consideration for NL methods is that the author is not aware of any published models that permit exact simultaneous matching of any user-input modulus reduction and damping curve. Desired modulus reduction and damping curves often deviate from hyperbolic behavior, forcing users to choose to fit certain behaviors while accepting misfits in others (Kwok et al. 2008). The model formulation in the next section provides a precise fit to a discrete user-input modulus reduction and damping curve.

5.4 Formulation of the Model

5.4.1 Backbone Curve

During initial/virgin loading, a backbone curve is derived from the desired modulus reduction curve, and is fit with cubic splines (Figure 5-1). Cubic spline interpolation is a mathematical method that has been extensively described in numerous textbooks (e.g. De Boor 1978). The cubic splines pass through all of the user-input data points, resulting in a smooth continuous modulus reduction curve and stress-strain backbone curve. For comparison with the cubic spline fit, Figure 5-1 also shows a hyperbolic fit performed using two different approaches. In the first approach, the hyperbola is fit by least squares regression to the G/G_{max} and $\log(\gamma)$ values. This fitting results in a misfit at high strain that causes an under-prediction of shear strength in this case. The second approach fits the hyperbola to the stress-strain data, which provides a better fit of shear strength, but significant misfit to the modulus reduction curve at small strains. The cubic spline method is more flexible than fitting a single hyperbola because the cubic spline interpolation passes through all of the data points, precisely fitting the user-input data.

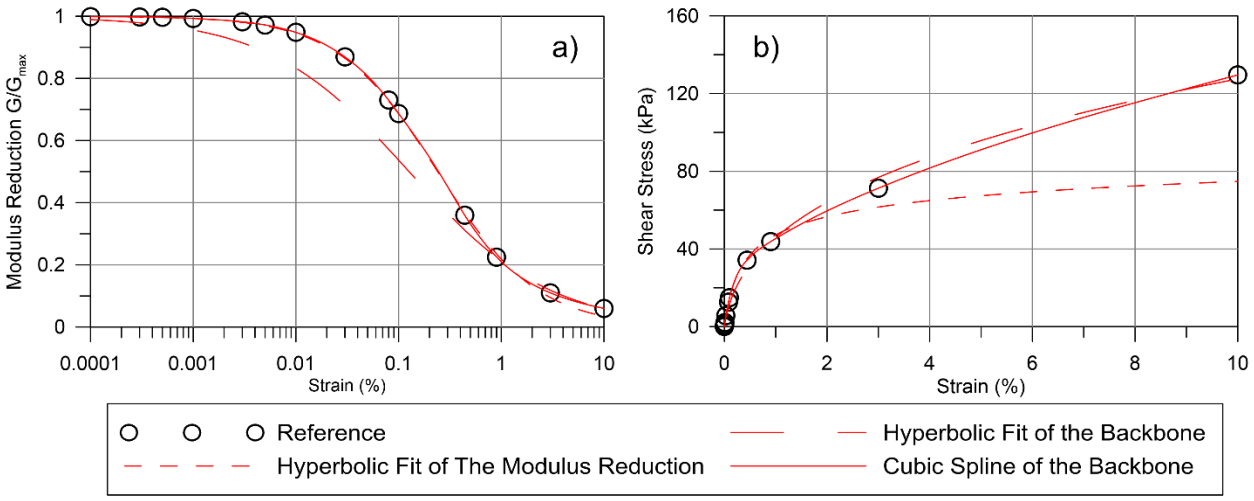

Figure 5-1Evaluation of the curve fitting method on (a) the modulus reduction curve and (b) the backbone curve

5.4.2 Unload/Reload Rule

The unload-reload rule is formulated to satisfy the following criteria:

(i) The secant modulus of the stress-strain loops matches a user-defined modulus-reduction curve,

(ii) When subject to uniform cyclic strain amplitude input, the stress-strain loops close and repeat, exhibiting no cyclic degradation or stiffening,

(iii) The area inside the stress-strain loops matches a user-defined damping curve, even at small strains where the modulus-reduction value is zero,

(iv) The stress-strain loops are concave about the secant modulus line.

5.4.2.1 Rotation of the Coordinate System

Upon the first unloading a coordinate transformation is introduced to control the modulus reduction and damping behavior. The values of strain and stress at the first unloading point are (γ_L, τ_L), and a target reversal point is defined as (γ_R, τ_R) = (-γ_L, -τ_L), as shown in

Figure 5-2. If unloading progresses, the curve will pass through the reversal point. A new coordinate system is defined such that the γ' axis lies along a line that runs through (γ_L, τ_L) and (γ_R, τ_R), at an angle θ from the γ axis, and the τ' axis is orthogonal to γ'. The origin of the rotated coordinate system, (γ_o, τ_o), lies at the center of (γ_L, τ_L) and (γ_R, τ_R), which happens to be (0,0) for the first unload cycle, but (γ_o, τ_o) may translate upon asymmetric loading, following rules described in the next section.

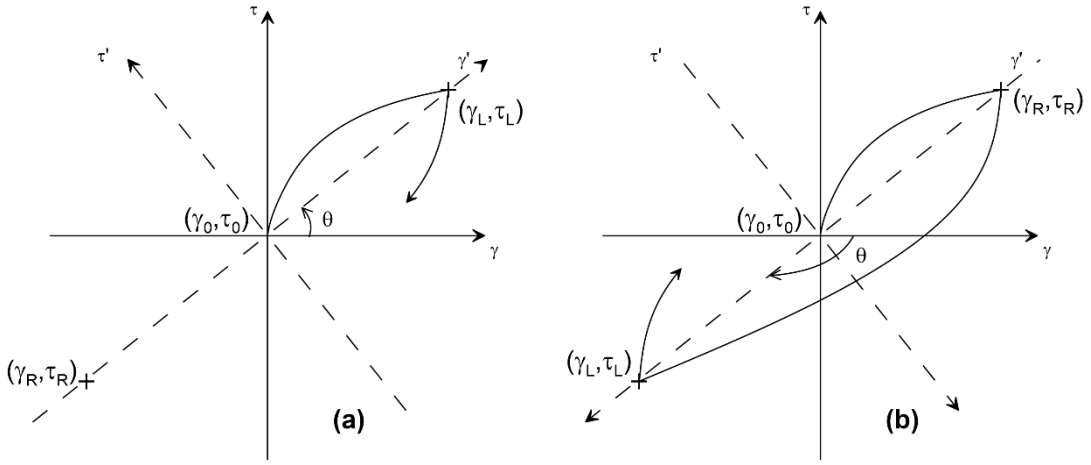

Figure 5-2: Stress-strain loops during (a) unloading and (b) reloading

The definition of θ depends on the loading direction, defined by Equation 5-1 for loading in the +γ direction and Equation 5-2 for loading in the –γ direction.

$$\theta = tan^{-1}\frac{\tau_R - \tau_L}{\gamma_R - \gamma_L} \qquad \textit{Equation 5-1}$$

$$\theta = tan^{-1}\frac{\tau_R - \tau_L}{\gamma_R - \gamma_L} - \pi \qquad \textit{Equation 5-2}$$

The coordinate transformation rules relating values in one coordinate system to those in another are given by Equation 5-3 and Equation 5-4. Note that the units of γ' and τ' are meaningless because the coordinate transformation is performed on axes with differing

units. However, this is inconsequential because the transformation is utilized merely as a means to satisfy the desired criteria, and an inverse transformation recovers the values of τ and γ.

$$\begin{pmatrix}\gamma\\ \tau\end{pmatrix} = \begin{pmatrix}\gamma' \cos\theta - \tau' \sin\theta + \gamma_0\\ \gamma' \sin\theta + \tau' \cos\theta + \tau_0\end{pmatrix} \qquad \textit{Equation 5-3}$$

$$\begin{pmatrix}\gamma'\\ \tau'\end{pmatrix} = \begin{pmatrix}(\gamma - \gamma_0)\cos\theta + (\tau - \tau_0)\sin\theta\\ -(\gamma - \gamma_0)\sin\theta + (\tau - \tau_0)\cos\theta\end{pmatrix} \qquad \textit{Equation 5-4}$$

To satisfy criterion (i), the value of θ must be selected to be compatible with a modulus reduction curve based on the cyclic shear strain amplitude. In this case, θ = atan(G_{sec}), and G_{sec} is interpolated from the modulus reduction curve at a cyclic strain amplitude, γ_c, defined as half of the peak-to-peak strain amplitude (Equation 5-5).

$$\gamma_c = \frac{|\gamma_R - \gamma_L|}{2} \qquad \textit{Equation 5-5}$$

5.4.2.2 Stress-Strain Curve in Rotated Coordinate Space

Having defined the coordinate transformation, a function is now selected to define the unload-reload behavior in the transformed coordinate space. A biquadratic equation (Equation 5-6) is selected because it is the simplest possible form that is symmetric about the τ' axis and contains three constants (a, b, and c) that can be solved to satisfy the three remaining criteria.

$$\tau' = a\,\gamma'^4 + b\,\gamma'^2 + c$$ *Equation 5-6*

The shape of the function describing a half loop in the transformed coordinate system is shown in Figure 5-3a, where the target reversal strain in the transformed system, γ'_{in}, is defined by Equation 5-7. Note that the stress-strain loop is symmetric about the γ' and τ' axis in τ'-γ'space, but do not appear symmetric about the γ' axis in the τ-γ space. The lack of symmetry is due to stretching of the axes upon coordinate transformation due to the stress and strain axes having different units. The stress-strain curves in τ-γ space nevertheless exhibit a reasonable shape.

$$\gamma'_{in} = \frac{\gamma_R - \gamma_0}{cos\theta}$$ *Equation 5-7*

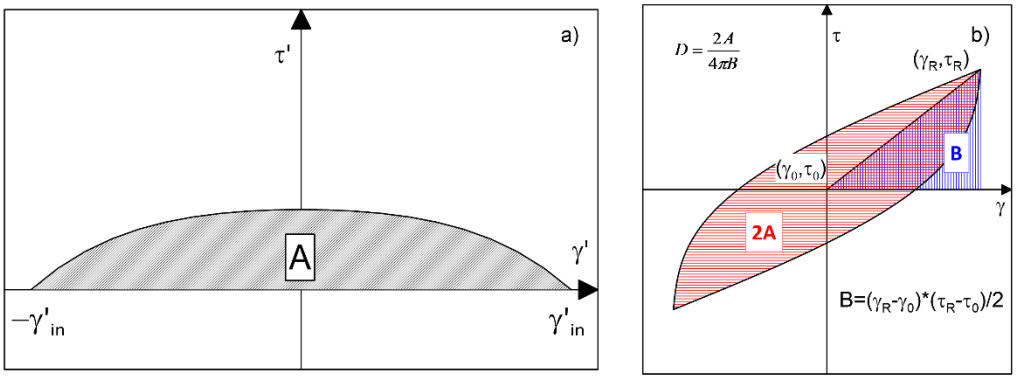

Figure 5-3 a) Half loop in the transformed coordinate system, and b) definition of damping

Criterion (ii), (iii), and (iv) are satisfied by Equation 5-8, Equation 5-9 and Equation 5-10, respectively.

$$\tau'(\gamma'_{in}) = 0$$ *Equation 5-8*

$$\int_{-\gamma'_{in}}^{\gamma'_{in}} \tau'(\gamma')d\gamma' = A = \gamma'_{in} D\pi(\tau_R - \tau_0)cos\theta$$ *Equation 5-9*

$$\frac{d^2(\tau')}{d(\gamma')^2} \leq 0 \; for \; \gamma' \in -\gamma'_{in} .. \gamma'_{in}$$ *Equation 5-10*

Criterion (ii), requiring that the unload-reload loops close with no cyclic degradation or hardening, is satisfied by setting $\tau' = 0$ at $\gamma' = \pm\gamma'_{in}$ (Equation 5-8). Criterion (iii), requiring the area inside the loop to match a target damping value, is satisfied by Equation 5-9. The equivalent viscous damping ratio *D* is selected from the input damping ratio curve based on the cyclic strain amplitude (Equation 5-5). The damping ratio is defined by $D=2A/(4\pi B)$, where *A* is the area beneath half of the loop as shown in Figure 5-3a, and *B* is the area of the triangle shown on Figure 5-3b and is equal to:

$$B = \frac{(\tau_R - \tau_0) * (\gamma_R - \gamma_0)}{2}$$ *Equation 5-11*

Criterion (iv), requiring that the stress-strain curve be concave about the secant shear modulus line is equivalent to requiring that $d^2(\tau')/d(\gamma')^2$ must be negative (Equation 5-10). A bi-quadratic equation has two inflexion points that are symmetrical with respect to the apex. Forcing the inflexion points to lie at $\pm\gamma'_{in}$ automatically satisfies Equation 5-10.

Substituting Equation 5-6 into Equation 5-8, Equation 5-9, and Equation 5-10 and solving the linear system of equations for *a*, *b*, and *c* results in EquationsEquation 5-12, Equation 5-13, and Equation 5-14:

$$a = \frac{5\pi D cos\theta(\tau_R - \tau_0)}{32{\gamma'}_{in}^{\ 4}} \qquad \textit{Equation 5-12}$$

$$b = -\frac{15\pi D cos\theta(\tau_R - \tau_0)}{16{\gamma'}_{in}^{\ 2}} \qquad \textit{Equation 5-13}$$

$$c = \frac{25\pi D cos\theta(\tau_R - \tau_0)}{32} \qquad \textit{Equation 5-14}$$

Applying an inverse coordinate transformation to Equation 5-6 using Equation 5-3 and Equation 5-4, an implicit relationship between strain and stress can be derived in τ-γ space (Equation 5-15):

$$\tau = [(\gamma - \gamma_0)\cos\theta + (\tau - \tau_0)\sin\theta]\sin\theta + [a((\gamma - \gamma_0)\cos\theta + (\tau - \tau_0)\sin\theta)^4 + b((\gamma - \gamma_0)\cos\theta + (\tau - \tau_0)\sin\theta)^2 + c]\cos\theta + \tau_0 \qquad \textit{Equation 5-15}$$

In Equation 5-15 the only unknown is τ, reducing the problem to a simple root-finding exercise. For the example problems presented herein, the root is solved using Ridders' Method (Ridders 1979), an algorithm based on the false position method which is unconditionally stable as long as the two initial guesses lie on each side of the root. The root is automatically bracketed when the initial guesses are set equal to the stress at the previous time step and the target stress point. Other methods converge more rapidly (e.g., Newton-Raphson), but are not always able to converge upon the desired root. Ridders' method converges more quickly than other unconditionally stable methods, such as the bisection method.

5.4.2.3 Asymmetrical Loading

Thus far, focus has been on symmetric loading, where (γ_R, τ_R) = (-γ_L, -τ_L), and (γ_o, τ_o) lies at (0,0). Asymmetrical loading conditions occur when (γ_R, τ_R) ≠ (-γ_L, -τ_L), meaning that the center of the unload-reload loop shifts away from the τ-γ origin, as illustrated in Figure 5-4 Asymmetrical loading (a) positive loading (b) negative loading and defined in Equation 5-16a and Equation 5-17b.

$$\gamma_0 = \frac{\gamma_R + \gamma_L}{2}$$ *Equation 5-16a*

$$\tau_0 = \frac{\tau_R + \tau_L}{2}$$ *Equation 5-17b*

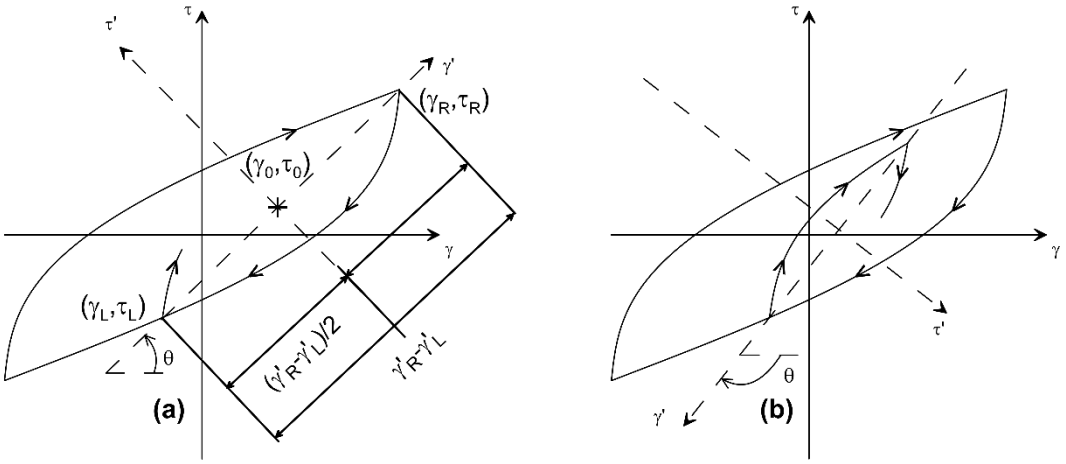

Figure 5-4 Asymmetrical loading (a) positive loading (b) negative loading

Defining the values of γ_L and τ_L is straightforward; these values are simply the strain and stress at which the current reverse loading cycle began. Defining the values of γ_R and τ_R (i.e., the target value of strain and stress) involves three unload/reload rules, demonstrated through an example problem in Figure 5-5 Evolution of the reversal strain vectors. For brevity, the example problem is formulated in terms of strains (i.e., γ_L and γ_R), and the stress updating is omitted but follows the same logic. In Figure 5-5a, monotonic loading progresses to the first reversal at γ_1 and begins unloading such that $\gamma_L = \gamma_1$. The size of the unloading loop is not known at the onset of unloading, so the simplest assumption is that the target reversal point is $\gamma_R = -\gamma_1$. The first unload / reload rule is:

> *Rule 1: When an unloading cycle initiates from the monotonic backbone curve,* $\gamma_R = -\gamma_L$.

Having defined γ_R, the shape of the unload curve is defined by Equation 5-15, and unloading progresses along this curve to a value γ_2 where a new reverse loading cycle begins. The value of γ_L is now updated to be equal to γ_2, while γ_R is updated to be equal to γ_1. The second unload / reload rule is:

> *Rule 2: When an unloading cycle initiates from a point that is not on the monotonic backbone curve,* γ_L *is updated to be the strain value at the start of the unloading cycle, and the previous value of* γ_L *becomes the current value of* γ_R.

Loading then progresses to a new unloading point at γ_3 (Figure 5-5c) which is less than γ_1. At this point, $\gamma_L = \gamma_3$, and $\gamma_R = \gamma_2$ in accordance with Rule 2. Unloading then occurs to

a new reloading point at γ_4 (Figure 5-5d) where $\gamma_L = \gamma_4$ and $\gamma_R = \gamma_3$ in accordance with Rule 2. A reload cycle then loads beyond γ_3 (Figure 5-5e) which brings us to the final unload / reload rule:

> *Rule 3: When a reloading cycle exceeds γ_R, the current values of γ_L and γ_R are erased as internal variables, and the previous values of γ_L and γ_R are reinstated.*

Rule 3 requires that all previous values of γ_L and γ_R must be stored in computer memory as internal variables until they are erased by a cycle that exceeds γ_R. In Figure 5-5e, the loading cycle continues back to the monotonic backbone curve at γ_1, at which point $\gamma_L = \gamma_1$ and $\gamma_R = -\gamma_1$ in accordance with Rule 1, and all previous values of γ_L and γ_R are erased from computer memory.

Upon unloading and reloading, these rules can produce stresses lower than the backbone curve as illustrated in Figure 5-5e. This departs from Masing rules, and is driven by the damping requirement.

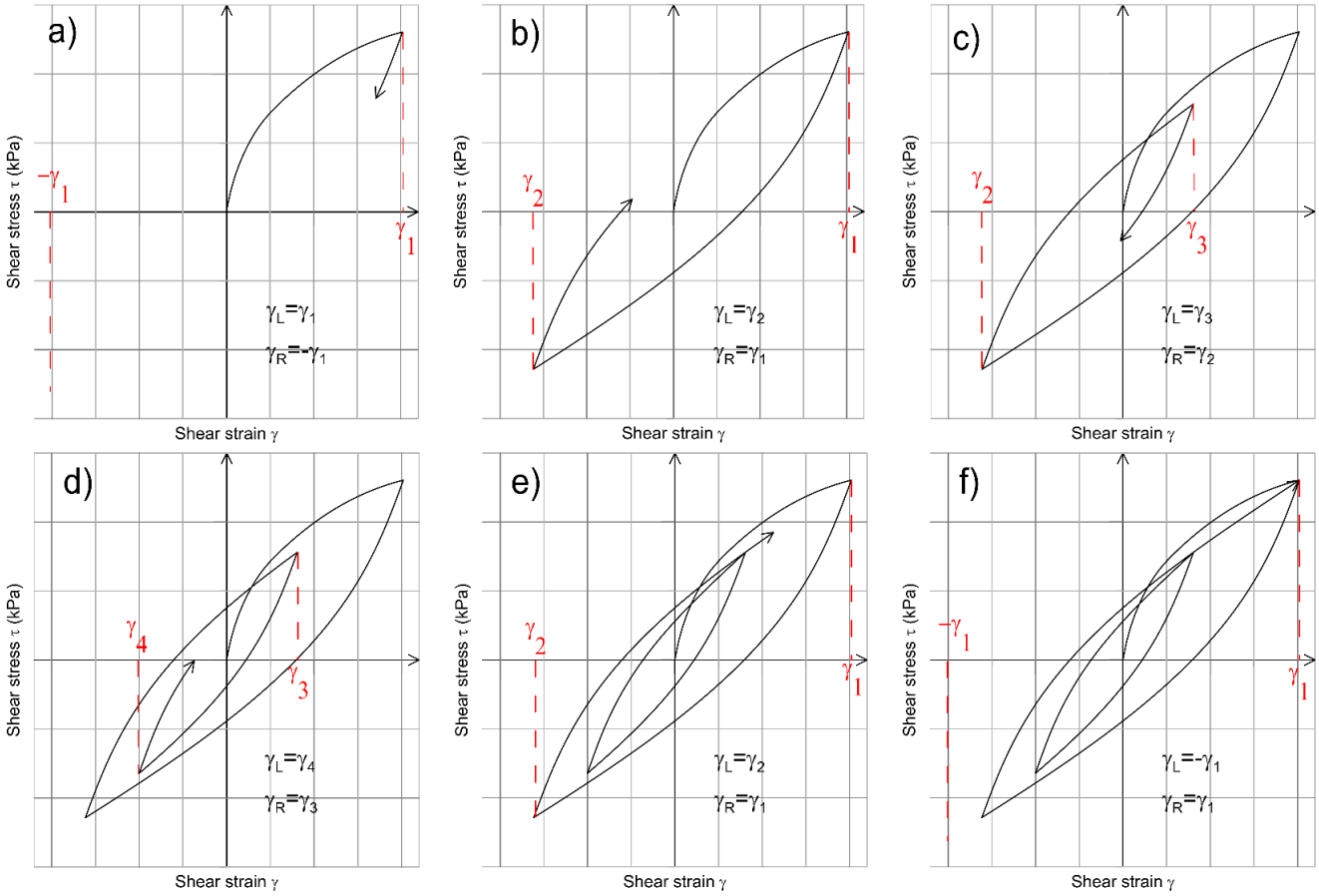

Figure 5-5 Evolution of the reversal strain vectors

5.5 Example Problems

An example problem is utilized to illustrate the following features of the model: (1) small-strain damping is explicitly modeled in the hysteretic formulation, (2) desired modulus reduction and damping curves can be perfectly matched, which differs from other commonly-used models, and (3) the solution does not depend on the size of strain increments utilized in a simulation. The target damping and modulus reduction curves for the example problem are calculated from Darendeli (2001) for a soft clay with the following characteristics: *PI=40, σ'_v=47.5 kPa, γ=15 kN/m^3, V_s=80 m/s, OCR=1.15, and K_0=0.5*. The procedure presented by Yee et al. (2013) was applied to the computed modulus

reduction curve to match a target undrained strength S_u = 17kPa and the transition strain was picked as γ_t = 0.03%. The target modulus reduction and damping curves are presented in Figure 5-6. The modulus reduction curve is adjusted at high-strain to match a desired shear strength using the Yee et al. procedure, but the damping curve was simply extrapolated from Darendeli's functional form due to absence of recommendations for high-strain damping.

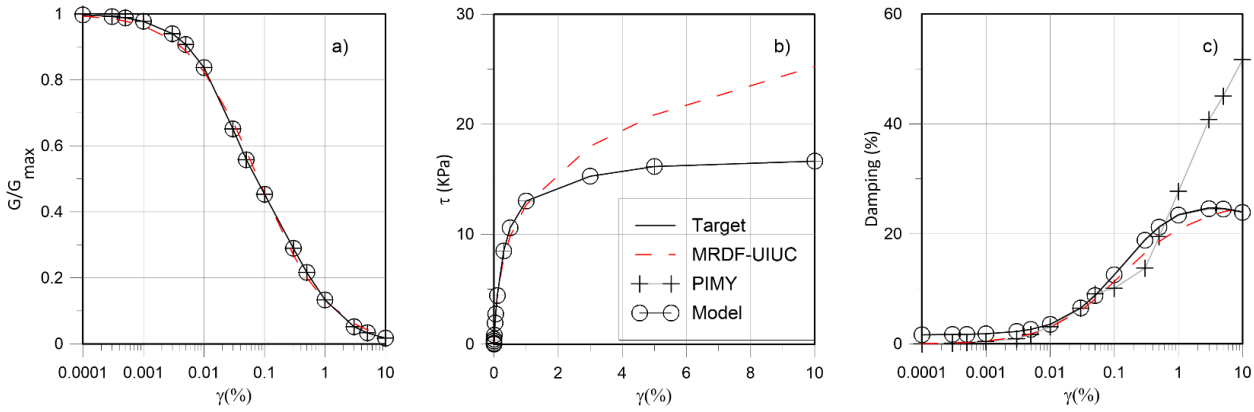

Figure 5-6. Modulus reduction (a), hysteretic damping ratio (b) and backbone (c) curves predictions of different models for a clay PI=40, σ'_v=47.5 kPa, γ=15 kN, V_s=80 m/s, OCR=1.15 K_0=0.5.

5.5.1 Comparison with Existing Models

Figure 5-6 compares the proposed model with two commonly used models: MRDF UIUC used in Deepsoil 5.1 (Phillips and Hashash 2009), and the PressureIndependMultiYield (PIMY) model in OpenSees (Elgamal et al., 2003). Response curves from the different models were back-calculated from the results of numerical simulations of a single element subjected to sinusoidal loading at different strain amplitudes, and comparisons with the desired modulus reduction and damping curves are presented in Figure 5-6. The proposed model and the PIMY both perfectly fit the target modulus reduction curve, while

the MRDF UIUC model results in a very slight misfit. The misfit appears very small when plotted as modulus reduction versus logarithm of shear strain, but is more significant when plotted as a stress-strain curve.

Figure 5-6c compares the hysteretic damping curves obtained with the different models. The proposed model explicitly includes small-strain hysteretic damping, whereas both the PIMY and MRDF UIUC models do not include small-strain hysteretic damping, relying instead on other formulations such as Rayleigh damping. OpenSees uses a two-point approach to Rayleigh damping (i.e., damping is specified at two frequencies, under-damping occurs between these frequencies, and over-damping occurs outside these frequencies). Frequency-dependent Rayleigh damping is not realistic, and care must be taken to ensure significant errors do not arise from this formulation. Deepsoil implements a frequency-independent Rayleigh damping formulation developed by Phillips and Hashash (2009) which solves this problem, but is computationally demanding.

At large strains the PIMY model over predicts damping, which is a well-known aspect of Masing's rules (Kwok et al. 2007). Deepsoil uses damping reduction factors at large strains, based on the formulation by Darendeli (2001). This results in a reasonable, but imperfect match of the damping curve. The proposed coordinate transformation model perfectly matches the damping curve at all strain levels, eliminating the need for Rayleigh damping, and avoiding over-damping at high strain. An outcome of including small-strain damping in the hysteretic formulation of the proposed model is that the initial unload-reload tangent modulus must be larger than the secant shear modulus to accommodate non-zero area inside the stress-strain loop. This behavior is consistent with experimental observations (e.g., Doroudian and Vucetic 1995).

5.5.2 Influence of Strain Increment

Many plasticity models utilize an explicit integration scheme that requires very small strain increments to achieve numerical stability, or an implicit integration scheme in which iterations are performed at each time step to ensure numerical stability. Both solutions are sensitive to the size of the strain increments in that different solutions will arise from different strain increment sizes because the tangent modulus for the increment is evaluated either the beginning (explicit) or end (implicit) of the increment. The algorithm presented herein is formulated differently in that the stress is computed as the physically meaningful root of Equation 15 rather than by assuming a constant tangent modulus for a particular increment. The solution therefore does not depend on strain increment size, provided that the peak strain values are captured in the discretization (for accurate representation of the γ_L and γ_R internal variables). Figure 5-7 presents the prediction of the model for a sample of clay subject to sinusoidal loading at different strain levels. Figure 5-7 shows that predictions for a cycle defined by 4 or 40 points lie exactly on the curves described by 400 points at every strain level. Thus the response of the model is independent of the amplitude of the strain increment. Figure 5-7a presents a cycle at very low amplitude, at which current models rely on frequency dependent damping to introduce damping. The present formulation is entirely hysteretic, and avoid the need for Rayleigh damping. However, viscous effects are not taken into account and therefore the tip of the loops is always sharp which is not realistic for clay and peat under sinusoidal loading (Vucetic 1990).

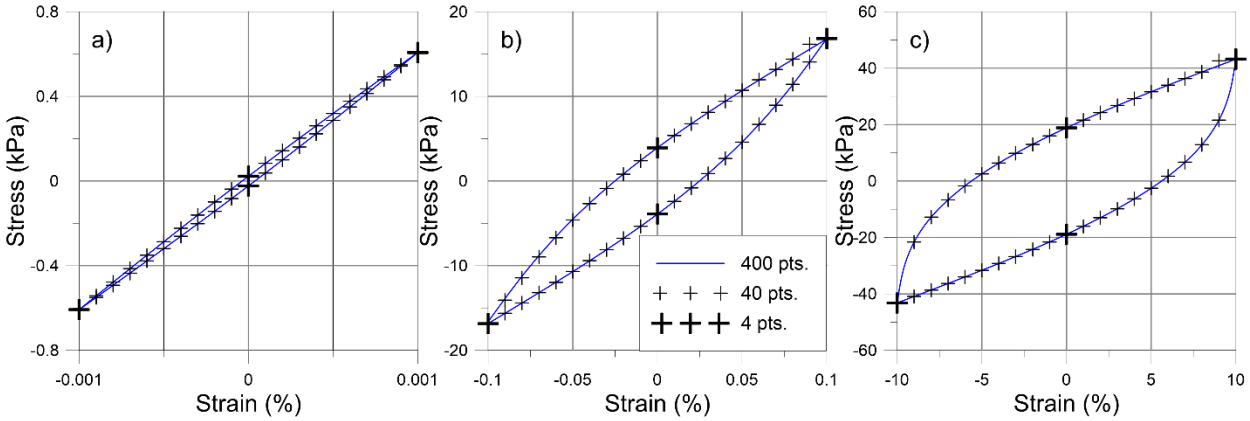

Figure 5-7 Comparison of the predictions of the model for cycles defined by 4, 40 and 400 points at strain level of (a) 0.001%, (b) 0.1%, (c) 10%.

5.6 Consistent Tangent during Unloading/Reloading

Although the Ridder's method is a robust method, which converges independently of the size of the strain increment, the method is computationally demanding and can be slow if the number of increments is large. Deriving a consistent tangent allows the model to be implemented in an explicit or implicit numerical scheme, without requiring the use of Ridder's method. The derivation of the consistent tangent is detailed in appendix A, and yields:

$$\frac{d\tau}{d\gamma} = \frac{\sin\theta + 4a\cos\theta\,[(\gamma-\gamma_0)\cos\theta + (\tau-\tau_0)\sin\theta]^3 + 2b\cos\theta\,[(\gamma-\gamma_0)\cos\theta + (\tau-\tau_0)\sin\theta]}{\cos\theta - 4a\sin\theta\,[(\gamma-\gamma_0)\cos\theta + (\tau-\tau_0)\sin\theta]^3 - 2b\sin\theta\,[(\gamma-\gamma_0)\cos\theta + (\tau-\tau_0)\sin\theta]}$$

Equation 5-18

Figure 5-8 compares the results of simulations using Ridder's method and an explicit integration scheme using the consistent tangent upon unloading/reloading. At every time step the explicit integration calculates the consistent tangent based on the previous stress

and strain values. The consistent tangent is then used in conjunction with the strain increment to calculate the stress increment. The performance of the integration schemes is studied through a convergence study where a single element of clay is subjected to 1.25 cycles of 1% strain amplitude. Modulus reduction and damping curves of the clay (Figure 5-9) are calculated based on Darendeli's equation (Darendeli 2001) for the properties listed in Table 5-1. The maximum shear modulus was calculated based on the assumption of a shear wave velocity of 120 m/s and a density of 1.5 g/cm^3. To study the performance of the explicit integration scheme, three different simulations are performed, where the loading is described with 100, 1000, and 10000 increments. Except when the loading is described by 100 increments, the explicit scheme is equivalent to the Ridder's method which corresponds to the exact solution.

Table 5-1 Soil properties for the example

Plasticity Index (PI)	200
Overconsolidation Ratio (OCR)	1
Confining Pressure (σ_v')	101.325 kPa
Maximum Shear Modulus (G_{max})	21600 kPa

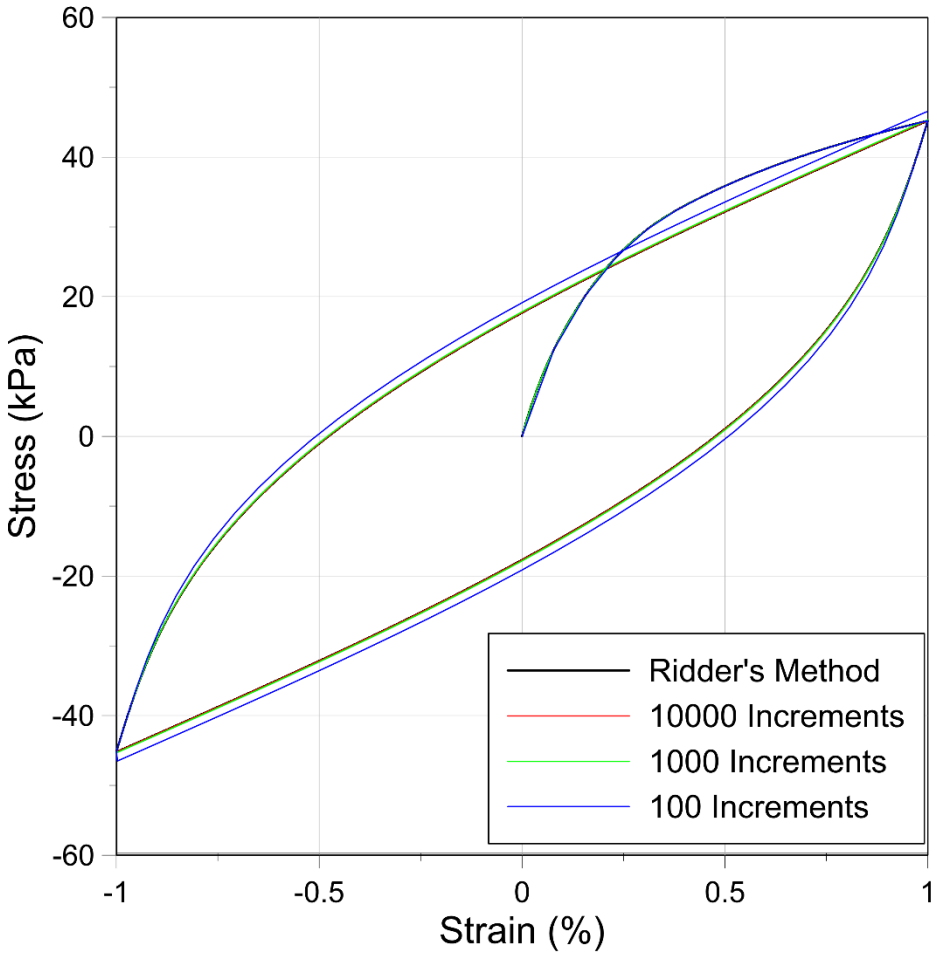

Figure 5-8 Convergence study: comparison between Ridder's method and the explicit method

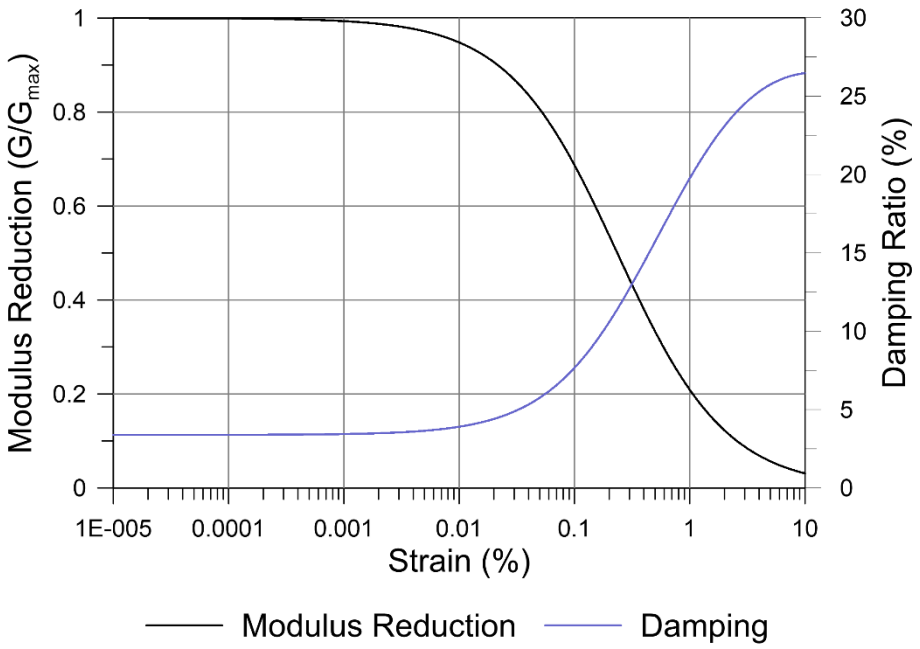

Figure 5-9 Modulus reduction and damping curves for the example

5.7 Comparison with Simple Shear Laboratory Tests

The University of California, Los Angeles (UCLA) bi-directional broadband direct simple shear device (Duku et al. 2007) was used to apply strain-controlled shear demands on Silica No. 2 dry sand and nearly saturated Sherman Island peat specimens with height and diameter of 25.4 and 72.6 mm respectively. The strain histories were deliberately irregular, involving local unloading and reloading cycles of small amplitudes. The results of the tests are compared with the predictions of our model, MRDF-UIUC in Deepsoil and the PressureIndependMultiYield (PIMY) Model in OpenSees.

5.7.1 Direct Simple Shear Tests

Silica No. 2 is a uniform sand with a median particle size D_{50}=*1.60 mm*, a coefficient of uniformity C_u=*1.29* (Duku et al 2008) and maximum and minimum dry densities of 1.61 and 1.35 gr/cm^3, respectively. The dry pluviated specimen of Silica No.2 was prepared at

a relative density of 42%, and then consolidated to a vertical pressure of 100kPa. The vertical pressure was kept constant during shear to simulate drained condition. The loading path consisted of strain-controlled triangular functions in which three cycles of constant strain amplitude of 0.03% were followed by three cycles at 0.08%, and so on for 0.44% and 0.9%. An irregular loading path was then applied in which small unloading and reloading cycles were superposed on the 0.9% amplitude triangular function.

A peat specimen retrieved from a depth of 1.7 m from Sherman Island in the Sacramento-San Joaquin Delta, California was tested under undrained conditions using a similar irregular triangular loading path, but with shear strain amplitudes of 1.3%, 6.8%, and 13.6%. Details of the peat properties are provided by Shafiee (2015). The specimen was consolidated to σ_{vc}' = 60.4 kPa, and then unloaded to 31.3kPa to achieve an overconsolidation ratio (OCR) of 1.93. The organic content of the sample was 75%. The vertical stress was varied during shearing to maintain constant specimen height using a servohydraulic actuator and feedback control loop. Constant height testing achieves undrained loading conditions.

5.7.2 Model Input Parameters

The input modulus reduction curves were derived using the cyclic testing on the simple shear device supplemented by inferred shear modulus at strains lower than the device capabilities. The maximum shear modulus was calculated by dividing the shear modulus measured at the lowest strain level, by the G/G_{max} ratio calculated from the empirical relationship at the same strain level, to ensure the curves are continuous. The inferred maximum shear modulus for sand and peat was 23504 kPa and 877 kPa, respectively,

which correspond to shear wave velocities of 128 m/s and 28 m/s. The inferred modulus values were then calculated by multiplying the normalized modulus reduction (G/G_{max}) calculated from Menq (2003) and Kishida et al. (2009), for sand and peat respectively, by the maximum shear modulus. The modulus reduction curves obtained and the associated hyperbolic fits are plotted in Figure 5-10.

The damping curves were derived by fitting cubic splines to the lab data and inferred points. For sand, the inferred points were calculated from Menq (2003). For peat, the inferred values were calculated from Kishida et al. (2009), adjusted to match the damping measured in the lab (1.9%) at the lowest strain level (1.3%) (Figure 5-10).

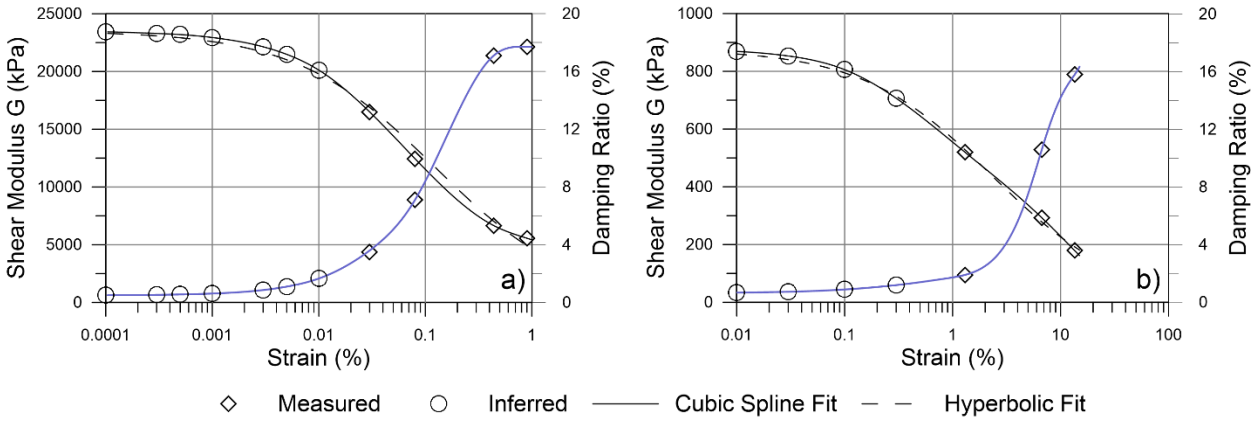

Figure 5-10 Input modulus reduction and damping curves a) test on sand b) test on peat

5.7.3 Simulations of Direct Simple Shear Tests

Figure 9 and 10 present the stress-strain loops measured in the lab and predicted by the present model (Figure 5-11a and Figure 5-12a), Deepsoil (Figure 5-11b and Figure 5-12b), and OpenSees (Figure 5-11c and Figure 5-12c), for the tests on sand and peat respectively. During shearing the sand sample exhibits hardening, and the secant shear modulus increases with the number of cycles. This behavior of dry cohesionless soils has

been reported previously by Silver and Seed (1971), and is related to densification of the sand during cyclic loading. Our model does not predict hardening because it utilizes a single modulus reduction curve (and hence monotonic backbone curve), but the qualitative nature of the loops are in close agreement with the test results. For both tests, the areas of the predicted stress strain loops agree with the damping curve, and plot very close to the test results. Furthermore, when a small unload-reload cycle moves back on to the monotonic backbone curve, a sharp change in slope is observed in both the test data and the model predictions.

The MRDF-UIUC model in Deepsoil under-predicts the stresses during initial loading for the test on sand (Figure 5-11b) but slightly over-predict the stresses for the test on peat. It also slightly under-predicts damping for both tests, which is expected since small strain damping is not captured in the hysteretic formulation in Deepsoil, and would be included using Rayleigh damping. The PIMY in Opensees follows the backbone curve, and is able to capture the initial loading of the soil properly for both the peat and sand (Figure 5-11c and Figure 5-12c). However, the PIMY model under-damps the sand response and over-damps the peat response at high strain. Furthermore, the stress-strain behavior exhibits piecewise linear behavior due to the nature of the nested yield surfaces, whereas the laboratory data exhibits a smooth stress-strain curve.

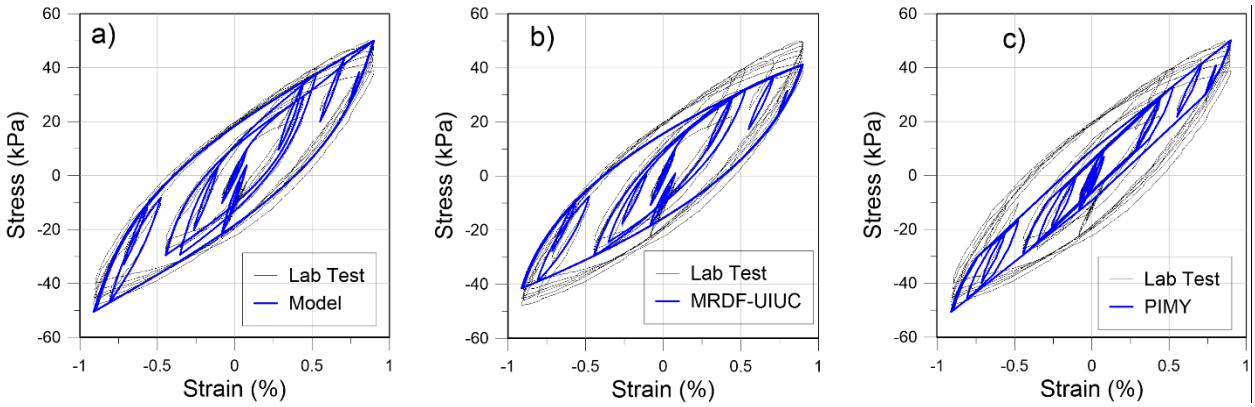

Figure 5-11 Stress-strain loops measured in simple shear test on Silica No. 2 dry sand and predicted by: a) proposed model, b) Deepsoil, c) OpenSees

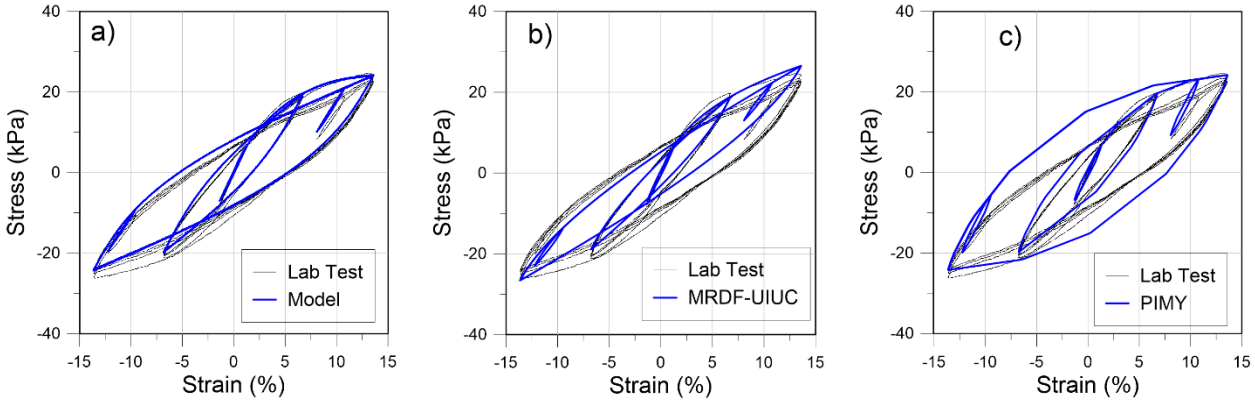

Figure 5-12 Stress-strain loops measured in simple shear test on Sherman Island peat and predicted by: a) our model, b) MRDF-UIUC in Deepsoil, c) PIMY in OpenSees

5.8 Conclusions

In this chapter I presented a one dimensional nonlinear model for site response analysis that departs from two concepts commonly used by site response models. Initial loading is not controlled by the widely used hyperbolic model, but instead uses a cubic spline fit of the backbone curve to match any modulus reduction curve. The hysteretic behavior of the soil is not controlled by the original or the extended Masing's rules, but is controlled by a new unloading and reloading rule that uses a coordinate transformation approach to

calculate the shear stress, regardless of the amplitude of the strain increment. This unloading reloading rule easily controls the damping in the transformed coordinate system and provides a perfect fit of any damping curve.

The model captures small-strain hysteretic damping, thereby eliminating the need for Rayleigh damping, and it does not over-damp at high strain, which is a well-known problem associated with Masing's rules. The model is well suited for total stress 1D site response analysis, though implementation in a site response code is beyond the scope of this paper and is reserved for future publications.

The model could be adapted for effective stress 1D ground response analysis by using the concept presented in chapter 4 and a pore pressure generation model such as Matasovic and Vucetic (1995). The initial loading would then be a function of pore pressure by using a modulus reduction curve that depends on the stress ratio. Upon unloading and reloading, the reversal stress ratios would be stored, and the target and previous reversal shear stress would be defined as the target and previous reversal stress ratios multiplied by the current effective stress.

The one-dimensional kinematic hardening framework developed herein is implemented in chapter 6 in a multi-dimensional plasticity formulation which can be used for more advanced numerical simulations. This formulation tracks reversal stress ratios as explained in the previous paragraph. Such formulation could potentially capture the cyclic stiffening behavior exhibited by the sand as it densified during shearing, and the cyclic degradation behavior exhibited by the peat in constant volume shearing.

6 FORMULATION OF A NONLINEAR CONSTITUTIVE MODEL FOR DYNAMIC SIMULATIONS

This chapter presents a multidimensional generalization of the nonlinear constitutive model presented in the previous section. The equations are presented in *q-p'* space for implementation in a 2D finite differences program (FLAC), where *q* is the second deviatoric stress invariant ($q=\sqrt{\frac{1}{2}((\sigma_1-\sigma_2)^2+(\sigma_2-\sigma_3)^2+(\sigma_1-\sigma_3)^2)}$) and *p'* is the mean effective stress ($p'=(\sigma_1'+\sigma_3'+\sigma_3')/3$). The model is formulated in terms of stress ratios ($\eta = \frac{q}{p'}$) and is presented here using relationships appropriate for peat, but can in principle be extended to model any soil type with only modest modification. The principles and input parameters are presented first. The rest of the chapter presents the equations governing initial loading, the volumetric response, and the inclusion of the unloading-reloading rule presented in chapter 5 in a multi-dimensional framework.

6.1 Motivations

In a 1D ground response analysis problem, the dynamic behavior of the soil profile is most often characterized by a set of modulus reduction and damping (MRD) curves. The analyses are performed using equivalent linear (EL) procedures, in which the shear modulus and damping are taken as time-invariant values set to be consistent with mobilized shear strains, or nonlinear (NL) procedures, in which a plasticity model is utilized to match desired modulus reduction and damping behavior. The current plasticity models are unable to perfectly match a set of target modulus reduction and damping curves, often leading to a mismatch of the desired soil behavior, especially at large

strains. The limitations of the existing plasticity models for 1D ground response analysis problem have been extensively discussed in the previous chapter.

Similarly, 2D site response analysis can be performed using the equivalent-linear method (for example using the software Quad4M (Hudson et al. 1994)) or the nonlinear method with a constitutive model. However, only a small number of constitutive models incorporate the modulus reduction and damping curve concept in their formulation. The pressure independent and pressure dependent multi-yield models (Elgamal et al. 2003, Yang et al. 2003) offer the capability to use a modulus reduction (MR) curve as an input parameter to define the backbone curve. A set of nested yield surfaces provides a piece-wise linear backbone curve that is set to match that implied by the modulus reduction curve. The input modulus reduction curve is not modified as a function of confining pressure, though the small-strain shear modulus does depend on effective stress in this model. The model also offers an alternative formulation in which the shear strength is specified, and the plastic modulus of the yield surfaces is set to match a hyperbolic shape that is consistent with the maximum shear modulus and the input shear strength. The hyperbola does not permit matching small-strain modulus-reduction behavior. The PM4Sand model (Boulanger and Ziotopoulou 2015) was configured to match modulus reduction curves from the Electric Power Research Institute (EPRI 1993), but does not permit users to input a desired curve. Furthermore, matching the EPRI curve required a complex and difficult calibration of the modeling constants.

In addition to modulus reduction behavior, configuring the unload-reload behavior to match a target damping curve is rather difficult. The nested yield surface formulation by Elgamal et al. (2003) produces unloading and reloading curves with the same shape as

the backbone curve enlarged by a factor of 2, which is equivalent to the Masing Rules (Masing 1926). The Masing rules typically overpredict damping at strains larger than 0.01% (Phillips and Hashash 2009).The overprediction of damping increases with strain amplitude and is a recurring problem with constitutive models, and is observed for example in the UBC sand (Beaty and Byrne 2011) and the bubble model (Al Tabbaa and Muir Wood 1989). The PM4Sand model does not utilize Masing's rules, and the unload-reload behavior was carefully configured to provide a good match to the EPRI damping curve. Most models use a finite elastic region within which hysteretic damping is zero, therefore small strain damping relies on an alternative damping formulation such as Rayleigh damping (Rayleigh and Lindsay 1945).

Therefore, a model having a damping curve as input parameter would be beneficial. Such a model should be able to capture the behavior of the soil at small and large strain, and be able to capture a desired shear strength. A model formulated in accordance with the principals of critical state soil mechanics is able to capture the salient features of the soil behavior, such as the strength, the dilative or contractive behavior of the soil under deviatoric loading, and the consolidation behavior. The present models aims to answer this need, and uses the concept of modulus reduction and damping curves as functions of stress ratio, as developed in chapter 4, to integrate the dynamic curves, and their dependence on effective stress in a plasticity model. This model does not intend to capture any viscous effect, and is therefore unable to model secondary compression. Future iterations of the model may incorporate viscous effects.

6.2 Principles and Input Parameters

The constitutive model presented here extends the unload-reload rule presented in Chapter 5 to a multi-dimensional plasticity stress-ratio-based model that is implemented in FLAC. The model includes the following features, which are illustrated in Fig. 6-1:

1. A stress ratio region, M_{SS}, within which the shape of the backbone curve is controlled by the input modulus reduction curve, and beyond which the backbone curve is controlled by a bounding surface plasticity formulation. The transition between these two regions is set based on the range of experimental validation of the modulus reduction curve, and in general will correspond to mobilized shear strains near 0.3% for typical MR curves. The transition region grows when loading exceeds the previous value of M_{SS} such that the current stress ratio may never exceed M_{SS}, which means that the unload-reload rules from Chapter 5 are utilized for all unloading cases.
2. A set of unloading-reloading rules based on the formulation described in Chapter 5 that controls the damping behavior of the model based on the input damping curve. That formulation is modified to be compatible with a stress ratio formulation, and integrated into a multidimensional framework. The model is also adapted from shear strain/stress relationships to deviatoric strain/stress relationships.
3. A critical state implementation of bounding and dilatancy surfaces following the formulation of Manzari and Dafalias (2004). The bounding surface and dilatancy stress ratios, M_b and M_d, respectively, become equal to the critical state stress ratio, M, when the state parameter is equal to zero. This results in mobilization of

a critical state condition in which plastic deviatoric strains produce zero plastic volumetric strain (i.e., dilatancy is zero).

4. A stress ratio region, M_{pp}, within which zero plastic volumetric strains occur, even when plastic deviatoric strains occur. This is consistent with observations by Vucetic (1994) that the threshold shear strain required to mobilize excess pore pressure is higher than the threshold shear strain for nonlinear stress-strain behavior. The value of M_{pp} can be set such that the correct threshold shear strain is achieved.
5. A volumetric cap intended to provide plastic volumetric strains upon constant stress-ratio loading. The cap is selected as the surface defined by Kutter and Sathialingam (1992) that is an adaptation of the modified Cam Clay model.

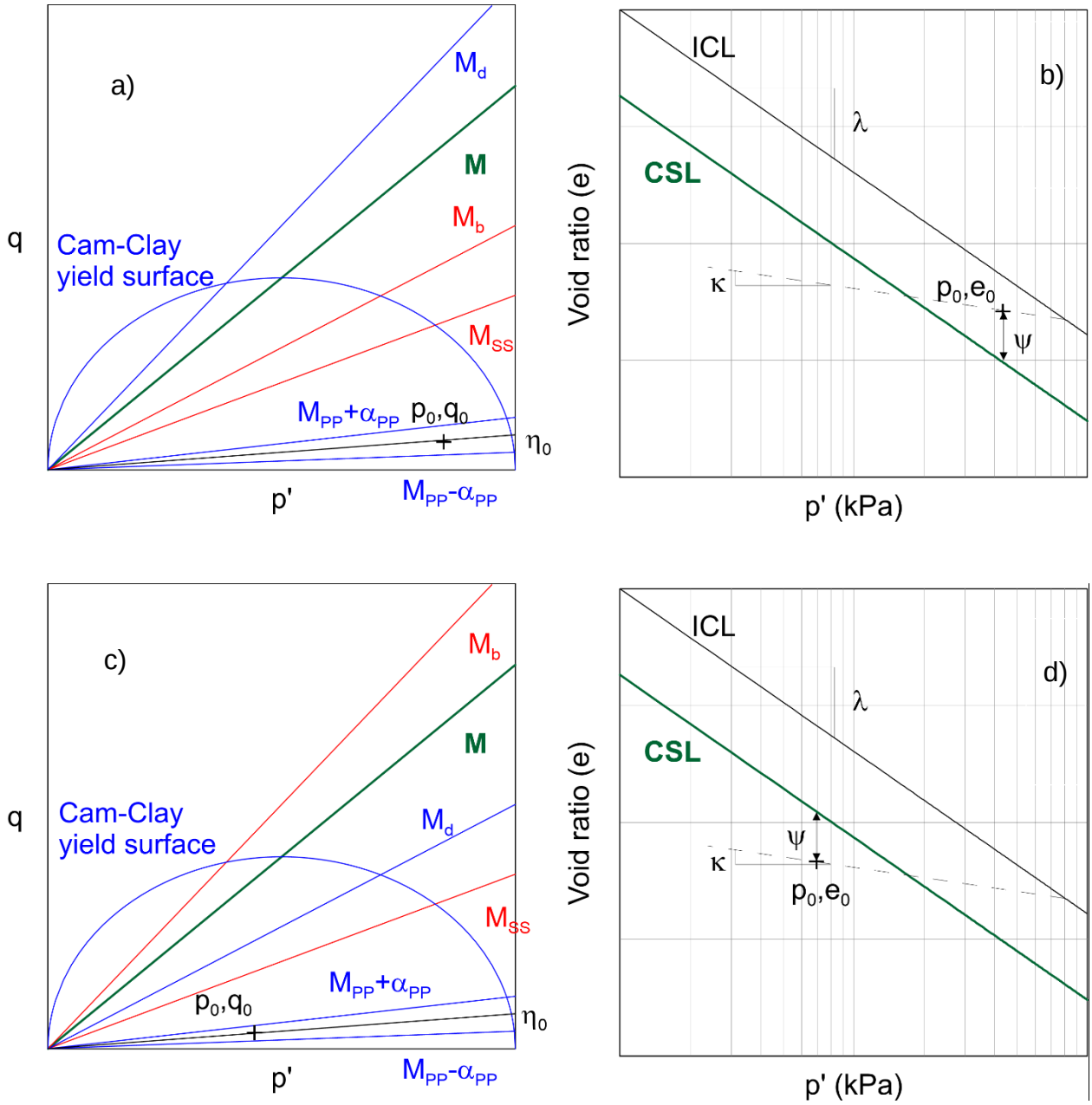

Figure 6-1Illustration of the model's surfaces for the lightly overconsolidated case (a and b) and a heavily overconsolidated sample (c and d)

The model uses 17 input parameters presented here. Their selection is described in chapter 7. The input parameters are:

- *M*, the slope of the critical state line in *p'-q* space
- κ, the slope of the recompression line

- λ, the slope of the virgin compression line
- e_1 and p_1 which specify a point on the isotropically normally consolidated line (ICL) in the void ratio vs. mean effective stress space (e-p').
- R which defines the position of the critical state line (CSL) with respect to the ICL, and controls the shape of the plastic volumetric surface.
- D_{min}, the small strain damping
- G/G_{max} vs. η curve, modulus reduction vs. stress ratio curve, as explained in chapter 4.
- D-D_{min} vs. η curve, damping ratio vs. stress ratio curve, as explained in chapter 4
- A_0, variable defining the amplitude of the pore pressure response
- n_d, variable defining the dilation surface
- n_b, variable defining the bounding (peak) surface
- γ_{SS}, the strain at which the model transitions from small strain to large strain response.
- γ_{PP}, the strain at which pore pressure is generated.
- n, m and A, that defines the maximum shear modulus depending on the confining pressure and the overconsolidation ratio.

6.3 Elastic Response

The elastic volumetric and deviatoric strain increments are defined in Equation 6-1 and Equation 6-2, where K is bulk modulus and G_{max} is the elastic shear modulus:

$$\dot{\varepsilon}_v^e = \frac{\dot{p}'}{K} \qquad \textit{Equation 6-1}$$

$$\dot{\varepsilon}_q^e = \frac{\dot{q}}{3G_{max}}$$ *Equation 6-2*

The stress increments are calculated based on total and plastic strain increments:

$$\dot{p} = K(\dot{\varepsilon}_v - \dot{\varepsilon}_v^p)$$ *Equation 6-3*

$$\dot{q} = 3G_{max}(\dot{\varepsilon}_q - \dot{\varepsilon}_q^p)$$ *Equation 6-4*

The bulk modulus *K* is defined as a function of the mean effective stress *p'*:

$$K = \frac{p'\upsilon_0}{\kappa}$$ *Equation 6-5*

where ν_0 is the initial specific volume. The elastic shear modulus G_{max} is defined by the following equation:

$$\frac{G_{max}}{p_a} = \mathrm{A} \cdot OCR^m \left(\frac{p'}{p_{at}}\right)^{\mathrm{n}}$$ *Equation 6-6*

Note that the elastic shear modulus G_{max} is typically called *G*. In order to avoid confusion between the secant shear modulus from modulus reduction curve (G/G_{max}) and the elastic shear modulus, G_{max} is used.

6.4 Backbone Curve at Small Strains (i.e. $\gamma < \gamma_{ss}$)

During initial loading at small strains, the backbone curve is defined from the input modulus reduction curve and G_{max}. The value of G/G_{max} is found by linear interpolation at the value $\eta - \eta_0$. The new deviatoric stress is calculated directly from the following equation:

$$q = \frac{G}{G_{max}} \cdot 3 \cdot G_{max} \cdot \varepsilon_q + \eta_0 \cdot p'$$ *Equation 6-7*

From the new deviatoric stress, the plastic volumetric strain can be calculated based on the stress increment:

$$\dot{\varepsilon}_q^p = \dot{\varepsilon}_q - \frac{\dot{q}}{3 \cdot G_{max}}$$ *Equation 6-8*

6.5 Unloading/Reloading Rule

Upon Unloading/Reloading, the model uses a modification of the unloading/reloading rules presented in chapter 5 to account for multidimensional loading, and pore pressure generation. The model presented in chapter 5 uses a coordinate transformation to match an input modulus reduction and damping curves formulated in terms of shear strain. In the 1D model the changes in loading direction are tracked, and the stress/strain points at which they happen are stored. In the present chapter, the coordinate transformation is utilized to match input modulus reduction and damping curves vs. stress ratios. The unload/reload rules are formulated in terms of deviatoric strain/stress rather than shear strain/stress like in the 1D model and the changes in loading direction are tracked by storing stress ratio/strain points at which the change in direction happens. The unload/reload rules are used as long as the maximum target reversal point is not reached

6.5.1 From Shear to Deviatoric Stress/Strain

The 1D model in chapter 5 is formulated in terms of shear stress (τ) and shear strain (γ) because it makes sense in a 1D framework since pure shear is the only mode of

deformation considered. In 2 and 3D, deviatoric stress invariant (*q*) and deviatoric strain (ε_q), calculated from the full deviatoric stress and strain tensors respectively (Equations 2-7 and 2-9), are used to account for more complicated stress paths. Based on the case of a simple shear stress path, the following relationships are derived to create an equivalence between the formulation of the 1D model and a formulation with invariants that can be used in a multidimensional framework:

$$\tau = \frac{q \cdot signq}{\sqrt{3}} \qquad \textit{Equation 6-9}$$

$$\gamma = \sqrt{3} \cdot \varepsilon_q \cdot sign\varepsilon_q \qquad \textit{Equation 6-10}$$

Stress and strain invariants ε_q and *q* are always positive by definition (following equations 2-7 and 2-9), by contrast with τ and γ, which may change sign. Tracking the loading direction in the 1-D model is as simple as tracking when either the increments of τ or γ change sign. However, increments of ε_q and *q* might change sign at points that do not correspond to a change in loading direction, as illustrated in Fig. 6-2. To remedy this problem, 3 variables are introduce to keep track of the direction of loading, *load*, and the "artificial" signs of ε_q and *q*, *sign*ε_q and *signq* respectively. All the variables are initially equal to 1. The direction of loading changes sign when both $\dot{q}$ and $\dot{\varepsilon}_q$ change sign simultaneously. When only $\dot{q}$ or $\dot{\varepsilon}_q$ changes sign, only *signq* or *sign*ε_q changes sign. Figure 6-2 shows two equivalent hysteretic loops for ε_q and *q,* and τ and γ. On both figures, the direction of loading is changing at point A because $\dot{q}$ and $\dot{\varepsilon}_q$ change signs at the same time. At point B, the loop crosses the γ axis, and τ becomes negative. At this point $\dot{q}$ changes sign and *signq* becomes -1, even though *q* is still positive. At point C, the loop

crosses the τ axis and γ now becomes negative. Since only $\dot{\varepsilon}_q$ changes sign, *sign*ε_q becomes -1, and *signq* does not change.

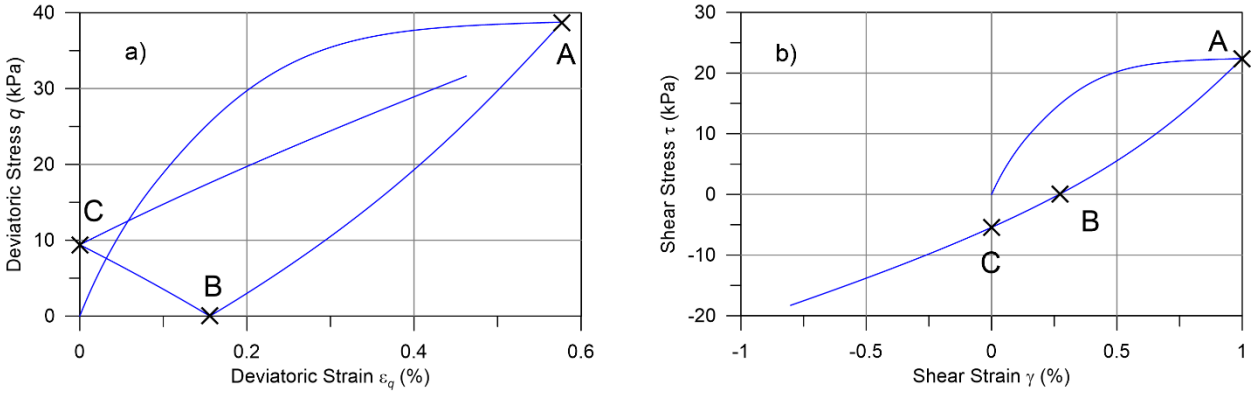

Figure 6-2 Hysteretic loops in terms of a) deviatoric stress/strain b) shear stress/strain

6.5.2 From Shear Stress to Stress Ratios

The 1D model keeps track of the reversal points at which unloading happens, and defines rules to select the target (γ_R and τ_R) and previous (γ_L and τ_L) stress/strain points. In the multidimensional model, the reversal points are tracked in terms of stress ratio vs strain points. The equations are formulated in terms of deviatoric stress and strain, but remain essentially the same. The deviatoric stresses are calculated from the previous and target stress ratios (η_L and η_R) multiplied by mean effective stress (p'). The selection of ε_{qL}, ε_{qR}, η_L and η_R is based on four rules similar to the 1D case.

When unloading begins ε_{qL} and η_L are the strain and stress ratios at which the current reverse loading cycle begins. ε_{qL} and η_L have the signs of *sign*ε_q and *signq* respectively. When unloading starts right after initial loading, the size of the unloading loop is not known at the onset of unloading. The same assumption as the 1D model is made, which is that

$\varepsilon_{qR} = -\varepsilon_{qL}$. For stress ratios however, the initial stress ratio has an influence, and the target stress ratio is $\eta_R = -\eta_L + 2\eta_0$. Therefore the first rule is:

> *Rule 1: When an unloading cycle initiates from the monotonic backbone curve,* $\varepsilon_{qR} = -\varepsilon_{qL}$ *and* $\eta_R = -\eta_L + 2\eta_0$.

During unloading/reloading, M_b and M_d change as a result of development of plastic volumetric strains. If unloading happens at a stress ratio equal to M_b, the absolute values of η_R and η_L can become larger than M_b upon unloading/reloading. Since this is not desirable, η_R and η_L are adjusted in order to be always equal or lower than M_b. The second rule is:

> *Rule 2: If during unloading/reloading the absolute values of* η_R *and* η_L *become larger than* M_b*, they are adjusted to be equal to* M_b.

When the reversal of loading happens during an unloading or reloading cycle, the previous point ε_{qL} becomes the target point ε_{qR}, and the point of reversal becomes the previous point. ε_{qL} and η_L have the signs of $sign\varepsilon_q$ and $signq$ respectively. The third unload / reload rule is:

> *Rule 3: When an unloading cycle initiates from a point that is not on the monotonic backbone curve,* ε_{qL} *is updated to be the strain value at the start of the unloading cycle, and the previous value of* ε_{qL} *becomes the current value of* ε_{qR}*. Previous and target stress ratios follow the same logic and the signs are conserved as well.*

In the 1D model, under cyclic loading at constant strain amplitude, the loops are all the same, there is no softening or hardening. In the model this translates into reaching τ_R when reaching γ_R. When γ_R is exceeded, the current values of γ_L and γ_R are erased as internal variables, and the previous values of γ_L and γ_R are reinstated. In the multidimensional loading, η_R is reached when ε_{qR} is reached. The fourth rule is:

> *Rule 4: When a reloading cycle exceeds ε_{qR}, the current values of η_L , η_R , ε_{qL} and ε_{qR} are erased as internal variables, and the previous values of η_L , η_R , ε_{qL} and ε_{qR} are reinstated.*

Rule 4 requires that all previous values of ε_{qL} and ε_{qR} must be stored in computer memory as internal variables until they are erased by a cycle that exceeds ε_{qR}. Upon loading at constant peak strain amplitude, the peak stress ratio does not change. However, since p' evolves with loading, the peak deviatoric stress changes as a function of p' and can exhibit softening or hardening, depending if p' decreases or increases respectively.

6.5.3 Constitutive Equations during Unloading/Reloading

To find the new stress during unloading and reloading, the model uses a coordinate transformation much like the 1D model of chapter 5, but uses deviatoric strains and deviatoric stresses calculated from the previous and target stress ratios multiplied by the mean effective stress. The center of the new coordinate system, illustrated in Figure 6-3, follows the same definition:

$$\varepsilon_{q_0} = \frac{\varepsilon_{q.R} + \varepsilon_{q.L}}{2}$$ *Equation 6-11*

$$q_0 = \frac{\eta_R \cdot p' + \eta_L \cdot p'}{2}$$ *Equation 6-12*

The rotation of the coordinate system θ, as illustrated in Figure 6-3, depends on the loading direction.

$$\theta = \tan^{-1}\frac{\eta_R \cdot p' - \eta_L \cdot p'}{\left(\varepsilon_{q.R} - \varepsilon_{q.L}\right)} \;\; if \; load = 1$$ *Equation 6-13*

$$\theta = \tan^{-1}\frac{\eta_R \cdot p' - \eta_L \cdot p'}{\left(\varepsilon_{q.R} - \varepsilon_{q.L}\right)} - \pi \;\; if \; load = -1$$ *Equation 6-14*

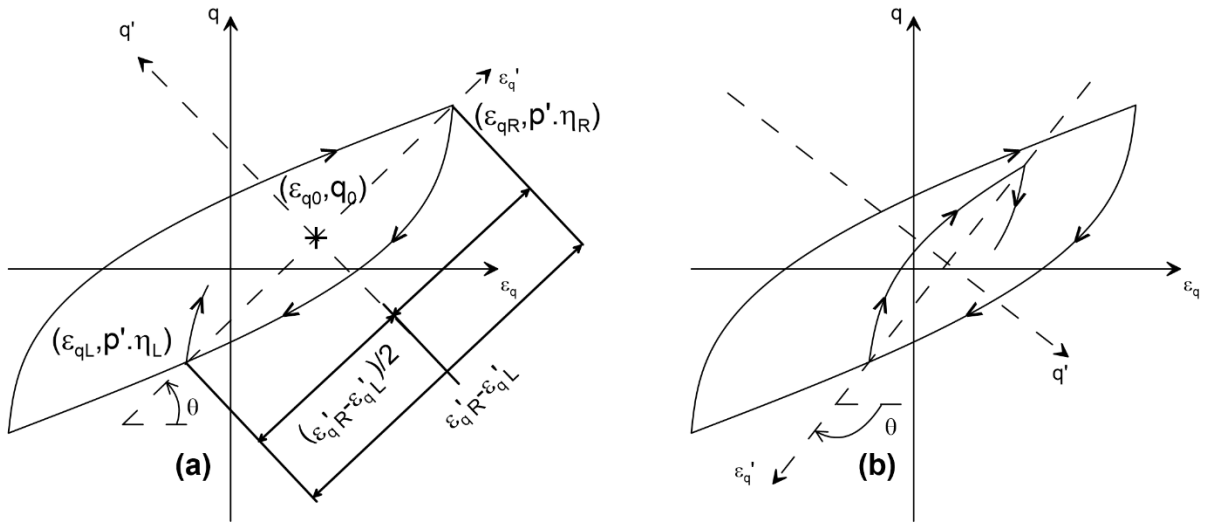

Figure 6-3 (a) Positive loading (b) negative loading

The equations to go from one coordinate system to another are similar to the 1D model:

$$\begin{pmatrix} \varepsilon_q \\ q \end{pmatrix} = \begin{pmatrix} \varepsilon_q{}' \cos\theta - q' \sin\theta + \varepsilon_{q_0} \\ \varepsilon_q{}' \sin\theta + q' \cos\theta + q_0 \end{pmatrix}$$ *Equation 6-15*

$$\begin{pmatrix} \varepsilon_q{}' \\ q' \end{pmatrix} = \begin{pmatrix} (\varepsilon_q - \varepsilon_{q_0}) \cos\theta + (q - q_0) \sin\theta \\ -(\varepsilon_q - \varepsilon_{q_0}) \sin\theta + (q - q_0) \cos\theta \end{pmatrix}$$ *Equation 6-16*

The unload-reload rule is formulated to satisfy the following criteria:

(i) When subject to uniform cyclic strain amplitude input, if the target and previous stresses do not change, the stress ratio-strain loops close and repeat, exhibiting no cyclic degradation or stiffening,

(ii) The area inside the stress-strain loops matches a user-defined damping curve, even at small strains where the modulus-reduction value is zero,

(iii) The stress-strain loops are concave about the secant modulus line.

The function describing the shape of the loop in the transformed coordinate system is the same as the 1D model:

$$q' = a\, \varepsilon_q{}'^4 + b\, \varepsilon_q{}'^2 + c$$ *Equation 6-17*

Where *a*, *b* and *c* are three constants that satisfy the three conditions. The shape of the loop in the transformed system is shown on Figure 6-4. In the figure $\varepsilon_q{}'_{in}$ is the target reversal strain in the transformed system:

$$\varepsilon_q{}'_{in} = \frac{\varepsilon_{q.R} - \varepsilon_{q_0}}{cos\theta}$$ *Equation 6-18*

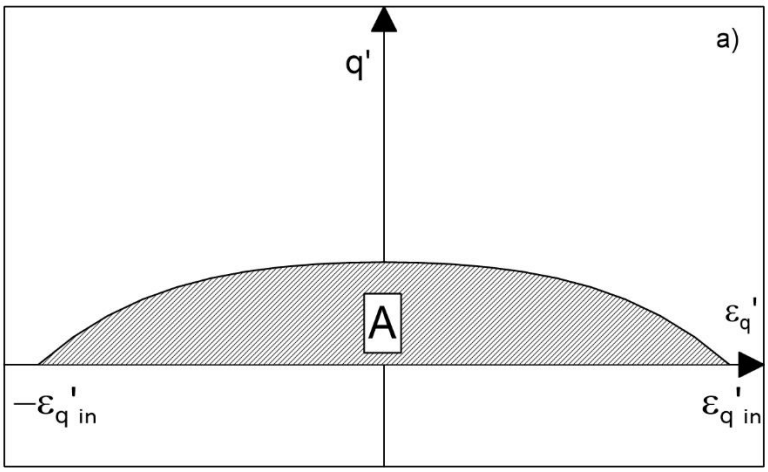

Figure 6-4 Half loop in the transformed coordinate system

The three criteria (i), (ii) and (iii) translate to the followin three equations, respectively:

$$q'(\varepsilon_q{}'_{in}) = 0 \qquad \textit{Equation 6-19}$$

$$\int_{-\varepsilon_q{}'_{in}}^{\varepsilon_q{}'_{in}} q'(\varepsilon_q{}')d\varepsilon_q{}' = \varepsilon_q{}'_{in} D\pi(\eta_R \cdot p' - q_0)cos\theta \qquad \textit{Equation 6-20}$$

$$\frac{d^2(q')}{d(\varepsilon_q{}')^2} \leq 0 \; for \; \varepsilon_q{}' \in -\varepsilon_q{}'_{in} .. \varepsilon_q{}'_{in} \qquad \textit{Equation 6-21}$$

where D is the hysteretic damping of the considered loop. In the 1D model, the cyclic strain amplitude (equation 5-5) is used to define amplitude of loading, and interpolate the hysteretic damping of the considered loop. In the multidimensional loading, the equivalent stress ratio amplitude is used:

$$\eta_{eq} = \frac{|\eta_R - \eta_L|}{2} \qquad \textit{Equation 6-22}$$

This equivalent stress ratio is used to calculate D-D_{min} from linear interpolation on the input damping curve. The damping ratio for the loop is then simply calculated by adding D_{min}.

The constants a, b and c, are found by solving the previous system of equations (Equation 6-19, Equation 6-20 and Equation 6-21):

$$a = \frac{5\pi D cos\theta (p' \cdot \eta_R - q_0)}{32{\varepsilon_q}'_{in}{}^4} \qquad \textit{Equation 6-23}$$

$$b = \frac{-15\pi D cos\theta (p' \cdot \eta_R - q_0)}{16{\varepsilon_q}'_{in}{}^2} \qquad \textit{Equation 6-24}$$

$$c = \frac{25\pi D cos\theta (p' \cdot \eta_R - q_0)}{32} \qquad \textit{Equation 6-25}$$

The new stress is found by solving the following equation:

$$\begin{aligned} q = &\left[\left(\varepsilon_q - \varepsilon_{q_0}\right)\cos\theta + (q - q_0)\sin\theta\right]\sin\theta \\ &+ \left[a\left((\varepsilon_q - \varepsilon_{q_0})\cos\theta + (q - q_0)\sin\theta\right)^4\right. \\ &\left. + b\left((\varepsilon_q - \varepsilon_{q_0})\cos\theta + (q - q_0)\sin\theta\right)^2 + c\right]\cos\theta + q_0 \end{aligned} \qquad \textit{Equation 6-26}$$

This equation can be solved using Ridder's method (Ridder's 1979), or by calculating the consistent tangent. The consistent tangent differs from the 1D rule because of the influence of p' which adds an extra term. The derivation of the consistent tangent is too lengthy to be repeated here, and is presented in appendix B. The tangent calculated is $\frac{\partial q}{\partial \varepsilon_q}$ and the stress increment is:

$$\dot{q} = \frac{\partial q}{\partial \varepsilon_q} \cdot \left|\dot{\varepsilon}_q\right| \cdot signq \quad \textbf{OR} \quad \dot{q} = \frac{\partial q}{\partial \varepsilon_q} \cdot \dot{\varepsilon}_q \cdot sign\varepsilon_q \cdot load \cdot signq$$ *Equation 6-27*

Once the new stress is calculated, $\dot{\varepsilon}_q^p$ can be calculated based on Equation 6-8.

6.6 Critical State Compatibility

The model integrates the formulation of Dafalias and Manzari (2004) in order to have the deviatoric and volumetric responses of the model compatible with the concept of critical state soil mechanics.

Upon initial loading, the model transitions from small strain loading defined by the input modulus reduction curve to a bounding surface algorithm where the response of the model depends of the distance between the current stress ratio and the bounding surface. The bounding surface is defined by M_b which follows the definition from Dafalias and Manzari (2004):

$$M_b = Me^{-\mathrm{n}_b\psi}$$ *Equation 6-28*

Ψ is the state parameter and is defined as the distance between the current stress ratio and the void ratio at critical state at constant mean effective stress:

$$\psi = e - e_{cs}$$ *Equation 6-29*

For peat, the CSL can be taken as parallel to the isotropic normal consolidated line (ICL). In the void ratio-mean effective stress (*e-p')* space, the ICL is defined as a straight line:

$$e = e_1 - \lambda \ln \frac{p'}{p_1}$$ *Equation 6-30*

Therefore the CSL in the *e-p'* space is also defined as a straight line parallel to the ICL:

$$e_{cs} = \Gamma - \lambda \ln \frac{p'}{p_1}$$ *Equation 6-31*

where Γ is the specific volume at critical state at p_1:

$$\Gamma = \upsilon_1 - (\lambda - \kappa) \ln \mathrm{R}$$ *Equation 6-32*

The variable *R* controls the distance between the ICL and the CSL. The general definitions of the ICL and the CSL can be modified in order to model the behavior of sand better.

At critical state, the bounding surface collapses onto the critical state line. The two surfaces are illustrated in Figure 6-1. Depending on the initial stress state, and whether the state parameter is negative or positive, M_b can be greater or lower than *M*. If M_b is greater than *M*, the response of the model will exhibit a peak stress ratio greater than *M*. Depending on n_b, the model can exhibit a peak shear stress greater than the ultimate shear strength or not. A discussion on the typical predictions of the model is presented in chapter 7.

When the model transitions from small to large strain response, the departure stress ratio η_{in} is defined as the stress ratio at which the transition occurs. The departure stress ratio can be modified upon unloading and reloading if the current stress ratio gets lower than

the departure stress ratio. When η_{in} is modified, an initial plastic ratio H_0 is defined, so that the slope of the stress ratio vs ε_q is continuous at the transition strain (Figure 6-5):

$$H_0 = \frac{\dot{\eta}}{\dot{\varepsilon}_q^p}$$ *Equation 6-33*

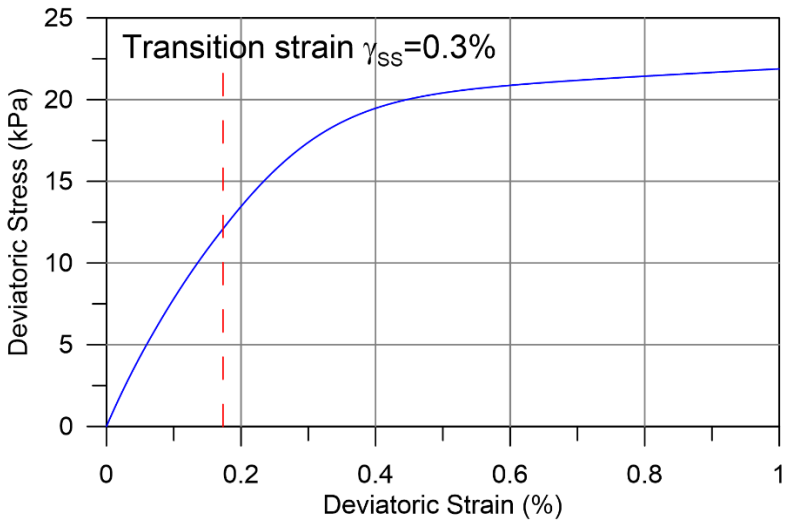

Figure 6-5 Continuity of the stress/strain curve during initial loading

During initial loading at large strains, the plastic deviatoric strains follow the definition of Dafalias and Manzari (2004):

$$\dot{\varepsilon}_q^p = \frac{\dot{\eta}}{H}$$ *Equation 6-34*

The plastic modulus H is defined so that the two following conditions are satisfied: (1) H is equal to H_0 when the stress ratio is η_{in}, and (2) H approaches zero at critical state, i.e. when M_b and η approach M. The following equation is proposed:

$$H = H_0 \frac{\mathrm{M}_b - \eta}{\mathrm{M}_b - \eta_{in}}$$ *Equation 6-35*

Any equation satisfying the two aforementioned conditions can be used, but this equation was chosen because of its simplicity.

Upon shearing, if the stress ratio is changing, plastic deviatoric strains develop, and plastic volumetric strains are coupled with deviatoric strains according to the following equation:

$$d\varepsilon_v^p = d\left|d\varepsilon_q^p\right| \qquad \textit{Equation 6-36}$$

Where d is the dilatancy defined as:

$$d = A_0(M_d - \eta) \qquad \textit{Equation 6-37}$$

Where M_d is the dilatancy surface defined as:

$$M_d = Me^{n_d\psi} \qquad \textit{Equation 6-38}$$

This dilatancy surface collapses onto the critical state line at critical state. When the soil is on the contractive side of the critical state line, M_d is greater than M, and the model's response is contractive. When the soil is on the dilatant side of the critical state line, M_d is lower than M, the soil behavior is initially contractive, and becomes dilative when crossing M_d.

6.7 Plastic Volumetric Wedge

Previous researchers have studied the existence of the cyclic volumetric threshold γ_{tv}, that separates cyclic shear strains that do and do not cause pore pressure generation under undrained cyclic loading (Vucetic 1994). This concept is used here to introduce a

wedge in which no plastic volumetric strain is created upon shearing, i.e. *d=0*. The wedge is illustrated in Figure 6-1. The wedge is centered on α_{PP} and the pore pressure slope M_{PP} is defined as:

$$M_{PP} = \frac{1}{p} \cdot \frac{G}{G_{max}} \cdot \sqrt{3} \cdot G_{max} \cdot \gamma_{PP} \qquad \textit{Equation 6-39}$$

G/G_{max} is calculated based on the input modulus reduction curve and therefore M_{PP} evolves during initial loading. Once γ_{PP} is exceeded during initial loading, the value of M_{PP} does not evolve anymore. The pore pressure wedge is defined by the following equation:

$$f = |\eta - \alpha_{PP}| - M_{PP} = 0 \qquad \textit{Equation 6-40}$$

α_{PP} is set up initially as η_0 and evolves with loading so that $f \leq 0$.

6.8 Volumetric Cap

Upon constant stress ratio loading, such as in a consolidation problem, the deviatoric stress formulation only exhibits elastic deviatoric strains, and therefore no plastic volumetric strains are introduced from the coupling of plastic volumetric and deviatoric strains. To introduce plastic volumetric strains induced by constant stress ratio loading, a volumetric cap is introduced. This volumetric cap models the behavior of soils during consolidation by introducing another component of plastic volumetric strains. This surface shown in Figure 6-1, follows the formulation from Kutter and Sathialingam (1993), that modifies the Modified Cam Clay surface, based on the position of the critical state line. The surface is composed of two ellipses (Figure 2-8) with the following equations for ellipse 1 and 2 respectively:

$$f = (p' - p'_0)\left[p' + \left(\frac{R-2}{R}\right)p'_0\right] + (R-1)^2\left(\frac{q}{M}\right)^2$$ *Equation 6-41*

$$f = p'\left[p' - 2\frac{p'_0}{R}\right] + \left(\frac{q}{M}\right)^2$$ *Equation 6-42*

Where p_0 is the preconsolidation pressure on the ICL, i.e. the intersection of the volumetric cap with the hydrostatic axis. In the modified Cam Clay the plastic strains are defined as:

$$\dot{\varepsilon}_q^p = \dot{\gamma}\frac{\partial f}{\partial q}$$ *Equation 6-43*

$$\dot{\varepsilon}_v^p = \dot{\gamma}\frac{\partial f}{\partial p}$$ *Equation 6-44*

In the present model, $\dot{\varepsilon}_q^p$ is calculated based on the equations for initial loading. Using the consistency condition ($\dot{\gamma}\dot{f}(\sigma, q) = 0$), the following expression can be defined for $\dot{\gamma}$:

$$\dot{\gamma} = \frac{\frac{\partial f}{\partial p}K\dot{\varepsilon}_v + \frac{\partial f}{\partial q}3G\dot{\varepsilon}_q}{K\left(\frac{\partial f}{\partial p}\right)^2 + 3G\left(\frac{\partial f}{\partial q}\right)^2 - \frac{\partial f}{\partial p_0}\frac{\partial f}{\partial p}\frac{vp_0}{\lambda - \kappa}}$$ *Equation 6-45*

The extra component of plastic volumetric strain introduced is:

$$\dot{\varepsilon}_v^{pc} = \dot{\gamma}\frac{\partial f}{\partial p}$$ *Equation 6-46*

The plastic volumetric strains combine the plastic strains induced by shearing and by constant stress ratio loading. The stress increment is then calculated as:

$$\dot{\mathrm{p}} = \mathrm{K}(\dot{\varepsilon}_v - \dot{\varepsilon}_v^p - \dot{\varepsilon}_v^{pc})$$ *Equation 6-47*

The preconsolidation pressure evolves with the plastic volumetric strain following the equation:

$$\dot{p_0} = \frac{v p_0 \left(\dot{\varepsilon}_v^p + \dot{\varepsilon}_v^{pc}\right)}{\lambda - \kappa} \qquad \textit{Equation 6-48}$$

The preconsolidation pressure evolves with plastic volumetric strains, whether they are due to shearing or constant stress ratio loading.

7 IMPLEMENTATION IN A FINITE DIFFERENCE PROGRAM: FLAC

The model presented in chapter 6 is implemented in a finite difference program called FLAC (Fast Lagrangian Analysis of Continua), in order to be used in numerical simulations presented in chapter 8. This chapter presents the implementation and some examples. The chapter first discusses how FLAC works, and how users can implement their own constitutive models. I then present the implementation of the model and how it interacts with FLAC. Monotonic and cyclic single elements simulations are presented to provide examples of typical predictions. The chapter also analyses the effect of the three variables A_0, n_b, and n_d, through single element simulations as well.

7.1 Introduction to FLAC

FLAC is a two dimensional explicit finite difference program for numerical simulations. This section presents a short introduction of the software. It first summarizes the theory behind it and explain how the calculations are performed. A short explanation on the creation of user-defined constitutive models is provided. For more information, the reader is invited to read the FLAC manual.

7.1.1 Explicit Finite Difference Method

The finite difference method is a numerical technique used to solve a set of governing differential equations, given boundary conditions. The governing equations are either the equation of motion, Fourier's law for conductive heat transfer, or Darcy's law for fluid flow in a porous solid, depending on the type of problems being solved.

The finite difference method approximates every derivative in the equations by finite differences formulated in terms of field variables at discrete points. Field variables are undefined within the elements. In comparison, in the finite element method, the field variables vary throughout the elements according to shape functions. Both methods would essentially yield the same equations that can then be solved using different solution schemes. FLAC uses an explicit solution, which is represented schematically in Figure 7-1. One loop in the Figure 7-1 represents one time step. In a calculation cycle, the new velocities and displacements are calculated from the equation of motion. These new velocities and displacements are used to derive a strain rate and a constitutive model would return the associated stresses and forces based on the state of the internal variables at the beginning of the time step. The equation of motion is then solved based on these new stresses and forces. In Figure 7-1, each box represents an update of every grid variables (e.g. stresses or velocities) based on initial values that are assumed to be constant within the box. For example, in the lower box the velocities are assumed to be constant and unaffected by the new stresses. This assumption requires a small time step in order to be stable. In an implicit scheme solution, the velocities are adjusted based on these new stresses, and iteration is required to reach a solution. For a mathematical description of the calculation process in FLAC, the reader is invited to read the FLAC Manual “1 Background- the Explicit Finite Difference Method” (Itasca Consulting Group 2011).

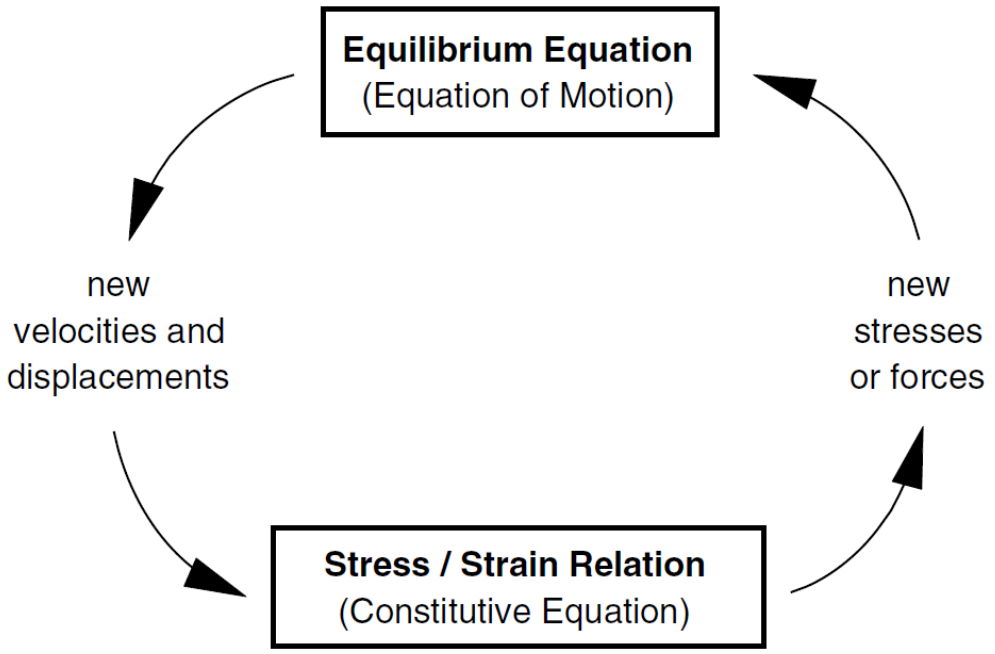

Figure 7-1 Calculation cycle in FLAC (Itasca Consulting Group 2011)

7.1.2 Grid, Zones and Subzones in FLAC

In FLAC, the user-defined mesh is composed of quadrilateral elements. Each element (i.e. zone) is subdivided in two overlaying sets of triangular elements, as shown in Figure 7-2. This subdivision was adopted in order to avoid the phenomenon of mesh locking. The stress and strain tensors are decomposed into their isotropic (i.e., on diagonal) and deviatoric (i.e., off diagonal) components. The isotropic components are averaged over each pair of triangles but the deviatoric components are different for every triangular subzone. To ensure that the isotropic stress and strain components are constant throughout the quadrilateral element, the diagonal elements of the strain and stress tensor are adjusted (see section 1.3.3.2 of the FLAC manual). As a result of this decomposition, sixteen stress components are stored for each zone, σ_{xx}, σ_{yy}, σ_{zz}, and σ_{xy} being stored for each subzone. If a set of triangles becomes unusable, for example when

one of the triangle becomes much smaller than the other, this pair of triangles is not used anymore, and only one set is used. If the two sets are badly deformed, FLAC returns an error message.

Figure 7-2 Sets of triangles in a quadrilateral element (Itasca Consulting Group 2011)

During a time step, a constitutive model is called 4 times, once per subzone. For each subzone, the model takes the strain increment tensor and the stress tensor as an input and returns the updated stress tensor. Material variables are constant throughout the element, and do not vary from one subzone to another. Material variables are updated at the end of the time step, once all the subzones have been processed.

7.1.3 User-Defined Constitutive Models in FLAC

In FLAC, users have the possibility to write their own constitutive models either in FISH (the programming language embedded in FLAC), or in C++. When written in C++, the code must be compiled in a DLL (Dynamic Link Library) and loaded in the FLAC directory.

This latter approach is more computationally efficient, and also easier to share than a FISH code, as other users can simply load the DLL in the FLAC directory and then use it just like a built-in model. This section summarizes the general approach when creating a DLL, and for more information the reader is referred to the section 2 of the FLAC manual on constitutive models: “Writing New Constitutive Models” (Itasca Consulting Group 2011).

User-defined models (UDM) are defined within a base class called *ConstitutiveModel*. This base class provides a framework for UDM and is constituted of several pure virtual member functions. The list of all the functions is provided in the manual. The functions are defined in a *.cpp* file, while the variables are defined in the header file. Most of the functions are not fundamentally modified from one model to another, and this section is only discussing the most important functions in the following list:

- *getProperties()* defines a list of string that defines the name of the model’s variables that can be accessed by a user in FLAC.
- *getProperty()* associates a variable’s name to every element of the list defined by *getProperties()*.
- *getStates()* lists the state indicators of the zone accessible from FLAC. State indicators are used to denote if a zone is yielding or has yielded in the past. Different modes of failure are available such as shear, tension or volume.
- *initialize()* is called at the beginning of every time step and is used to initialize local variables.
- *run()* is the most important function, and contains the algorithm of the model. The function *run()* is called four times per time step, once per subzone, and returns the

new stress tensor, based on the strain increment tensor and the previous stress tensor. At the end of the fourth zone, the model's variables are updated.

The strain increment tensor and the current stress tensor are accessed through the structure *State* defined in *state.h*. The structure is used to pass information between the model and FLAC. Information available through the structure *State* include:

- The zone and subzone volume,
- The rotation,
- The density,
- The temperature,
- The number of subzones,
- The identifier of the subzone being processed,
- The strain increment tensor
- The stress tensor

Once all the functions have been defined in the *.cpp* file, and the variables have been defined in the header file, a DLL can be compiled. Details on how to build the DLL are included in the manual. Once compiled, the DLL can be loaded in FLAC in two different ways. First the DLL can be copied in the directory of the current project, and called directly in the project by the command *Model load <model.dll>*. The second option is to copy the DLL directly in the following FLAC directory:

C:\...\Itasca\FLAC700\Exe32\plugins\models

When the DLL is copied directly in the FLAC directory, the UDM can be called like any built in model.

7.2 Implementation of the Model in FLAC

This section summarizes the implementation of the model and explains the fundamental algorithm of the model. In particular, the input parameters are listed, the initialization of the model is thoroughly described, and the algorithm of the function *run()* is explained.

7.2.1 Input Parameters in FLAC

As mentioned in chapter 6, the model has 17 parameters. However, when using the model in FLAC, not all parameters need to be defined as some have predefined values. This section summarizes the input parameters and the options offered to the user when using the model. The following input parameters always need to be defined by the user, and the first word of each line is the keyword used in FLAC for the property:

- *kappa* which defines κ, the slope of the recompression line in the *e*-ln *p'* space
- *lambda* which defines λ, the slope of the critical state line in the *e*-ln *p'* space
- *mm*, defining M, the slope of the critical state line in *p'-q* space
- *me1*, the specific volume at unit pressure p_1
- *DTable* is the table identifier containing the damping vs. η curve
- *redTable* is the table identifier containing the modulus reduction vs. η curve

The following input parameters can be adjusted by the user, or left as their default value, presented in Table 7-1:

- *A0* which defines the variable A_0 that controls the pore pressure response.
- *nb* which defines n_b governing the size of the bounding surface.
- *nd* which defines n_d governing the size of the dilation surface.
- *strainSS* which defines γ_{SS} the strain at which the model transitions from small strain response to a bounding surface algorithm
- *strainPP* which defines γ_{PP} the strain at which pore pressure start to generate.
- *mp1*, the mean unit pressure p_1.
- *OCR*, the overconsolidation ratio
- *Dmin*, the small strain damping.
- *Flag*, which is initially set to 0. If this flag is set to 0, the model is initialized at the beginning of the function *run()* (See next section). If the model is set to 1, the model does not initialize. The Flag is automatically set to 1 at the end of initialization, and the user can decide to reinitialize the model at any time, by setting *Flag* to be 0.
- *MPC*, the preconsolidation pressure. Rather than setting directly the OCR, the user can decide to set up the preconsolidation pressure instead.
- *RHO* is the density of the soil, and only needed if *VS* is used too.
- *RR* defines *R* the shape of the volumetric yield surface, which also defines the position of the critical state line relative to the normally consolidated line. The default value is 2 which renders a volumetric yield surface that is equivalent to the Modified Cam Clay yield surface
- *gn* defining *n* which controls the effect of the confining pressure on the maximum shear modulus

- *gm* defining *m,* which controls the effect of overconsolidation on the maximum shear modulus.
- *gA* defining *A,* which defines the value of the maximum shear modulus

Table 7-1Default values of model parameter

Property	Default Value
A_0	0.2
n_b	0.75
n_d	0.3
g_{SS}	0.03%
g_{PP}	0.7%
p_1	1
OCR	1
FLAG	0
D_{min}	2%
R	2
m	0.5
n	0.5
A	174

Regarding the definition of the maximum shear modulus the user has two options, either defining *A* or defining directly the initial shear wave velocity V_s:

- *VS* is the initial shear wave velocity, which defines the initial maximum shear modulus.

If this latter approach is used, the initial shear modulus is calculated based on the density of the soil. Since the initial shear modulus, overconsolidation ratio, mean effective stress and the parameters *m* and *n* are known, the initial value of *A* is backcalculated by rearranging equation 6-6 and replacing G_{max} by V_s^2/ρ:

$$A = \frac{{V_s}^2}{\rho} \cdot \frac{1}{p_{at} \cdot {OCR_{ini}}^m \left(\frac{{p_{ini}}'}{p_{at}}\right)^n}$$ *Equation 7-1*

If the user is modeling peat, he has the option of giving the organic content as an input.

- *MOC,* the organic content *OC*

In this case, *m*, *n,* and *A,* if V_s is not specified, follow the definition from Kishida et al. (2006) based on the following equations:

$$X_3 = \frac{2}{1 + \exp(OC/23)}$$ *Equation 7-2*

$$n = 1 - 0.37X_3$$ *Equation 7-3*

$$m = 0.8 - 0.4X_3$$ *Equation 7-4*

$$A = e^{5.2+0.48X_3+0.74\left\{\frac{3X_3-1.5}{\ln\left(1+3e^{1+3X_3}\right)}-1\right\}}$$ *Equation 7-5*

If the minimum damping is not defined by the user, but the user is defining the organic content, then the definition of the small strain damping follow the definition from Kishida (2009):

$$D_{min} = e^{c_0+c_1X_1+c_2X_2+c_3X_3+c_4(X_1-\overline{X_1})(X_2-\overline{X_2})+c_5(X_2-\overline{X_2})(X_3-\overline{X_3})}$$ *Equation 7-6*

where:

$$X_2 = \ln p'$$ *Equation 7-7*

and

c_0= 2.86; c_1=0.571; c_2=-0.103; c_3= -0.141; c_4= 0.0419; c_5= -0.240 ;

X_1= ln(0.103); $\overline{X_1} = -1$; $\overline{X_2} = 4.0$; $\overline{X_3} = 0.5$;

The command *z_prop(zp, p_name)* is used to access the variable *p_name* in the zone *zp*. In addition to the input parameter previously mentioned, the following information can be accessed:

- *Bulk*, the bulk modulus
- *Shear,* the shear modulus
- *cv*, the specific volume
- *MeanP*, the mean effective stress *p*
- *DevQ*, the deviatoric stress *q*
- *epsQ*, the deviatoric strain ε_q
- *EV*, the volumetric strain ε_v

7.2.2 Initialization of the Model

The initialization of the model is performed at the beginning of the function *run()*, the first time that the function is called, if *Flag* is set to 0. The function *initialize()* is called every time the function *run()* is called, and therefore serves a different purpose. When the function *run()* is called, a check on *Flag* is instantly performed, and if it is set to 0, the initialization is performed. First, the initial values of mean confining pressure, and deviatoric stresses are set based on the current stress tensor. The initial stress ratio is also calculated at the same time. If the *OCR* is specified but not the preconsolidation

pressure, this latter is initialized. If none of them is specified, *OCR* is set equal to 1. The initial specific volume, bulk modulus, and maximum shear modulus are then initialized as well. The limit strains γ_{SS} and γ_{PP} are also set to their default values if they are not specified. The pore pressure slope, calculated from equation 6-39 is initialized. The following variables are set equal to 0: ε_q, the deviatoric strain, ε_{qlim}, the maximum deviatoric strain ever reached, IN, a variable tracking the transition between small strain and large strain initial loading (see Chapter 6 section 6-6). Finally, the initial plastic modulus H_0 is defined by the modulus reduction curve at small strain. Upon transitioning from small strain to large strain loading, H_0 is reevaluated to provide a smooth curve. The variables γ_L, γ_R, η_L and η_R, that track the different unloading and reloading strain/stress ratios, are defined as FILO (First-In Last-Out) stacks. These stacks are emptied upon initialization. The variables tracking the signs of q and ε_q, respectively *signq* and *signεq* are set equal to 1. The variable tracking the loading direction, *load*, is set equal to the sign of q_{trial}-q, where q_{trial} is calculated based on the previous stress and the strain increment tensor, if the material was elastic. If the sign of q_{trial}-q is 0, i.e. if the first deviatoric strain increment is 0, *Flag* is set equal to 2, otherwise *Flag* is set to 1. In both cases, initialization will not happen again. If the Flag is set to 2, the sign of q_{trial}-q is checked at every time step until it is different than 0, but the model does not initialize. Once this happens, *load* is set, and *Flag* is set equal to 1, and does not change until the user decides to reinitialize the model.

The function initialize(), called every time run() is called, reads the tables containing the curves D-D_{min} and G/G_{max} vs. η, and ensures that certain variables have realistic values.

For example, if the mean unit pressure or the preconsolidation pressure are negative, then an error message is issued.

7.2.3 Function run()

The function *run()* is the most important function of a UDM. As explained in the previous section, it initializes the model the first time the function is called, but is then used to calculate the new stress tensor of every subzone based on the previous stress tensor and strain increment tensor. Once the last subzone has been processed, the variables of the entire zone are updated.

When the function is called, the volumetric strain increment, the deviatoric strain increment and the total deviatoric strain are calculated based on the strain increment tensor and the previous strain tensor. This latter is not provided directly by the state structure, and is instead kept track of with internal variables that accumulate all the strain components. The deviatoric stress and the mean confining pressure of the zone are also calculated based on the stress tensor provided by the state structure. A trial value of the deviatoric stress is then calculated based on the assumption that the soil behaves elastically. This value is then used to verify if the direction of loading is changing, or if the sign of the deviatoric stress is changing (see section 6-5 in chapter 6). The sign of the deviatoric strain also evolves if the sign of $\dot{\varepsilon}_q$ changes but the sign of q_{trial}-q is the same as *signq*. The subzone values of γ_L, γ_R, η_L and η_R are updated according to the rules presented in chapter 6, e.g. when the direction of loading changes.

The model then checks if it is loading or unloading/reloading. When the model is in the initial loading case, a check on the deviatoric strain is done to see if it corresponds to the

small or large strains case. When the model transition from one to the other, a subzone variable η_{in}, the departing stress ratio, is used for the subzone, and the zone variable η_{in} is updated at the end of the time step. The equations provided in Chapter 6 are then used to calculate the new deviatoric stress and mean confining pressure. The new subzone stress tensor is updated based on the following equation:

$$\sigma_{ij} = \frac{\sigma_{trial_{ij}}}{q_{trial}} \cdot q - \delta_{ij} \cdot p \qquad \textit{Equation 7-8}$$

Where δ_{ij} is the Kronecker delta. If q_{trial} is equal to zero, then only the diagonal of the stress tensor is updated by adding to the trial stress value the difference p_{trial}-p.

When the forth subzone has been processed, the deviatoric strain, volumetric strain, mean pressure, and deviatoric stress are averaged over the zone. To average these quantities over the zone, stacks are used. The following stacks are used, tracking the associated variable:

- *Pav*: the mean confining pressure
- *Qav*: the deviatoric stress
- *Evav*: the volumetric strain increment
- *EvdPav*: the plastic deviatoric strain increment
- *EQav*: the deviatoric strain increment
- *Qtrav*: the previous deviatoric stress
- *E11, E22, E33, E12, E13, E23*: every component of the strain increment tensor.
- *Qtrial*: the trial value of the deviatoric stress
- *MPCav*: the preconsolidation pressure

These stacks are different from the FILO stacks mentioned in the previous section, and are initialized at the beginning of the first subzone being processed by the command *s->working_[stack]=0.0*. When a subzone has been processed, the stack is updated by adding the relevant quantity (e.g. the deviatoric stress or the volumetric strain) to the stack, multiplied by the subzone volume. When all the subzones have been processed, the stack is divided by the volume of the zone, and by the number of sets of triangles that were processed.

Some other variables are also updated for the entire zone such as ε_{qlim}, the specific volume, the bulk modulus and the shear modulus. The departure stress ratio η_{in}, and H_0, are also updated if the initial loading is transitioning from small to large strains. The direction of loading, the signs of q and ε_q are also updated, along with the stacks γ_L, γ_R, η_L and η_R. Finally the preconsolidation pressure and the overconsolidation ratio are updated.

7.3 Example of Predictions

This section presents some example single element simulations. Simulations of monotonic undrained and drained triaxial tests, monotonic undrained simple shear tests, and cyclic undrained triaxial tests are presented. The input parameters of the model are the same for all the tests and are presented in Table 7-2. These parameters are loosely based on Sherman Island peat but this section does not intend to simulate precisely the behavior of peat, rather to illustrate the typical predictions of the model. The D-D_{min} and G/G_{max} vs. η curves used for the simulations were derived based on the equations from Kishida et al. (2009) for peat, and are presented in Figure 7-3. The tests are presented

under different stress conditions, with varying *OCR*s, consolidation pressures, preconsolidation pressures, and K_0 coefficients.

Table 7-2 Input properties

Property	Value
λ	1.65
κ	0.175
M	1.1
ρ	1.1
γ_{PP}	0.01%
γ_{SS}	0.3%
OC	70
V_S	53
p_1	1
v_1	14.2
A_0	0.2
n_b	0.25
n_d	1

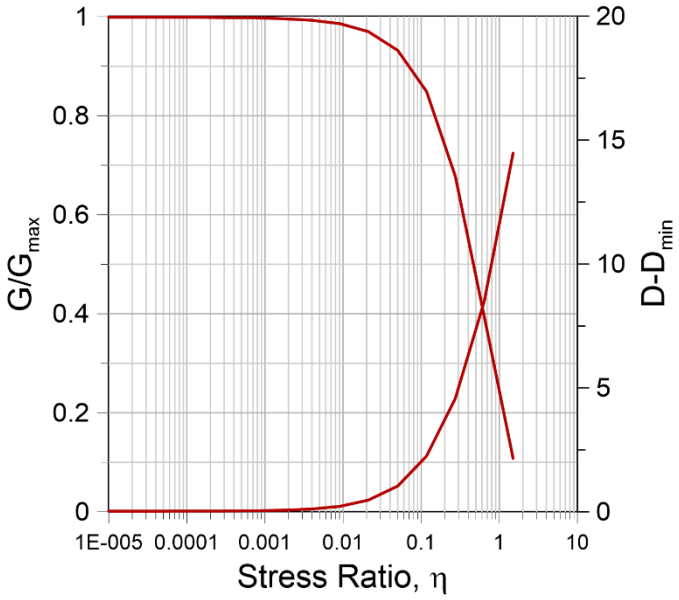

Figure 7-3 Input modulus reduction and damping curves

7.3.1 Monotonic Tests

7.3.1.1 Undrained Triaxial Tests

Undrained triaxial tests were simulated with the model presented in Figure 7-4. The bottom left corner was constrained in both directions, and the top left and bottom right nodes were allowed to slide in one direction. Vertical (σ_{yy}) and lateral stresses (σ_{xx}) were applied to consolidate the sample, and the two top nodes were displaced toward the bottom to load the sample. The groundwater module was turned on with flow turned off to create undrained loading conditions and allow development of excess pore water pressure.

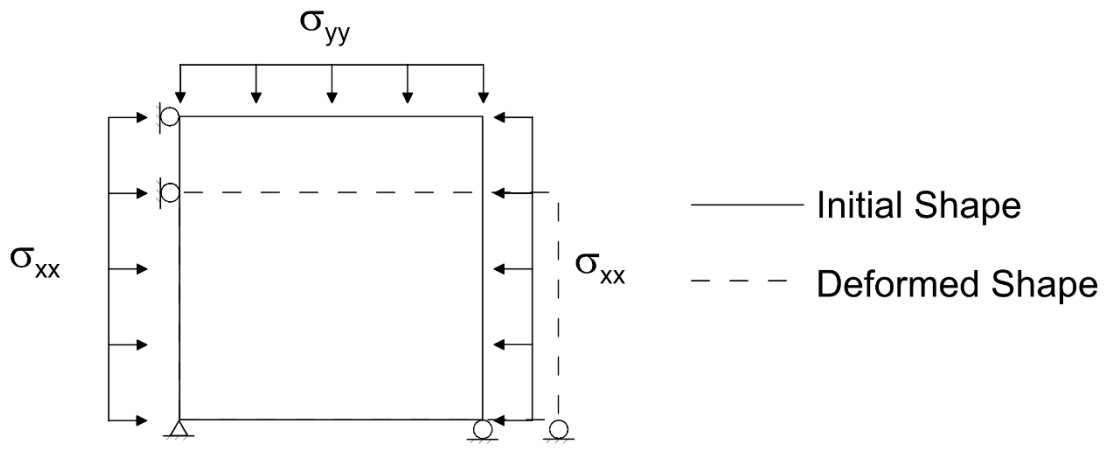

Figure 7-4 Triaxial test model

In the first simulation, four different cases are simulated. The samples are isotropically consolidated ($\sigma_{xx}=\sigma_{yy}$) at different confining pressure, 10, 25, 40 and 50 kPa, but with the same initial preconsolidation pressure, 50 kPa. The overconsolidation ratio of the four different samples are 5, 2, 1.25, and 1, respectively. The top nodes are displaced until reaching 20% strain, at which point the four samples are nearly at critical state. The results of the first simulation are presented in Figure 7-5.

The normally consolidated and slightly overconsolidated cases (*OCR=1* and 1.25 respectively) exhibit a peak shear stress but not a peak stress ratio (Stress ratio only increases). The most overconsolidated sample (*OCR=5*) exhibits a peak stress ratio but not a peak shear stress. The sample with *OCR=2* has a nearly vertical stress path in *p-q* space. With the modified Cam-clay model, when OCR=2 the stress path is perfectly vertical and the model's response is elastic perfectly plastic, which is not the case for the model presented here. In fact the present model would never exhibit an elastic perfectly plastic behavior unless the input modulus reduction curve was selected to display this behavior. All the samples are initially contractive and the pore water pressure is positive,

but the sample with *OCR=5* becomes dilative and the pore pressure decreases until becoming negative. The shear strength exhibited is higher for samples at higher confining pressure, though the sample with OCR = 5 mobilizes the highest stress ratio.

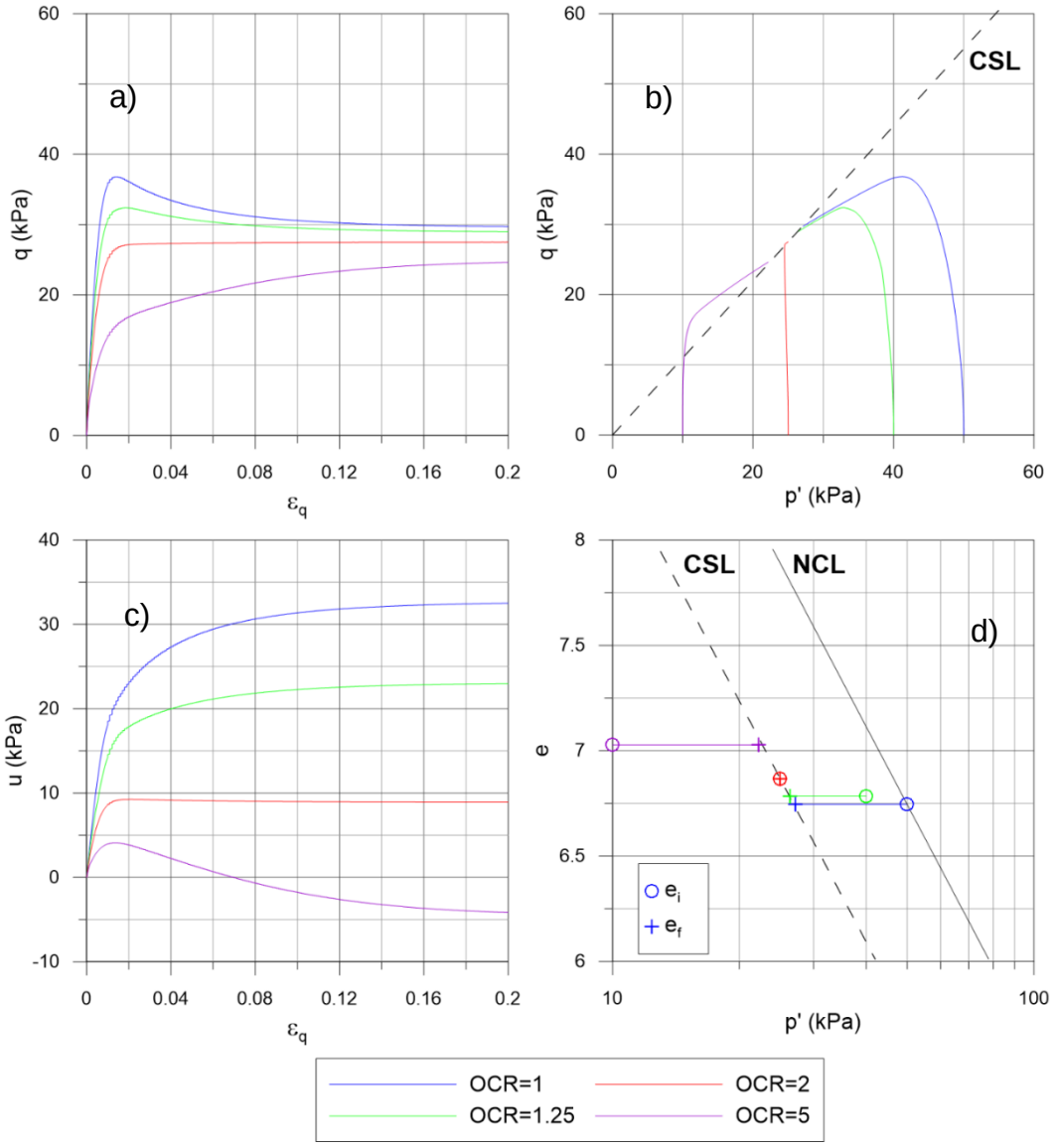

Figure 7-5 Undrained triaxial tests at different OCR and confining pressure but same initial preconsolidation pressure a) deviatoric stress vs. deviatoric strain, b) deviatoric stress vs. mean effective stress, c) pore pressure vs. deviatoric stress and d) void ratio vs. mean effective stress.

In the second example, the samples are consolidated at the same confining pressure, but with different *OCR*. The results are presented in Figure 7-6. The contractive/dilative

behavior of the different samples is similar to the previous example, all the samples exhibit a contractive response, but the most overconsolidated sample becomes dilative upon shearing and ends up with negative pore pressure. The shear strength exhibited is higher for higher *OCR*.

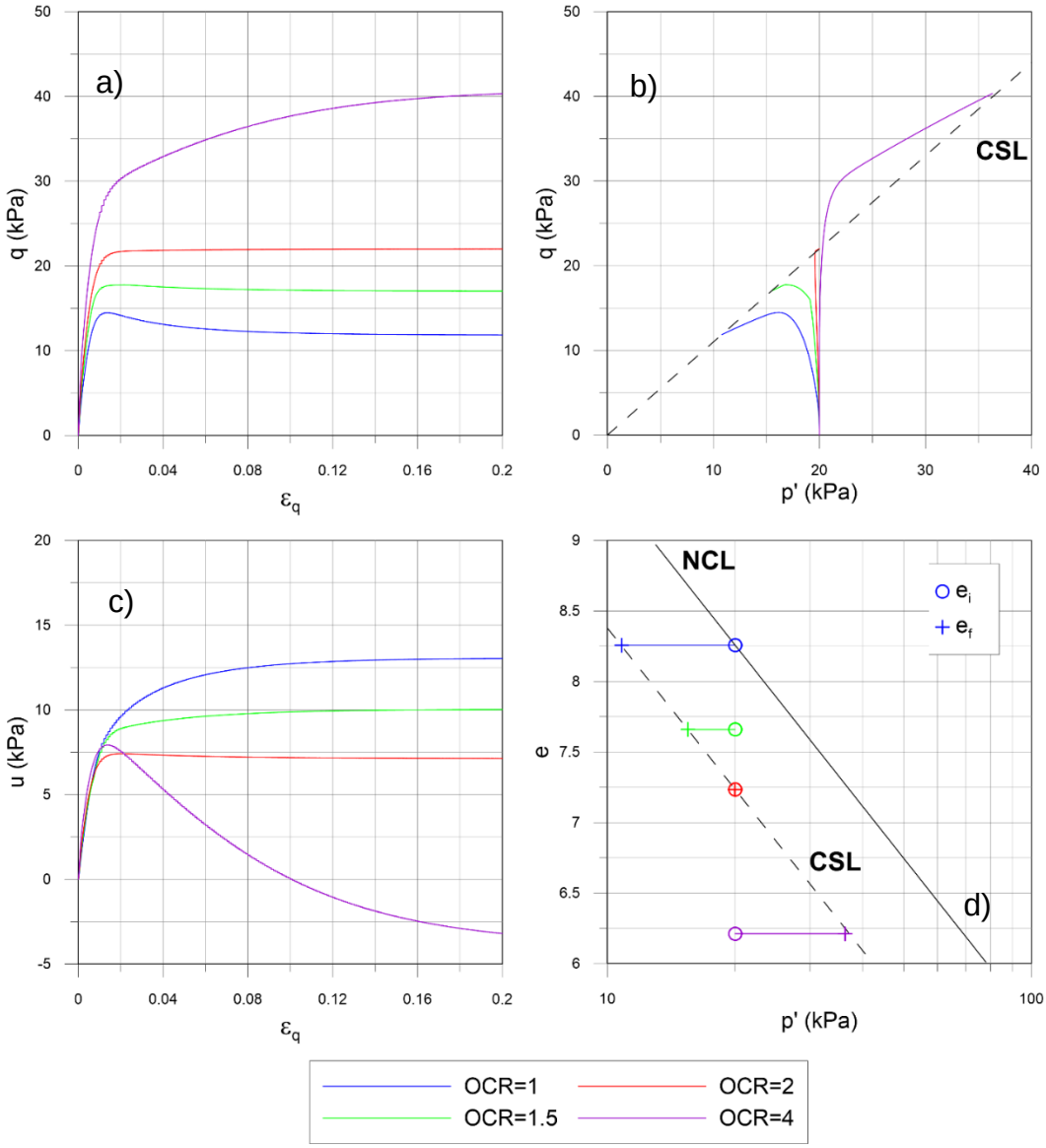

Figure 7-6Undrained triaxial tests at same initial confining pressure but different OCR a) deviatoric stress vs. deviatoric strain, b) deviatoric stress vs. mean effective stress, c) pore pressure vs. deviatoric stress and d) void ratio vs. mean effective stress

Figure 7-7 shows the Skempton's pore pressure parameter at failure (A_f=(Δu-$\Delta\sigma_3$)/($\Delta\sigma_1$-$\Delta\sigma_3$)) from the simulations and a comparison with laboratory test results compiled by Mayne and Stewart (1988). The model is in excellent agreement with previous observations. Note that in the model, A_f only depends on λ, κ, R, M, and OCR.

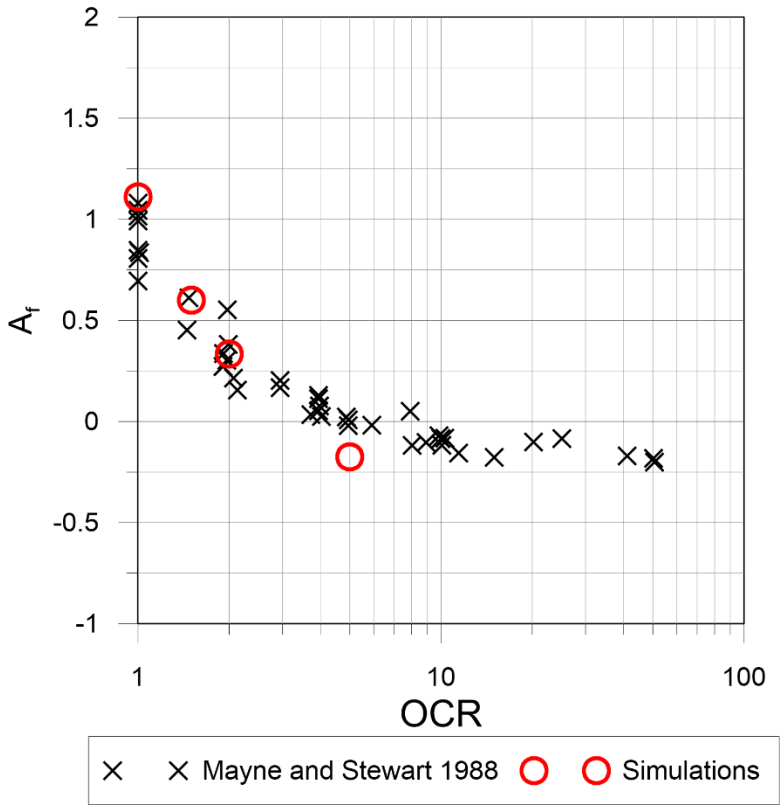

Figure 7-7 Comparison of the Skempton's pore pressure parameter at failure from Mayne and Stewart (1988) and simulations

In the third undrained triaxial test simulation, all the samples are K_0-consolidated: $\sigma_{xx}=K_0*\sigma_{yy}$. As a result the initial stress ratio is non-zero if K_0 is not 1. All the samples are consolidated under the same vertical effective stress (σ_{yy}) and therefore they are all normally consolidated at different mean pressure. The results are presented in Figure 7-8. The behavior of all the samples is contractive and the samples with a lower K_0 exhibit a lower shear strength since they are consolidated under a lower mean pressure.

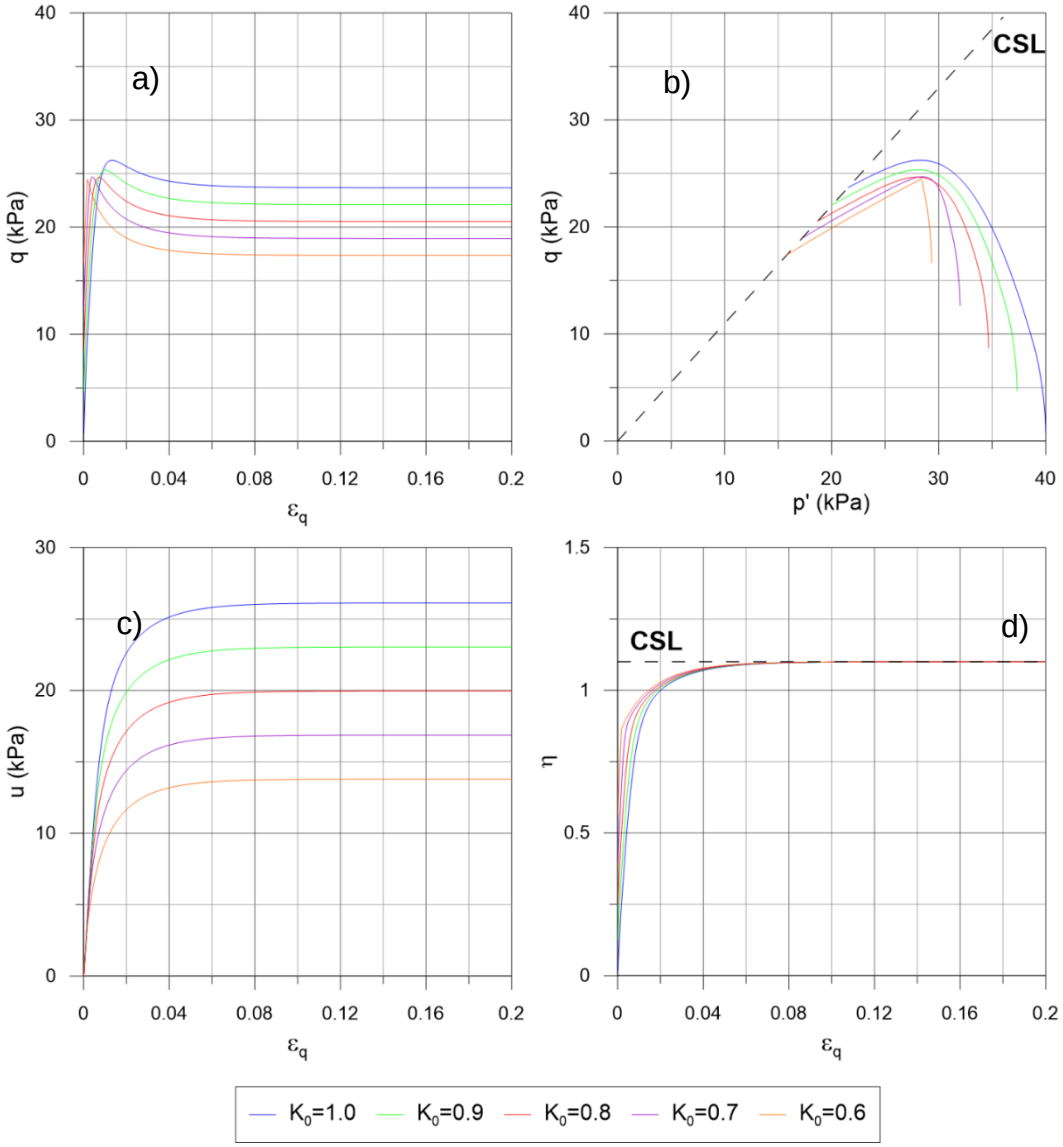

Figure 7-8Undrained triaxial tests K_0 consolidated a) deviatoric stress vs. deviatoric strain, b) deviatoric stress vs. mean effective stress, c) pore pressure vs. deviatoric stress and d) stress ratio vs. deviatoric strain

7.3.1.2 Drained Triaxial Tests

Two simulations were performed to simulate drained triaxial tests, similar to the first two undrained triaxial simulations presented. Drained triaxial tests are simulated with the same model shown in Figure 7-4, but the groundwater module of FLAC is turned off. The

first simulation shows four different samples isotropically consolidated at different confining pressure, with the same preconsolidation pressure. In the second simulation, all the samples are isotropically consolidated at the same confining pressure, but at different *OCR*s.

In drained triaxial tests the stress path in *q*-*p* space is a straight line with 3 to 1 slope, as can be seen in Figure 7-9 and Figure 7-10. In both simulations, only overconsolidated samples are exhibiting a peak response. All the samples are initially contractive with a void ratio decreasing, but the most overconsolidated sample becomes dilative and void ratio increases. The normally consolidated sample goes slightly above the normally consolidated line, which is not a desired feature, but does not affect the overall behavior of the model.

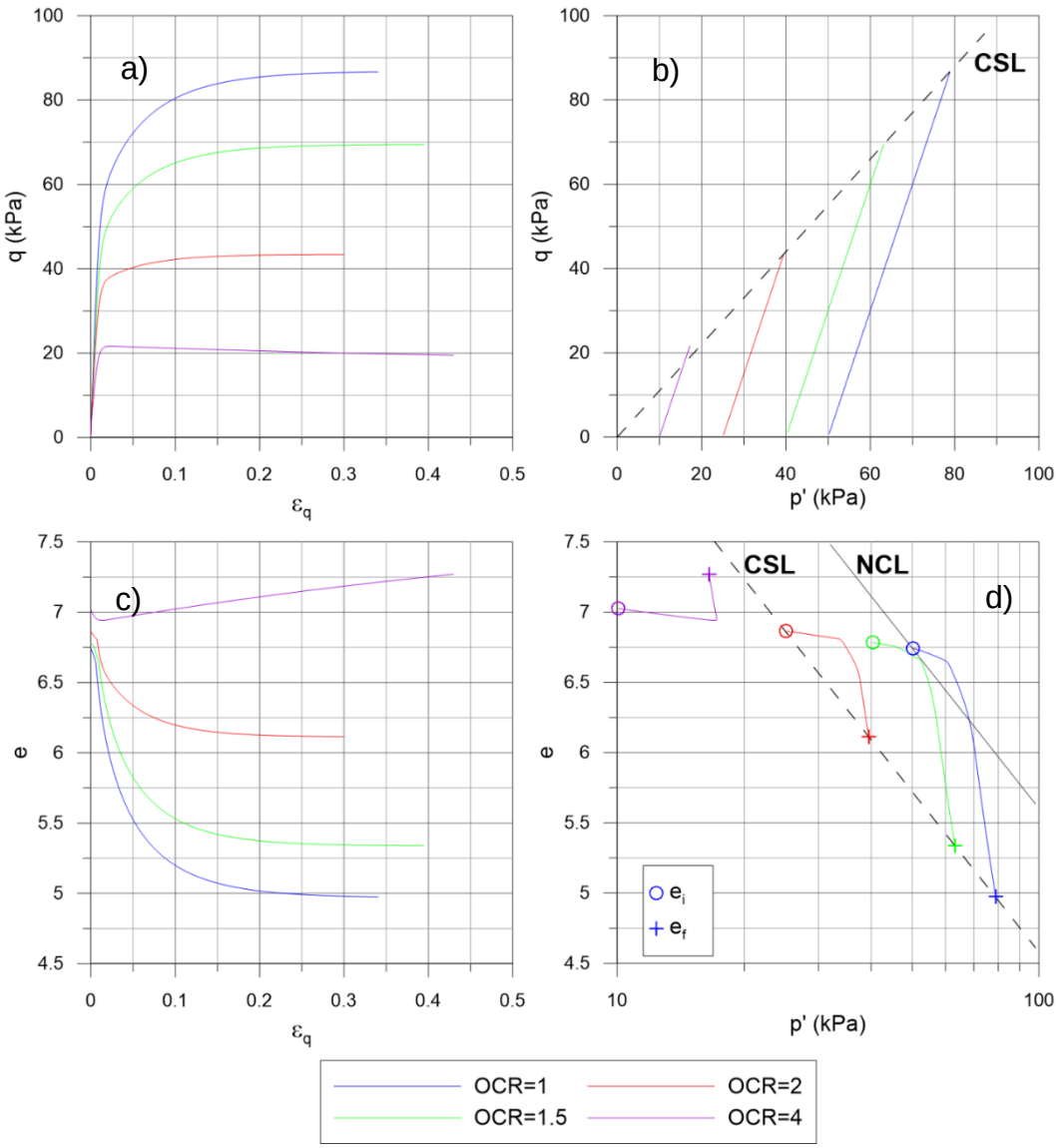

Figure 7-9 Drained triaxial tests at different initial confining pressure but same preconsolidation pressure a) deviatoric stress vs. deviatoric strain, b) deviatoric stress vs. mean effective stress, c) void ratio vs. deviatoric stress and d) void ratio vs. mean effective stress

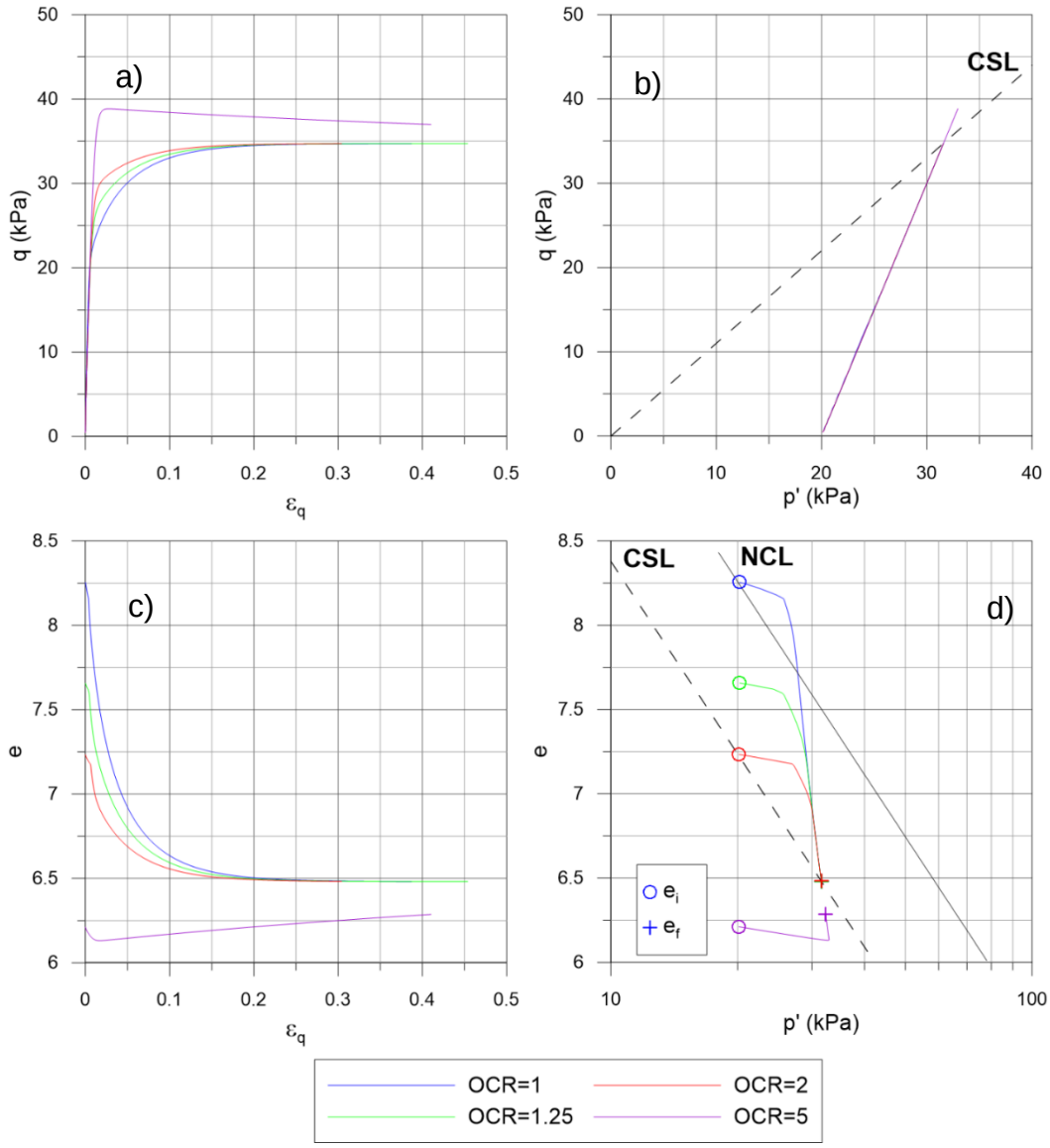

Figure 7-10 Drained triaxial tests at same initial confining pressure but different OCR a) deviatoric stress vs. deviatoric strain, b) deviatoric stress vs. mean effective stress, c) void ratio vs. deviatoric stress and d) void ratio vs. mean effective stress

7.3.1.3 Undrained Simple Shear Tests

Two simulations of undrained simple shear tests were performed, with the same initial conditions as the first two undrained triaxial tests. In the first simulation, the four samples are isotropically consolidated at different confining pressure, but with the same preconsolidation pressure, and in the second simulation, all the samples are consolidated

at the same confining pressure, but with different *OCRs*. The model used to model simple shear tests is presented in Figure 7-11. A vertical stress is applied and the same stress is applied laterally. This is not representative of a real simple shear test, since in reality no lateral stress is applied, and the soil is K_0 consolidated under the vertical stress, due to the resistance of the membrane. However, this would be representative of a simple shear test where K_0 is equal to 1. The bottom nodes are both constrained in both direction, and shear is simulated by deplacing the top nodes in the horizontal direction. In order to simulate a simple shear test, the top nodes are linked to each other by a cable with essentially 0 resistance, in order to make sure the two nodes are moving together, but without affecting the response of the model.

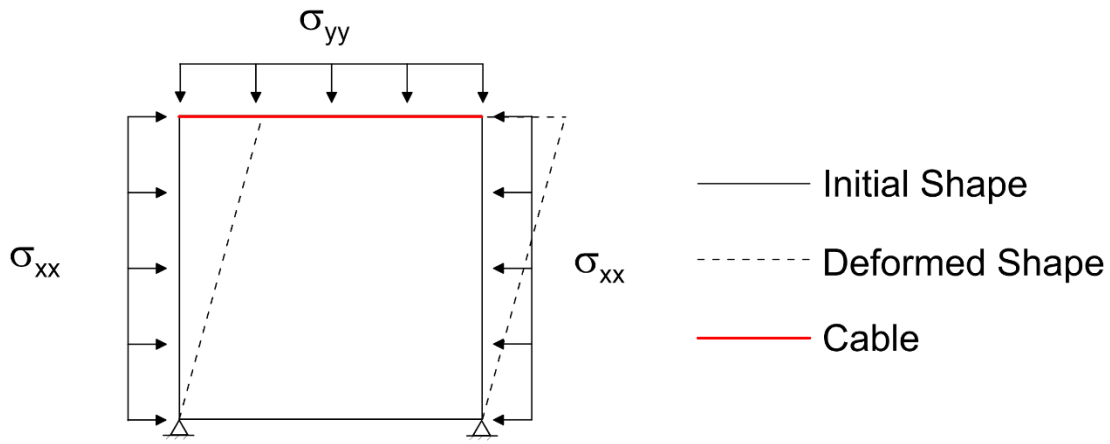

Figure 7-11 Simple shear model

The results of the two simulations, presented in Figure 7-12 and Figure 7-13 respectively, are essentially similar to the results of the undrained triaxial tests, which is expected. The normally consolidated and slightly overconsolidated samples exhibit peak stress, but no peak stress ratio, while the most overconsolidated sample exhibit a peak stress ratio, but no peak stress. All the samples are initially contractive and exhibit a positive pore

pressure response. The pore pressure response is slightly different from the undrained triaxial tests. The overconsolidated sample that starts on the CSL is exhibiting almost no pore pressure response. The most overconsolidated sample is exhibiting a very slight contractive response at the beginning and then becomes dilative and shows a large negative pore water pressure.

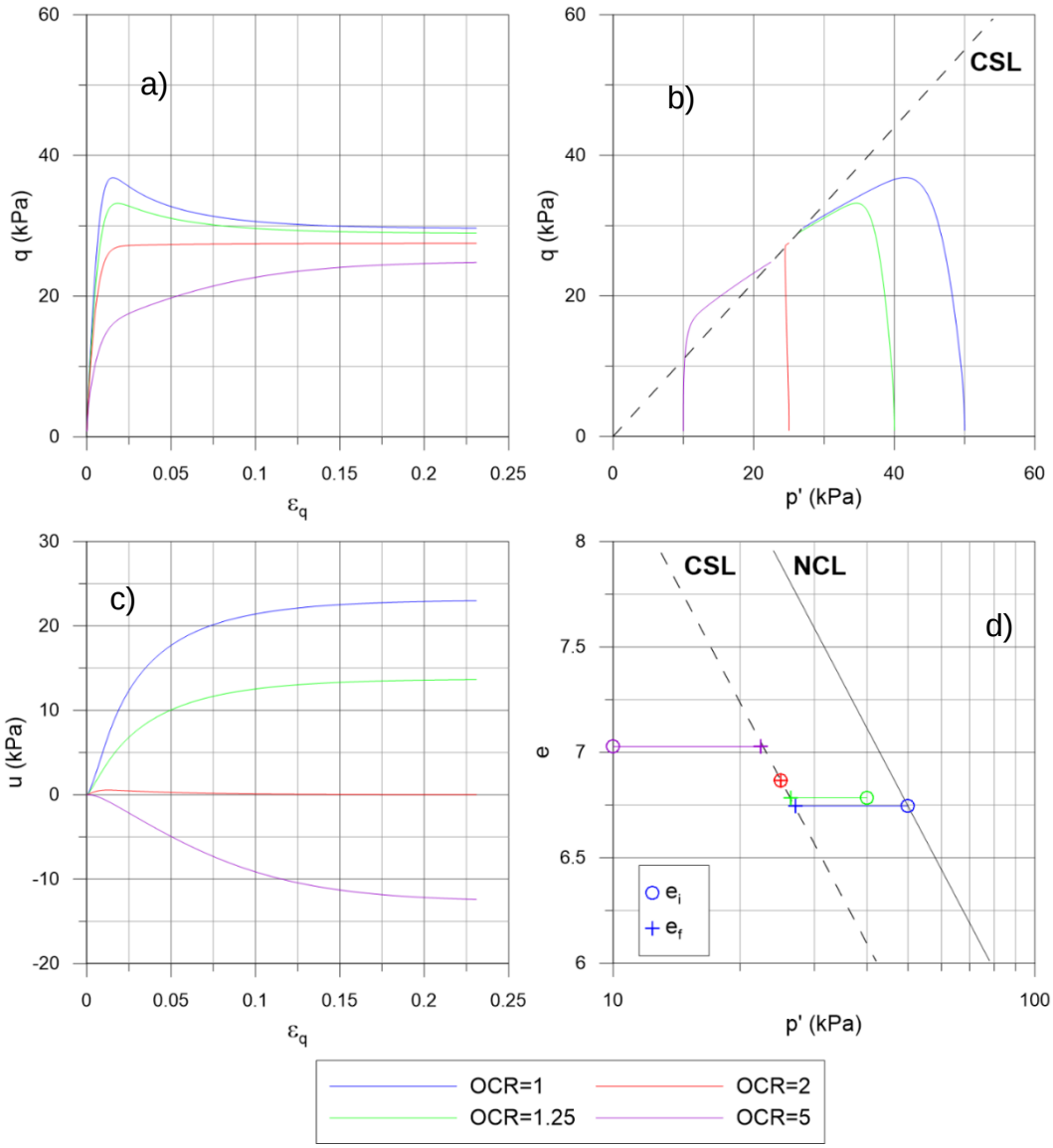

Figure 7-12Undrained simple shear tests at same different confining pressure but same preconsolidation pressure a) deviatoric stress vs. deviatoric strain, b) deviatoric stress vs. mean effective stress, c) pore pressure vs. deviatoric stress and d) void ratio vs. mean effective stress

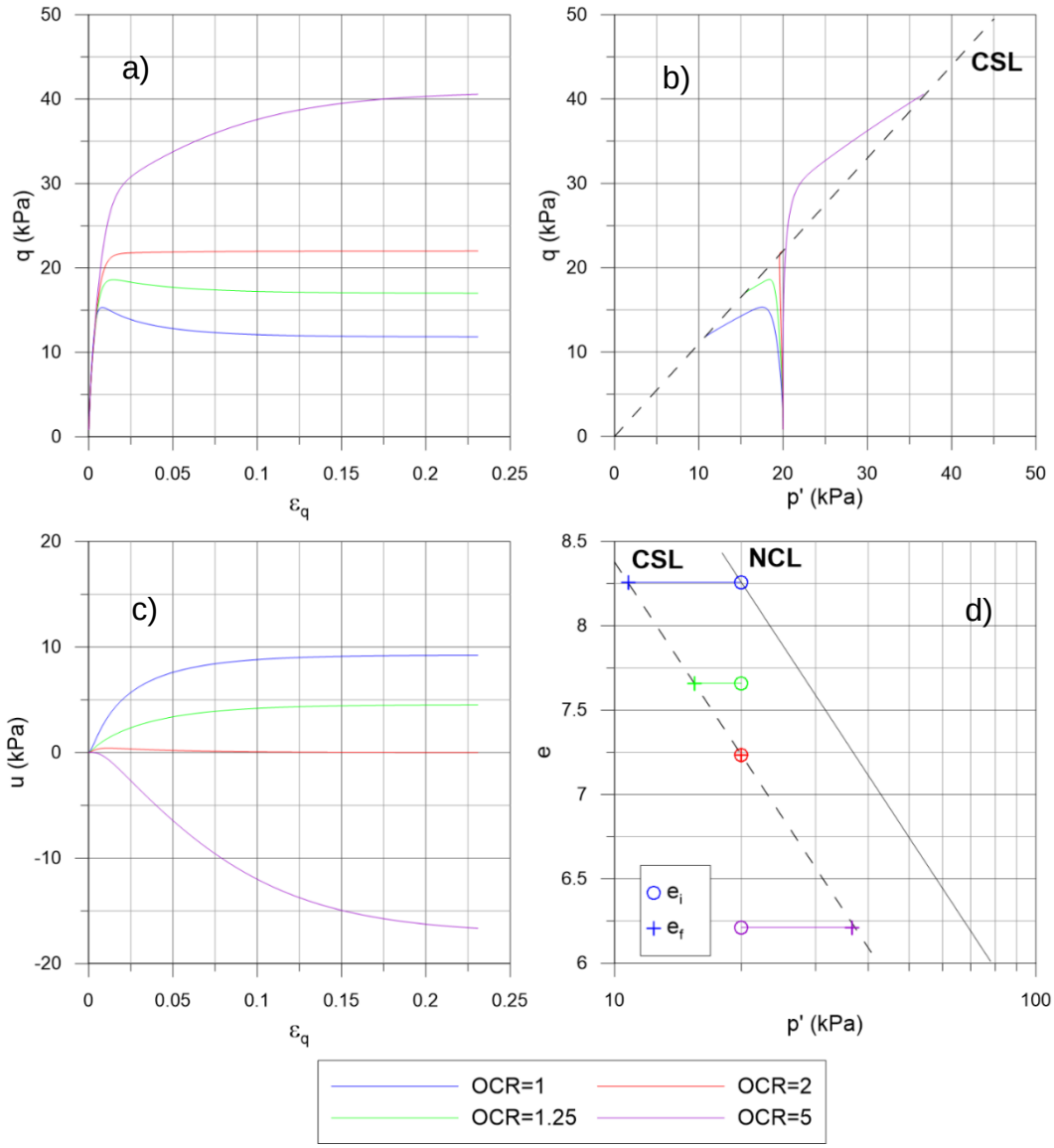

Figure 7-13 Undrained simple shear tests at same initial confining pressure but different OCR a) deviatoric stress vs. deviatoric strain, b) deviatoric stress vs. mean effective stress, c) pore pressure vs. deviatoric stress and d) void ratio vs. mean effective stress

7.3.2 Undrained Cyclic Triaxial Tests

Two simulations of undrained cyclic triaxial tests on isotropically consolidated samples were performed with the same model presented in Figure 7-4. Instead of pushing the top two nodes only downward, the nodes are pushed alternatively up and down. Three different samples are used in both simulations. In the first simulations, all the samples

have the same preconsolidation pressure (50 kPa) but three different initial mean pressure (10, 25 and 50 kPa) which renders three different OCRs (5, 2 and 1 respectively). In the second simulation, the three samples are consolidated at the same pressure (20kPa) but at different OCRs: 1, 2 and 5. In both sets of simulations, the samples are loaded with 4 cycles of deviatoric strain amplitude of 1%. The loading is applied triangularly, and the loading frequency is 0.25Hz.

The results of the two simulations are presented in Figure 7-14 and Figure 7-15. In the figure the change of vertical stress $\Delta\sigma_v$ and the axial strain ε_a are plotted instead of the deviatoric stress and strain. From the first simulation, it can be seen clearly that the normally consolidated sample exhibit more cyclic degradation and higher pore pressure response. The most overconsolidated sample exhibits negative pore pressure, and the sample stiffens a little bit. In the second simulation, the same trends are observed. The negative pore pressure shown by the overconsolidated sample is a result of the relatively high value of n_d. Since the state variable is negative for overconsolidated soil samples, the dilatancy line is low M_d is small and the response is dilative.

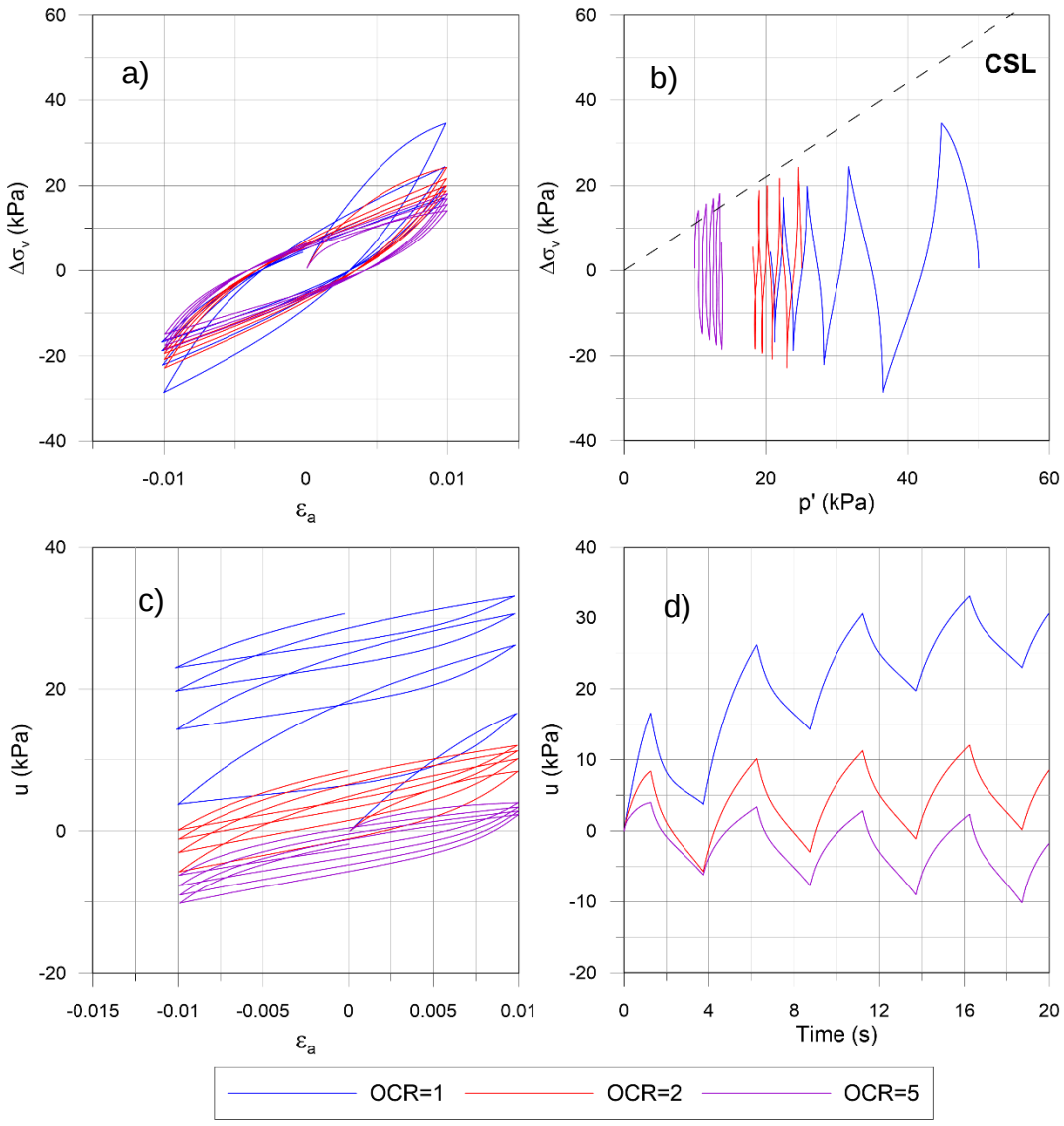

Figure 7-14Cyclic undrained simple shear tests at different initial confining pressure but same preconsolidation pressure a) deviatoric stress vs. deviatoric strain, b) deviatoric stress vs. mean effective stress, c) pore pressure vs. deviatoric stress and d) pore pressure vs. time

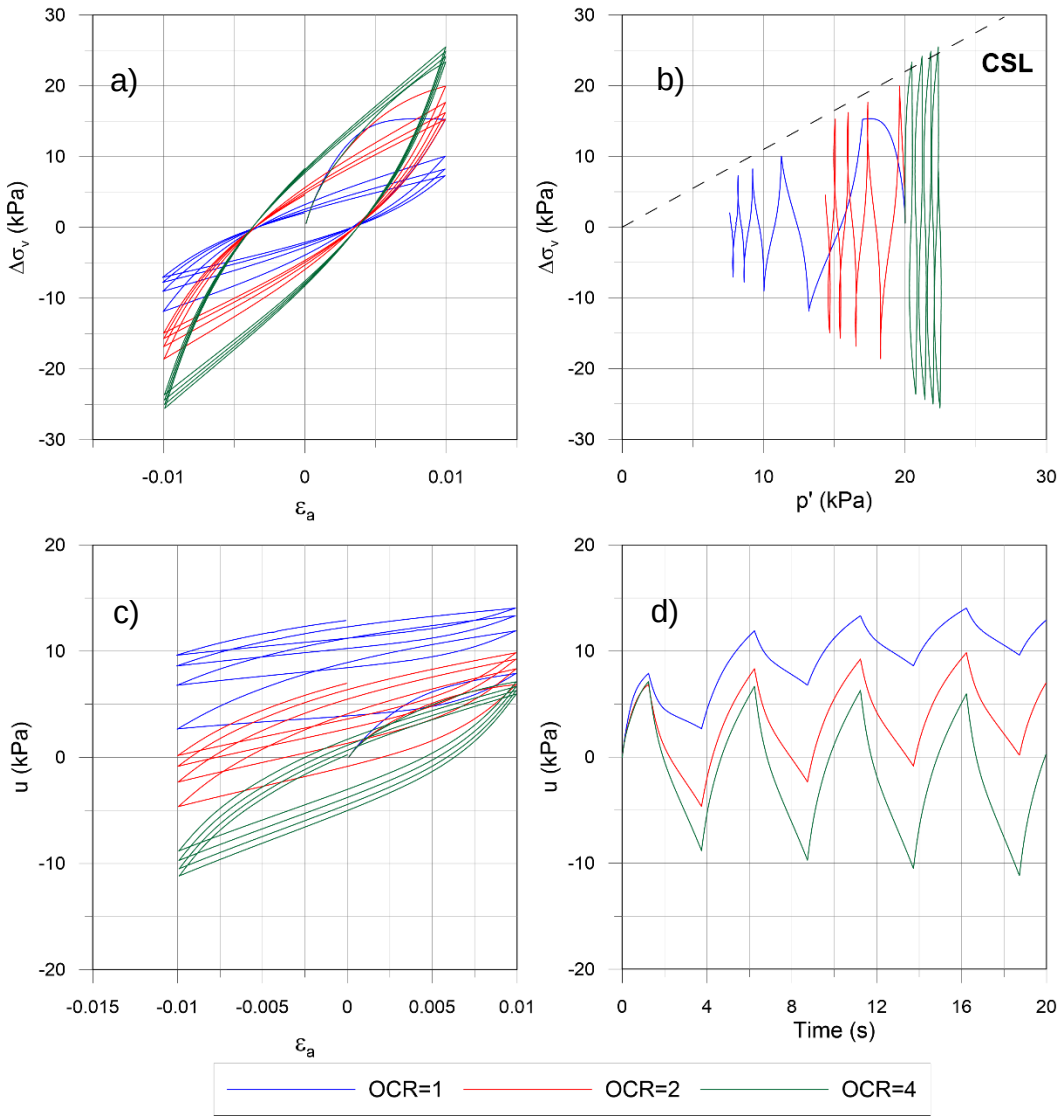

Figure 7-15 Cyclic undrained simple shear tests at same initial confining pressure but different OCRs a) deviatoric stress vs. deviatoric strain, b) deviatoric stress vs. mean effective stress, c) pore pressure vs. deviatoric stress and d) pore pressure vs. time

7.4 Sensitivity Analysis: Effect of A_0, n_b, and n_d in Undrained Triaxial Tests

This section presents a sensitivity analysis of the variables A_0, n_b, and n_d, through monotonic and cyclic undrained triaxial tests. For every variable, three sets of simulations are presented: monotonic on normally consolidated sample, monotonic on overconsolidated sample, and cyclic loading on slightly overconsolidated sample. Within

each sets the results are presented for different values of the variable studied. This section intends to give the reader a sense of how the three variables influence the response of the model, and how they can be modify to adjust the response of the model.

7.4.1 Summary of the Tests

The three different tests mentioned above (monotonic on normally and overconsolidated samples and the cyclic test on slightly overconsolidated samples) were all performed using the model described in Figure 7-4. In each tests the samples are isotropically consolidated to 20kPa. The tests on overconsolidated samples have an overconsolidation ratio of 4. The monotonic tests all reach a maximum deviatoric strain of 20%. The input parameters are listed in Table 7-3. The table lists values of A_0, n_b, and n_d, that are used when they are not the studied parameter.

Table 7-3 Input properties for the sensitivity study

Property	Value
λ	1.65
κ	0.175
M	1.1
ρ	1.1
γ_{PP}	0.01%
γ_{SS}	0.3%
OC	70
V_S	53
p_1	1
v_1	14.2
A_0	0.5
n_b	0.75
n_d	1

The cyclic tests were strain controlled undrained triaxial tests on slightly over consolidated samples (OCR=1.5) isotropically consolidated to 20 kPa. During the cyclic tests the samples were loaded with four cycles of deviatoric strain amplitude 1%. The loading is applied triangularly, and the loading frequency is 0.25Hz.

7.4.2 A_0

A_0 is the variable controlling the amplitude of the volumetric strains associated with deviatoric strains. Recall equations 7-9 and 7-10:

$$d = A_0(M_d - \eta) \qquad \textit{Equation 7-9}$$

$$d\varepsilon_v^p = d\left|d\varepsilon_q^p\right| \qquad \textit{Equation 7-10}$$

7.4.2.1 Monotonic Loading

During monotonic loading, A_0 controls the volumetric response which governs the evolution of p'. As a result, larger values of A_0 yield faster pore pressure response both in the normally consolidated case (Figure 7-16), and overconsolidated case (Figure 7-17). As a result of the pore pressure increasing faster, p' decreases faster, and critical state is reached faster. For lower values, critical state is reached so slowly that the response exhibits a peak stress for the normally consolidated case. The higher values of A_0 yield higher peak stress values. This does not happen in the overconsolidated case, where only a peak stress ratio can be observed. The amplitude of the peak stress ratio is not dramatically influenced by A_0 which mostly controls the rate at which the peak stress ratio and critical state are reached.

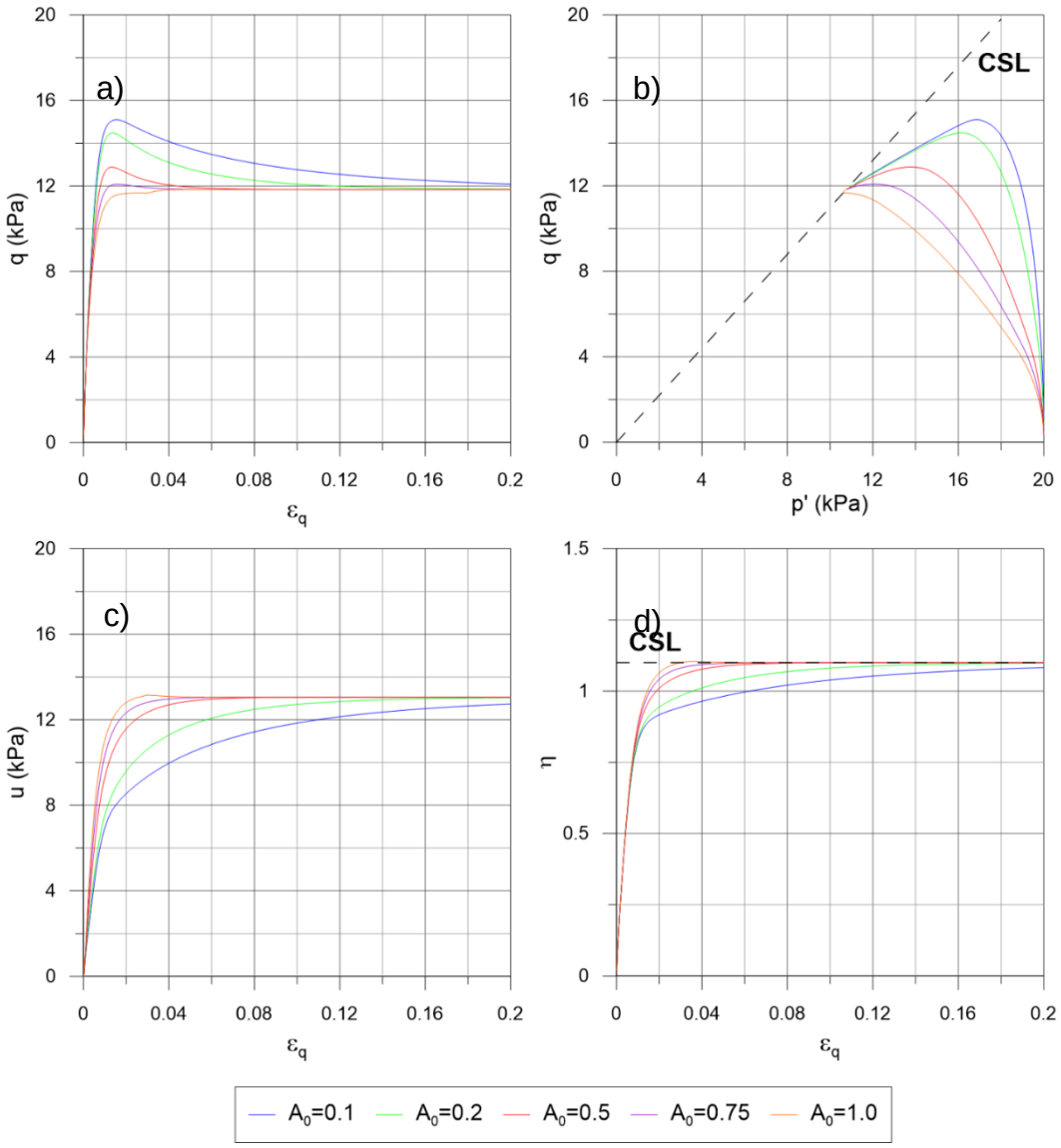

Figure 7-16 Effect of A_0 on monotonic undrained triaxial tests on normally consolidated samples a) deviatoric stress vs. deviatoric strain, b) deviatoric stress vs. mean effective stress, c) pore pressure vs. deviatoric stress and d) stress ratio vs. deviatoric strain

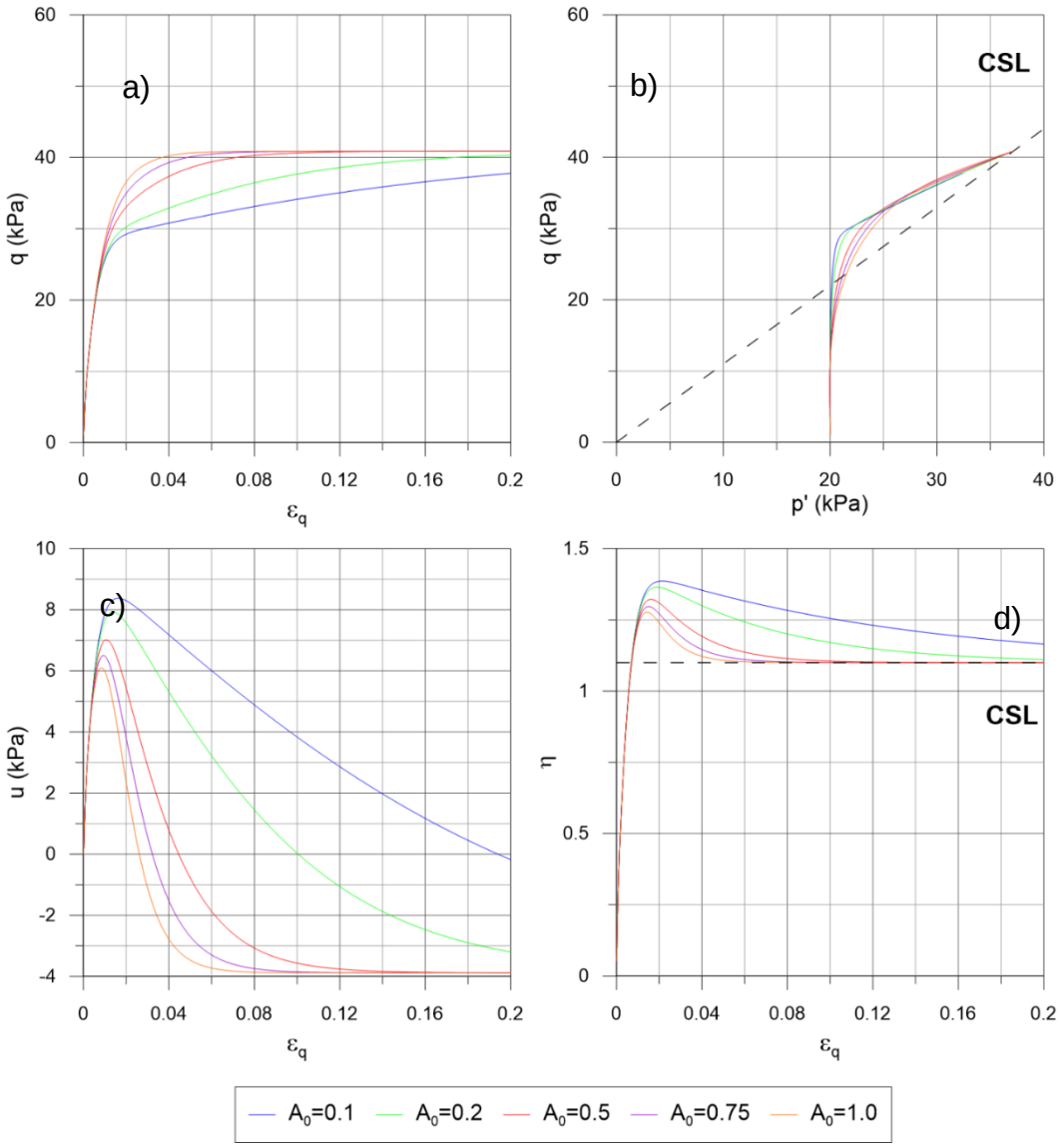

Figure 7-17 Effect of A_0 on monotonic undrained triaxial tests on overconsolidated samples a) deviatoric stress vs. deviatoric strain, b) deviatoric stress vs. mean effective stress, c) pore pressure vs. deviatoric stress and d) stress ratio vs. deviatoric strain

7.4.2.2 Cyclic Loading

Results of cyclic undrained triaxial tests are presented in Figure 7-18. Only three different values of A_0 are used here to make the plots clearer. As expected, higher values of A_0 generate more pore pressure, and p decreases faster but the difference between A_0=0.5

and 1 is not that important. Higher values of A_0 are also creating more cyclic degradation, which is due to pore pressure generation.

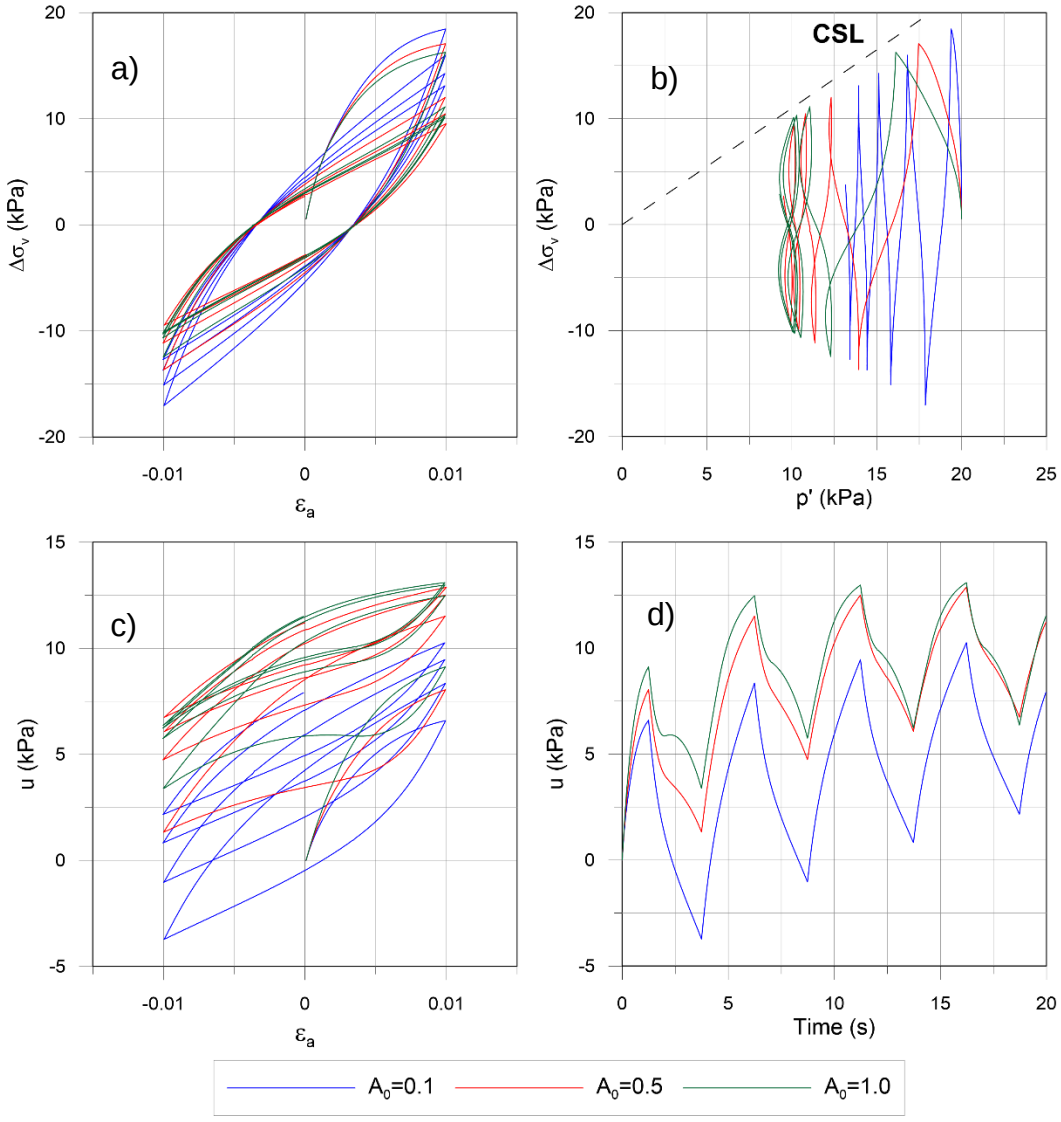

Figure 7-18Effect of A_0 on cyclic undrained triaxial tests on normally consolidated samples a) deviatoric stress vs. deviatoric strain, b) deviatoric stress vs. mean effective stress, c) pore pressure vs. deviatoric stress and d) pore pressure vs. time

7.4.3 n_b

The variable n_b controls the size of the bounding surface according to the following equation:

$$M_b = Me^{-n_b\psi}$$ *Equation 7-11*

This latter is then used to calculate the plastic modulus which is proportional to the difference M_b-η.

7.4.3.1 Monotonic Loading

On normally consolidated sample n_b has no influence on the pore pressure response (Figure 7-19), and only affects the deviatoric response. Normally consolidated samples never exhibit a peak stress ratio but exhibit a peak deviatoric stress for low values of n_b. For lower values of n_b, critical state is reached slower, at a higher deviatoric strain.

For the overconsolidated case (Figure 7-20), higher n_b yield higher peak stress ratios. For the higher values of n_b, the samples exhibit a peak stress, which is not the case for lower values. For overconsolidated case, n_b has also an influence on the pore pressure response. Initially, the behavior is contractive, and exhibit positive pore pressure response. It then becomes dilative and negative pore pressure develops. The final pore pressure is the same for all the sample, but the initial contractive response is greater for higher values of n_b and the final value of negative pore pressure is also reached faster. Overall, the response of the model is stiffer for higher values of n_b.

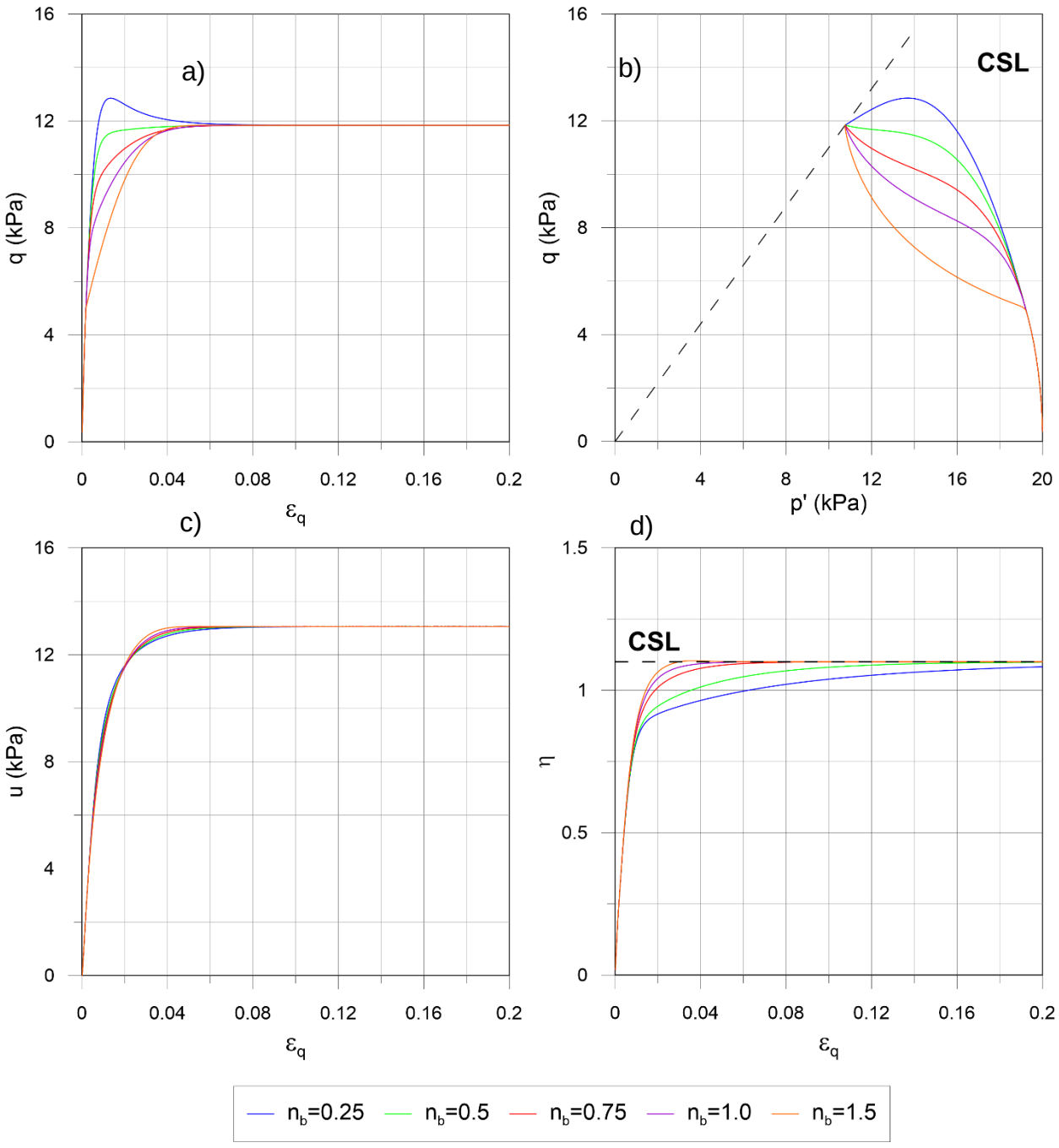

Figure 7-19 Effect of n_b on monotonic undrained triaxial tests on normally consolidated samples a) deviatoric stress vs. deviatoric strain, b) deviatoric stress vs. mean effective stress, c) pore pressure vs. deviatoric stress and d) stress ratio vs. deviatoric strain

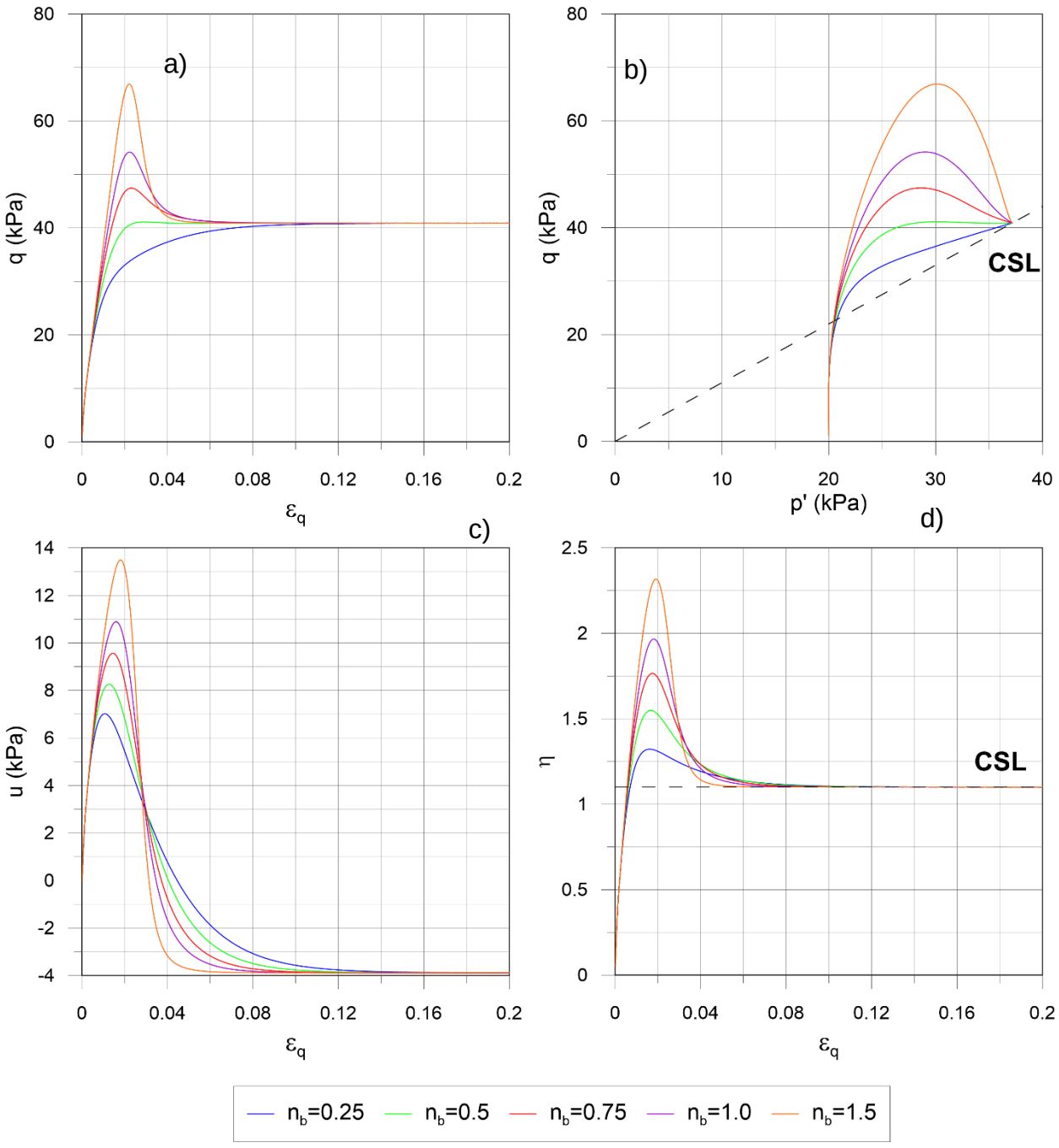

Figure 7-20 Effect of n_b on monotonic undrained triaxial tests on overconsolidated samples a) deviatoric stress vs. deviatoric strain, b) deviatoric stress vs. mean effective stress, c) pore pressure vs. deviatoric stress and d) stress ratio vs. deviatoric strain

7.4.3.2 Cyclic Loading

Since n_b defines the position of the bounding surface, it has very little influence on the cyclic behavior of the model (Figure 7-21), since the bounding surface is not used during cyclic loading. The simulations differ only because the initial loading is different, and unloading happens at different deviatoric stresses and different stress ratios. Once unloading begins, n_b has no influence on the pore pressure response, and on the overall cyclic behavior.

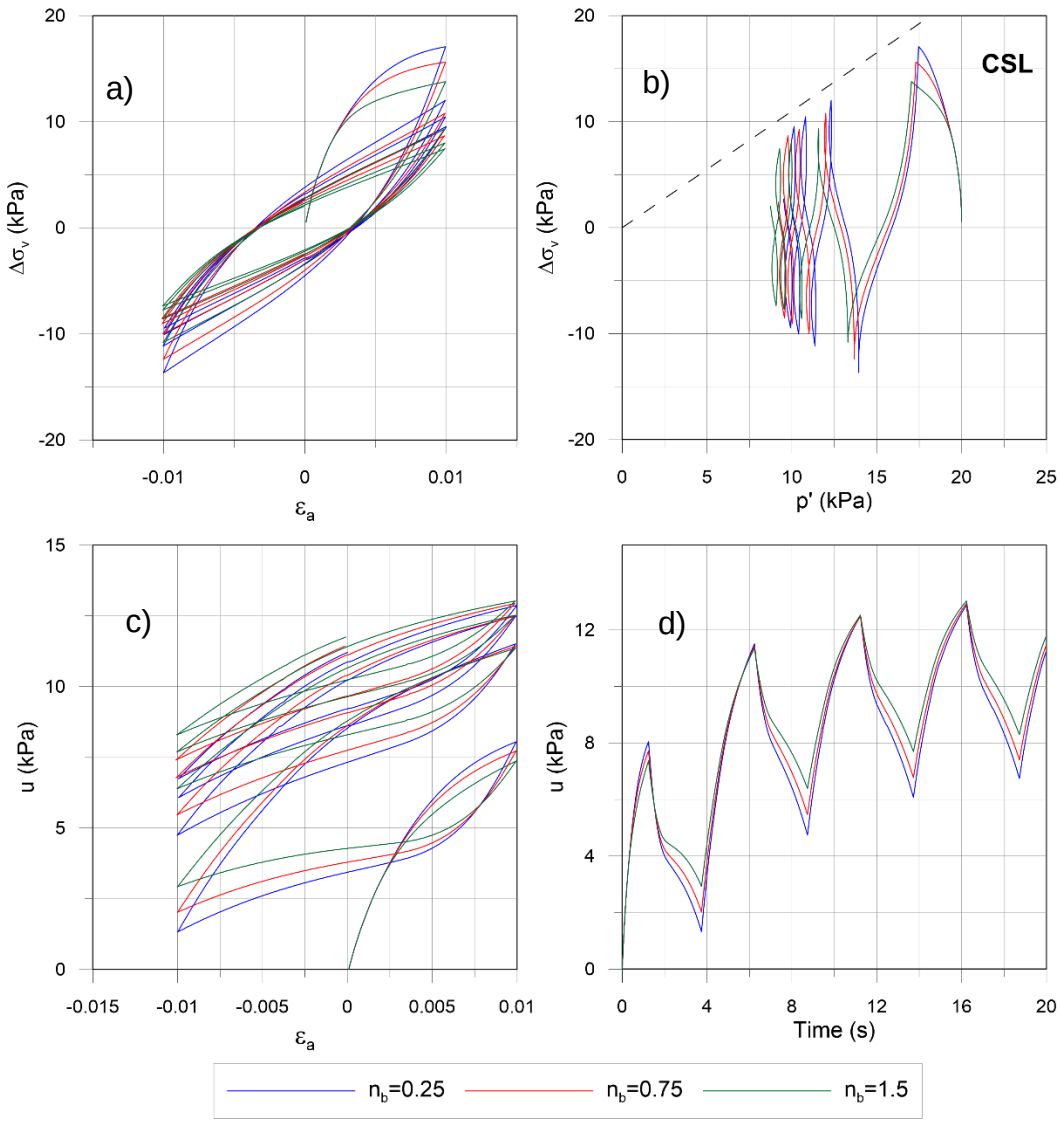

Figure 7-21 Effect of n_b on cyclic undrained triaxial tests on normally consolidated samples a) deviatoric stress vs. deviatoric strain, b) deviatoric stress vs. mean effective stress, c) pore pressure vs. deviatoric stress and d) pore pressure vs. time

7.4.4 n_d

The variable n_d is used to define the position of the dilation surface based on the state variable, with the following equation:

$$M_d = Me^{n_d\psi} \qquad \textit{Equation 7-12}$$

This dilation surface is used to calculate the plastic volumetric strains with the equations Equation 7-9 and Equation 7-10.

7.4.4.1 Monotonic Loading

During monotonic loading n_d controls the pore pressure response. For higher values of n_d, pore water pressure is generated faster and the critical state is reached faster. Since pore pressure develops faster, the stress path is less vertical for higher values of n_d. The same trends are observed for normally consolidated (Figure 7-22) and over consolidated (Figure 7-23). For overconsolidated soils, the peak stress is about the same for any value of n_d but the peak stress ratio is lower for higher values of n_d. The peak of positive pore water pressure is lower for higher n_d but the final pore pressure is reached faster.

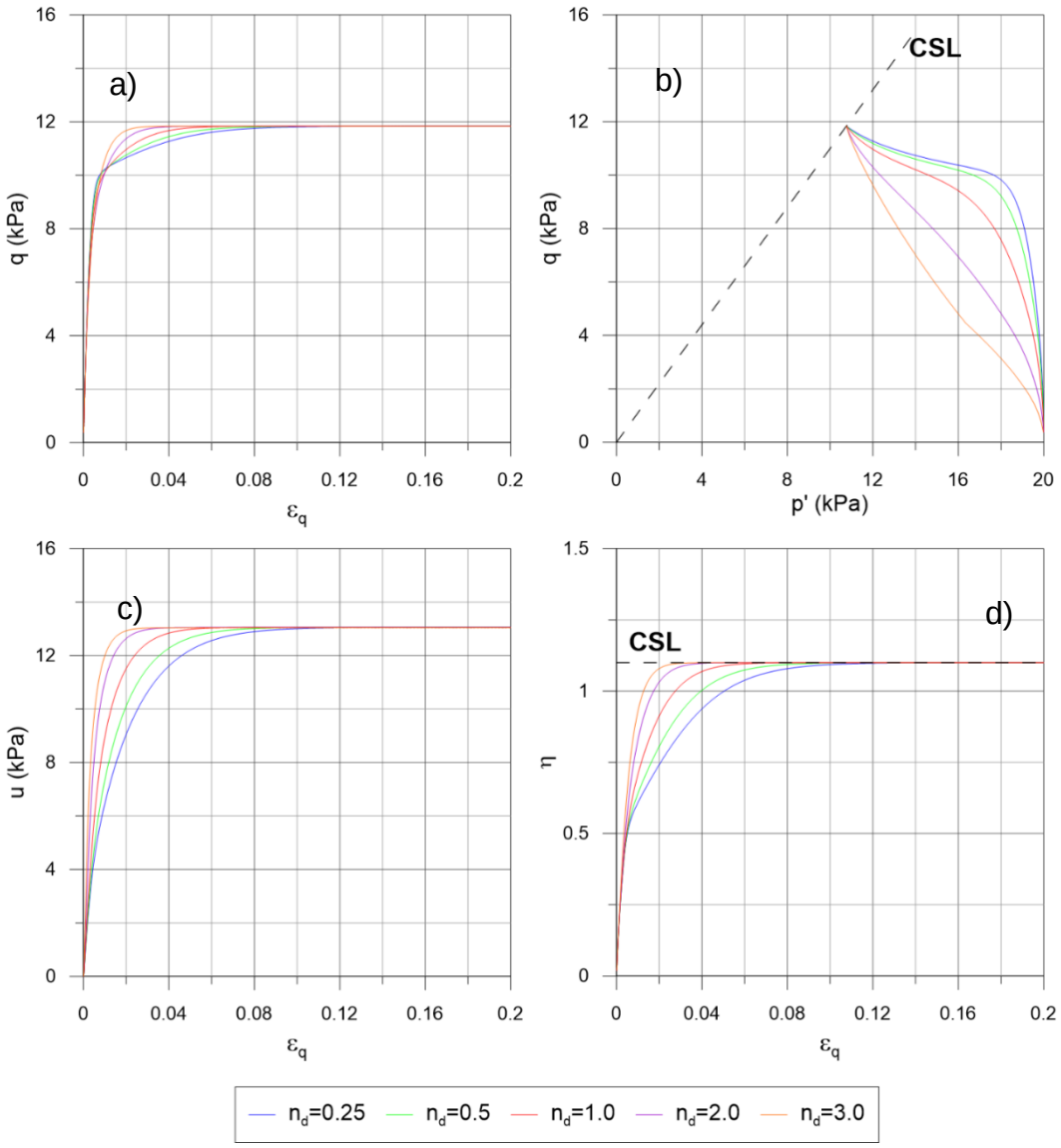

Figure 7-22 Effect of n_d on monotonic undrained triaxial tests on normally consolidated samples a) deviatoric stress vs. deviatoric strain, b) deviatoric stress vs. mean effective stress, c) pore pressure vs. deviatoric stress and d) stress ratio vs. deviatoric strain

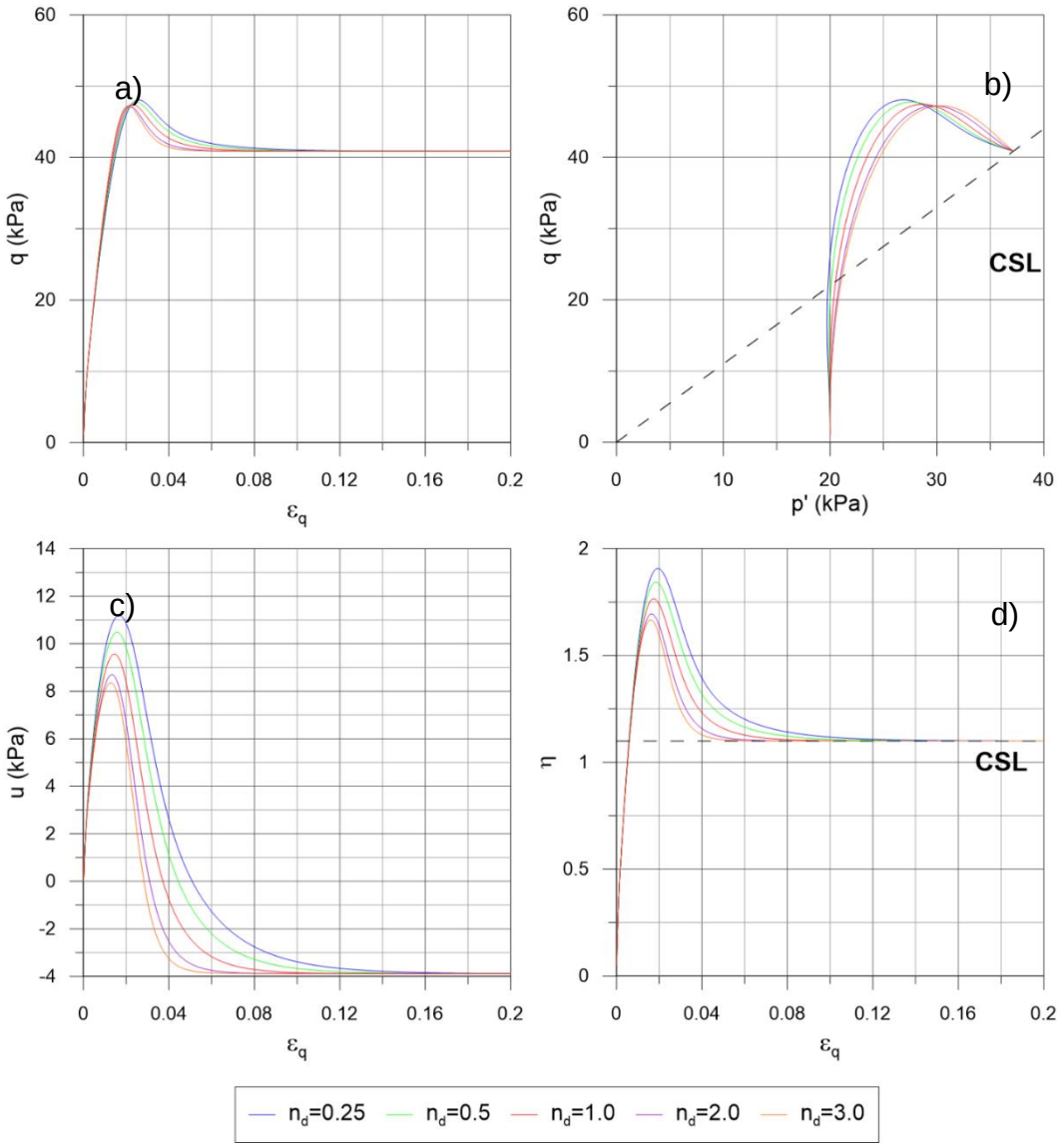

Figure 7-23 Effect of n_d on monotonic undrained triaxial tests on over consolidated samples a) deviatoric stress vs. deviatoric strain, b) deviatoric stress vs. mean effective stress, c) pore pressure vs. deviatoric stress and d) stress ratio vs. deviatoric strain

7.4.4.2 Cyclic Loading

In cyclic simulations (Figure 7-24), the initial part of the curve yields the same stress-strain curve, and only exhibits more pore water pressure. During unloading/reloading higher pore pressure response develops for lower values of n_d, and therefore there is

more cyclic degradation. The behavior becomes dilative for higher values of n_d at large strains.

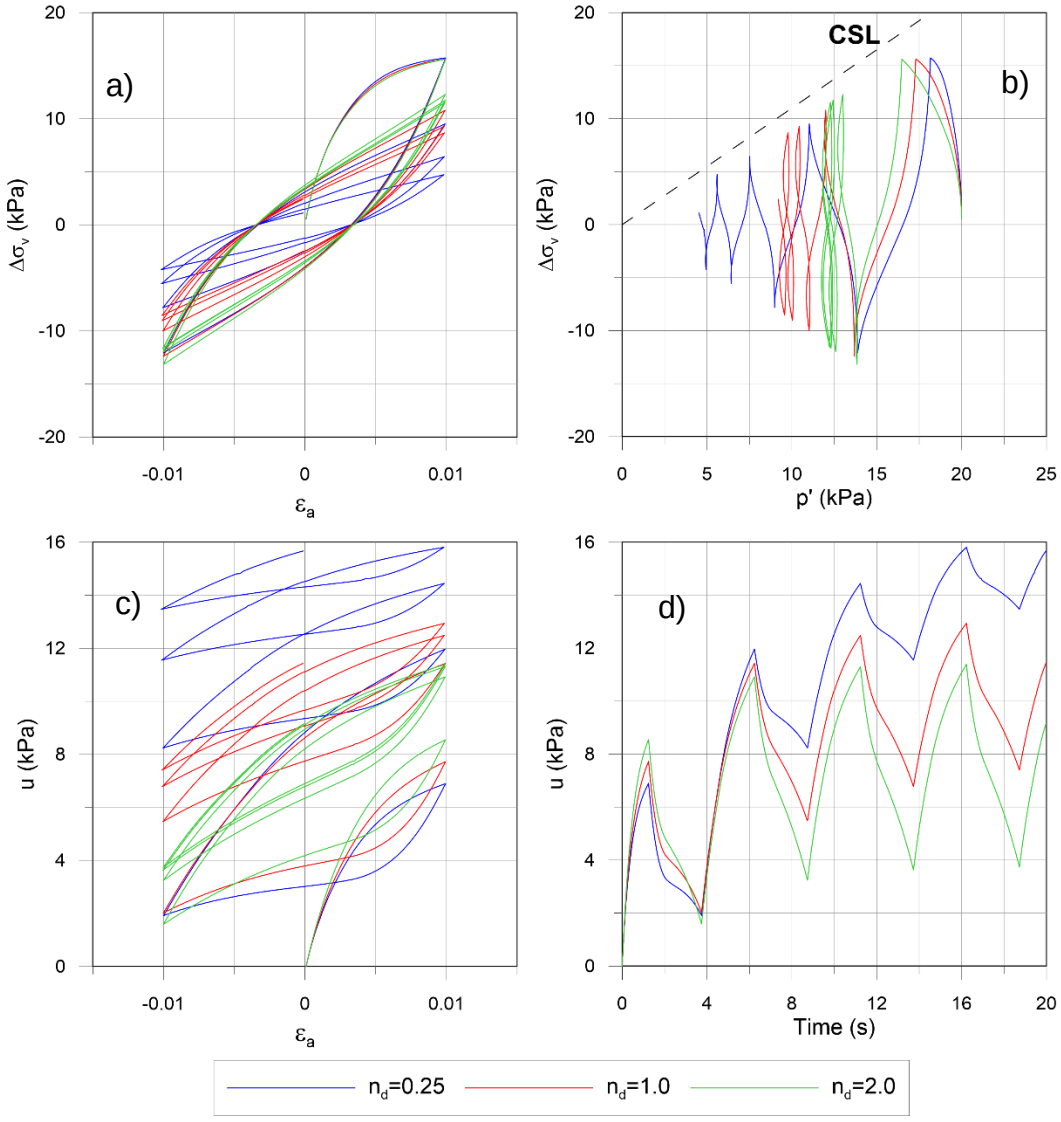

Figure 7-24 Effect of n_d on cyclic undrained triaxial tests on normally consolidated samples a) deviatoric stress vs. deviatoric strain, b) deviatoric stress vs. mean effective stress, c) pore pressure vs. deviatoric stress and d) pore pressure vs. time

7.5 Selection of Material Properties

This section explains how to select the different material properties for any material, except A_0, n_d, and n_b. For these three variables, the next chapter explains their calibration

process for peat, based on lab tests done by Ali Shafiee (2016). When using the model for another material than peat, the reader is advised to follow the same calibration process, but also to modify the definitions of the critical state line, maximum shear modulus, bulk modulus, and minimum damping.

7.5.1 Critical State Parameters

The model uses different parameters related to critical state soil mechanics, that are similar to the input parameters used in the modified cam-clay. The following parameters can be obtained through oedometer tests:

- κ, the slope of the recompression line, which can also be calculated from the recompression index: $\kappa = C_r/\ln(10)$
- λ, the slope of the virgin compression line, also related to the compression index: $\lambda = C_c/\ln(10)$
- e_1 and p_1 which specify any point on the isotropically normally consolidated line (ICL) in the void vs. mean effective stress space (e-p')

Numerous empirical relationships have been published to determine the compression index based on soil characteristics such as Terzaghi and Peck (1967) and Azzouz et al. (1976). These relationships are better suited for clays, and for peat, the following relationship (Moran et al. 1958, Keene and Zawodniak 1968) can be used:

$$C_c = w_0/100$$ *Equation 7-13*

Where w_0 is the initial water content. C_r is typically assumed to be 5 to 10% of C_c. Specific correlations for Sherman Island peat can be found in Shafiee (2016)

A triaxial or simple shear test, performed until critical state is reached, is used to determine *M*, the slope of the critical state line in *p-q* space. For a triaxial compression stress path, *M* is also correlated to the friction angle through the following equation:

$$M = \frac{6 \sin \phi'}{3 - \sin \phi'} \qquad \textit{Equation 7-14}$$

Mesri and Ajlouni (2007) lists typical values of ϕ' of different peaty soils, and this can be used to set M, if no strength tests are available. *M* can also be set by measuring the strength stress ratio, and published relationships (e.g. Ladd 1991) can be used.

7.5.2 Shape Ratio R

The shape ratio *R* as originally defined by Kutter and Sathialingam (1992), defines the shape of the yield surface. The intersection of the yield surface with the p-axis is the preconsolidation pressure, and corresponds to a point on the NCL. The ratio of the preconsolidation pressure at critical state to the mean effective stress at critical state is equal to *R*. Therefore, *R* also defines the position of the CSL relative to the NCL. In the *e-p* space the CSL has the following equation:

$$e_{cs} = \Gamma - \lambda \ln \frac{p}{p_1} \qquad \textit{Equation 7-15}$$

Where:

$$\Gamma = e_1 - (\lambda - \kappa) \ln \mathrm{R}$$

Equation 7-16

Different values of *R* yield different CSL (Figure 7-25). If the CSL and NCL are the same line, R=1. In the Cam-Clay model, R=2. If no information about the critical state line is available, *R* can be set to 2. More information about the position of *R* can be obtained with a triaxial or a simple shear test, if this latter reaches critical state.

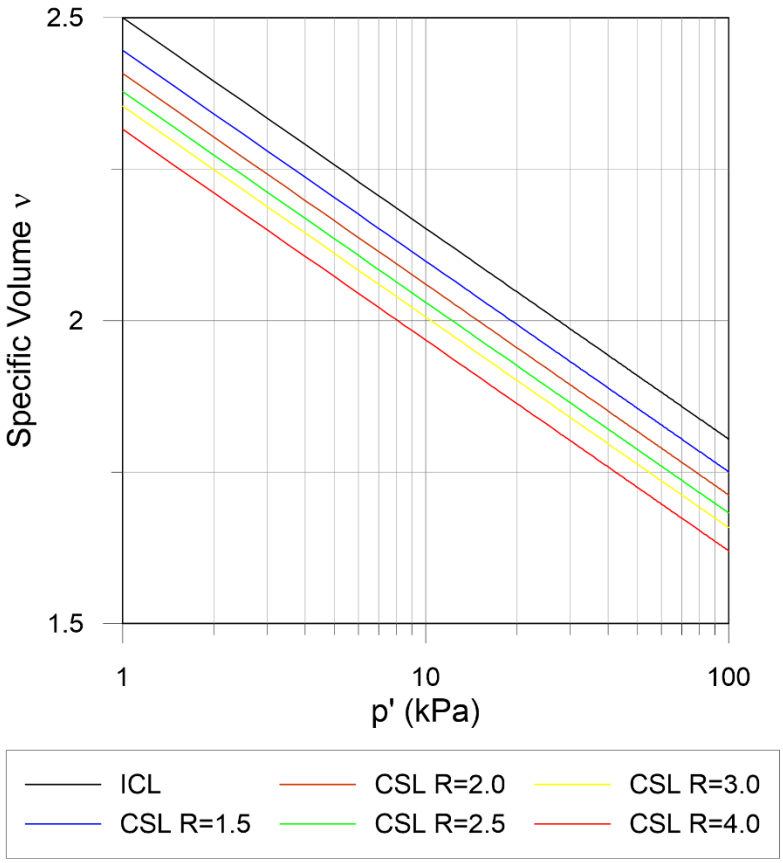

Figure 7-25 Effect of R on the position of the CSL

The shape ratio can also be defined with based on a normally consolidated strength ratio *S* (τ/σ'_v), following the concept developed by Ladd (1991). Based on the position on the critical state line in *q-p'* and *e-p'* space, the following equation can be derived:

$$R = e^{\frac{-\lambda \ln \frac{2 \cdot S}{M}}{\lambda - \kappa}}$$ *Equation 7-17*

7.5.3 Input Curves

The input curves G/G_{max} and $D\text{-}D_{min}$ vs. η, can be derived from modulus reduction and damping (MRD) curves plotted vs. shear strain following the procedure described in chapter 4. This can be done by calculating MRD curves plotted vs. shear strain from published empirical relationships. In chapter 4, three models were discussed, Darendeli (2001) for clay, Menq (2003) for sand, and Kishida et al (2009) for peat. The curves can also be derived from lab tests, using resonant columns tests to obtain the behavior at small strains, and using cyclic simple shear or triaxial tests at larger strains.

7.5.4 Selection of Fundamental Shear Strains: γ_{SS} and γ_{PP}

The model uses two so-called "fundamental" shear strains γ_{SS} and $\gamma_{PP.}$ γ_{SS} is the shear strain at which the model transitions from the "small strain" to the "large strain" algorithm during initial loading. At small strain, initial loading is controlled by the input modulus reduction curve, and at large strain the response of the model is controlled by a bounding surface algorithm. The strain γ_{SS} has no physical meaning, and cannot be observed or measured in a lab test. It represents the range of empirical validation of the modulus reduction curve. Empirical relationships typically use database that are limited to tests up to 0.3% shear strain. This limit is set as a default value but a user can modify it. If the user does not think the curve models the soil well at large strain, he can decrease this limiting strain. On the contrary, if the user believes the curve represents the soil behavior well at

larger strains, the user can decide to increase this limit. However, it is advised to set γ_{SS}<3%.

The strain γ_{PP} represents the threshold at which pore pressure starts to be generated, i.e. plastic volumetric strains develop under shear. In essence this is equivalent to the concept of volumetric cyclic threshold shear strain (γ_{tv}) described in Vucetic (1994). The volumetric cyclic threshold shear strain is described as the threshold separating cyclic strains that cause or do not cause significant permanent changes of soil microstructure. In the model these permanent changes of soil microstructure are modeled with the plastic volumetric strains. This threshold is defined by default as 0.01%, and can be modified by the user, following the recommendations of Vucetic (1994).

7.5.5 Other Material Properties

Besides critical state parameters, and dynamic curves, the model needs to know the overconsolidation ratio and the shear wave velocity. The overconsolidation ratio of the soil is most commonly obtained from an oedometer test (ASTM 2435). However, correlations between cone tip resistance and OCR can also be used such as Robertson and Cabal (2015).

Shear wave velocity can be calculated from empirical relationships (Kishida et al. 2006), field tests, or lab tests. For example, in the lab, the shear wave velocity can be calculated with bender elements in a triaxial cell. The maximum shear modulus can also be measured in resonant columns tests and the shear wave velocity can be calculated directly from it. In the field, geophysical methods such as spectral-analysis-of-surface-waves (SASW) can be used to obtain a profile of shear wave velocities.

Finally, if the model is used for peat, the organic content of the peat is needed. Organic Content is determine with a furnace (ASTM D2974) by burning the organic matter and weighing what remains. For peat the organic content is one of the most important parameter since numerous empirical relationships use it (Shafiee 2016).

8 CALIBRATION OF MODEL WITH LABORATORY DATA AND ONE-DIMENSIONAL GROUND RESPONSE SIMULATIONS

8.1 Introduction

This chapter presents the calibration of the model for the highly organic Sherman Island peat used in the centrifuge tests. The calibration is based on lab tests, and on measurements of shear wave velocity done during the centrifuge tests. The lab tests include index tests done on peat retrieved from the centrifuge experiments, and consolidation and strength laboratory tests done by Shafiee (2016) on Sherman Island peat with similar organic content. A list of the different tests performed is listed, and the selection of all the different model's input parameters is explained.

In order to present an example of the performance of the model, a comparison of one-dimensional ground response analyses performed in FLAC and in Deepsoil is presented. The simulations aim to represent the first phase of the test RCK02 where a 6.1 m thick clayey levee atop a 5.1 m thick peat layer was shaken with a recording from Kobe Earthquake. The displacement, acceleration and strain time series are compared, along with the response spectra of the output motions. The section does not intend to provide a thorough comparison among Deepsoil, FLAC, and the centrifuge measurements, but rather provides an example simulation for a single case.

8.2 Calibration of the Model for Sherman Island Peat

8.2.1 Peat Properties in the Centrifuge Test

The peat used in the centrifuge test was described in section 3.3.2.1, this section is summarized here. The peat was retrieved from Sherman Island in the Sacramento-San Joaquin Delta at depths of 2-3 m at the field test site documented by Reinert et al. (2014). During the test, two sets of bender elements recorded shear wave velocities at accelerations of 1, 5, 10, 20, 40, and 57g during spin-up, thereby enabling characterization of the shear wave velocity as a function of confining pressure. The following equation is used to characterize shear wave velocity as a function of vertical effective stress, σ_v':

$$V_s = V_{s1}\left(\frac{\sigma_v'}{p_a}\right)^b \qquad \textit{Equation 8-1}$$

V_{s1} and n are determined via least squares regression of the measurement from the centrifuge tests, and are found to be 33 m/s and 0.31, respectively. However, because of scatter at large confining pressure, and uncertainty at low confining pressure, this regression must be considered with caution. This regression also does not consider the effect of over consolidation on the shear wave velocity.

After the centrifuge tests, 14 samples of Sherman Island peat were retrieved from the models at different locations and different depths. The organic content was measured following the procedure described in ASTM D2974 and the average organic content was 68.8%, with a standard deviation of 3.3%. These measurements are consistent with

Shafiee's findings (2016) that found that organic content of peat is the highest at a depth of around 2m, and is between 60 to 80%.

8.2.2 Description of the Lab Tests and of the Calibration Process

Shafiee (2016) performed multiple tests on Sherman Island peat from 22 Shelby tube samples retrieved at depths ranging from 1 to 6 m. The samples tested cover a wide range of organic content, but only the tests on peat with organic content from 60 to 85% are used for the calibration of the model because their behavior is expected to be closer to the behavior of the peat used in the centrifuge tests.

Besides organic content, specific gravity was also measured following the procedure described in ASTM D 854-06 (ASTM 2010). At the range of organic content of interest, specific gravity is typically comprised between 1.7 and 1.9. For the sake of simplicity, 1.8 was selected.

Consolidation tests in an oedometer cell were conducted to measure the compression index (C_c), the recompression index (C_r), and the coefficient of secondary compression (C_α). The compression index and the recompression index are equal to $\lambda \cdot ln(10)$ and $\kappa \cdot ln(10)$, respectively. A summary of the tests used to calibrate the model is presented in Table 8-1. One of the tests was done on a peat sample retrieved from the centrifuge tests, and the results presented in Figure 8-1 are comparable to the average values obtained from the other tests. Therefore, this test was used to pick C_c and C_r and to determine the position of the NCL: p_1=10 kPa and e_1=9.6.

Table 8-1 Table of consolidation tests

Specimen ID	State of the sample	Depth (m)	OC	C_c	C_r	C_α
BH3S1_1.65	Undisturbed	1.65	64	6.70	0.57	0.32
BH6S2_2.10	Undisturbed	2.10	67	2.96	0.17	0.24
BH8S1_1.75	Undisturbed	1.75	66	5.59	0.47	0.28
BH8S2_2.20	Undisturbed	2.20	69	3.16	0.13	0.21
BH9S3_1.90	Undisturbed	1.90	78	5.90	0.82	0.35
BH8S1_R	Reconstituted	1.70-2.15	66	4.20	0.42	0.25
Centrifuge	Reconstituted	-	-	3.90	0.40	-
Average			68.33	4.63	0.43	0.28
Standard Deviation			4.87	1.52	0.26	0.05

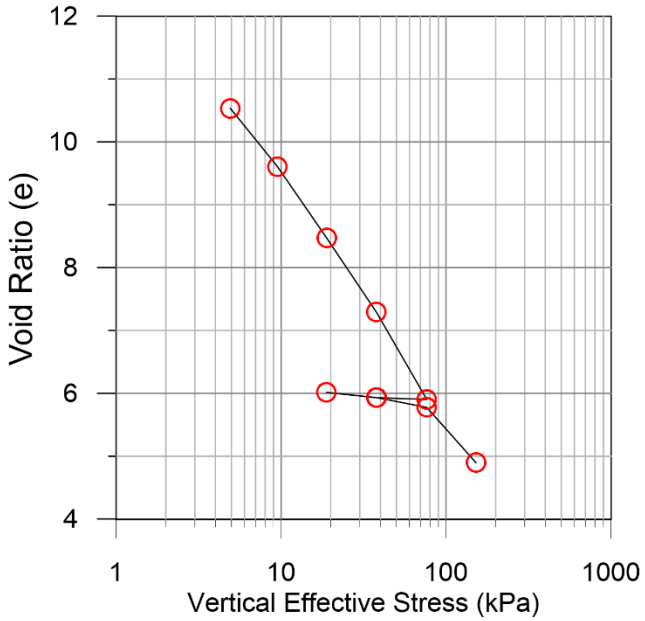

Figure 8-1 Consolidation test on peat retrieved from the centrifuge tests

A single monotonic undrained triaxial compression test was used in the calibration, and multiple cyclic and monotonic constant volume direct simple shear tests were also carried out. The cyclic direct simple shear tests were first used to derive the dynamic curves G/G_{max} and D-D_{min} vs η. Every sample was cyclic loaded in stages of different strain amplitudes. The loading was applied at the loading frequency of 1 Hz and for each stage

N sinusoidal cycles were applied. The list of all the tests used is presented in Table 8-2. More details on those tests is provided in Shafiee (2016).

Table 8-2 Summary of cyclic direct simple shear tests

Test ID	Borehole	Sample	Stage	Depth	N	γ_c %	σ_v	OCR	OC
CSS1	BH3	2	stage 1	1.7	15	0.91	39	1.14	65
CSS2	BH3	2	stage 2	1.7	15	2.74	39	1.14	65
CSS3	BH3	2	stage 3	1.7	15	9.10	39	1.14	65
CSS4	BH6	4	stage 1	2.25	15	1.34	12.1	4.83	67
CSS5	BH6	4	stage 2	2.25	15	4.02	12.1	4.83	67
CSS6	BH6	4	stage 3	2.25	15	13.38	12.1	4.83	67
CSS7	BH8	1	stage 1	2.2	15	0.04	100	1.75	70
CSS8	BH8	1	stage 2	2.2	15	0.14	100	1.75	70
CSS9	BH8	1	stage 3	2.2	15	0.38	100	1.75	70
CSS10	BH8	1	stage 4	2.2	15	1.30	100	1.75	70
CSS11	BH8	1	stage 5	2.2	15	3.97	100	1.75	70
CSS12	BH8	1	stage 6	2.2	15	13.18	100	1.75	70
CSS13	BH8	3	stage 1	2.25	5	1.09	32.7	2.04	70
CSS14	BH8	3	stage 2	2.25	5	3.24	32.7	2.04	70
CSS15	BH8	3	stage 3	2.25	5	10.78	32.7	2.04	70
CSS16	BH9	8	stage 1	2.45	15	0.04	34	1.18	60
CSS17	BH9	8	stage 2	2.45	15	0.12	34	1.18	60
CSS18	BH9	8	stage 3	2.45	15	0.36	34	1.18	60
CSS19	BH9	8	stage 4	2.45	15	1.14	34	1.18	60
CSS20	BH9	8	stage 5	2.45	15	3.48	34	1.18	60
CSS21	BH9	8	stage 6	2.45	15	11.51	34	1.18	60
CSS22	BH9	8	stage 1	2.45	30	1.28	26.7	2.15	60
CSS23	BH9	8	stage 2	2.45	30	3.40	26.7	2.15	60
CSS24	BH9	8	stage 3	2.45	30	10.69	26.7	2.15	60

The single monotonic undrained triaxial compression test was used to get strength parameters such as the critical state ratio *M* and the shape ratio *R*. A few cyclic direct simple shear tests were then used to calibrate n_d, n_b and A_0. Once the model was calibrated, it was used to simulate all the cyclic tests presented in Table 8-2. Finally, the calibration was validated against simulations of the monotonic tests. The monotonic tests

were also used to verify the strength parameter and the associated critical state ratio *R*. All the monotonic tests are summarized in Table 8-3.

Table 8-3 Summary of monotonic tests

Test ID	Specimen ID	Type of test	Depth (m)	OC	OCR	σ_v
Trx1	BH8_8_5	Triaxial	-	70	1.02	41.13
SS1	BH9S2_1.95	Direct Simple Shear	1.95	85	1.2	82.1
SS2	BH8S7_2.05	Direct Simple Shear	2.05	80	1.4	54.92
SS3	BH9S2_2.00	Direct Simple Shear	2	85	3.4	48.6
SS4	BH9S2_1.85	Direct Simple Shear	1.85	85	3.4	26.3
SS5	BH8S6_2.00	Direct Simple Shear	2	80	4.3	15.4

8.2.3 Modulus Reduction and Damping Curves

Input modulus reduction (G/G_{max}) and damping (D-D_{min}) vs. stress ratio (η) curves were derived from cyclic constant volume direct simple shear tests. For each stage, the secant shear modulus, damping ratio and stress ratio were calculated. The stress ratio was calculated by dividing the shear stress (τ) by the vertical effective stress (σ'_v). Since the results of the direct simple shear test at low strains do not permit precise measurement of the maximum shear modulus, Equation 8-1 was used to calculate the maximum shear modulus, with the relationship $G_{max}=V_s^2.\rho$. In the centrifuge, V_{s1} was found to be 38.6 m/s and b was found to be 0.486, when only the measurements at confining pressure greater than 10 kPa were considered. When calculating the normalized modulus reduction G/G_{max} with this relationship, values much greater than one were found at small strains, which is impossible. A possible explanation is that the relationship was derived for peat with high organic content (68.8% on average), but relatively normally consolidated. The peat tested in the direct simple shear device had a slightly lower organic content on average and some of the tests were ran on overconsolidated samples. Those two effects

would increase the maximum shear modulus. In order to account for that, V_{s1} was picked as 50 m/s. This value yields normalized modulus reduction values very close to 1 (Figure 8-2a) at small strains, and is therefore considered reasonable.

In order to plot a damping curve independent of the confining pressure (see chapter 4), a minimum damping value is needed. However, the simple shear device cannot accurately measure small-strain damping. Hence, the relationship by Kishida et al. (2006) was used which permits to capture the small strain damping dependence on confining pressure. When the D-D_{min} vs. η values from the lab tests are plotted, the scatter observed is small (Figure 8-2b).

In order to obtain a single modulus reduction and damping curve, a curve is fitted to the data with a least square regression. For the modulus reduction, a hyperbola is selected (Equation 8-2), because of its simplicity. The least square regression analysis yields a=0.285 and η_r=1.032. On Figure 8-2 are also plotted M_{SS}, the stress ratio at which the model stops using the modulus reduction curve, and M, the critical state stress ratio. Between the two lines defined by M_{SS} and M the model uses a bounding surface algorithm to control the strength, to eventually reach M. For the damping curve, Equation 8-3 was selected, and a and b were found to be 15.064 and 1.169 respectively. That equation forces D-D_{min} to be zero at small stress ratios, and provides a good fit of the data (Figure 8-2b). The extrapolation at large stress ratios (greater than 2) seems to over predict damping ratio but this is not problematic since the stress ratio for peat would not exceed 1.5. For a stress ratio of 1.5, the damping ratio is predicted to be 24.2%, which is reasonable. Since the cyclic tests were performed at high cyclic strains, the derived

modulus reduction is believed to represent accurately the soil behavior up to large strains, and γ_{SS} is therefore selected as 3%.

$$G/G_{max} = \frac{1}{1 + \left(\frac{\eta}{\eta_r}\right)^a}$$ *Equation 8-2*

$$D - D_{min} = a \cdot \eta^b$$ *Equation 8-3*

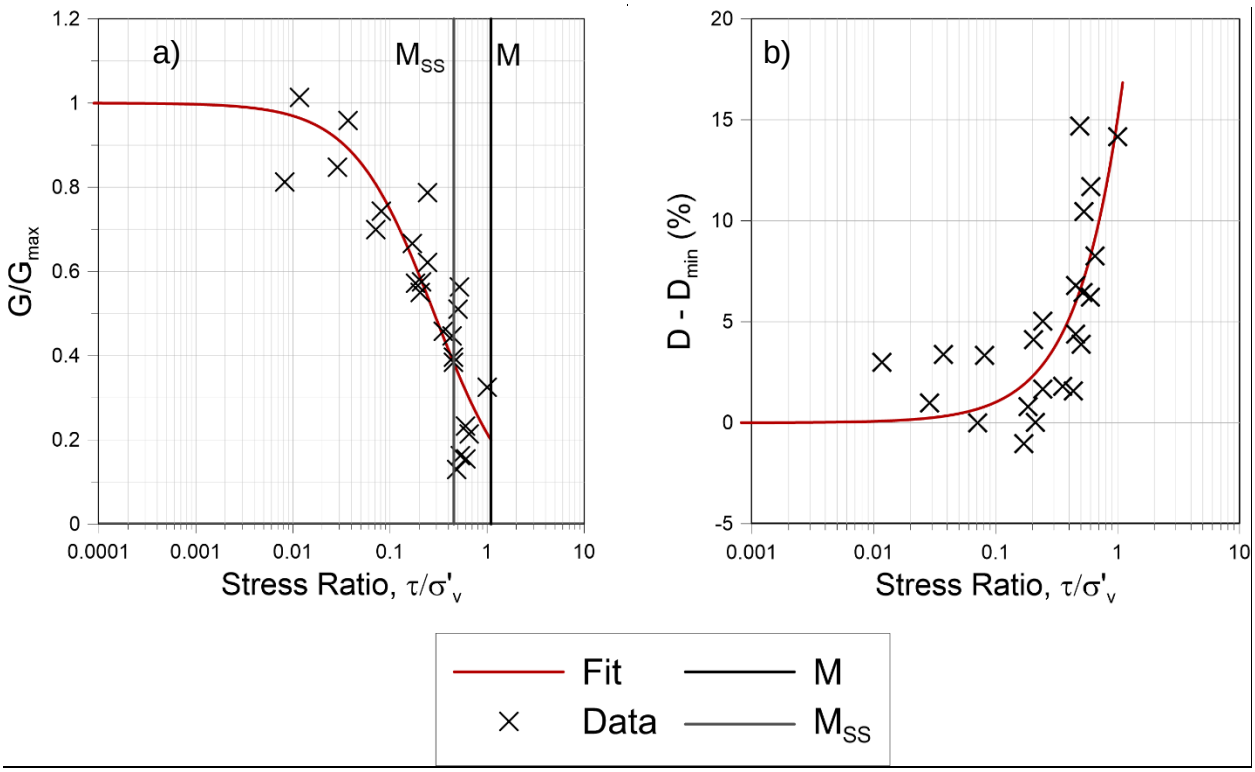

Figure 8-2 Input modulus reduction (a) and damping curves (b) derived from lab data

8.2.4 Monotonic Triaxial Tests

The results of a monotonic undrained triaxial compression test were used to obtain the critical state stress ratio *M*, and the shape ratio *R*. The triaxial test was used rather than a direct simple shear test because in a triaxial test, the full stress and strain tensors are known at any time. In a classic direct simple shear device, the lateral pressure is not

measured, therefore the stress tensor is not known and the critical state stress ratio is not directly measured.

The results of the triaxial test are presented in Figure 8-3. *M* was calculated directly from the data, by dividing the maximum deviatoric stress (*q*) by the mean effective stress (*p'*). The critical state stress ratio was found to be 1.9, which is equivalent to a friction angle of 46.2°. The friction angle measured is in the range of the observations of previous researchers that measured the friction angle of peat (Mesri and Ajlouni 2007). In particular Marachi et al. (1983) tested peat from the Sacramento San Joaquin Delta, and found a friction angle of 44°.

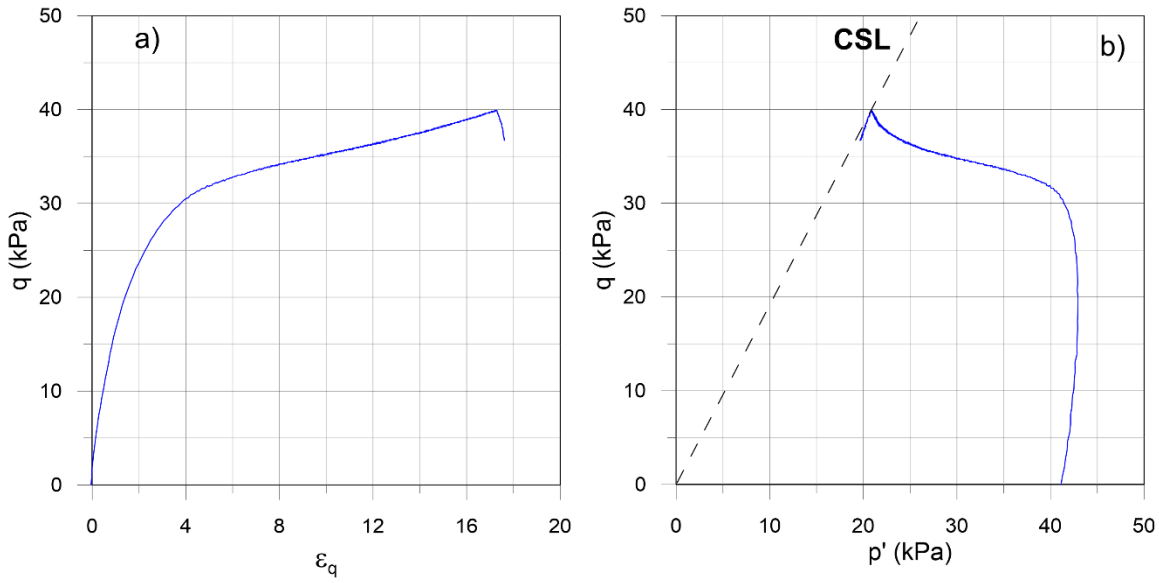

Figure 8-3 Triaxial test on peat, stress strain curve (a) and stress path (b)

The shape ratio R was calculated from the consolidation constants λ and κ, the position of the ICL and the mean effective stress at critical state (p_{cs}) according to Equation 8-4. The ICL has a slope λ of 1.69 and the recompression line has a slope κ of 0.17. The position of the ICL was defined by p_1=10 kPa and e_1=9.6, according to the section 8.2.2.

The mean effective stress at critical state was determined from the lab test and was 20.8 kPa. The shape ratio *R* was calculated as 2.17 which is close to the common assumption made by the Modified Cam-Clay of the shape ratio being equal to 2.

$$R = e^{\frac{e_1 - e_0 - \lambda \cdot \ln\left(\frac{p_{cs}}{p_1}\right)}{\lambda - \kappa}}$$ *Equation 8-4*

8.2.5 Cyclic Simple Shear Tests

The tests presented in Table 8-2 are simulated in order to calibrate the following parameters A_0, n_d and n_b. A few simulations were ran to manually tune the different parameters and find a set that simulates accurately the behavior of peat. Once a set was selected, all the tests were simulated to analyze the accuracy of the prediction. In particular the residual pore water pressure ratios obtained from the simulations were compared with the results of the lab tests. Shafiee (2016) developed a model to predict the residual pore water pressure due to cyclic loading, and considered that for high organic content, no pore water pressure is generated for strain levels up to 0.7%. This value was therefore selected as the pore pressure strain γ_{PP}.

8.2.5.1 Simulations of Cyclic Tests

At this point, the only missing parameters are A_0, n_d, and n_b. These parameters are manually adjusted on a few tests to provide the best fit possible, and their final values are presented in Table 8-4.The selection of the other parameters is described in the previous sections and two parameters are function of the confining pressure, and therefore different for every test. The density is calculated based on the initial void ratio and the

specific gravity, and the shear wave velocity is calculated based on Equation 8-1, with V_{s1}=50 m/s. All the tests were simulated with this set of input parameters, and some of the results are presented here, to illustrate the predictive capability of the model.

Table 8-4 Input properties for the cyclic simulations

Property	Value
λ	1.65
κ	0.175
M	1.9
R	2.17
γ_{PP}	0.70%
γ_{SS}	3.00%
p_1	10 kPa
e_1	9.6
A_0	0.002
n_b	0.75
n_d	0.3

Figure 8-4 presents the results of a test at small strains, the test CSS9. The strain amplitude for this test is lower than γ_{PP}, and as a result, no excess pore water pressure is generated, which is in agreement with the test results. This simulation also illustrates that the model is capable of producing realistic hysteretic loops even at small strains. However, the test results show a rounded tip, while the model has a sharp tip. The difference is explained by the viscous behavior of the soil, and therefore cannot be captured by the current formulation of the model.

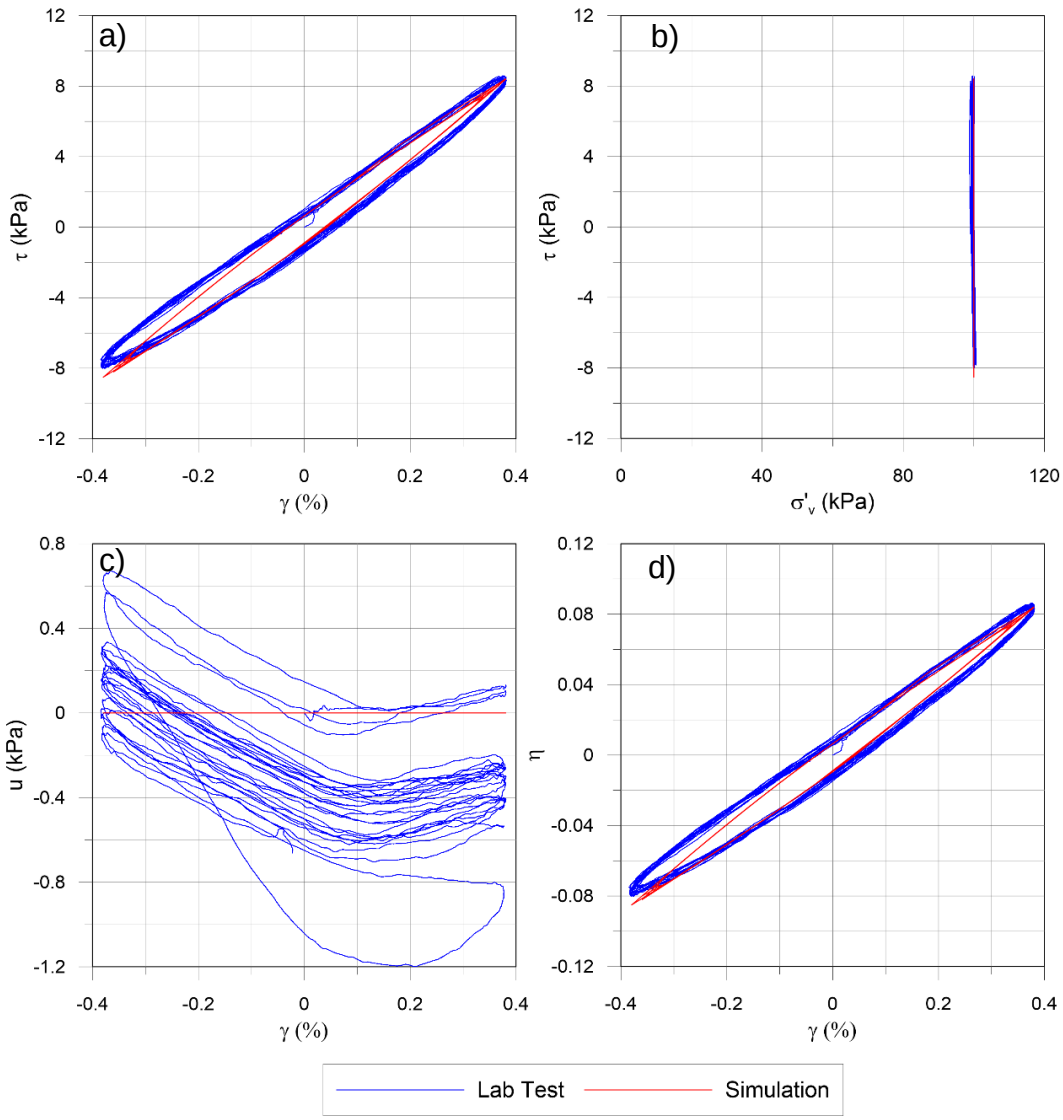

Figure 8-4 Simulation of CSS9

The simulation of the test CSS5 is shown in Figure 8-5. The simulation illustrates the capability of the model to produce hysteretic loops that are reasonable, and to match the damping behavior of the soil. In this example, the initial loading does not introduce too much excess pore water pressure, and the pore water pressure response of the model is realistic.

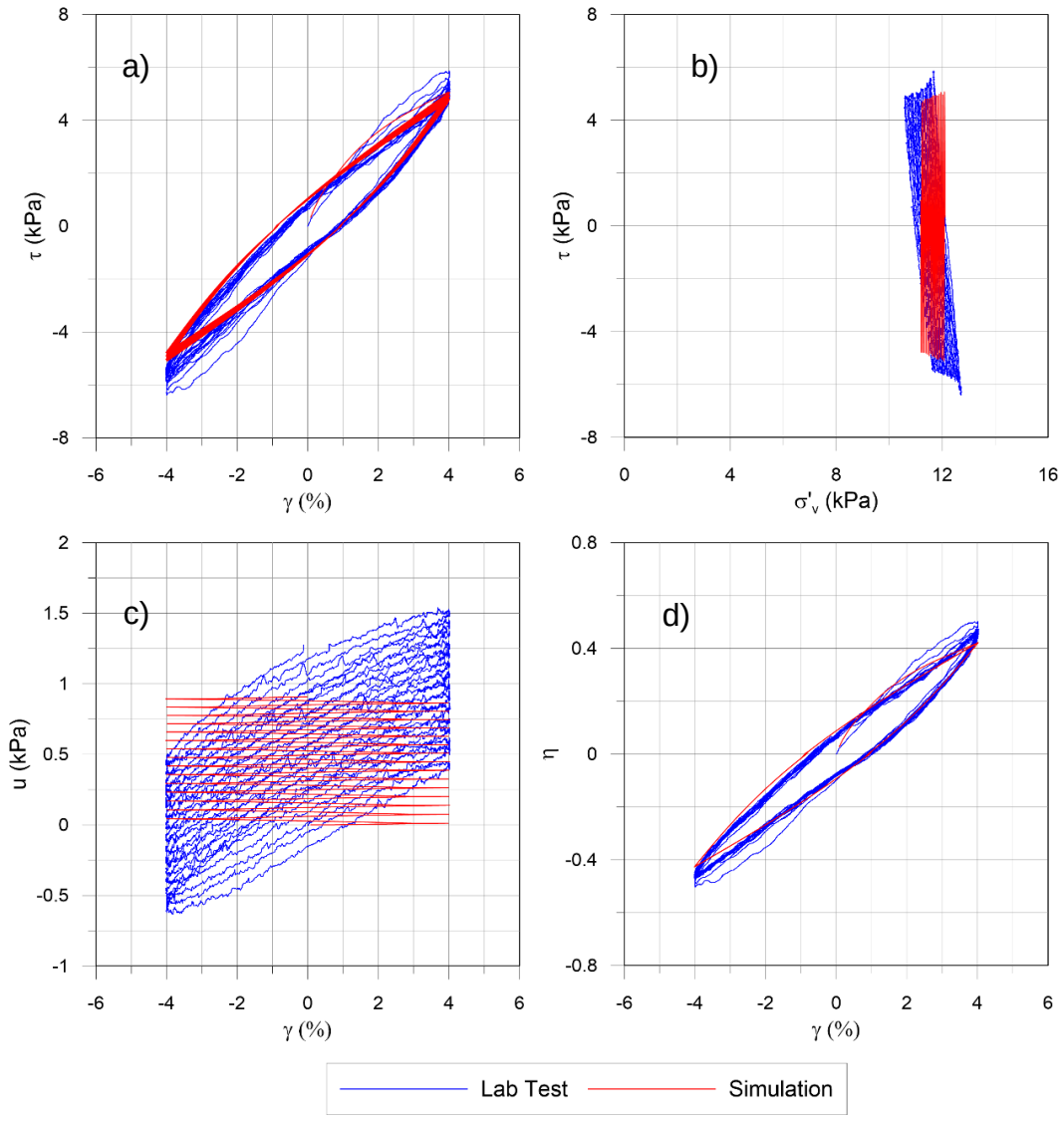

Figure 8-5 Simulation of CSS5

Figure 8-6 presents the simulation of the test CSS3. The test CSS3 is done on a slightly overconsolidated sample, and at an initial vertical stress of about 40 kPa. During initial loading, the model introduces too much pore pressure due to the formulation of the volumetric cap. Therefore the overall pore pressure response is slightly too contractive, but the stress-strain curve matches closely the test results. The stress ratio vs. strain curve shows an excellent match to the soil behavior, and confirms the inherent

assumption of the model that at upon constant cyclic strain amplitude, the peak stress ratio does not change. As a result, the stress ratio vs. strain does not exhibit degradation.

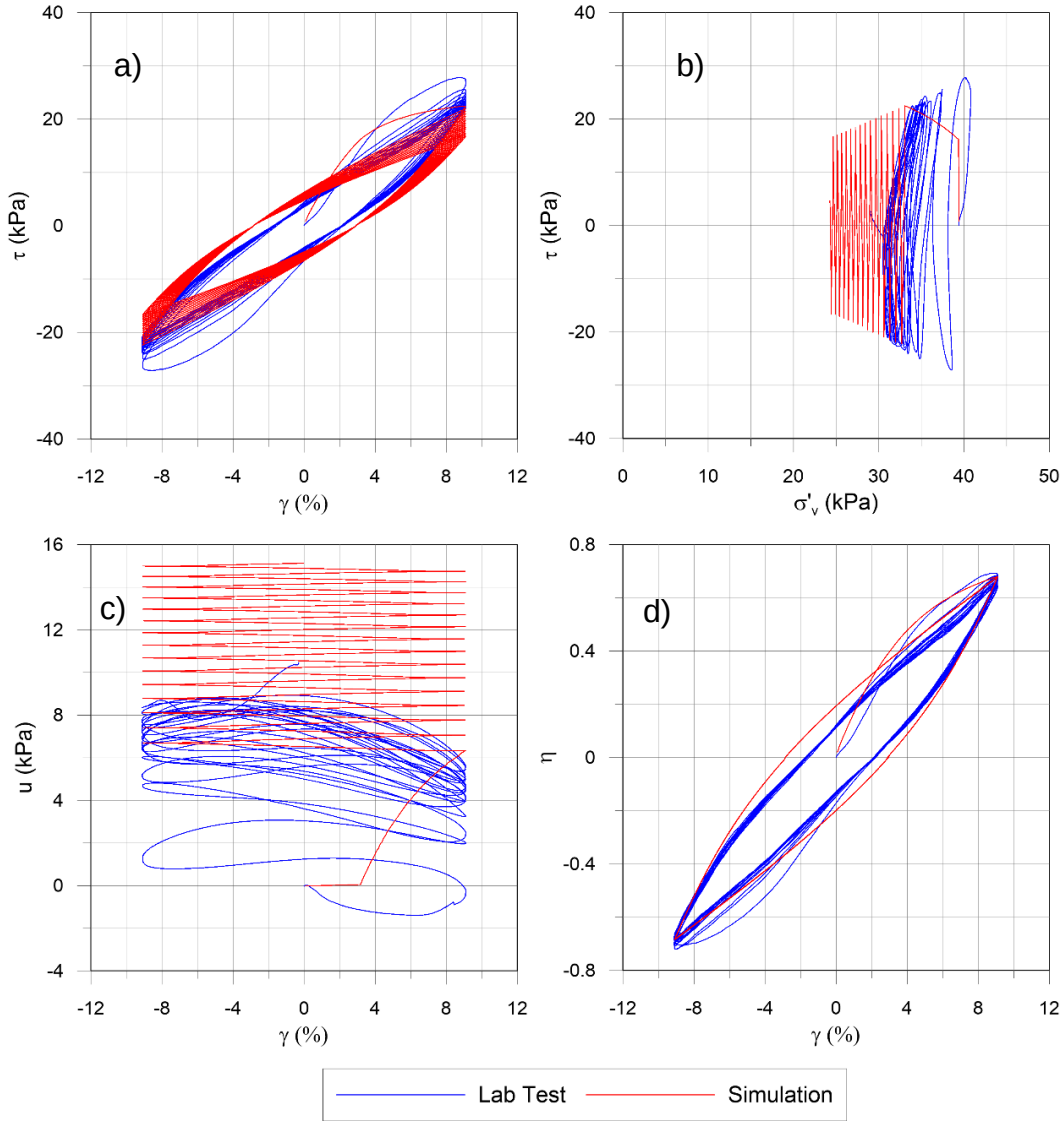

Figure 8-6 Simulation of CSS3

The simulation presented in Figure 8-7 confirms the excellent agreement of the stress ratio/strain loops (Figure 8-7d), and that stress ratio vs. strain curves do not exhibit degradation, contrarily to the stress strain curve. In this simulation, the soil is slightly more overconsolidated than the previous simulation (OCR=1.75), and therefore the pore

pressure response does not show an excessive pore water pressure generation upon initial loading. As a result, the overall pore pressure response matches more closely the test results.

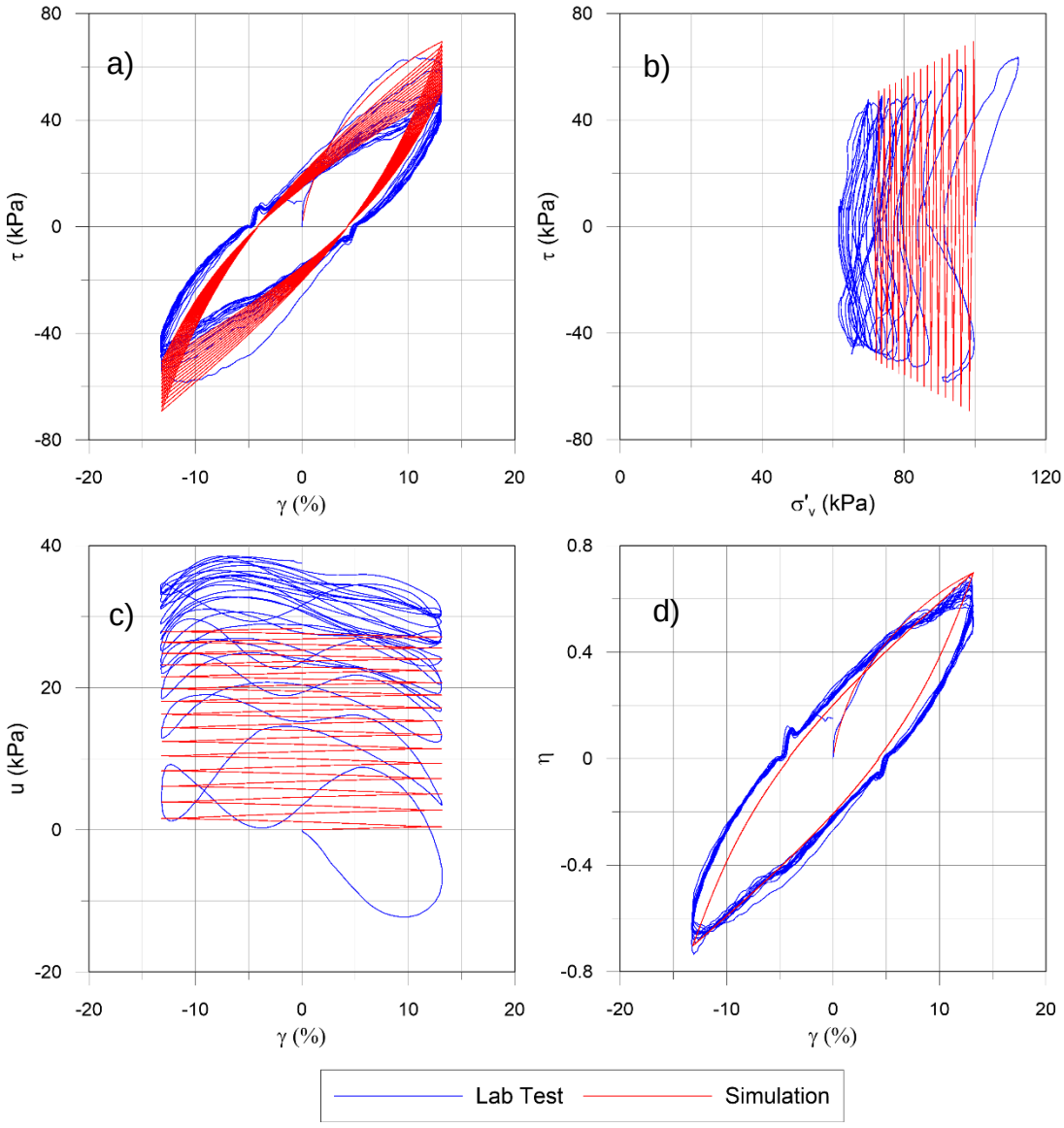

Figure 8-7 Simulation of CSS12

8.2.5.2 Residual Pore Water Pressure

The residual pore water pressure ratio resulting from the simulations of the cyclic direct simple shear tests are compared with measurements. The comparison is shown in Figure 8-8. The simulations and the lab tests are in good agreement overall. Some dispersion is observed, and appears to be increasing with the amplitude of the residual pore water pressure ratio.

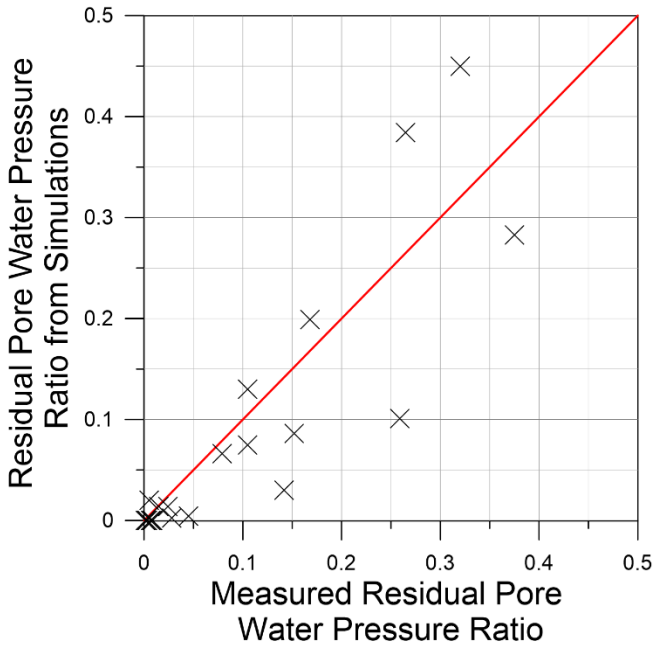

Figure 8-8 Comparison of residual pore water pressure obtained from the simulations and measured in the lab

8.2.6 Monotonic Simple Shear Tests

The five monotonic tests presented in section 8.2.2 are simulated with the set of input parameters presented in the previous section. The monotonic tests are simulated in order to verify that the parameters developed for cyclic loading provide a reasonable behavior upon monotonic loading.

8.2.6.1 Normally Consolidated Tests

The simulations of the monotonic tests are presented in Figure 8-9 and Figure 8-10. In both tests the strength is relatively well captured, but the initial response is stiffer than the real soil behavior. The stress path is reasonable, and the overall behavior is satisfactory.

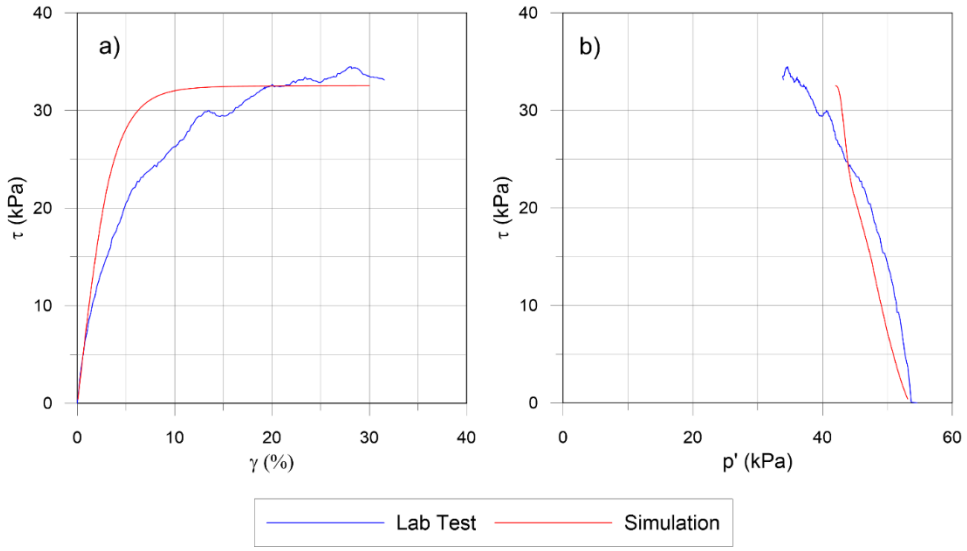

Figure 8-9 Simulation of SS1

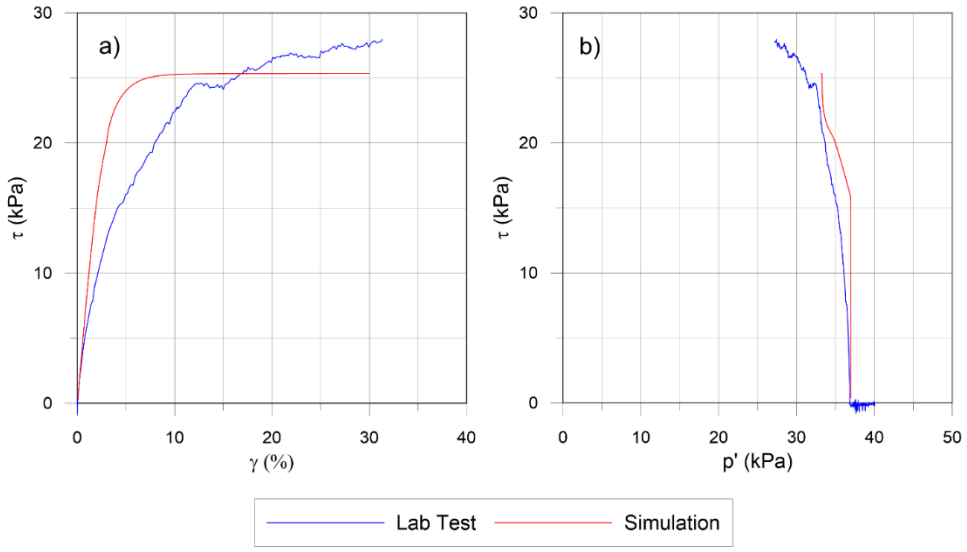

Figure 8-10 Simulation of SS2

8.2.6.2 Over-consolidated Tests

The simulations of the three over-consolidated tests are presented in Figure 8-11, Figure 8-12, and Figure 8-13. The strength is correctly captured in the three tests, although the strength is slightly over-predicted for the test SS5. Since A_0 is small in order to give a reasonable pore pressure response upon cyclic loading, the stress path is essentially vertical.

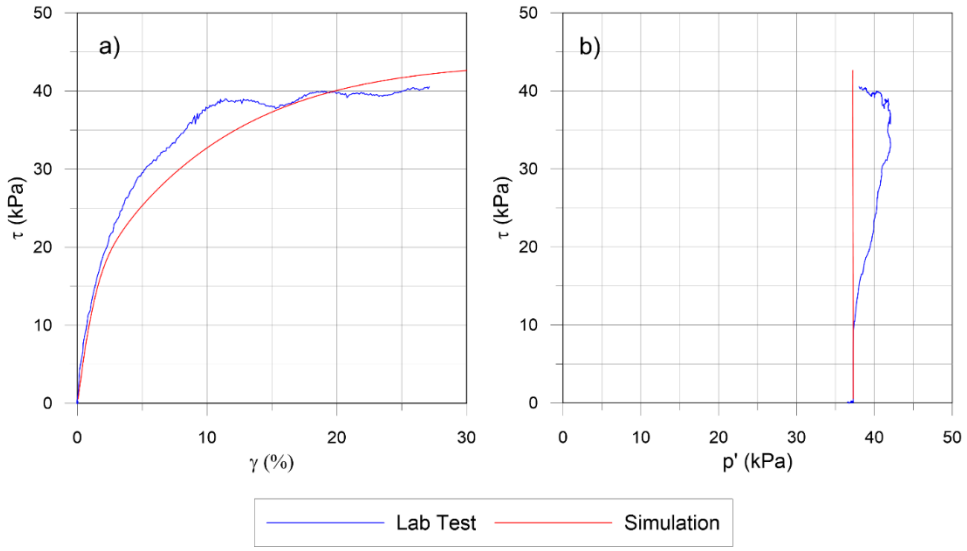

Figure 8-11 Simulation of SS3

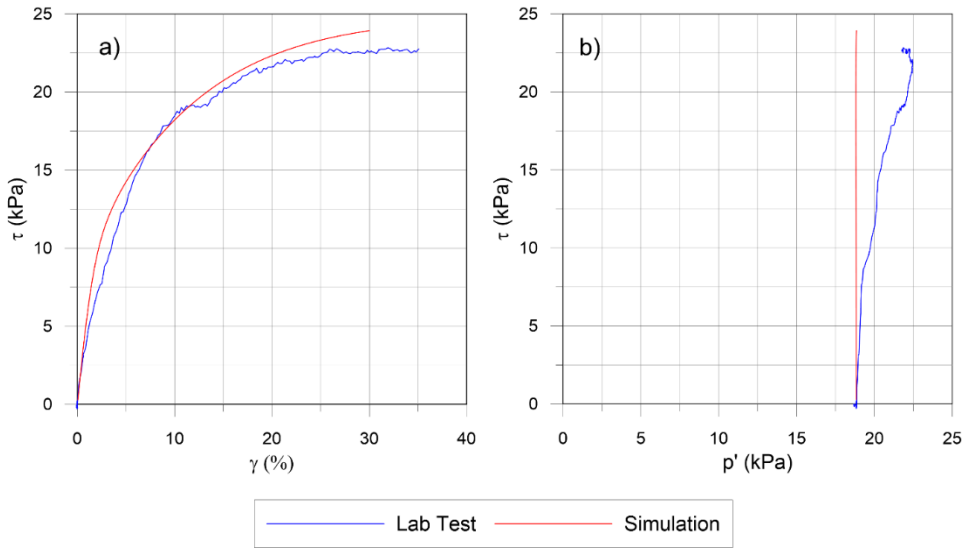

Figure 8-12 Simulation of SS4

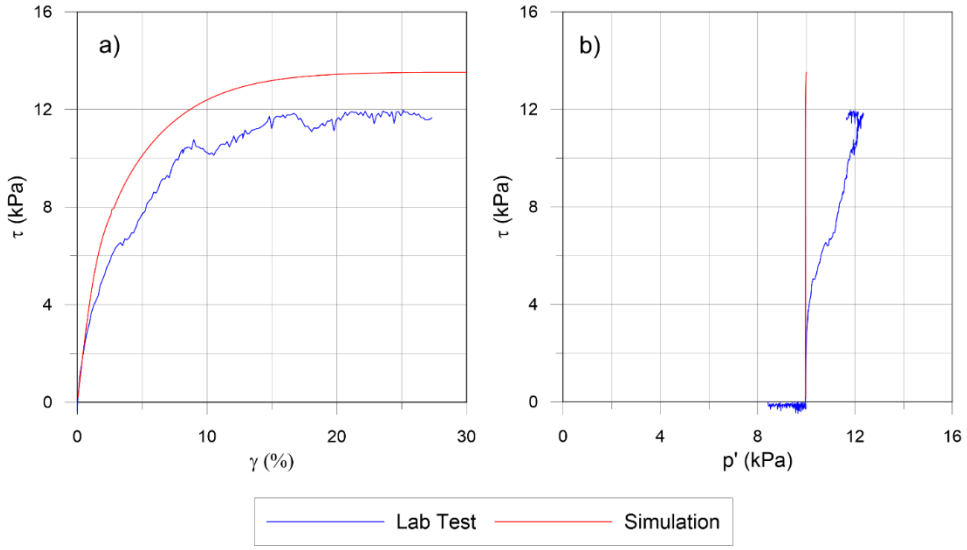

Figure 8-13 Simulation of SS5

The calibration process presented here yields satisfying input parameters to use in the site response simulations presented in the next section.

8.3 One Dimensional Ground Response Analysis of the Centrifuge Tests

8.3.1 Centrifuge Model

The model used in the centrifuge tests is presented in Figure 8-14. The one-dimensional simulations aim to represent the center of the model, indicated with a black line, where the peat layer is 5.1 m thick and the levee is 6.1 m thick in prototype scale. The 8.5 m thick layer of coarse sand situated beneath the peat layer is also modeled. The one-dimensional simulation is an approximation that fails to capture two-dimensional effects such as levee rocking. Nevertheless, one-dimensional simulations are often used for levee problems, with topographic amplification factors applied to account for two-dimensional effects (e.g., Kishida et al. 2009b).

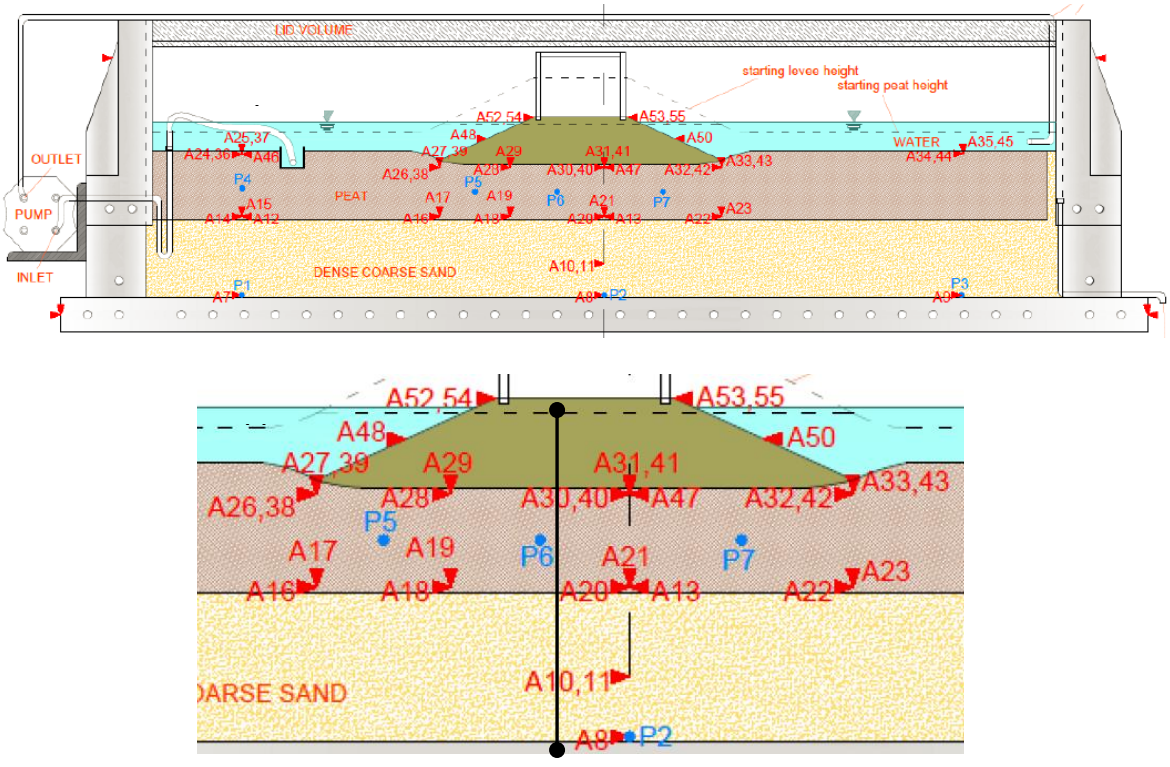

Figure 8-14 Centrifuge model in RCK02: a) instrumentation b) close-up

8.3.2 Numerical Models

The mesh used for the FLAC simulation consists of a single column of 74 elements (Figure 8-15 Numerical models used in FLAC and Deepsoil, and stress, shear wave velocity and unit weight profiles). The size of the elements was selected based on the work from Kuhlemeyer and Lysmer (1973), which states that to represent accurately the transmission of the motion the element size must be a tenth of the wavelength of the highest frequency component of the input wave that contains appreciable energy. In the centrifuge recordings, the motion does not show a significant Fourier amplitude for frequencies higher than 15 Hz. Based on a shear wave velocity of 39m/s, 0.2 m thick elements would be able to propagate signals up to 19 Hz, which is satisfying. Note that this assumption is only valid for elastic material, but provides a first approximation when defining a numerical mesh. The thickness of the bottom element of the levee and of the peat layer was only 0.1 m in order to model the prototype dimensions. The elements at the bottom of the mesh that model the layer of dense sand were 0.5 m thick. The width of all the elements was set to 0.5 m.

The bottom of the mesh was fixed in both directions, and all the nodes were constrained in the vertical direction. In order to model a one dimensional site response, nodes at the same elevation were forced to have the same horizontal displacements by using the “cable/slave” option in FLAC. Figure 8-16 Detail of the FLAC modelpresents a close-up of the bottom of the model, and shows the cables, along with the boundary conditions. The input acceleration record is applied at the bottom of the mesh.

The model simulates a total ground response analysis by not turning on the ground water module so that no pore pressure develops. In the absence of any knowledge of the K_0 coefficient, the soil was isotropically consolidated with total stresses calculated from the soil unit weight.

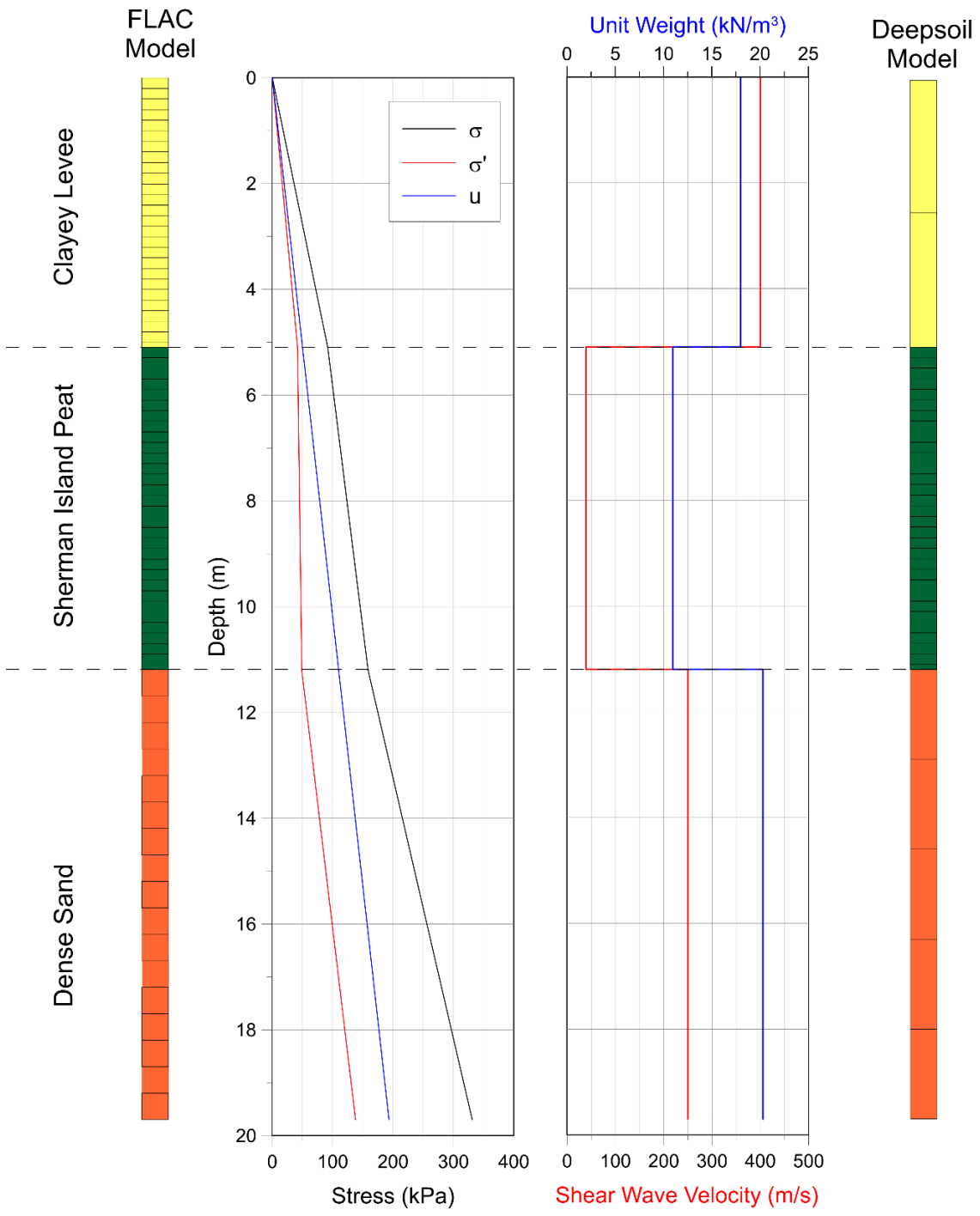

Figure 8-15 Numerical models used in FLAC and Deepsoil, and stress, shear wave velocity and unit weight profiles

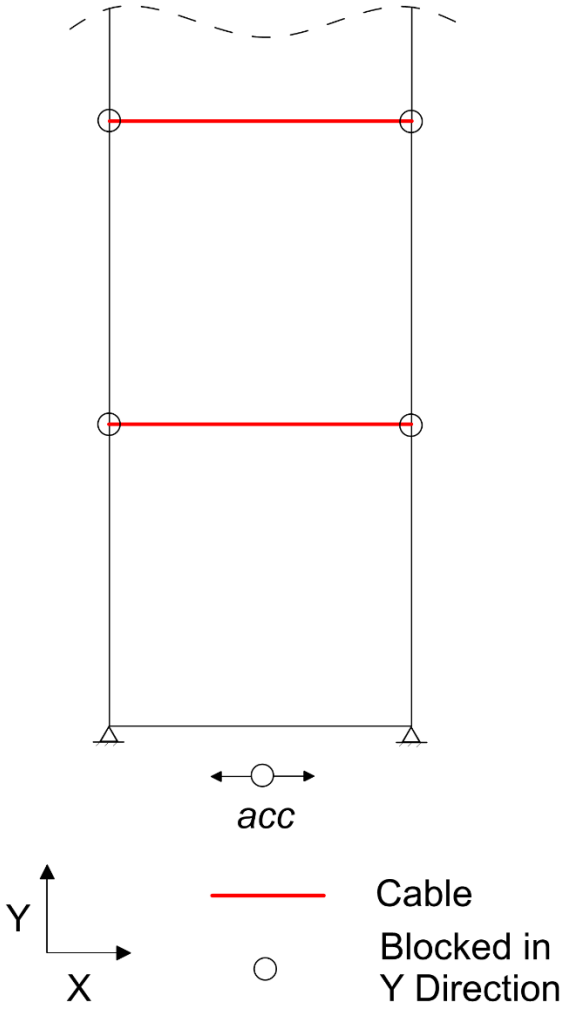

Figure 8-16 Detail of the FLAC model

A nonlinear total stress ground response analysis was performed in Deepsoil. The thickness of the layers modeling the peat layer were 0.2 m thick to be consistent with the FLAC model. Since the levee is more rigid than the peat, it was modeled with only 2 layers. The layer of dense sand at the bottom of the model was modeled, using 1.7m thick elements and the groundwater table was set to be at the top of the first layer. The model is presented in Figure 8-16. The maximum frequency which can be propagated through the profile is about 40 Hz. A rigid half-space was selected at the base of the model, following the recommendations from Hashash et al. (2015) for a within motion.

8.3.3 Input Parameters

For the sake of simplicity, the unit weight, the shear wave velocity were considered constant over depth for the clay, the peat and the sand (Figure 8-15 and Table 8-5). In the centrifuge test, the peat is initially normally consolidated and becomes overconsolidated as a result of secondary compression. Based on the overconsolidation ratio observed in samples tested in the lab, resulting from the secondary compression, the overconsolidation ratio was picked as 1.2 for the entire peat layer. Because of the low unit weight of the peat, the effective stress does not vary significantly in the peat layer (from 41.9 to 49.3 kPa), and the theoretical unit weight, using the parameters derived previously, shows little variation (from 10.84 to 11.06 kN/m^3), and was set to 10.95 kN/ m^3. The shear wave velocity was picked as 39 m/s based on the previously established relationship (Table 8-5 Material properties).

Table 8-5 Material properties

Material	Unit Weight (kN/m^3)	Shear Wave Velocity (m/s)
Clayey Levee	18	400
Peat	10.95	39
Dense Sand	20.3	250

The levee was simulated with an elastic material. The shear wave velocity of the modeling clay used for the levee was measured with bender elements and found to be 400 m/s. The unit weight of the clay was measured in the lab as 18 kN/m^3. Hence the modeling clay has a shear modulus of about 294000 kPa. Assuming that the clay is roughly incompressible, a Poisson's ratio of 0.49 yields a bulk modulus of 14602 MPa. The levee is much stiffer than the peat, and behaves essentially as a rigid body. Hence, I do not

anticipate that the simulations are sensitive to the material properties of the levee in this case.

The sand layer at the bottom is also modeled as an elastic material. Based on the properties of the Monterrey Sand described in Cappa et al. (2014b), the unit weight was 20.3 kN/m^3, and the shear modulus was 128700 kPa, based on a shear wave velocity of 250m/s. A Poisson's ratio of 0.49 was used to calculate the bulk modulus (6391900 kPa).

In FLAC the model presented in chapter 6 was used with the input parameters presented in Table 8-4. The modulus reduction and damping curves vs. stress ratios presented in Figure 8-2 were used. In Deepsoil, the input modulus reduction and damping curves for the peat layers were based on the same curves, but plotted in terms of shear strain. To do so, the inverse of the procedure presented in chapter 4 was used to obtain a different set of modulus reduction and damping curves for every layer, depending on the confining pressure.

In Deepsoil, all the layers were modeled using the MRDF-UIUC model. The levee and the dense sand were modeled with no modulus reduction and a constant damping ratio to model an elastic material. The MRDF-UIUC does not have the capability of fitting a straight line and render an elastic behavior, but the modulus reduction curve fit obtained from the clay layer was stiff enough to avoid introducing deformations in the clayey levee. The MRDF-UIUC does not provide a perfect fit of the input modulus reduction and damping curves, especially at large strains. However, the fit proved to be reasonable for all the peat layers. The simulations in Deepsoil could be further refined by using the latest GQ/H model, which would provide a better fit of the modulus reduction curves.

8.3.4 Viscous Damping

The model presented in this dissertation is introducing hysteretic damping even at low strains and therefore Rayleigh damping is not necessary to introduce small-strain damping. Therefore, no Rayleigh damping was used for the peat layer. However, if the damping is believed to be frequency dependent, a user can decide to use viscous Rayleigh damping in addition to the hysteretic damping provided by the model.

The input motion at the bottom of the sand layer is the motion recorded in the centrifuge at the bottom of the peat layer, i.e. at the top of the sand layer. The damping characteristics of the bottom sand layer were defined in order to retrieve the measured input motion at the top of the sand layer, so that the sand layer does not amplify or deamplify the motion. To do so, Rayleigh damping was used with a damping ratio of 25%, and a center frequency of 15 Hz. This was found by trial and error, and is not expected to introduce error in the simulation since the motion recorded at the bottom of the peat is retrieved. Rayleigh damping was also used to model the damping behavior of the clayey levee. The clayey levee being stiff, it is not anticipated to damp much energy. The damping ratio was set to 1.7%, with a center frequency of 6 Hz. The center frequency was determined based on a modal analysis from Deepsoil.

In the Deepsoil simulations, the frequency-independent Rayleigh damping matrix scheme implemented was used. This latter uses a modification of the Rayleigh formulation to match the target small strain damping at every frequency.

8.3.5 Input Motion

The sand at the bottom of the model was not tested in the lab, and its dynamic properties are unknown. To reduce the uncertainty, the motion recorded by the sensor A20 was used as input motion at the base of the model, and the sand was modeled as a relatively stiff elastic material that does not amplify nor deamplify the motion, as explained in the previous sections. In the simulations, the motion obtained at the bottom of the peat layer is similar to what was recorded by A20 during the centrifuge test. The recording from the centrifuge was filtered with a third order high pass filter with a corner frequency of 0.2 Hz. The corner frequency was selected based on the Fourier spectrum of the motion. The obtained acceleration record and response spectrum are presented in Figure 8-17.

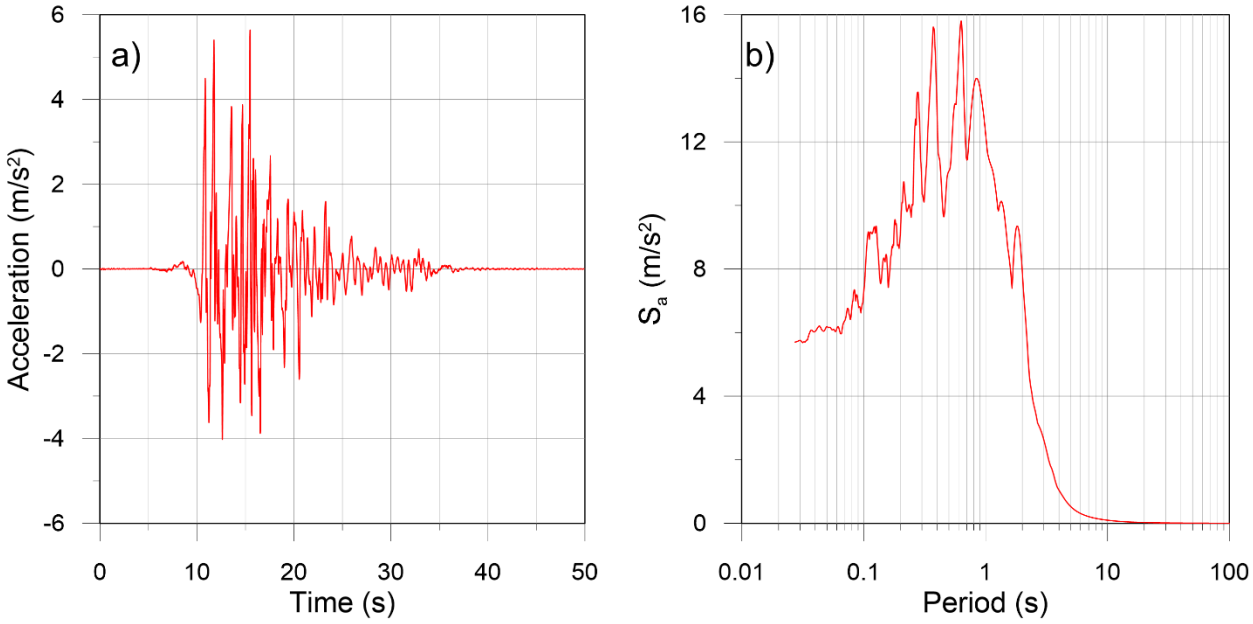

Figure 8-17 Input motion a) acceleration time series b) response spectrum

8.3.6 Preliminary Results of the Simulations

8.3.6.1 Displacements and Strains

The displacements at the top of the peat layer predicted by FLAC and Deepsoil are compared with displacements calculated from the centrifuge. The accelerations recorded by the sensors A18, A19, A20, A21, A28, A29, A30, and A31 (Figure 8-14) are double integrated to obtain displacements, which are then used to calculate the shear strain at the middle of the peat layer (Cappa et al. 2016).

The displacement time series recorded at the top of the layer are presented in Figure 8-18. The three recordings are in relatively good agreement, especially at the beginning of the record. Later the simulations become slightly out of phase with the recording.

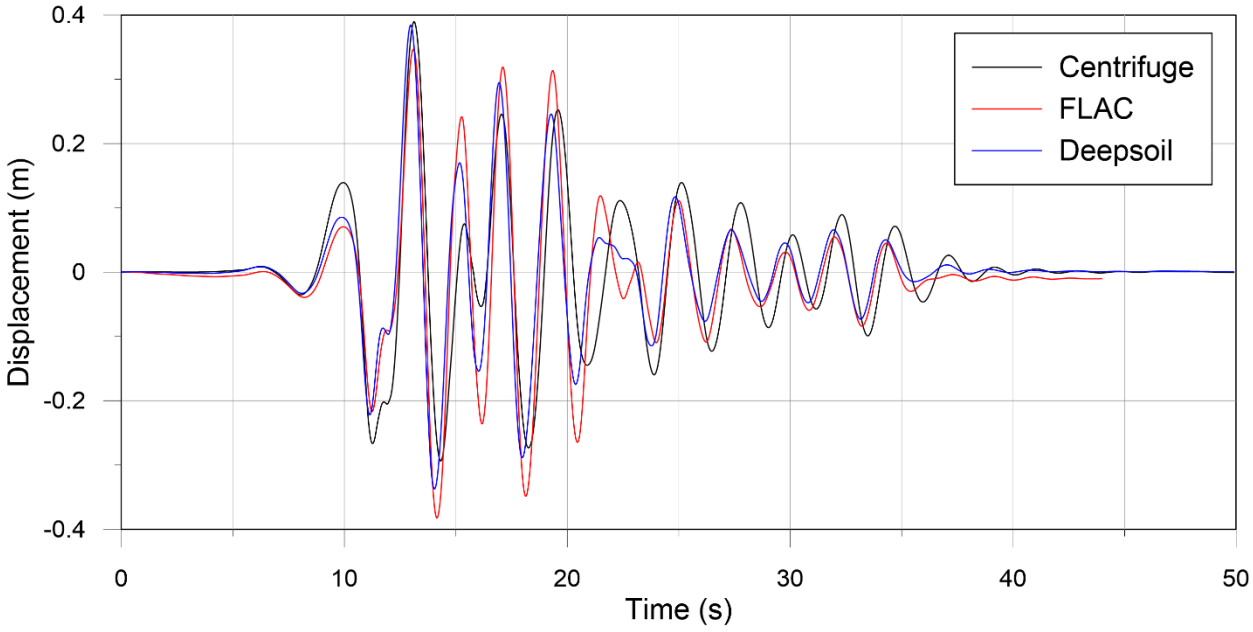

Figure 8-18 Comparison of displacement records

The strains from the simulations and the centrifuge are compared in Figure 8-19. The maximum strain is slightly overestimated by the Deepsoil simulations but well matched by FLAC. The simulations and the centrifuge results tend to become out of phase after a few cycles. The simulations tend to overpredict the strains and the overall match is not very good.

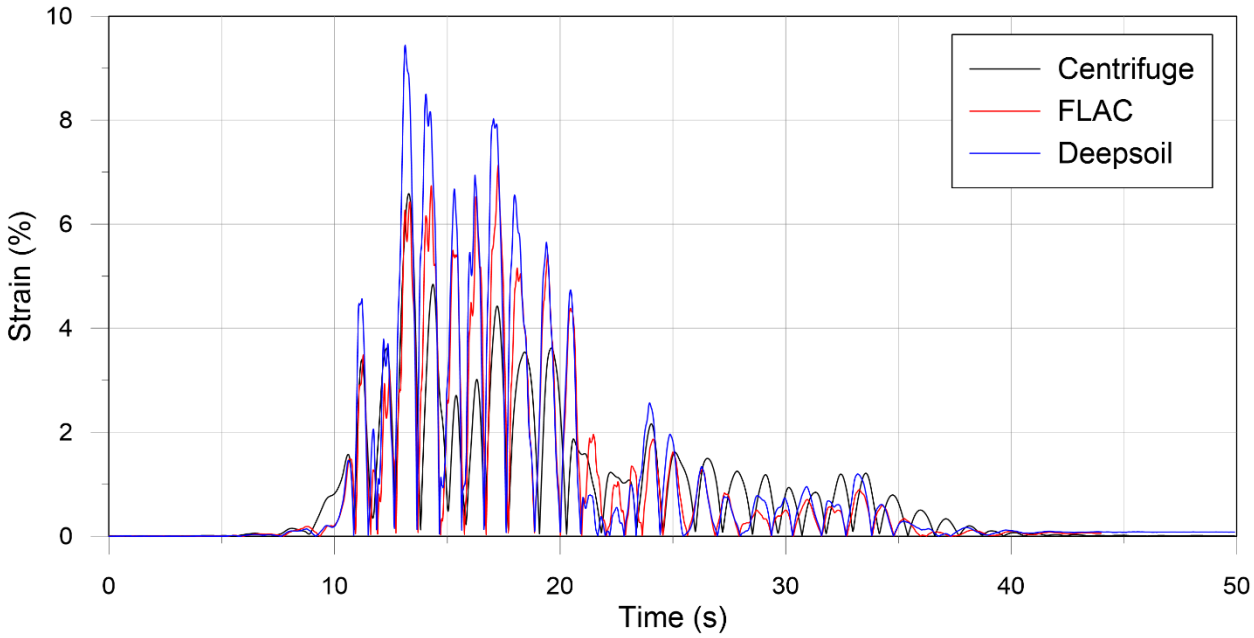

Figure 8-19 Strain time series

The maximum relative displacement and maximum shear strain profiles are presented in Figure 8-20. The simulations agree well with each other and with the centrifuge tests. The strain profile obtained in Deepsoil shows oscillations because of the misfit of the different modulus reduction curves induced by the MRDF model. The model yields modulus reduction curve that are either too stiff or too soft compared to the desired soil behavior. However, the general trend of those two profiles is satisfying.

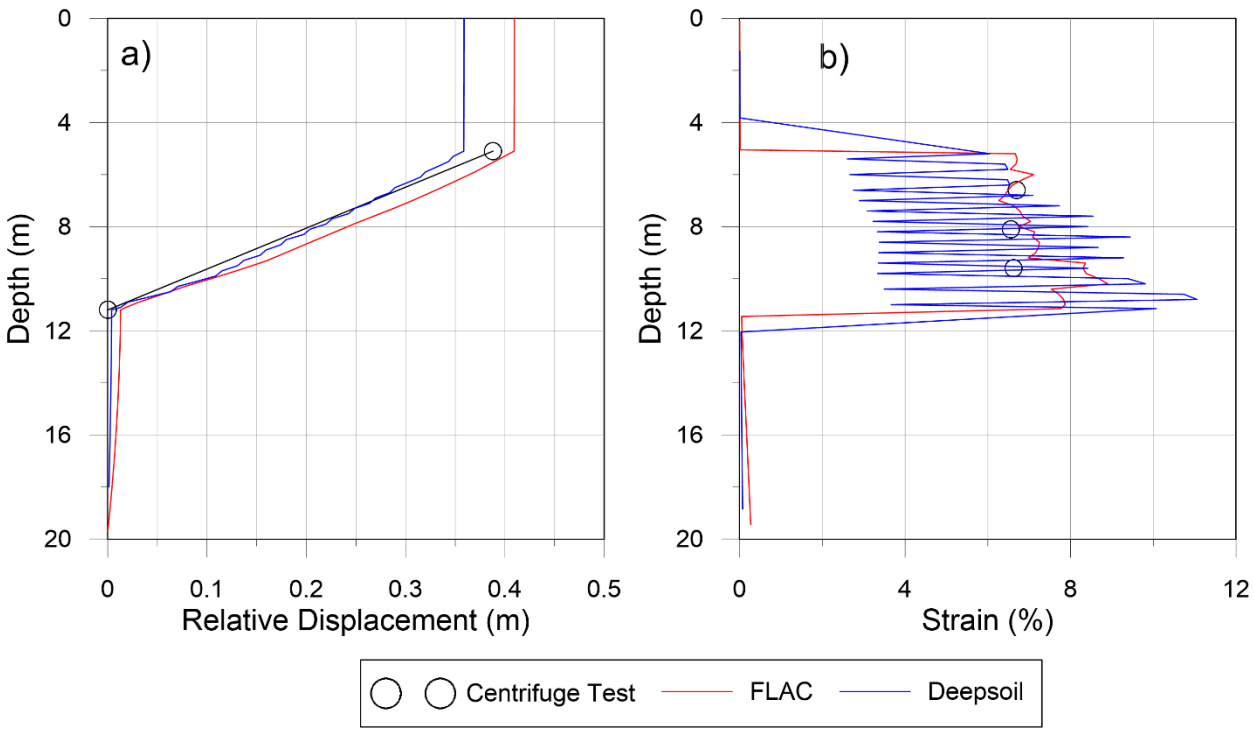

Figure 8-20 Relative displacement (a) and maximum strain (b) profiles

8.3.6.2 Acceleration Time Series

Acceleration time series at the top of the peat layer presented in Figure 8-21 show that the maximum acceleration at the top of the layer is well captured by both models. The two models are in good agreement, and both show a high frequency noise that does not appear in the recordings.

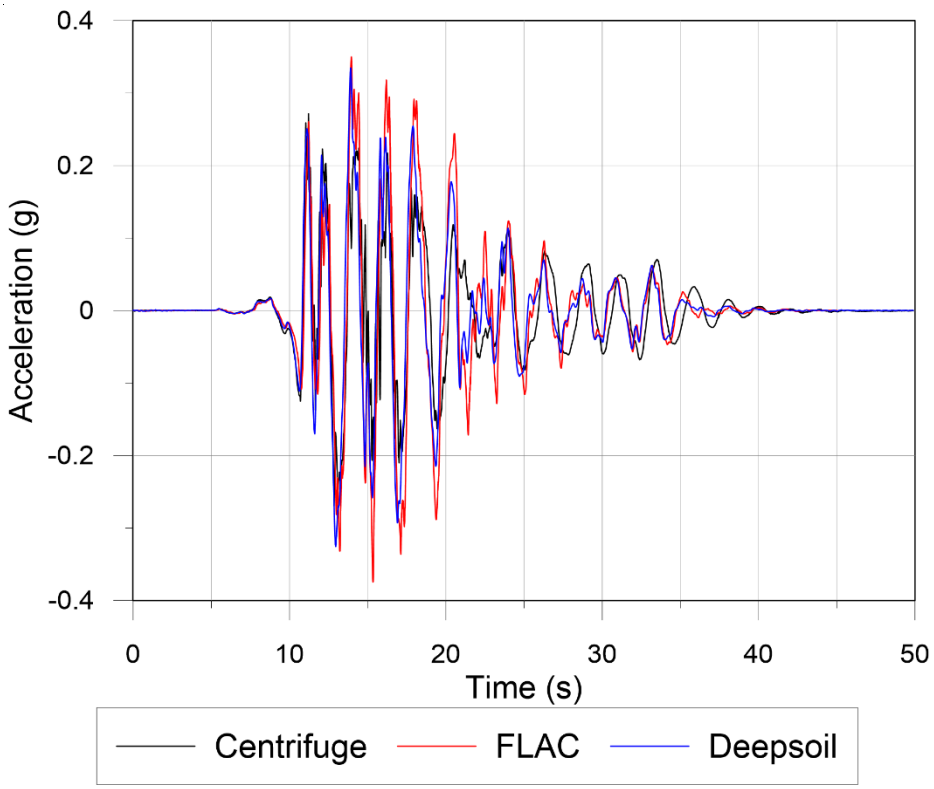

Figure 8-21 Acceleration time series at the top of the peat layer

8.3.6.3 Response Spectra

Response spectra from the accelerations recorded at the top of the peat layer are presented in Figure 8-22. The amplitude of the Fourier spectra is overestimated by Deepsoil and FLAC. At around 0.2s a peak is observed in the response spectra obtained from the centrifuge test that is not present in the simulations, which might be indicating a solicitation coming from 2D effects such as rocking. The response spectrum obtained in FLAC is satisfying and in excellent agreement with Deepsoil.

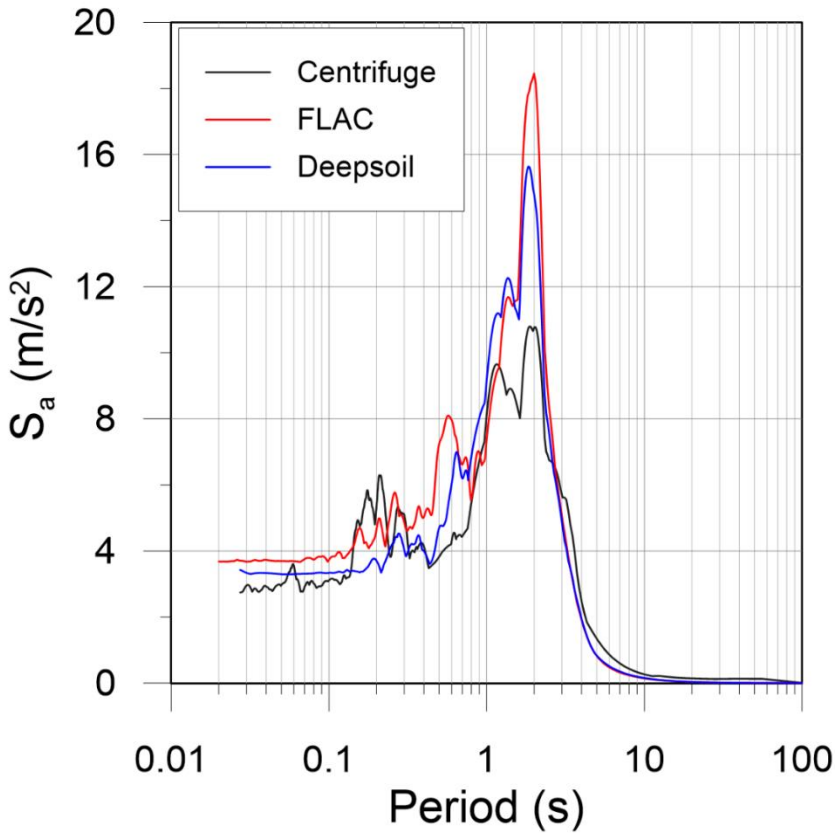

Figure 8-22 Response spectra of the motions at the top of the peat layer

8.3.7 Conclusions

The model was used in a 1D ground response analysis and is in good agreement with a similar simulation performed in Deepsoil. Although the two software cannot be compared because of the differences in their formulations, it should be noted that the computational time for both simulations was roughly the same. The simulations are not in perfect agreement with the recordings from the centrifuge which is expected since the centrifuge problem is a 2D problem. The simple example presented here shows that the model presented in this dissertation is well suited for ground response analysis.

9 SUMMARY AND CONCLUSIONS, AND FUTURE WORK

9.1 Summary and Conclusions

9.1.1 Centrifuge Tests

Two large centrifuge tests, and 12 small centrifuge tests were carried out at the UC Davis Center for Geotechnical Modeling. These tests provide an important body of data and new insights regarding the cyclic and post cyclic behavior of the levees atop peaty organic soils. This dissertation summarized the construction of the tests, and presented the device created to saturate the sand used for the levee fill. This vacuum saturation system presented is well suited for use in the centrifuge test where the saturation of sand in the centrifuge container poses problem. Examples of recordings from the centrifuge tests were also presented.

Insights gained from the centrifuge tests are developed extensively in Cappa (2016). In particular, the development of excess pore water pressure as a result of cyclic straining is analyzed. The correlation from Shafiee (2016) is compared to the data, and found to predict the centrifuge results fairly well. The soil-structure interaction between the levee and foundation soil is also studied and a rocking mode is highlighted.

9.1.2 Modulus Reduction and Damping Curves Plotted vs. Stress Ratio

A new approach where modulus reduction and damping curves are plotted against stress ratio has been presented and discussed. Modulus reduction and damping curves have traditionally been plotted versus cyclic shear strain. However, this approach has several drawbacks: (1) G/G_{max} and D versus γ_c depend on p', which can cause problems for

undrained loading where effective stress may change due to development of excess pore pressure, and (2) advanced constitutive models typically represent shear modulus as a function of η rather than γ_c, requiring sometimes complex calibration procedures to achieve desired modulus reduction and damping behavior. Plotting G/G_{max} and $D\text{-}D_{min}$ versus η results in pressure-independent modulus reduction and damping curves for three commonly-used relationships. This finding is potentially useful for implementation in one-dimensional effective stress codes for undrained loading conditions, and in advanced plasticity models.

9.1.3 1D Nonlinear Constitutive Model

A one dimensional nonlinear model for site response analysis that departs from two concepts commonly used by site response models was presented. Initial loading is controlled by using a cubic spline fit of the backbone curve to match any modulus reduction curve. A new unloading reloading rule has been derived to control the hysteretic behavior of the soil. The new rule uses a coordinate transformation approach to calculate the shear stress, regardless of the amplitude of the strain increment. This unloading-reloading rule easily controls the damping in the transformed coordinate system and provides a perfect fit of any damping curve, even capturing small-strain hysteretic damping, thereby eliminating the need for Rayleigh damping. The model is well suited for total stress 1D site response analysis.

9.1.4 3D Nonlinear Constitutive Model

A three-dimensional constitutive model controlling the damping response of the model was presented. Its formulation is based on the 1D model presented earlier in the

dissertation and also uses the concept of plotting the modulus reduction and damping curves as a function of stress ratio to incorporate these curves in a 3D model.

The model uses a bounding surface algorithm to control the shear strength, and the volumetric response is controlled by a pore pressure surface, a dilation surface and a volumetric yield surface. The model incorporates concepts developed by Dafalias and Manzari (2004) and Kutter and Sathialingam (1992).

The model is implemented in FLAC and examples of typical predictions were provided. This document provides enough information for the reader to comprehend how the model works, the influence of input parameters, and how to use the model in FLAC. The calibration process for peat based on lab tests was also presented in order to use the model in simulations of the centrifuge tests.

The preliminary results of a 1D ground response simulation using the developed model was presented. The simulation aim to represent the center array of the centrifuge test. Results from simulations using our model in FLAC are compared with simulation using the 1D ground response analysis software Deepsoil and the results from the centrifuge. The simulation captures the main trend shown in the data, and agrees well with the Deepsoil simulations.

9.2 Future Work

9.2.1 Implementation of the 1D Nonlinear Model in Deepsoil

The 1D model presented in this dissertation is well suited for 1D ground response analyses. In its current form, it is performing better than most of the established models.

However, it not yet implemented in a 1D ground response code. The new version of the widely used ground response code DEEPSOIL (Hashash et al. 2015), allows users to define their own constitutive models. Implementing the model in DEEPSOIL would therefore expose the model to more potential users, whether they are practitioners or researchers.

Although the model performs well and is able to match any input modulus reduction and damping curve, it is strain-rate independent, and would therefore show no difference in behavior under triangular or sinusoidal loading. In reality soils exhibits a strain rate dependence during loading and unloading. As a result, soils, especially clays and peat, often exhibit rounded tip upon sinusoidal loading (Vucetic 1990). This typically increases the energy dissipated during cyclic loading, i.e. the damping response of the soil. Introducing viscous effects in the 1D model would be an important achievement since it has never been done before. During earthquake loading, the strain rate changes, and the loading is closer to a sinusoidal loading than triangular loading. The shear strength is also rate dependent (Afacan et al. 2014), and the introduction of viscous effects should capture this behavior.

Finally, when the model is unloading/reloading, and passes a previous reversal point, it goes back to the previous loop. This process is usually associated with a sharp change in stiffness. This is observed with every model using the Masing rules or one of its modifications. Although it is not too detrimental, and still yields reasonable stress-strain curves (chapter 5), introducing a smooth transition would be better. This smooth transition could be introduced by shifting the center of reference (γ_0, τ_0) smoothly rather than abruptly. This formulation would depart completely from the second Masing rules.

9.2.2 Improvement of the 3D Nonlinear Model

The 3D model being largely based on the 1D model, it could be improved in a similar manner. First, viscous effects need to be introduced in order to simulate the behavior of the peat better. In its current formulation, the model is best suited for ground response analysis, and not for consolidation problems. In order to do so, the secondary compression needs to be introduced through viscous effects. In particular, secondary compression resets upon cyclic loading (Shafiee et al. 2015), and this needs to be integrated in a constitutive models. These viscous effects could also help capture the strain rate effect and the viscous behavior described in the previous section.

The aforementioned problem about the smoothness of the loops in the 1D model is also applicable for the multidimensional model. The same kind of solution can be implemented, and lead to a smooth transition from one cyclic loading to another.

Finally, the variables A_0, n_{pk}, and n_d were calibrated for peat, but not for other materials. Empirical relationships for these variables based on simple soil properties such as the plasticity index for clay, and grain size distribution for sand, are valuable because they would help practitioners use the model.

9.2.3 Future Numerical Simulations

This dissertation presents an example of ground response simulations that can be done with the model developed in Chapter 6. The simulation presented in chapter 8 simulates the model tested in the centrifuge. More site response simulations can be performed to study more extensively the peat response.

Complete simulations of the centrifuge tests need to be performed. The peat in the centrifuge tests will be modeled using the aforementioned constitutive model. The clayey levee will be considered perfectly elastic, and the sandy levee will be modeled using the PM4 Sand model (Boulanger and Ziotopoulou 2015). The simulations will consist of three different stages. In the first stage, a steady state seepage analysis will be performed as the water will seep through the levee from the reservoir. In the second stage, the model will be loaded with different input motions of different amplitude and frequency content, in an undrained dynamic analysis. Finally, a coupled fluid-mechanical simulation will be used to study the consolidation process as shear-induced excess pore pressures dissipate. The simulations will validate the use of our constitutive model in real field conditions, and study the potential of failure of levees in the Delta, considering all the possible failure mechanisms.

Appendix A. DERIVATION OF THE CONSISTENT TANGENT FOR THE 1D MODEL

Recall equation 5-15:

$$\tau = [(\gamma - \gamma_0)\cos\theta + (\tau - \tau_0)\sin\theta]\sin\theta + [a((\gamma - \gamma_0)\cos\theta + (\tau - \tau_0)\sin\theta)^4 + b((\gamma - \gamma_0)\cos\theta + (\tau - \tau_0)\sin\theta)^2 + c]\cos\theta + \tau_0$$

Let's define:

$$F(\gamma, \tau) = a[(\gamma - \gamma_0)\cos\theta + (\tau - \tau_0)\sin\theta]^4 \cos\theta \quad \textit{Equation 9-1}$$

$$G(\gamma, \tau) = b[(\gamma - \gamma_0)\cos\theta + (\tau - \tau_0)\sin\theta]^2 \cos\theta \quad \textit{Equation 9-2}$$

Equation 5-15 can be rewritten as:

$$\tau = [(\gamma - \gamma_0)\cos\theta + (\tau - \tau_0)\sin\theta]\sin\theta + F(\gamma, \tau) + G(\gamma, \tau) + c\,.\cos\theta + \tau_0 \quad \textit{Equation 9-3}$$

The derivative of equation 5-15 with respect to γ yields:

$$\frac{d\tau}{d\gamma} = \sin\theta\cos\theta + \frac{\partial\tau}{\partial\gamma}\sin^2\theta + \frac{\partial F(\gamma,\tau)}{\partial\gamma} + \frac{\partial F(\gamma,\tau)}{\partial\tau}\frac{\partial\tau}{\partial\gamma} + \frac{\partial G(\gamma,\tau)}{\partial\gamma} + \frac{\partial G(\gamma,\tau)}{\partial\tau}\frac{\partial\tau}{\partial\gamma} \quad \textit{Equation 9-4}$$

Where:

$$\frac{\partial F(\gamma,\tau)}{\partial\gamma} = 4a\cos^2\theta\,[(\gamma - \gamma_0)\cos\theta + (\tau - \tau_0)\sin\theta]^3 \quad \textit{Equation 9-5}$$

$$\frac{\partial F(\gamma,\tau)}{\partial\tau} = 4a\sin\theta\cos\theta\,[(\gamma - \gamma_0)\cos\theta + (\tau - \tau_0)\sin\theta]^3 \quad \textit{Equation 9-6}$$

$$\frac{\partial G(\gamma,\tau)}{\partial \gamma} = 2b\cos^2\theta\left[(\gamma-\gamma_0)\cos\theta+(\tau-\tau_0)\sin\theta\right] \qquad \textit{Equation 9-7}$$

$$\frac{\partial G(\gamma,\tau)}{\partial \tau} = 2b\sin\theta\cos\theta\left[(\gamma-\gamma_0)\cos\theta+(\tau-\tau_0)\sin\theta\right] \qquad \textit{Equation 9-8}$$

Equation A-4 yields:

$$\frac{d\tau}{d\gamma}\left(1-\sin^2\theta-\frac{\partial F(\gamma,\tau)}{\partial \tau}-\frac{\partial G(\gamma,\tau)}{\partial \tau}\right)=\sin\theta\cos\theta+\frac{\partial F(\gamma,\tau)}{\partial \gamma}+\frac{\partial G(\gamma,\tau)}{\partial \gamma} \qquad \textit{Equation 9-9}$$

Rearranging A-9 yields:

$$\frac{d\tau}{d\gamma}=\frac{\sin\theta\cos\theta+\frac{\partial F(\gamma,\tau)}{\partial \gamma}+\frac{\partial G(\gamma,\tau)}{\partial \gamma}}{\cos^2\theta-\frac{\partial F(\gamma,\tau)}{\partial \tau}-\frac{\partial G(\gamma,\tau)}{\partial \tau}} \qquad \textit{Equation 9-10}$$

Combining equations A-10, A-5, A-6, A-7 and A-8 and simplifying by $\cos\theta$:

$$\frac{d\tau}{d\gamma}=\frac{\sin\theta+4a\cos\theta\left[(\gamma-\gamma_0)\cos\theta+(\tau-\tau_0)\sin\theta\right]^3+2b\cos\theta\left[(\gamma-\gamma_0)\cos\theta+(\tau-\tau_0)\sin\theta\right]}{\cos\theta-4a\sin\theta\left[(\gamma-\gamma_0)\cos\theta+(\tau-\tau_0)\sin\theta\right]^3-2b\sin\theta\left[(\gamma-\gamma_0)\cos\theta+(\tau-\tau_0)\sin\theta\right]}$$

Equation 9-11

Appendix B: DERIVATION OF THE CONSISTENT TANGENT FOR THE 3D MODEL

Recall equation 6-35:

$$q = \left[\left(\varepsilon_q - \varepsilon_{q_0}\right)\cos\theta + (q - q_0)\sin\theta\right]\sin\theta + \left[a\left((\varepsilon_q - \varepsilon_{q_0})\cos\theta + (q - q_0)\sin\theta\right)^4 + b\left((\varepsilon_q - \varepsilon_{q_0})\cos\theta + (q - q_0)\sin\theta\right)^2 + c\right]\cos\theta + q_0$$

We define:

$$f_1 = \left[\left(\varepsilon_q - \varepsilon_{q_0}\right)\cos\theta + (q - q_0)\sin\theta\right]\sin\theta \qquad \textit{Equation B-12}$$

$$f_{2.1} = a\cos\theta\left((\varepsilon_q - \varepsilon_{q_0})\cos\theta + (q - q_0)\sin\theta\right)^4 \qquad \textit{Equation B-13}$$

$$f_{2.2} = b\cos\theta\left((\varepsilon_q - \varepsilon_{q_0})\cos\theta + (q - q_0)\sin\theta\right)^2 \qquad \textit{Equation B-14}$$

Equation 6-35 can be rewritten:

$$q = f_1 + f_{2.1} + f_{2.2} + c\cos\theta + q_0 \qquad \textit{Equation B-15}$$

There are 3 variables $q,\ \varepsilon_q,$ and p'.

$$q = f(q, \varepsilon_q, p') \qquad \textit{Equation B-16}$$

$$\frac{dq}{d\varepsilon_q} = \frac{\partial f}{\partial q}\cdot\frac{\partial q}{\partial \varepsilon_q} + \frac{\partial f}{\partial \varepsilon_q} + \frac{\partial f}{\partial p'}\cdot\frac{\partial p'}{\partial \varepsilon_q} \qquad \textit{Equation B-17}$$

The derivatives of *f* with respect to q and ε_q are similar to the 1D case:

$$\frac{\partial f}{\partial q} = \sin^2\theta + 4a\sin\theta\cos\theta\left[(\varepsilon_q - \varepsilon_{q_0})\cos\theta + (q - q_0)\sin\theta\right]^3 + 2b\sin\theta\cos\theta\left[(\varepsilon_q - \varepsilon_{q_0})\cos\theta + (q - q_0)\sin\theta\right] \qquad \textit{Equation B-18}$$

$$\frac{\partial f}{\partial \varepsilon_q} = \sin\theta\cos\theta + 4a\cos^2\theta\left[(\varepsilon_q - \varepsilon_{q_0})\cos\theta + (q - q_0)\sin\theta\right]^3 + 2b\cos^2\theta\left[(\varepsilon_q - \varepsilon_{q_0})\cos\theta + (q - q_0)\sin\theta\right]$$

Equation B-19

$$\frac{\partial f}{\partial p'} = \frac{\partial f}{\partial \theta}\cdot\frac{\partial \theta}{\partial p'} + \frac{\partial f}{\partial q_0}\cdot\frac{\partial q_0}{\partial p'} + \frac{\partial f}{\partial a}\cdot\frac{\partial a}{\partial p'} + \frac{\partial f}{\partial b}\cdot\frac{\partial b}{\partial p'} + \frac{\partial f}{\partial c}\cdot\frac{\partial c}{\partial p'}$$

Equation B-20

The derivatives of *f* with respect to *a, b* and *c* are:

$$\frac{\partial f}{\partial a} = \cos\theta\left((\varepsilon_q - \varepsilon_{q_0})\cos\theta + (q - q_0)\sin\theta\right)^4$$

Equation B-21

$$\frac{\partial f}{\partial b} = \cos\theta\left((\varepsilon_q - \varepsilon_{q_0})\cos\theta + (q - q_0)\sin\theta\right)^2$$

Equation B-22

$$\frac{\partial f}{\partial c} = \cos\theta$$

Equation B-23

The derivatives of *a*, *b* and *c* with respect to *p'* are:

$$\frac{\partial a}{\partial p'} = \frac{-5\cdot\pi\cdot D\cdot\eta_L\cdot\cos^5\theta}{32\cdot(\varepsilon_{q_L} - \varepsilon_{q_0})^4} + \frac{\partial a}{\partial \theta}\cdot\frac{\partial \theta}{\partial p'} + \frac{\partial a}{\partial q_0}\cdot\frac{\partial q_0}{\partial p'} + \frac{\partial a}{\partial D}\cdot\frac{\partial D}{\partial p'}$$

Equation B-24

$$\frac{\partial b}{\partial p'} = \frac{15\cdot\pi\cdot D\cdot\eta_L\cdot\cos^3\theta}{16\cdot(\varepsilon_{q_L} - \varepsilon_{q_0})^2} + \frac{\partial b}{\partial \theta}\cdot\frac{\partial \theta}{\partial p'} + \frac{\partial b}{\partial q_0}\cdot\frac{\partial q_0}{\partial p'} + \frac{\partial b}{\partial D}\cdot\frac{\partial D}{\partial p'}$$

Equation B-25

$$\frac{\partial c}{\partial p'} = \frac{-25\cdot\pi\cdot D\cdot\eta_L\cdot\cos\theta}{32} + \frac{\partial c}{\partial \theta}\cdot\frac{\partial \theta}{\partial p'} + \frac{\partial c}{\partial q_0}\cdot\frac{\partial q_0}{\partial p'} + \frac{\partial c}{\partial D}\cdot\frac{\partial D}{\partial p'}$$

Equation B-26

D-D_{min} is independent of p' and only depends on the equivalent stress ratio η_{eq} which is a constant until η_L and η_R change. However, D_{min} depends on *p'* if the formulation from Kishida is used (see Chapter 7). In this case, the term $\frac{\partial D}{\partial p'}$ is not zero, but follows the following equation:

$$\frac{\partial D}{\partial p'} = 0.01\cdot e^{c_0 + X_3 c_3 + X_5 c_1 + c_2\ln(p') - c_5(X_3 - X_{3b})\cdot(X_{2b} - \ln(p')) - c_4(X_5 - X_{5b})\cdot(X_{2b} - \ln(p'))}\left[\frac{c_2}{p'} + \frac{c_5(X_3 - X_{3b})}{p'} + \frac{c_4(X_5 - X_{5b})}{p'}\right]$$

Equation B-27

$$\frac{\partial a}{\partial D} = \frac{-5 \cdot \pi \cdot (p' \cdot \eta_L - q_0) \cdot \cos^5 \theta}{32 \cdot (\varepsilon_{q_L} - \varepsilon_{q_0})^4}$$ *Equation B-28*

$$\frac{\partial b}{\partial D} = \frac{15 \cdot \pi \cdot (p' \cdot \eta_L - q_0) \cdot \cos^3 \theta}{16 \cdot (\varepsilon_{q_L} - \varepsilon_{q_0})^2}$$ *Equation B-29*

$$\frac{\partial c}{\partial D} = \frac{-25 \cdot \pi \cdot (p' \cdot \eta_L - q_0) \cdot \cos \theta}{32}$$ *Equation B-30*

The other partial derivatives are:

$$\frac{\partial a}{\partial \theta} = \frac{25 \cdot \pi \cdot D \cdot (p' \cdot \eta_L - q_0) \cdot \sin \theta}{32 \cdot \varepsilon_{q'_{in}}{}^4}$$ *Equation B-31*

$$\frac{\partial b}{\partial \theta} = \frac{-45 \cdot \pi \cdot D \cdot (p' \cdot \eta_L - q_0) \cdot \sin \theta}{16 \cdot \varepsilon_{q'_{in}}{}^2}$$ *Equation B-32*

$$\frac{\partial c}{\partial \theta} = \frac{25 \cdot \pi \cdot D \cdot (p' \cdot \eta_L - q_0) \cdot \sin \theta}{32}$$ *Equation B-33*

$$\frac{\partial f}{\partial \theta} = 2 \sin \theta \cos \theta \, (q - q_0) + (\cos^2 \theta - \sin^2 \theta) \cdot \left(\varepsilon_q - \varepsilon_{q_0}\right) - \sin \theta \cdot c + \frac{\partial f_{2.1}}{\partial \theta} + \frac{\partial f_{2.2}}{\partial \theta}$$ *Equation B-34*

$$\frac{\partial f_{2.1}}{\partial \theta} = -\sin \theta \, a \left(\left(\varepsilon_q - \varepsilon_{q_0}\right) \cos \theta + (q - q_0) \sin \theta\right)^4 + 4a \cos \theta \left[(q - q_0) \cos \theta - \left(\varepsilon_q - \varepsilon_{q_0}\right) \sin \theta\right] \left[\left(\varepsilon_q - \varepsilon_{q_0}\right) \cos \theta + (q - q_0) \sin \theta\right]^3$$ *Equation B-35*

$$\frac{\partial f_{2.1}}{\partial \theta} = -\sin \theta \, b \left(\left(\varepsilon_q - \varepsilon_{q_0}\right) \cos \theta + (q - q_0) \sin \theta\right)^2 + 2b \cos \theta \left[(q - q_0) \cos \theta - \left(\varepsilon_q - \varepsilon_{q_0}\right) \sin \theta\right] \left[\left(\varepsilon_q - \varepsilon_{q_0}\right) \cos \theta + (q - q_0) \sin \theta\right]$$ *Equation B-36*

$$\frac{\partial f}{\partial q_0} = -\sin^2\theta + 1 - \cos\theta\left[4a\sin\theta\left[(\varepsilon_q - \varepsilon_{q_0})\cos\theta + (q - q_0)\sin\theta\right]^3 + 2b\sin\theta\left[(\varepsilon_q - \varepsilon_{q_0})\cos\theta + (q - q_0)\sin\theta\right]\right]$$ *Equation B-37*

$$\frac{\partial q_0}{\partial p'} = \frac{\eta_R + \eta_L}{2}$$ *Equation B-38*

$$\frac{\partial a}{\partial q_0} = \frac{5 \cdot \pi \cdot D \cdot \cos^5\theta}{32 \cdot (\varepsilon_{q_L} - \varepsilon_{q_0})^4}$$ *Equation B-39*

$$\frac{\partial b}{\partial q_0} = \frac{-15 \cdot \pi \cdot D \cdot \cos^3\theta}{16 \cdot (\varepsilon_{q_L} - \varepsilon_{q_0})^2}$$ *Equation B-40*

$$\frac{\partial c}{\partial q_0} = \frac{25 \cdot \pi \cdot D \cdot cos\,\theta}{32}$$ *Equation B-41*

Finally, the tangent is calculated by rearranging B-6 and substituting all the partial derivatives (B-7 to B-30):

$$\frac{dq}{d\varepsilon_q} = \frac{\frac{\partial f}{\partial \varepsilon_q} + \frac{\partial f}{\partial p'} \cdot \frac{\partial p'}{\partial \varepsilon_q}}{1 - \frac{\partial f}{\partial q}}$$ *Equation B-31*

REFERENCES

Afacan, K., Brandenberg, S., and Stewart, J. (2014). ”Centrifuge Modeling Studies of Site Response in Soft Clay over Wide Strain Range.” *J. Geotech. Geoenviron. Eng.*, 140(2), 04013003.

Ajlouni, M. A. (2000). “Geotechnical properties of peat and related engineering problems.” *Ph.D. thesis*, Univ. of Illinois at Urbana–Champaign, Urbana, Ill.

Al Tabbaa, A., & Wood, D. M. (1989). “An experimentally based bubble model for clay.” In *Proceedings of the 3rd International Symposium on Numerical Models in Geomechanics (NUMOG III)* (pp. 90-99). Elsevier.

Arulnathan, R. (2000). “Dynamic properties and site response of organic soils.” *Ph.D. thesis*, Dept. of Civil and Environmental Engineering, Univ. of California, Davis, California

Assimaki, D., Kausel, E., and Whittle, A. J. (2000). "Model for dynamic shear modulus and damping for granular soils." *J. Geotech. Geoenvion. Eng.,* 126(10), 859-869.

ASTM D 854-06, “Standard Test Methods for Specific Gravity of Soil Solids by Water Pycnometer”

ASTM D2974-07a, “Standard Test Methods for Moisture, Ash, and Organic Matter of Peat and Other Organic Soils”

Azzouz, A. S., KRIZEK, R. J., & CoRoTis, R. B. (1976). “Regression analysis of soil compressibility.” *土質工学会論文報告集*, 16(2), 19-29.

Beaty, Michael H., and Peter M. Byrne (2011). "UBCSAND constitutive model version 904aR." *Documentation report: UBCSAND constitutive model on Itasca UDM Website.*

Bjerrum, L. (1967). “Engineering geology of Norwegian normally-consolidated marine clays as related to settlements of buildings.” *Geotechnique*, *17*(2), 83-118.

Boulanger, R. W., Arulnathan, R., Jr, L. F. H., Torres, R. A., & Driller, M. W. (1998). “Dynamic properties of Sherman Island peat.” *Journal of Geotechnical and Geoenvironmental Engineering*, *124*(1), 12-20.

Boulanger, R. W., Ziotopoulou K. (2015). "PM4SAND (Version 3): A sand plasticity model for earthquake engineering applications." *Report No. UCD/CGM-15-01*, Center for Geotechnical Modeling, Department of Civil and Environmental Engineering, University of California, Davis, CA, 108 pp.

Brennan, A. J., Thusyanthan, N. I., & Madabhushi, S. P. (2005). “Evaluation of shear modulus and damping in dynamic centrifuge tests.” *Journal of Geotechnical and Geoenvironmental Engineering*, 131(12), 1488-1497.

Cappa, R., Yniesta, S., Lemnitzer, A., Brandenberg, S. J., & Stewart, J. P. (2014a). “Centrifuge experiments to evaluate the seismic performance of levees on peaty

soils in the Sacramento-San Joaquin delta*." In Association of State Dam Safety Officials Annual Conference 2014,* Dam Safety 2014 (Vol. 1).

Cappa, R., Yniesta, S., Brandenberg, S., Stewart, J., and Lemnitzer, A., (2014b), "NEESR: Levees and Earthquakes: Averting and Impending Disaster—Data Report for Centrifuge Experiments 12L and 13L" *NSF Final Project Report*, Network for Earthquake Engineering Simulation (distributor).

Cappa, R., Yniesta, S., Brandenberg, S., Stewart, J., and Lemnitzer, A., (2014c), "NEESR: Levees and Earthquakes: Averting and Impending Disaster—Data Report for Centrifuge Experiments 14M and 15M" *NSF Final Project Report*, Network for Earthquake Engineering Simulation (distributor).

Cappa, R., Yniesta, S., Lemnitzer, A., Brandenberg, S., and Shafiee, A. (2015) "Settlement Estimations of Peat during Centrifuge Experiments." *Proceedings, IFCEE 2015*: pp. 152-160. doi: 10.1061/9780784479087.016

Cappa (2016) "Seismic and Post-seismic Behavior of Embankments atop Peat" *Ph.D. thesis*, Dept. of Civil and Environmental Engineering, Univ. of California, Irvine, California

Chaney, R. C., Stevens, E., & Sheth, N. (1979). "Suggested test method for determination of degree of saturation of soil samples by B value measurement. " *Geotechnical Testing Journal,* GTJODJ, Vol. 2, No. 3, pp. 158-162.

Chiu, P., D.E. Pradel, A.O.L. Kwok and J.P. Stewart (2008). “Seismic response analyses for the Silicon Valley Rapid Transit Project,” *Proc. 4th Decennial Geotechnical Earthquake Engineering and Soil Dynamics Conference*, ASCE, Sacramento, CA

Cola, S., & Cortellazzo, G. (2005). “The shear strength behavior of two peaty soils.” *Geotechnical & Geological Engineering*, *23*(6), 679-695.

Conti, R., & Viggiani, G. M. (2011). “Evaluation of soil dynamic properties in centrifuge tests.” *Journal of Geotechnical and Geoenvironmental Engineering*, 138(7), 850-859.

Dafalias, Y. F., & Popov, E. P. (1975). “A model of nonlinearly hardening materials for complex loading.” *Acta mechanica*, 21(3), 173-192.

Dafalias, Y.F. and E.P. Popov (1979). “A model for nonlinearly hardening materials for complex loading,” *Acta Mechanica*, 21(3), 173–192

Dafalias, Y. F. (1982). “Bounding surface elastoplasticity-viscoplasticity for particulate cohesive media.” In *Proc. IUTAM Symposium on Deformation and Failure of Granular Materials* (pp. 97-107). AA Balkema, Publishers, Rotterdam.

Dafalias, Y. F., & Herrmann, L. R. (1982). “Bounding surface formulation of soil plasticity.” *Soil mechanics-transient and cyclic loads*, 10, 253-282.

Dafalias, Y. F. (1986). “Bounding surface plasticity. I: Mathematical foundation and hypoplasticity.” *Journal of Engineering Mechanics*, 112(9), 966-987.

Manzari, M. T., & Dafalias, Y. F. (1997). “A critical state two-surface plasticity model for sands.” *Geotechnique*, 47(2), 255-272.

Dafalias YF, Manzari MT. (2004) “Simple plasticity sand model accounting for fabric change effects.” *Journal of Engineering Mechanics,* 130(6), 622–634.

Dafalias, Y. F., Manzari, M. T., & Papadimitriou, A. G. (2006). “SANICLAY: simple anisotropic clay plasticity model.” *International Journal for Numerical and Analytical Methods in Geomechanics*, *30*(12), 1231-1257.

Darendeli, M. (2001). “Development of a new family of normalized modulus reduction and material damping curves.” *Ph.D. Thesis*, Dept. of Civil Eng., Univ. of Texas, Austin.

Dashti, S. (2009). “Toward Developing an Engineering Procedure for Evaluating Building Performance on Softened Ground”, *Ph.D. Thesis, University of California, Berkeley, CA.*

De Boor, Carl. (1978) "A Practical Guide to Splines" Springer-Verlag, New York 1978

Delta Vision (2008) *http://deltavision.ca.gov/*

Doroudian, M. and Vucetic, M., (1995). “A Direct Simple Shear Device for Measuring Small-Strain Behavior,” *ASTM Geotechnical Testing Journal*, Vol. 18. No. 1, pp. 69-85.

Drexler, J.Z., C.S. de Fontaine, and T.A. Brown. (2009). “Peat accretion histories during the past 6,000 years in marshes in the Sacramento-San Joaquin Delta, California, USA.” *Estuaries and Coasts 32*: 871-892

DRMS, URS Corporation and Jack Benjamin and Associates Inc. (2009). "Delta Risk Management Strategy. Phase 1 Final Report." California Department of Water Resources.

Duku, PM, JP Stewart, DH Whang, and R Venugopal (2007). “Digitally controlled simple shear apparatus for dynamic soil testing,” *Geotech. Testing Journal*, ASTM, 30 (5), 368-377.

Duku, PM, JP Stewart, DH Whang, and E Yee, (2008). “Volumetric strains of clean sands subject to cyclic loads,” *J. Geotech. & Geoenv. Engrg.*, ASCE, 134 (8), 1073-1085.

Duvaut, G., & Lions, J. L. (1972). “Les inéquations en mécanique et en physique” (Vol. 18). Paris: Dunod.

Electrical Power Research Institute, EPRI (1993). “Guidelines for determining design basis ground motions,” *Rpt. No. EPRI TR-102293*, Electrical Power Research Institute, Palo Alto, CA.

Elgamal A, Yang Z, Parra E, Ragheb (2003) “A Modeling of cyclic mobility in saturated cohesionless soils.” *Int J Plasticity*, 19:883-905.

Elgamal, A., Yang, Z., Lai, T., Kutter, B. L., & Wilson, D. W. (2005). “Dynamic response of saturated dense sand in laminated centrifuge container.” *Journal of Geotechnical and Geoenvironmental Engineering*, 131(5), 598-609.

Fox, P. J. (1999). “Solution charts for finite strain consolidation of normally consolidated clays.” *Journal of geotechnical and geoenvironmental engineering*, 125(10), 847-867.

Garnier, J. and Cottineau, L. M., (1988), “La Centrifugeuse du LCPC: Moyens de Preparation des Modeles et Instrumentation,” *Proceedings of Centrifuge ‘88*, Paris, April 25–27, 1988, Balkema, Rotterdam, pp. 83–90.Gens 1982

Groholski, D. R., Hashash, Y. M. A., Musgrove, M., Harmon, J., and Kim, B. (2015) ”Evaluation of 1-D Non-linear Site Response Analysis using a General Quadratic/Hyperbolic Strength Controlled Constitutive Model” *6th International Conference on Earthquake Geotechnical Engineering, Christchurch, New Zealand*

Hardin, B.O. and V.P. Drnevich (1972a). “Shear modulus and damping in soils: design equations and curves,” J. of the Soil Mechanics and Foundations Div., ASCE, 98 (SM7), 667–692

Hardin, Bobby O., and Drnevich, V.P., (1972b). “Shear Modulus and Damping in Soils I. Measurement and Parameter Effects.” *Journal of the Soil Mechanics and Foundations Division*, ASCE, Vol. 98, No. SM6, June, pp. 603 624.

Hardy, R. M., & Thomson, S. (1956). “Measurements of shearing strength of muskeg.” *In Proc., Eastern Muskeg Research Conf., NRC, Ottawa, ACSSM Technical Memorandum* (Vol. 42, pp. 16-24).

Hashash, Y.M.A. and D. Park (2001). “Non-linear one-dimensional seismic ground motion propagation in the Mississippi embayment,” *Eng. Geology*, Amsterdam, 62(1–3), 185–206.

Hashash, Y.M.A. and D. Park (2002). “Viscous damping formulation and high frequency motion propagation in nonlinear site response analysis,” *Soil Dynamics and Earthquake Engineering.*, 22(7), 611–624.

Hashash Y. M. A., Phillips C., and Groholski D. R. (2010) “Recent advances in non-linear site response analysis.” *Fifth International Conference on Recent Advances in Geotechnical Earthquake Engineering and Soil Dynamics, San Diego 2010.*

Hashash, Y.M.A., Musgrove, M.I., Harmon, J.A., Groholski, D.R., Phillips, C.A., and Park, D. (2015) “DEEPSOIL 6.0, User Manual” 114 p.

Hayashi, H., Yamazoe, N., Mitachi, T., Tanaka, H., & Nishimoto, S. (2012). “Coefficient of earth pressure at rest for normally and overconsolidated peat ground in Hokkaido area.” *Soils and Foundations*, 52(2), 299-311.

Herrmann, L. R., Shen, C. K., Jafroudi, S., DeNatale, J.S. & Dafalias, Y. F. (1981). “A verification study for the bounding surface plasticity model for cohesive soils.” *Final*

report to the Civil Engineering Laboratory, Naval Construction Battalion Center, Port Hueneme, California.

Hudson, M., I.M. Idriss, and M. Beikae (1994). “QUAD4M – A computer program to evaluate the seismic response of soil structures using finite element procedures and incorporating a compliant base.” Center for Geotechnical Modeling, Dept. Civil and Envir. Eng., Univ. of Calif., Davis, CA

Ishihara, K., Tatsuoka, F., and Yasuda, S. (1975). ‘‘Undrained deformation and liquefaction of sand under cyclic stresses.*’’ Soils Found.*,15(1), 29–44.

Itasca Consulting Group, Inc. (2011) FLAC — Fast Lagrangian Analysis of Continua, Ver. 7.0. Minneapolis: Itasca.

Iwan, W. D. (1967). “On a class of models for the yielding behavior of continuous and composite systems.“ ASME.

Jaky, J. (1944). “The coefficient of earth pressure at rest.” *Journal of the Society of Hungarian Architects and Engineers*, 78(22), 355-358.

Kaklamanos, J., Bradley, B. A., Thompson, E. M., & Baise, L. G. (2013). Critical Parameters Affecting Bias and Variability in Site-Response Analyses Using KiK-net Downhole Array Data. *Bulletin of the Seismological Society of America*, 103(3), 1733-1749

Kaklamanos, J., Baise, L. G., Thompson, E. M., & Dorfmann, L. (2015). Comparison of 1D linear, equivalent-linear, and nonlinear site response models at six KiK-net validation sites. *Soil Dynamics and Earthquake Engineering*, 69, 207-219.

Keene, P., & Zawodniak, C. D. (1968). “Embankment construction on peat utilizing hydraulic fill.” *Proceedings of Advances in Peatland Engineering*, 45-50.

Kishida, T., Boulanger, R. W., Abrahamson, N. A., Wehling, T. M., & Driller, M. W. (2009a). “Regression models for dynamic properties of highly organic soils.” *Journal of geotechnical and geoenvironmental engineering*, *135*(4), 533-543.

Kishida, T., Boulanger, R. W., Abrahamson, N. A., Driller, M. W., & Wehling, T. M. (2009b). “Site effects for the Sacramento-San Joaquin Delta.” *Earthquake Spectra*, 25(2), 301-322..

Kishida, T., Boulanger, R. W., Wehling, T. M., & Driller, M. W. (2006). “Variation of small strain stiffness for peat and organic soil.” In *Proc., 8th US National Conf. on Earthquake Engineering*. Earthquake Engineering Research Institute.

Kondner, R. L., and J.S. Zelasko (1963). “A hyperbolic stress-strain formulation of sands,” *Proc. of 2nd Pan American Conference on Soil Mechanics and Foundation Engineering,* Sao Paulo, Brasil, 289–324

Kramer, S. L. (2000). “Dynamic response of Mercer Slough peat.” *Journal of geotechnical and geoenvironmental engineering*, *126*(6), 504-510.

Kuhlemeyer, R. L., & Lysmer, J. (1973). “Finite element method accuracy for wave propagation problems.” Journal of Soil Mechanics & Foundations Div, 99(Tech Rpt).

Kutter, B.L. (1992). *Dynamic Centrifuge Modeling of Geotechnical Structures.* Transportation Research Record, TRB, National Research Council, 1336: 24-30.

Kutter, B. L., & Sathialingam, N. (1992). “Elastic-viscoplastic modelling of the rate-dependent behaviour of clays.” *Géotechnique*, *42*(3), 427-441.

Kwok, O.L.A., J.P. Stewart, Y.M.A. Hashash, N. Matasovic, R.M. Pyke, Z.L. Wang, and Z. Yang (2007). “Use of exact solutions of wave propagation problems to guide implementation of nonlinear seismic ground response analysis procedures,” *J. of Geotech. & Geoenviron. Eng.*, ASCE, 133, no. 11, 1385–1398

Kwok, A. O., Stewart, J. P., & Hashash, Y. M. (2008). “Nonlinear ground-response analysis of Turkey flat shallow stiff-soil site to strong ground motion*.” Bulletin of the Seismological Society of America*, 98(1), 331-343.

Chicago Ladd, R. S. (1974). “Specimen preparation and liquefaction of sands.” *Journal of Geotechnical and Geoenvironmental Engineering*, *100*(Proc. Paper 10857 Proceeding).

Ladd, C. C. (1991). “Stability evaluation during staged construction.” *Journal of Geotechnical Engineering*, *117*(4), 540-615.

Lai, C.G., Rix, G.J., (1998). “Simultaneous inversion of Rayleigh phase velocity and attenuation for near-surface site characterization.” *Report No. GIT-CEE/GEO-98-2*. Georgia Institute of Technology, School of Civil and Environmental Engineering

Lee, J. S. and Santamarina, J. C., (2005), “P-Wave Reflection Imaging,” *Geotech. Testing J.*, Vol. 28, No. 2, pp. 197–206.

Lee, K. L., & Seed, H. B. (1967). “Drained strength characteristics of sands.” *Journal of Soil Mechanics & Foundations Div.*

Lemnitzer, A., Cappa, R., Yniesta, S., & Brandenberg, S. (2015). “Centrifuge Testing of Model Levees atop Peat: Experimental Data.” *Earthquake Spectra*.

Li, X. S., and Wang, Y. (1998). ‘‘Linear representation of steady-state line for sand.’’*J. Geotech. Geoenviron. Eng.,* 124(12), 1215–1217.

Li, X. S., and Dafalias, Y. F. (2000). ‘‘Dilatancy for cohesionless soils.’’ *Geotechnique*, 50(4), 449–460.

Liu, M., and Gorman, D. G. (1995). "Formulation of Rayleigh damping and its extensions." *Computers and Structures*, 57(2), 277-285.

Lowe, J. and Johnson, T. C., (1960), “Use of Back-Pressure to Increase Degree of Saturation of Triaxial Test Specimens,” *ASCE Research Conference on Shear Strength of Cohesive Soils*, Boulder, CO, pp. 819–836.

Lund, J., Hanak, E., Fleenor, W., Howitt, R., Mount, J., and Moyle, P. (2007). "Envisioning futures for the Sacramento-San Joaquin Delta." *Public Policy Institute of California*. San Francisco, CA, 325 p.

Lysmer, J., H.B. Seed and P.B. Schnabel (1971). “Influence of base-rock characteristics on ground response.” *Bull. Seism. Soc. Am*., 61(5), 1213–1232

MacFarlane, I. C. (1969). “Engineering characteristics of peat.” *Muskeg engineering handbook*, I. C. McFarlane, ed., Univ. of Toronto Press, Canada, 78–126.

Marachi, N. D., Dayton, D. J., and Dare, C. T. (1983). “Geotechnical properties of peat in San Joaquin Delta.” *Testing of peat and organic soils*, STP 820, ASTM, West Conshohocken, Pa., 207–217.

Masing, G. (1926). “Eigenspannungen and verfertigung beim messing.” *Proc. 2nd Int. Congress on Applied Mech.*, Zurich, Switzerland

Matasovic, N. and M. Vucetic (1993a). “Cyclic Characterization of Liquefiable Sands,” *J. of Geotech. Eng.*, ASCE, 119(11), 1805-1822

Matasovic, N. (2006). “D-MOD_2 – A Computer Program for Seismic Response Analysis of Horizontally Layered Soil Deposits, Earthfill Dams, and Solid Waste Landfills.” *User’s Manual*, GeoMotions, LLC, Lacey, Washington, 20 p. (plus Appendices).

Matasovic, N. and Vucetic M. (1993). “Seismic Response of Composite Horizontally-Layered Soil Deposits,” *UCLA Research Report No. ENG-93-182*, Civil Engineering Department, University of California, Los Angeles, CA, March, 452 p.

Matasovic, Neven, and Mladen Vucetic (1995). "Generalized cyclic-degradation-pore-pressure generation model for clays." *Journal of geotechnical engineering* 121.1: 33-42.

Matasovic, N. and Vucetic, M. (1995). “Seismic Response of Soil Deposits Composed of Fully-Saturated Clay and Sand Layers”, *Proceedings of the 1st International Conference on Geotechnical Earthquake Engineering, Tokyo, Japan*, Editor: Ishihara, K., Publisher: A.A. Balkema, Rotterdam/Brookfield, Vol. I, pp. 611-616. November.

Matesic, L. and Vucetic, M. (2003). “Strain-rate Effects on Soil Secant Shear Modulus at Small Cyclic Strains”, *J. Geotech. Geoenviron. Eng.*, Vol. 129, No. 6, pp. 536-549

Mayne, Paul W., and Harry E. Stewart (1988). "Pore Pressure Behavior of K o-Consolidated Clays." *Journal of Geotechnical Engineering* 114.11: 1340-1346.

Mejia, L. H., and E. M. Dawson. (2006) “Earthquake Deconvolution for FLAC” in *FLAC and Numerical Modeling in Geomechanics (Proceedings of the 4th International FLAC Symposium, Madrid, Spain, May 2006)*, pp. 211-219. P. Varona & R. Hart, eds. Minneapolis, Minnesota: Itasca Consulting Group Inc. (2006).

Menq F.Y. (2003) “Dynamic properties of sandy and gravelly soils”, *Ph.D. Dissertation*, University of Texas at Austin, TX, USA, 364.

Mesri, G., & Godlewski, P. M. (1977). “Time and stress-compressibility interrelationship.” *Journal of the Geotechnical Engineering Division*, *103*(5), 417-430.

Mesri, G., & Ajlouni, M. (2007). “Engineering properties of fibrous peats.” *Journal of Geotechnical and Geoenvironmental Engineering*, *133*(7), 850-866.

Miura, S. and Toki, S., (1982), “A Sample Preparation Method and Its Effect on Static and Cyclic Deformation-Strength Properties of Sand,” *Soils Found*., Vol. 22, No. 1, pp. 61–77.

Moran, D. E., et al. (1958). “Study of deep soil stabilization by vertical sand drains.” *OTS Rep., PB151692, Publication No. 88812*, Bureau of Yards and Docks, Dept. of the Navy, Washington, D.C., 429.

Mroz, Z. (1967). “On the description of anisotropic work hardening,” *J. Mech. And Physics of Solids*, 15, 163-175

Mroz, Z., Norris, V. A., & Zienkiewicz, O. C. (1979). “Application of an anisotropic hardening model in the analysis of elasto–plastic deformation of soils.” *Geotechnique*, 29(1), 1-34.

Muir wood D., (1990) “*soil Behaviour and Critical State Soil Mechanics*” Cambridge, Cambridge University Press

Naesgaard, E., Byrne, P. M., & Wijewickreme, D. (2007). “Is P-wave velocity an indicator of saturation in sand with viscous pore fluid?”. *International Journal of Geomechanics*, *7*(6), 437-443.

Newmark, N.M. (1959). “A method of computation for structural dynamics,” *J. Eng Mech. Div.*, ASCE, 67-94

Okamura, M. and Inoue, T., (2012), “Preparation of Fully Saturated Models for Liquefaction Study,” *Int. J. Phys. Modell. Geotech*., Vol. 12, No. 1, pp. 39–46.

Park, D. and Y.M.A. Hashash (2004). “Soil damping formulation in nonlinear time domain site response analysis,” *J. of Earthquake Eng.,* 8(2), 249-274.

Perzyna, P. (1963). “The constitutive equations for rate sensitive plastic materials.” *Q. Appl. Math*. 20, 321- 332.

Perzyna, P. (1966) “Fundamental problems in viscoplasticity.” *Adv. Appl. Math.* 9, 243-377

Phillips C., and Hashash Y. M. A. (2009) “Damping formulation for nonlinear 1D site response analyses.” *Soil Dynamics and Earthquake Engineering*, 29(7), 1143-1158.

Poncelet, N., (2012), “Elaboration et Implémentation d’un Protocole de Laboratoire pour l’Etude du Potentiel de Liquéfaction de Résidus Miniers [Development and implementation of a laboratory procedure to study the liquefaction potential of mine

tailings],” Master’s thesis, Ecole Polytechnique de Montreal, Montreal, Canada (in French).

Prevost, J.H. (1977). “Mathematical modeling of monotonic and cyclic undrained clay behavior,” *Int. J. Numerical and Analytical Methods in Geomechanics*, 1 (2), 195-216

Prevost, J.H. (1985). “A simple plasticity theory for frictional cohesionless soils,” *Soil Dyn. Earthquake Eng.*, 4(1), 9-17

Pyke, R.M. (1979). “Nonlinear soil models for irregular cyclic loadings,” *J. Geotech. Eng.*, ASCE, 105(GT6), 715-726.

Pyke, R.M. (2000). *TESS: A computer program for nonlinear ground response analyses*. TAGA Engineering Systems & Software, Lafayette, Calif.

Rad, N. S. and Clough, G. W., (1984), “New Procedure for Saturating Sand Specimens,” *J. Geotech. Eng.,* Vol. 110, No. 9, pp. 1205–1218.

Rayleigh, J.W.S and R.B. Lindsay (1945). *The theory of sound, Dover Publications*, New York

Reinert, E., Stewart, J.P., Moss, R.,E.,S., and Brandenberg, S., (2014). “Dynamic Response of a Model Levee on Sherman Island Peat: A Curated Data Set”, *Earthquake Spectra*, May 2014, Vol. 30, No. 2 pp. 639-656

Restorethedelta.org, *http://www.restorethedelta.org/about-the-delta/overview-of-delta-agriculture/*

Richart, F. E., Jr., Hall, J. R., Jr., and Woods, R. D. (1970). "*Vibrations of soils and foundations*," Prentice-Hall, Englewood Cliffs, N.J.

Ridders C. J. F. (1979) "A New Algorithm for Computing a Single Root of a Real Continuous Function." IEEE Transactions on circuits and systems, 979-980.

Rietdijk, J., Schenkeveld, F. M., Schaminee, P. E. L., and Bezuijen, A., (2010), "The Drizzle Method for Sand Sample Preparation," *Physical Modelling in Geotechnics,* Taylor & Francis, London.

Robertson, P. K., & Cabal, K. L. (2015). "Guide to cone penetration testing for geotechnical engineering." *Gregg drilling*.

Rocscience (2014). Settle 3D – Settlement and Consolidation Analysis. https://www.rocscience.com/products/7/Settle3D

Roesset, J.M. and R.V. Whitman (1969). "Theoretical background for amplification studies." *Research report R69-15, Soils publications no. 231*, Massachusetts Institute of Technology, Cambridge, Massachusetts

Roscoe, K. H., Schofield, A., & Thurairajah, A. (1963). "Yielding of clays in states wetter than critical." *Geotechnique*, *13*(3), 211-240.

Roscoe, K.H. and J.B. Burland (1968). “On the generalized stress-strain behavior of ‘wet’ clay,” *J. Heyman and F.A. Leckie, eds., Eng. Plasticity*, University Press, Cambridge, 535-609

Rouainia, M., and D. Muir Wood. (2001) "Implicit numerical integration for a kinematic hardening soil plasticity model." *International journal for numerical and analytical methods in geomechanics* 25.13: 1305-1325.

Santamarina, J. C., Klein, K., and Fam, M., 2001, *Soils and Waves: Particulate Materials Behavior, Characterization and Process Monitoring*, Wiley, Chichester, UK, 488 pp.

Schnabel, P.B, J. Lysmer and H.B. Seed (1972). “SHAKE: A computer program for earthquake response analysis of horizontally layered site,.” *Report no. UCB/EERC-72/12*, Earthquake Engrg. Research Center, Univ. of Calif., Berkeley, California, 102p

Schneider, J.A., Hoyos, L., Jr., Mayne, P.W., Macari, E.J., and Rix, G.J. (1999), “Field and laboratory measurements of dynamic shear modulus of Piedmont residual soils”, *Behavioral Characteristics of Residual Soils*, GSP 92, ASCE, Reston, VA, pp. 12-25.

Seed, H. B., and Idriss, I. M. (1969). "Influence of soil conditions on ground motions during earthquakes." *ASCE J Soil Mech Found Div*, 95, 99-137.

Seed, H., Wong, R., Idriss, I., and Tokimatsu, K. (1986). ”Moduli and Damping Factors for Dynamic Analyses of Cohesionless Soils.” *J. Geotech. and Geoenviron. Eng.*, ASCE, 112(11), 1016–1032.

Shafiee, A., Brandenberg, S. J., & Stewart, J. P. (2013). “Laboratory investigation of the pre-and post-cyclic volume change properties of Sherman Island peat.” ASCE.

Shafiee, A., Stewart, J.P., and Brandenberg, S.J. (2015). “Reset of secondary compression clock for peat by cyclic straining.” *Journal of Geotechnical and Geoenvironmental Engineering*, Vol. 141, No. 3.

Shafiee A. (2016) “Cyclic and Post-Cyclic Behavior of Sherman Island Peat”, *Ph.D. Dissertation*, University of California, Los Angeles, CA, USA.

Sheahan, T.C., C.C. Ladd, and J.T. Germaine (1996) “Rate-dependent undrained shear behavior of saturated clay,” *J. Geotech. Engr.,* ASCE, 122 (2), 99-108

Silver, M. L., and Seed, H. B. (1971). "Volume changes in sands during cyclic loading." *Journal of Soil Mechanics and Foundation Division, American Society of Civil Engineers*, 97(SM9), 1174-1178

Skempton, A. W. (1954). “The pore-pressure coefficients A and B.” *Geotechnique*, *4*(4), 143-147.

Stewart, J.P., Kwok, A.O., Hashash, Y.M.A., Matasovic, N., Pyke, R., Wang, Z., and Yang, Z. (2008). "Benchmarking of nonlinear geotechnical ground response

analysis procedures," *Report PEER 2008/04*, pacific Earthquake Engineering Research Center, University of California, Berkeley.

Stokoe, K. H., II, Bay, J. A., Rosenbald, B. L., Hwang, S. K., and Twede, M. R., (1996), ‘‘In Situ Seismic and Dynamic Laboratory Measurements of Geotechnical Materials at Queensboro Bridge and Roosevelt Island,’’ *Geotechnical Engineering Rep. No. GR94-5*, Civil Engineering Dept., Univ. of Texas at Austin.

Stuit, H. G., (1995), *Sand in the Geotechnical Centrifuge*, Delft University of Technology, The Netherlands.

Taiebat, M., & Dafalias, Y. F. (2008). “SANISAND: simple anisotropic sand plasticity model.” *International Journal for Numerical and Analytical Methods in Geomechanics*, 32(8), 915-948.

Takahashi, H., Kitazume, M., Ishibashi, S., and Yamawaki, S., 2006, “Evaluating the Saturation of Model Group by P-Wave Velocity and Modelling of Models for a Liquefaction Study,” *Int. J. Phys, Modell. Geotech*., Vol. 6, No. 1, pp. 13–25.

Terzaghi, K. (1925). “*Erdbaumechanik auf bodenphysikalischer Grundlage”* (p. 399). Vienna: F. Deuticke.

Terzaghi, K., & Peck, R. B. (1967). *Soil Mechanics in Enginnering Practice.* Second Edition, Wiley, New York, 729 p.

Terzaghi, K., Peck, R. B., and Mesri, G. (1996). “*Soil mechanics in engineering practice*”, Wiley, New York, 549 p.

Tokimatsu, K., & Sekiguchi, T. (2007, June). “Effects of dynamic properties of peat on strong ground motions during 2004 mid Niigata prefecture earthquake.” In *Proc., 4th Int. Conf. on Earthquake Geotechnical Engineering, Thessaloniki.*

Torres, R.A., Abrahamson, N.A., Brovold, F.N., Cosio, G., Driller, M.W., Harder, L.F., Marachi, N.D., Neudeck, C.H., O’Leary, L.M., Ramsbotham, M., Seed, R.B. (2000). “Seismic vulnerability of the Sacramento – San Joaquin Delta Levees,” Levees and Channels Technical Team, Seismic Vulnerability Sub-Team, *CALFED Bay-Delta Program*, 30 pp. plus appendices.

Tressider, J. O. (1958). “A review of existing method of road construction over peat.” *Tech. Paper No. 40*, DSIR, RRL, London.

Verdugo, R., & Ishihara, K. (1996). “The steady-state concepts and static liquefaction of silty sands.” *J Geotech Eng*, 124(9), 869-877.

Von Mises, R. (1913). “Göttinger nachrichten.” *Math-Phys Klasse*, 582.

Vucetic, M. (1990). “Normalized behavior of clay under irregular cyclic loading.” *Canadian Geotech. J.*, 27, 29-46.

Vucetic, M., & Dobry, R. (1991). “Effect of soil plasticity on cyclic response” .*Journal of Geotechnical Engineering*, *117*(1), 89-107.

Vucetic, M. (1994). “Cyclic threshold shear strains in soils.” *Journal of Geotechnical engineering*, 120(12), 2208-2228.

Vucetic, M., G. Lanzo, and M. Doroudian (1998). “Damping at small strains in cyclic simple shear test.” *J. Geotech. and Geoenviron. Eng.*, ASCE, 124(7), 585-594.

Wang, Z.L., Q.Y. Han, and G.S. Zhou (1980). “Wave propagation method of site seismic response by visco-elastoplastic model,” *Proc. of Seventh World Conf. on Earthquake Eng.*, V2, 379-386

Wang, Z.L., Y.F. Dafalias, C.K. Shen (1990). “Bounding surface hypoplasticity model for sand,” *J. Eng. Mech.,* ASCE, 116 (5)

Wehling, T. M., Boulanger, R. W., Arulnathan, R., Harder Jr, L. F., & Driller, M. W. (2003). “Nonlinear dynamic properties of a fibrous organic soil.” *Journal of geotechnical and geoenvironmental engineering*, *129*(10), 929-939.

WGCEP (Working Group for California Earthquake Probabilities) (2003). "Earthquake probabilities in the San Francisco Bay Area: 2002−2031." *U.S. Geological Survey*, Open- File Report 03-214.

Yamaguchi, H., Ohira, Y., Kogure, K., and Mori, S. (1985a). “Undrained shear characteristics of normally consolidated peat under triaxial com- pression and extension conditions.” *Japanese Society of Soil Mech., and Found. Eng.*, 25(3), 1–18.

Yamaguchi, H., Ohira, Y., Kogure, K., and Mori, S. (1985b). “Deformation and strength properties of peat.” *Proc., 11th Int. Conf. on Soil Mechanics and Foundation Engineering*, Vol. 4, 2461–2464.

Yamaguchi, H., Yamaguchi, K., and Kawano, K. (1987). “Simple shear properties of peat.” *Proc., Int. Symp. on Geotechnical Engineering of Soft Soils*, M. J. Mendoza and L. Montañez, eds., Sociedad Mexicana de Mecánica de Suelos, Coyoacán, Mexico, 1, 163–170.

Yang, Z. (2000). “Numerical modeling of earthquake site response including dilation and liquefaction,” *PhD Thesis*, Dept. of Civil Eng. and Eng. Mech., Columbia University, NY, New York

Yee E., Stewart J.P., Tokimatsu K. (2013) “Elastic and large-strain nonlinear seismic site response from analysis of vertical array recordings”, *J. Geotech. Geoenvion. Eng.,* 139 (10), 1789-1801.

Yniesta, S., Lemnitzer, A., Cappa, R., and Brandenberg, S., (2015) "Vacuum Pluviation Device for Achieving Saturated Sand", *Geotechnical Testing Journal*, Vol. 38, No. 3, pp. 355-360.

Yniesta S. and Brandenberg, S., (2016) “Stress-Ratio-Based Interpretation of Modulus Reduction and Damping Curves” *J. Geotech. Geoenviron. Eng.*, under review.

Yniesta, S., Brandenberg, S.J., and Shafiee A. (2016) “One-dimensional Non-linear Model for Site Response Analysis” *Soil Dynamics and Earthquake Engineering*, under review.

Zalachoris, G., and E. M. Rathje (2015). Evaluation of one-dimensional site response techniques using borehole arrays, *J. Geotech. Geoenviron. Eng.*, Paper 04015053.

Zhao, Y., Gafar, K., Elshafi, M. Z. E. B., Deeks, A. D., Knappett, J. A., and Madabhushi, S. P. G., 2006, “Calibration and Use of a New Automatic Sand Pourer,” *Proceedings of the 6th International Conference on Physical Modelling in Geotechnics, 6th ICPMG ’06*, Hong Kong, Aug 2–6, 2006, CRC, Boca Raton, FL, pp. 265–270.